UNIVERSITY OF BIRMINGHAM

Inclusions and Hydrogen and Their Effects on the Quality of Direct Chill Cast and Flat Rolled Aluminium Alloys for Aerospace Applications

By
Alexander James Gerrard

A thesis submitted to the college of Engineering
and Physical Sciences of
The University of Birmingham
For the degree of
Doctor of Engineering

School of Metallurgy and Materials
College of Engineering and Physical Sciences
University of Birmingham
Birmingham B15 2TT
United Kingdom
September 2014

Abstract

Flat rolled Al alloys manufactured using the Direct Chill (DC) casting process are used in safety critical applications and therefore need to be of the highest possible quality. The presence of inclusions and pores can be damaging to the mechanical properties, so the liquid metal is cleaned using a mixture of inert Ar and reactive Cl gases before casting. These gases are bubbled up through the molten metal and remove inclusions, (such as oxides), by agglomeration and floatation, and dissolved H, (that is responsible for porosity within in the casting), by diffusion and floatation of the gas out of the melt. This project is comprised of three sections, with the central theme aimed at better understanding the formation and control of inclusions and porosity in DC cast and hot rolled Al alloys.

The first section explores the aetiology of defects in DC cast and hot rolled Al plate, found using ultrasound. Inclusions extracted from 7050 alloy plate, (typically 2.3% Cu, 2.5% Mg, 6.2% Zn, 0.12% Zr), were extracted and examined using scanning electron microscopy (SEM). The inclusions were composed of two phases. A second type of defect found in thin gauge, (<45 mm), 7475 alloy plate, (typically 1.5% Cu, 2.3% Mg, 6.7% Zn, 0.21% Cr), was established to be a coarse grain structure, caused by excessive widening of large cross section ingots during hot rolling.

The second section aimed to provide a better understanding of the role of Cl on degassing. Ar and Ar and Cl containing gas bubbles were trapped in solidifying Al alloys. Gases were extracted using a mass spectrometer and the composition was established to be a mixture of H_2, N_2 and H_2O. The metal-gas interface was then examined using Scanning Electron Microscopy (SEM). The effects of Cl on the degassing performance of a Spinning Nozzle Inert Floatation (SNIF) degassing unit were then approached statistically using ALSCAN. While different 7xxx alloys appeared to be influenced by Cl differently, with average improvement or reduction in degassing efficiency ranging from +8 to -5%, the degassing of 7xxx alloys was, on the whole, not significantly affected by the presence of Cl. Finally, 20 kg melts of Al and Al alloys were doped with H and subsequently degassed, and the reduction in H over time was measured using ALSPEKH, over a range of 0.35 ml/100g to 0.15 ml/100g. The degassing rate of a 7010 alloy (typically 1.7% Cu, 2.3% Mg, 5.2% Zn, 0.13% Zr) appeared to be reduced the most when Cl was present, compared to 5083 alloy, (typically 4.5% Mg, 0.7% Mn, 0.15 Cr), and pure Al.

In the third section the LECO H determination device was used to degas Al specimens to very low levels, (<0.005 ppm H), in order to simulate the H absorption into double oxide film defects. Such defects have been proposed to act as reservoirs into which H can diffuse and promote the formation of H gas porosity. Degassed specimens were melted under air or N_2 atmosphere, so that when cracks formed in the surface oxide layer either Al_2O_3 or AlN formed. After subsequent exposure to pure H_2 gas the specimens that formed AlN were found to have absorbed more H than those heated in air, because the AlN was porous compared to fully dense alumina.

The research and work presented within therefore provides a better understanding of: the formation of specific defects in wrought Al alloy plate, the influence of Cl on the degassing of Al alloys, and the process of diffusion of H into double oxide film defects as they react with the surrounding melt.

For my family; Linda, Tony and Michael.

Acknowledgements

I wish to express by warm and sincere thanks to my friends and colleagues at the University of Birmingham and Alcoa Europe for their enthusiasm, motivation, friendship and support throughout my EngD. It has been both challenging and rewarding, and has undoubtedly changed my life for the better.

I would like to acknowledge and thank the EPSRC and Alcoa for financial support, and for providing sponsorship, access to equipment and training and the opportunity to work in a thrilling technical and industrial environment. I would like to acknowledge the teaching and administration staff at the University of Birmingham, and the various technicians who have assisted me at various points throughout my studies.

In particular I would like to thank Adrian Caden for his technical knowledge, skills and assistance with experiments at the University of Birmingham. I would like to thank fellow PhD students Elizabeth Hinton and Richard Sheridan for taking the time to help with experimental work at various points throughout this project, and I would also like to thank my numerous colleagues in the Remelt, Plate, Quality and Technical departments at Alcoa Europe, in particular, my industrial supervisors Neil Merill and Alex Morris for their guidance and support.

I would also like to thank my friends and family for keeping me (more or less) sane over the last five years. Without them I simply would not have made it.

Finally I would like to express my deep and sincere gratitude to my supervisor, Bill Griffiths, for giving me this opportunity. He has provided guidance, knowledge, resource, motivation and without his support it would not have been possible to complete this work. It has been an honour to work under his supervision.

Table of Contents

List of Figures

List of Tables

Chapter 1 Introduction

Alcoa is the third largest aluminium producer worldwide and involved with every facet of the aluminium industry; from extraction and refinement of bauxite ore to smelting of aluminium to production and recycling of aluminium products. Alcoa Flat Rolled Products based in Kitts Green, Birmingham, UK, is a producer of wrought aluminium plate products for use within the aerospace, defence, marine and automotive industries. Alcoa Kitts Green produces 47 different alloys and in 2009 over 62,000 tons of aluminium alloys were cast in the foundry. In 2013 this figure increased to over 80,000 tons. Due to the numerous cutting, sawing and cropping operations required throughout the production process the recovery of cast tons is about 50%. This leads to the generation and utilisation of vast amounts of in-house scrap that is re-melted and re-cast cyclically.

Kitts Green produces aluminium plate, primarily 7xxx wrought alloys, for example 7010 (typically 1.7% Cu, 2.3% Mg, 6.0% Zn, 0.13% Zr), 7050 (typically 2.3% Cu, 2.1% Mg, 6.0% Zn, 0.12% Zr) and 7075 (typically 1.6% Cu, 2.5% Mg, 5.6% Zn, 0.23% Cr). Alongside these are 2xxx, 5xxx and 6xxx alloys, and to a lesser extent 8xxx (and 2xxx) alloys containing Li. The detailed composition ranges of each alloy used in this project can be found in Table 3.1. Plate products are produced by first Direct Chill (DC) casting ingots (ranging from about 900 mm – 1500 mm width, 325 – 525 mm thick and up to 5 m in length), see Figure 1.1. Ingots are scalped, homogenised and hot rolled into plate, to a thickness (gauge) range of about 5 – 300 mm, and up to 30 m in length, see Figure 1.2. Hot rolled plates are solution treated, quenched and stretched before being artificially aged and ultrasonically evaluated for defects such as pores or inclusions.

The quality of the plate product is controlled primarily by the quality of the liquid metal feeding the casting. A quality product will have predictable mechanical properties, it will be homogeneous, free from damaging inclusions and porosity and other gross physical defects such as cracks and laminations and surface damage such as scratches.

Figure 1.1 An example of DC cast Ingot that has been scalped. Figure 1.2 An example of rolled aluminium plate.

Producing aluminium plate is a multi-stage process and as such material can take up to two months to reach completion (from first casting the ingot to the plate product leaving the plant). A failure at any stage of the process will produce scrap and necessitate a remake which is costly to the business and should be avoided or minimised. The most undesirable situation is that a plate fails ultrasonic testing because at this point the most value has been added to the product (by energetic processes, labour and time occupying plant capital). The cost to scrap material (2013 Figures) is estimated to be approximately £200/t after casting, but closer to £1000/t if material is scrapped after ultrasonic evaluation [1].

In 2009 an internal review of the performance of Alcoa Flat rolled products was undertaken, focused on evaluating causes of scrap within production processes across the site. The primary objective was to identify the major sources of scrap in order to make improvements and improve profitability. Maintaining low manufacturing costs, eliminating costly rejections which require additional re-make material and improving on time delivery to customers are critical to a successful, more efficient, and leaner business.

During the period 2004 – 2008 overall rejection rates (for all causes) had remained unmoved, less than 10% per year [2]. Features detected within the plates, (using ultrasound), are commonly referred to as ultrasonic indications. Such indications suggest that defects, (such as inclusions or porosity), may be present within the material, which may cause the plate to be scrapped as a result. Plates scrapped due to the presence of these indications were two of the top three issue generating scrap during 2008, accounting for 24% and 13% [2] of the top 10 causes of scrap respectively, (these figures are based on the total weight of material scrapped during this period). These issues are summarised in Figure 1.4. Improvements in these areas would have significant positive impact on costs and thus profitability.

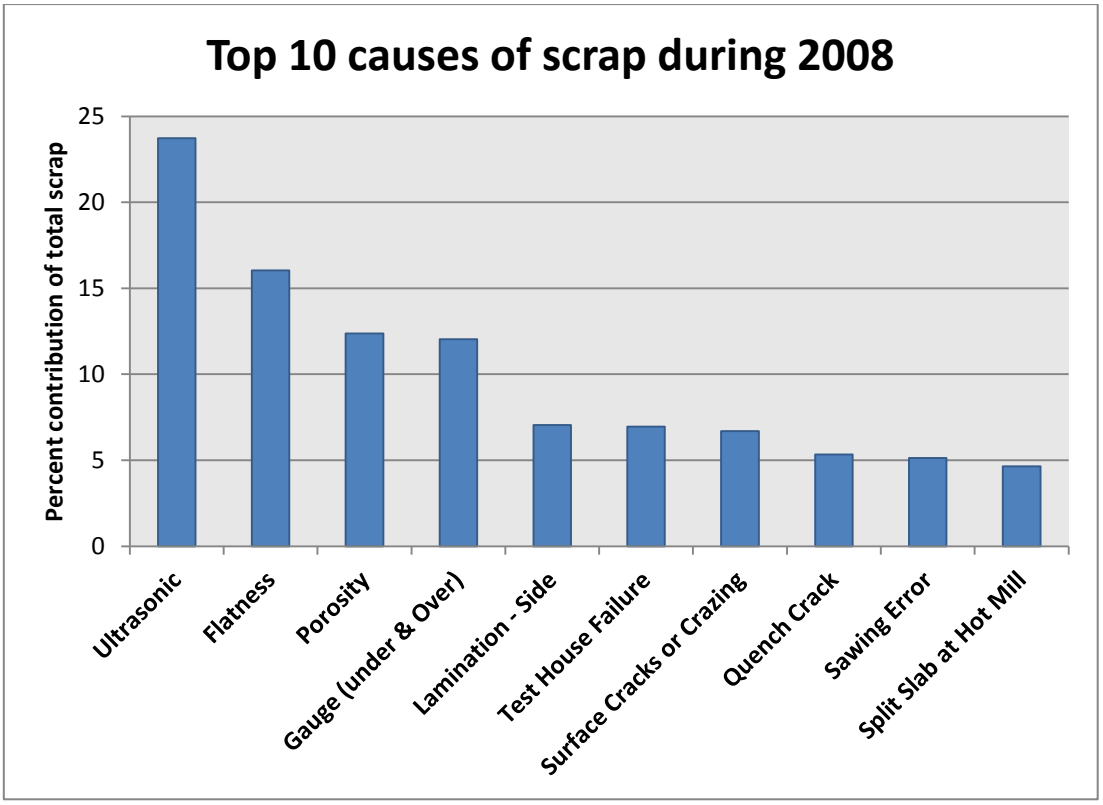

Figure 1.3 The top ten causes of scrap material at Alcoa Kitts green during 2008. Ultrasonic indications (inclusion) and porosity are responsible for 24% and 13% of the total, respectively [1].

The work within this thesis is focused on three main areas which are described briefly and then in detail.

1) The aetiology of ultrasonic indications in DC cast and hot rolled products.
    a. Inclusions in 7050 alloy plate.
    b. “High noise” at the edges of thin gauge (<45 mm) 7475 alloy plate, (typically 1.5% Cu, 2.3% Mg, 5.7% Zn, 0.21% Cr).

2) Improved understanding of the effects of Cl on the degassing of Al alloys.
    a. An examination of Ar and Ar + Cl gas bubbles trapped in solidifying Al alloys; 7010, 5083 (typically 4.5% Mg, 0.7% Mn, 0.15 Cr) and 2L99 (typically 0.3% Mg, 7% Si) using a Pore Gas Analyser (PGA).
    b. The effects of Cl on the degassing performance of 7010, 7050 and 7075 alloys using a Spinning Nozzle Inert Floatation (SNIF) unit, measured using ALSCAN technology.
    c. The effects of Cl and alloy Mg content on the degassing rate of pure Al and Al alloys; 7010 and 5083, measured using ALSPEK H technology.

3) The absorption of H in Al alloys using LECO.
    a. The degassing and absorption of H into Al and Al alloys measured using LECO technology.
    b. The absorption of H into LECO samples across aluminium oxide (Al_2O_3) and aluminium nitride (AlN) layers formed on Al and Al alloy 5083; simulating the absorption of H into a double oxide film defect.

The first section reviews two specific defects that were noted to have generated scrap material at Alcoa. In both instances plates were ultrasonically scanned and indications that were revealed during the scan suggested that plates were of inferior quality, which led to the plate (or part of the plate) being scrapped. The aim within this first section was to investigate the causes of these indications and to eliminate them from future production. Both investigations were carried out in an industrial setting.

In 1a, two 7050 variant alloys, referred to as AE (typically 2.2% Cu, 2.2% Mg, 6.2% Zn, 0.11 - 0.15 % Zr) and AT (typically 2.2% Cu, 2.2% Mg, 6.2% Zn, 0.11 - 0.14% Zr), were observed to have significantly different scrap / plate rejection rates. Various AE plates were found to contain a dispersion of point defects that indicated inclusions were present within the plates, although the composition and origins of these defects was not understood.

The scrap generated (for this type of "point defect" ultrasonic indication) during quarter 1 (Q1) 2009 is shown, (by contributing alloy), in Figure 1.5. Examples of plates containing these defects can be seen in Figures 4.1 - 4.3. AA, AB and AC are 7010 alloy variants, (typically 1.7% Cu, 2.0% Mg, 6.0% Zn, with Fe contents of <0.1, <0.13 and <0.15 respectively), AE and AT are 7050 alloy variants and H is a 6082 alloy variant (typically 1% Si, 0.8% Mn). The volumes of material produced, (and scrapped), is commercially sensitive information, so values are expressed as percentages over a period of time. The AE alloy was accountable for 45%, and AT 19%, of the total material scrapped during Q1 2009.

3.6% of all the AE alloy plate produced during Q1 2009 were scrapped for "point defect" ultrasonic indications, compared to just 0.7% of AT alloy plate. Based on the volume of material produced, (significantly more AT was produced than AE during this period), scrap rates were about 5 times higher in AE compared to AT.

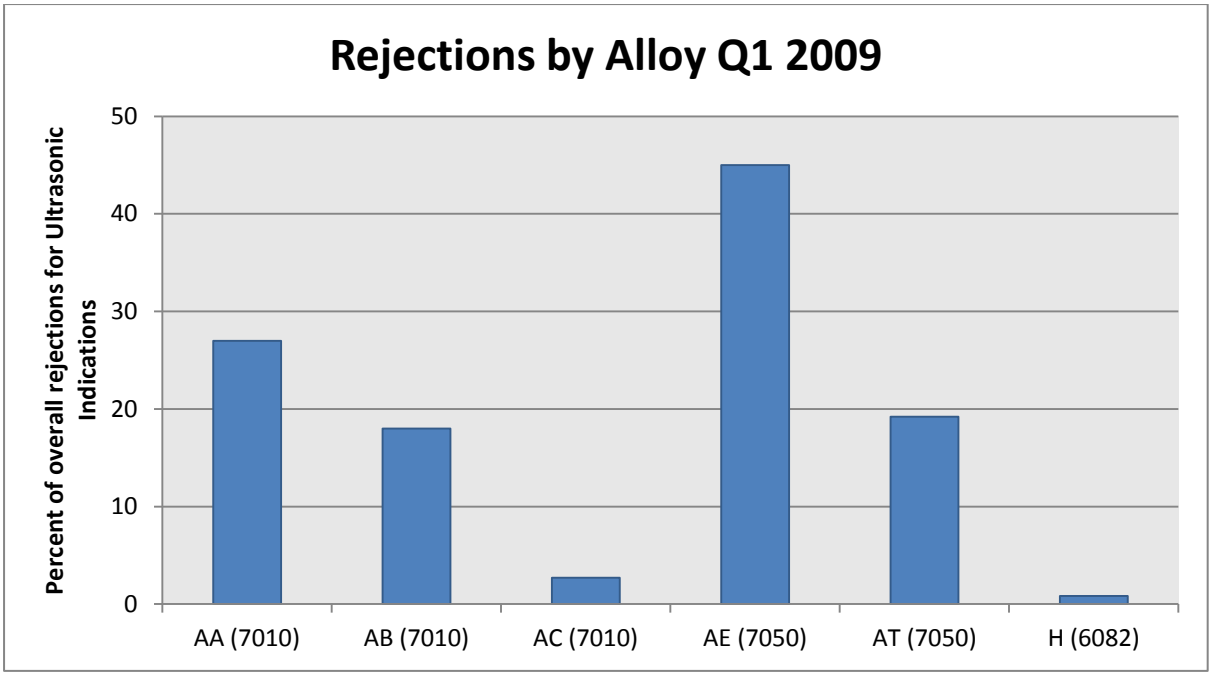

Figure 1.4 Ultrasonic rejection rates for common alloys cast at Alcoa during Q1 2009 [1].

In 1b, a particular type of defect was found to occur only in 7475 alloy plates that were less than 45 mm thick. The defect occurred down the parallel edges of the plate and often required these areas to be cut away and scrapped. The ultrasonic response was attributed to the presence of sub-surface porosity by the operators (due to the type of ultrasonic response), but there was no evidence for this conclusion. 5.4% of thin gauge plates, (typically <45 mm thick), produced during 2009 contained this particular type of defect. The source of this porosity was not clear and required detailed investigation.

Section two investigates the effects of Cl on the removal of H (commonly referred to as degassing) of Al alloys. The literature on this subject is contradicting, with authors reporting positive, neutral and negative effects on the rate of H removal when Cl is present as an addition to the inert gases (typically Ar or N_2) used in this process. Experiments were designed to evaluate the effects of Cl and Mg on the degassing efficiency of wrought alloys.

In 2a inert and chlorinated gas bubbles were caught within solidifying Al and their contents were assessed using the PGA, before dissection and evaluation by Scanning Electron Microscopy (SEM). Images were analysed using secondary electron (SE) imaging, (for evaluating topography), or backscattered electron analysis (BSE), (for highlighting contrasts in chemical composition). Finally, Energy-dispersive X-ray spectrometry (EDX) is used for the elemental analysis, (chemical characterisation), of samples. The chemical reactions that take place at the bubble – metal interface would play a key role in the flux of H and the removal of inclusions during degassing, and experiments were designed to investigate these interactions.

In 2b two ALSCAN units were used to assess the performance of a SNIF degassing unit that was present on Alcoa's DC3 casting station. The degasser was used to treat the liquid metal with and without Cl additions and the effects on degassing rate were examined statistically. This section evaluates the degassing of Al alloys in an industrial setting. In section 2c an ALSPEK H unit was used to assess the degassing process of small (20 kg) Al melts, with and without Cl and with varying alloy Mg content. Experiments were designed to monitor the rate of degassing as a function of alloy composition (specifically Mg content) and the composition of the gas used to flux H out of the metal.

The third section, 3a, is an appreciation of the LECO H determination device and how it can be used to degas Al samples to very low levels (<0.001 ppm). The absorption of H into samples and the removal of H was assessed using the LECO. In section 3b LECO samples that were degassed using the procedure developed in 3a were heated in various gaseous atmospheres and exposed to pure H_2 gas. The absorption of H then was measured using the LECO and related to the oxide or nitride surface layer that formed on the surface of the

sample during processing. This was done to better understand the diffusion of H in double oxide film defects, (otherwise referred to as bifilms), and their effects on Al alloys.

Chapter 2 literature review

2.1 Wrought aluminium alloys:

Al alloys are the primary material used in aerospace components such as wing skins and fuselages due to the appealing properties that these alloys offer: a high strength to weight ratio, good strength, toughness, fatigue resistance and acceptable corrosion resistance, (some 2xxx and 7xxx alloys may be clad with pure Al for protection against the environment). High strength Al alloys are commonly used in structural aerospace components in the aerospace and defence industries and as part of safety critical components. Such alloys need to be of a high quality to ensure optimal performance.

Al in its pure form has excellent corrosion resistance, thermal and electrical properties but has a poor strength, less than 100 MPa [3] depending on purity. Alloying Al with elements such as Cu and Mg will improve the strength through solute hardening. Additions of Si (in combination with Mg) and Zn will allow precipitation and age hardening. The 2, 6 and 7xxx series alloys (wrought) are heat treatable systems, which respond to solution and age hardening, having a profound effect on mechanical properties. The other alloy series can only be hardened further by cold working and grain refinement. The strongest Al alloys are based on the Al-Cu-Mg-Zn system and can have tensile strengths in excess of 550 MPa [3].

Al alloys are divided into two categories; cast and wrought. Casting alloys tend to contain large additions of Si as it increases melt fluidity and ease of casting and they are commonly used in the automotive industry. The wrought alloy system is divided into 9 categories, by

the major alloying elements in use. The applications for each series can be quite varied and are briefly outlined in Table 2.1.

Flat rolled products such as those produced at Alcoa Kitts Green are typically from the two, five, six and seven series systems.

Series	Alloying elements	Example of typical use
1xxx	Controlled unalloyed (Fe, Si).	Thermal and electrical applications
2xxx	Cu (Mg).	Aircraft plate
3xxx	Mn.	Aluminium foil
4xxx	Si.	Welding rods and brazing sheet
5xxx	Mg.	Marine applications, beverage cans
6xxx	Mg, Si.	Extrusions, e.g. Bicycle frame.
7xxx	Zn, Cu, Mg (Cr, Zr).	Aircraft structural components
8xxx	Li or Sn. Miscellaneous category.	Al-Li alloys
9xxx	Reserved for future use.	N/A

Table 2.1 The wrought aluminium alloy series, major alloying elements (minor elements are in brackets) along with typical examples where they might be used [4], [5], [6].

2.1.1 Direct chill (DC) casting of aluminium alloys:

DC casting was invented independently by VAW (Germany) and Alcoa (USA) [7] [8] and was an essential technological evolution to improve the quality of large castings which were originally produced using book, or permanent moulds. Problems arose because of the increasing demand for larger plate for larger aircraft, which in turn generated demand for

larger pre-cursor ingots. During and after casting, larger ingots will cool slower as they contain a greater thermal mass and because of this ingots cast using those original techniques suffered from macro segregation of alloying elements (and thus non-homogenous properties) [9], problems associated with macroscopic porosity and gross volume defects.

The properties of these alloys are enhanced using DC casting process as it rapidly solidifies the ingot compared to any sand or mould based casting process. This is achieved by first forming a thin solid shell layer (primary cooling) formed when the molten metal makes contact with a water cooled mould. The solidifying metal ingot is then sprayed with water (secondary cooling) as detailed in Figure 2.1. This process rapidly chills and solidifies the interior of the ingot.

The benefits of rapid solidification through DC casting are;

- Macro segregation is eliminated, although a homogenisation heat treatment is typically still required after casting is completed to relieve micro segregation. Micro segregation may occur over a few tens of μm's, while macro segregation occurs over many mm's [9].
- Primary cast porosity (composed of macroscopic shrinkage porosity, feeding and dimensional defects) are eliminated [10].
- Microscopic inter-dendritic porosity is reduced, as is the growth of H induced gas porosity.
- Rapid cooling encourages formation of a finer grain structure [11] which will lead to improved mechanical properties.

DC castings still require degassing to remove dissolved H gas from the liquid metal before casting and also require additions of grain refining inoculants (such as TiBAl) to produce an equiaxed grain structure and provide acceptable mechanical properties in the final product [12], [13].

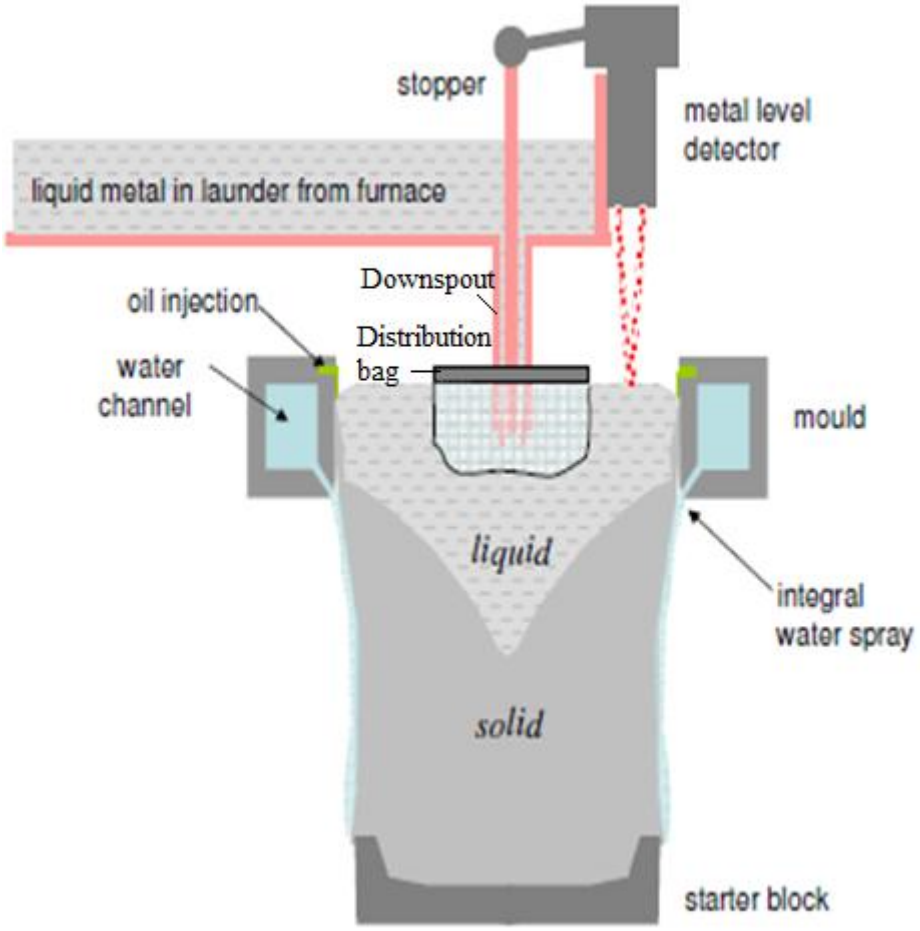

Figure 2.1 Schematic of the Direct Chill (DC) casting process [11].

2.2 Molten metal quality:

Al is a reactive metal, which is why it is so energy intensive and expensive to extract from ore. Producing components using entirely primary Al is not an economic option. There is therefore a driving force for producers to use as much secondary Al as possible, by recycling, because the amount of energy required to re-melt Al is only a fraction, about 5%, [15] of that required to produce primary Al from Al_2O_3 using electrolysis. The drawback is that secondary Al will have been melted and processed at least once previously, and can contain increasing amounts of contaminants and undesirable alloying elements (e.g. Fe, Si) with each cycle of use. These contaminants can then influence the chemistry, processing or mechanical properties of future castings, and cannot be removed by techniques such as fluxing.

Obtaining a consistent casting quality and being able to reproduce mechanical properties is the primary challenge for foundries. The liquid metal quality is one of the most important factors that influence the quality of the casting and the liquid quality is controlled by three factors:

- The levels of dissolved H within the melt, and subsequent porosity in the casting.
- The concentration of non-metallic inclusions present in the liquid metal, primarily oxides.
- The concentration of trace elements dissolved within the metal.

This review will discuss in detail the influence of these three factors on molten metal quality. The focus of the review will then move to the methods of monitoring H gas content and inclusions and their removal from the melt.

2.2.1 Solubility of hydrogen in aluminium and its alloys

Al (unlike many of the other non-ferrous metals) can only dissolve one gas within its microstructure. H is capable of diffusing into Al in the atomic state [16] [17], whereas other gases such as O_2 and N_2 can only enter the bulk in the form of compounds, after reacting with the melt surface, or within bi-films, entrained under the surface of the melt.

H dissolved in the solid metal must fit in appropriate interstices within aluminium's FCC structure as shown in Figure 2.2. Octahedral (the largest) sites have an effective radius of 0.059 nm in the solid [18] and the H, as a diatomic molecule H_2, occupies 0.074 nm so cannot fit within the Al lattice. The monatomic atom or proton (H^+) however has a radius of 0.053 nm and can fit in the octahedral position, so all H that enters the solid solution will be in this form [19]. The increase in volume on melting increases the size of these 'holes' to about 0.060 nm [19].

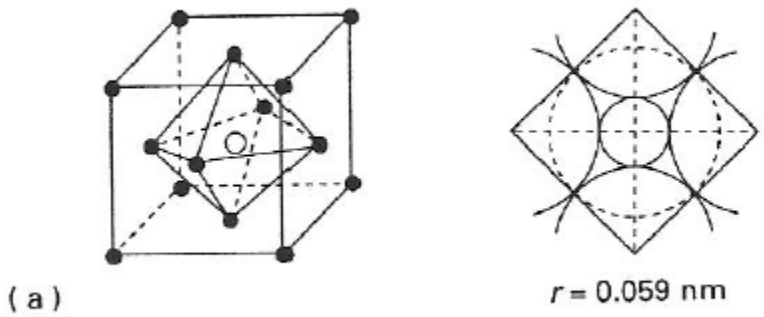

Figure 2.2 H protons residing within the octahedral sites within the aluminium FCC lattice structure [18].

H enters the metal through reaction between the melt and various H sources such as damp refractory ceramics (which are often hygroscopic), wet tools, melt additions or re-melt material which will contain elevated levels of H, and by reaction with water vapour in the air.

The reaction between water and Al is shown in Eq.1 and illustrated in Figure 2.3. Essentially, the melt is oxidised and the reaction liberates H_2 which is free to either disperse into the environment or enter the metal. The oxidation reaction is exothermic and so highly favourable that virtually all traces of water contacting the metal are converted to H. This principle also applies to Mg as shown in Eq.2.

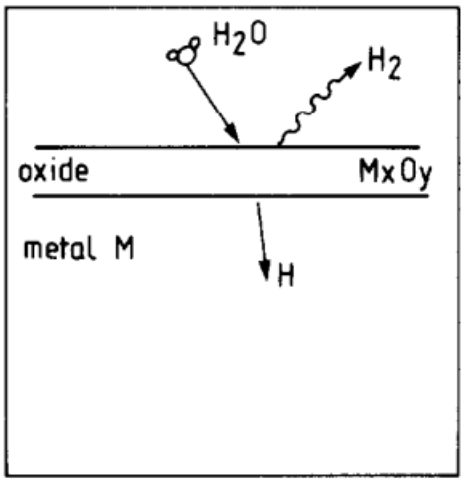

Figure 2.3 The reaction of Al and Mg with water vapour; oxidation of the melt surface occurs forming an oxide layer at the surface of the melt. H_2, the bi-product of the reaction, is either lost to the environment or absorbed into the melt as a proton [20].

$$3H_20 + 2Al \rightarrow Al_2O_3 + 6H\ldots \text{ Eq.1}$$

$$H_20 + Mg \rightarrow MgO + 2H \ldots \text{ Eq.2}$$

As water vapour is always present in production environments it is virtually impossible to eliminate H from solution in the liquid metal. In reality water vapour is so abundant that only reaction kinetics and the capacity of the metal to receive the gas affect absorption.

The equation predicting the partial pressure of H in equilibrium with a given concentration of H in solution in the melt is given by Sieverts law:

$$[\mathrm{H}]^2 = \mathrm{kP_{H2}} \approx \mathrm{kP_{H2O}} \ldots \text{Eq.3}$$

which describes the squared relationship between a diatomic gas and its pressure. The constant k is determined, and is affected by alloying element additions and the metal temperature.

The change in solubility of H with temperature is approximately linear, with the H content of the metal roughly doubling with every 110^{o}C increase in temperature at a constant pressure above the melting point [21]. Units used to express H content in Al are parts per million (ppm) and millilitres or cubic centimetres of H, corrected to standard temperature and pressure, per 100 g of metal. The relationship between the two is 1 ppm = 1.12 ml/100g.

To put the solubility levels into context, the calculated maximum solubility of H in pure Al is 0.88 ml/100g at 700^{o}C [22] but the actual H content in solution is dependent on the local atmospheric vapour pressure of water (ambient relative humidity, RH). For example at 10^{o}C and 50% RH air contains 0.6% water (0.006 atmospheres) which corresponds to an equilibrium H content of approximately only 0.06 ml/100g within pure Al.

The metal will absorb H readily until it reaches equilibrium with the atmosphere and efforts to raise the H content above this point will lead to a natural degassing process. Likewise,

driving the H content below equilibrium levels will lead to a net increase in H content over time [16] [23] as demonstrated in Figure 2.4. It is difficult to drive the H content of the metal to high or low extremes, for instance driving the H content of pure (99.8%) Al at 700^{o}C to its maximum solubility requires steam injection directly into the melt over a prolonged period of time to increase the melt H content to this value [24].

Furnaces using hydrocarbon fuels create environments that are both hot, 800 - 1000^{o}C, and humid due to the production of water vapour through combustion (see Eq.4), where the flame is directed at the melt surface, significantly increasing the H content of the metal above atmospheric conditions [18]. In reality one might expect to see metal H content values in the range of 0.3 – 0.4 ml/100g exiting a flame fuelled furnace around 700^{o}C [25]. The maximum solubility of H in pure Al at different temperatures is shown in Figure 2.5.

$$CH_4 + 2O_2 \rightarrow CO_2 + 2H_2O \text{... Eq.4}$$

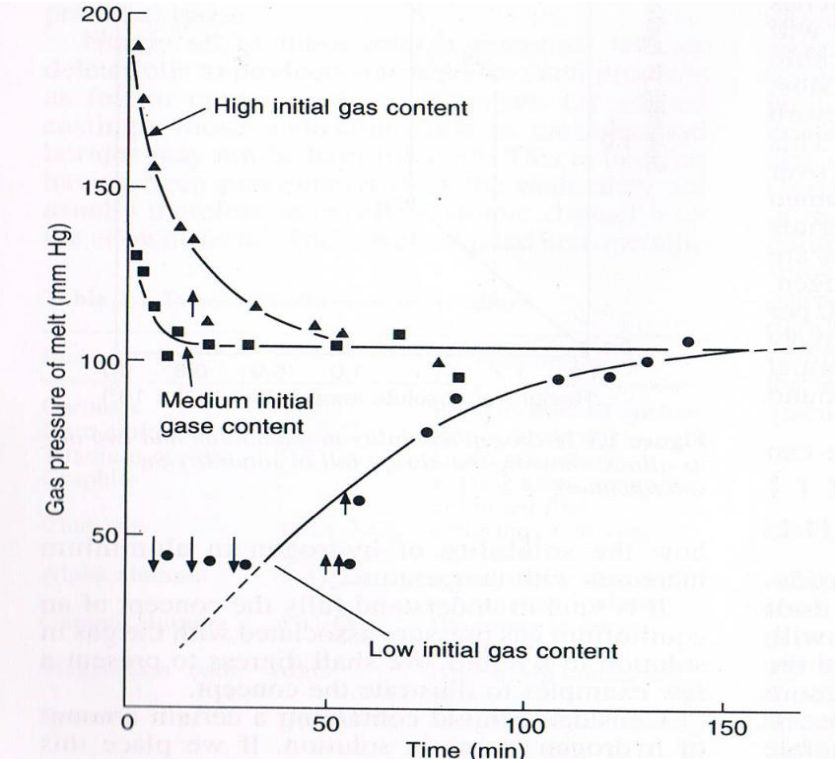

Figure 2.4 The H content of liquid Al will naturally come to equilibrium with the environment over time [18].

Temperature		State	Solubility, S (cm^3/100 g)
°C	T/K		
450	723	Solid	0.004
500	773	Solid	0.008
550	823	Solid	0.015
600	873	Solid	0.026
660	933	Solid	0.046
660	933	Liquid	0.67
700	973	Liquid	0.88
750	1023	Liquid	1.20
800	1073	Liquid	1.60
850	1123	Liquid	2.07
900	1173	Liquid	2.62

Figure 2.5 The solubility of H at 101 kPa (1 atm) in pure Al determined by Talbot [18].

Alloying elements will have an influence on the solubility of H within the Al melt because they change the mean atom size of the melt and influence the size of interstitial sites where H resides [19] [21] [26] [27] [28]. Alloying elements will raise or lower the solubility depending on the particular element and the amount present. Si, Fe and Cu are reported to decrease the H solubility in the melt while Mg and Li increase the solubility. Zn and Ti have only minor effects, as shown in Figure 2.6. The change in solubility occurs because the mean atom size is changed when alloying elements are introduced into the melt which in turn affects the size of the inter-atomic spacing and either increases or decreases the number sites in which H protons can reside.

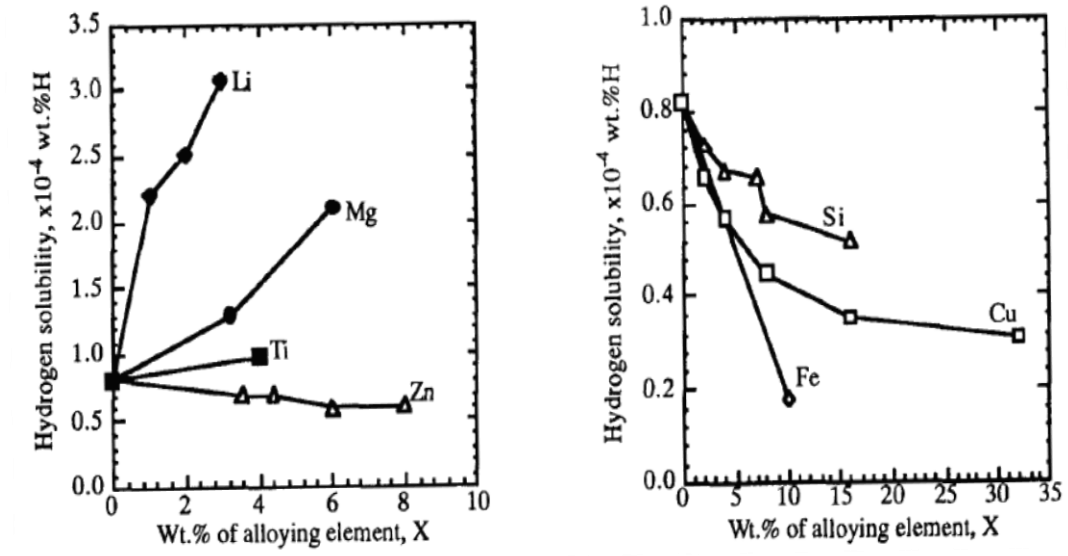

Figure 2.6 The influence of various alloying elements on the solubility of H in Al [27].

2.2.2 Hydrogen in liquid aluminium

H protons in solution are free to diffuse interstitially [18] throughout the metal in both the liquid and solid state, and do so rapidly when compared to elements that move by substitution type diffusion like Mg or Cu, as shown in Figure 2.7. The diffusivity of H is measured in m/s governed by the equation:

$$d = (Dt)^{1/2} \ldots \text{Eq.5}$$

Where d is the average distance an element can diffuse, (whether in solid, liquid or gas) in m^2, and t is time in seconds. D is the diffusion coefficient, and is reported (for H) to be 3.5×10^{-7} $m^2 s^{-1}$ at 700°C [30].

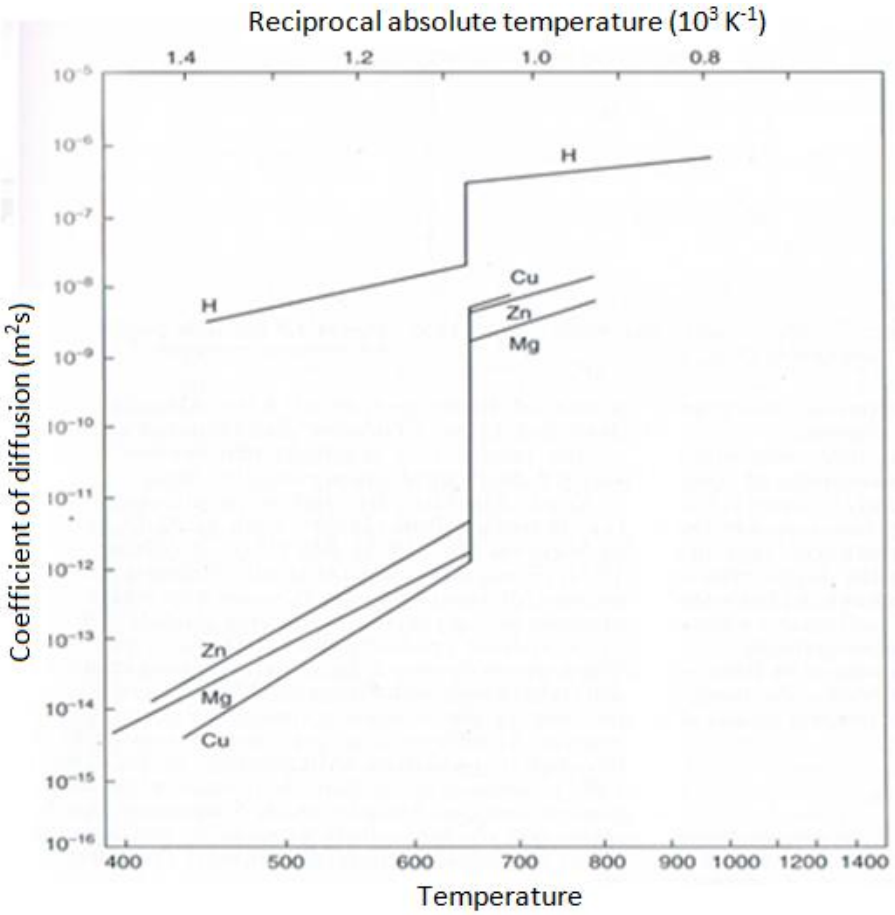

Figure 2.7 The diffusivity of various alloying elements and H in pure Al [30].

To demonstrate the diffusivity of H in liquid Al Ransley and Talbot [22] showed that applying steam to the surface of a pure Al melt at 740^{o}C increased the H content (measured by vacuum extraction) of the Al inside a U shaped crucible. The crucible openings at A and B were 75 mm in diameter at the top and the mean distance through the metal, (between the surfaces at points A and B), was approximately 700 mm, as illustrated in Figure 2.8. Applying steam to the metal surface (at point A) led to a rapid increase in the H content of the melt in that area. The H diffused through the liquid and began to increase the H content on the other side of the crucible (point B) after about 4 – 5 minutes. After 10 minutes the H content of the melt at point B had reached approximately 0.8 ml/100g, equivalent to about 85% of the H content measured at position A at the same time. Talbot estimated the diffusion coefficient from these results to be about $1x10^{-4}$ m^2 s^{-1}, which is about 3 or 4 orders of magnitude greater than the value for stationary metal at 700^{o}C. Talbot discussed that the true diffusion coefficient was uncertain, and difficult to calculate accurately due to the error from convection currents facilitating the migration of H through the melt. Applying the estimated diffusion coefficient to Eq.5 suggests that H would diffuse approximately 170 mm in 300 second, (the approximate time at which that the H content of the melt at point B begins to increase), which suggests that the diffusion coefficient was actually significantly higher than estimated; closer to $1.6x10^{-3}$ m^2 s^{-1}. This value is obtained by rearranging Eq.5; dividing the diffusion distance (d^2 = 0.49 m^2), by time (t = 300 seconds).

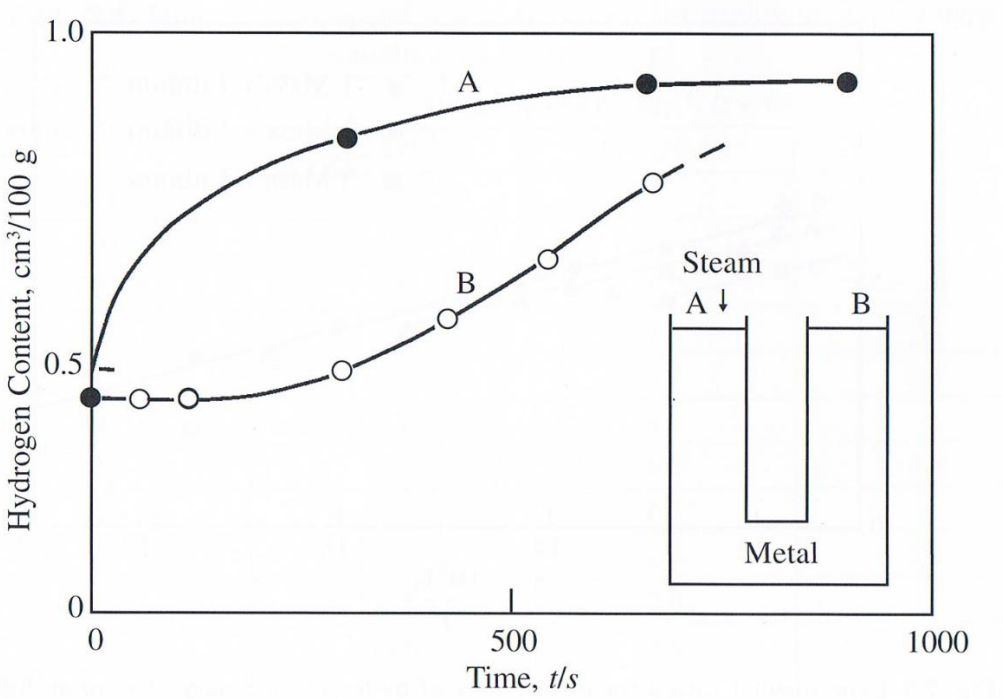

Figure 2.8 The diffusion of H in pure (99.8%) liquid Al, between points A and B in a u-tube furnace, up-gassed by steam [18].

Within molten Al, H resides in two forms; in solution and as a diatomic gas within any pre-existing gas phases within the melt, such as bubbles. In solid Al H typically exists in solid solution, within inter-dendritic and gas porosities (instead of bubbles) and is also partitioned between lattice defects such as vacancies, dislocations and grain boundaries. Solid metal hydrides are also known to form but this is only reported to occur in alloys containing Li [18].

The spaces or areas where H resides outside of solution are referred to as trap sites. Such sites can accommodate either only a limited amount of H (such as vacancy sites or dislocations) or an amount of H dependant on the gas pressure within the metal, such as pores / cavities and at grain boundaries [20] [29] [31] [32]. Sites that can absorb additional H_2 as a diatomic gas, which can expand under heating, may actually cause deformation of

the surrounding metal and cause surface damage such as surface blisters during heat treatments as described in Figure 2.9.

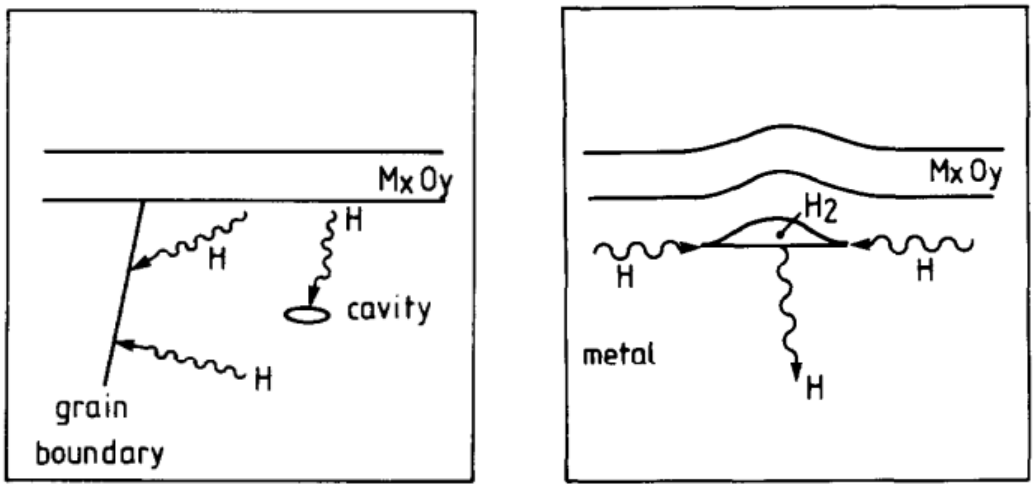

Figure 2.9 Illustrations of the diffusion and collection of H at certain trap sites a) grain boundaries and internal cavities (e.g. pores) b) near surface cavities causing blistering of the surface [20].

2.2.3 Oxidation of aluminium alloys

In pure liquid Al the absorption of H begins quickly at the surface of the melt due to oxidation of water vapour but will quickly be limited in humid environments due to the formation of a protective oxide at the melt surface [33].

The Al at the surface of the melt reacts almost instantaneously with O_2, forming an amorphous alumina layer, only a few nanometres thick [34] [35]. It is amorphous because it forms directly on the amorphous melt surface. This oxide layer quickly (within a few minutes) transforms to a predominantly ordered γ-Al_2O_3 crystal structure which nucleates from underneath the amorphous layer at the oxide – metal interface and grows into the metal, but leaves the amorphous layer unaffected [36]. The γ-Al_2O_3 layer is reported to be stable,

and passivates the surface against significant further oxidation unless temperatures are elevated above 700°C [37]. Above about 750°C the oxide film grows by a parabolic type rate, as shown in Figure 2.10 [37]. The γ-Al_2O_3 grows by the diffusion and migration of metal cations and oxygen anions through the non-porous oxide via lattice imperfections, the rate of which accelerates as the temperature increases [38].

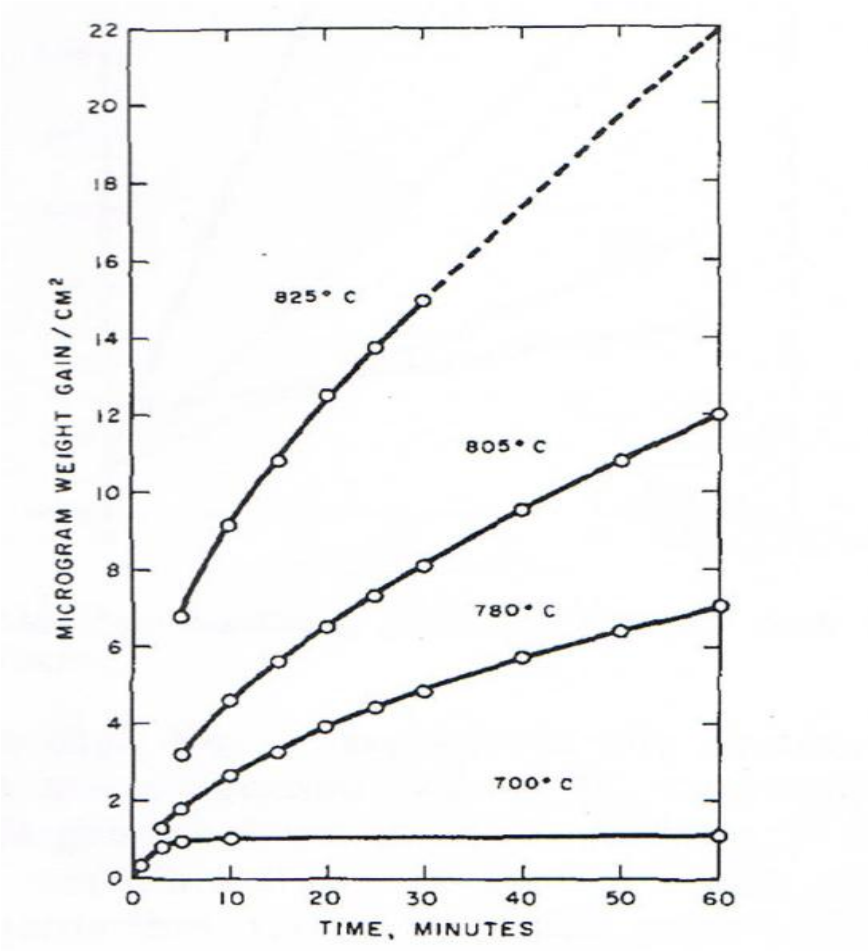

Figure 2.10 Oxidation of Al in dry O_2, from Sleppy [39].

After an apparent incubation period of several hours [40] the γ-Al_2O_3 transforms into α-Al_2O_3 (corundum), which is an ordered crystalline ceramic, and more favourable thermodynamically [41]. The α-Al_2O_3 is denser than γ-Al_2O_3, and the associated volume

change of about 24% [42] in oxide morphology causes stress in both the oxide layer and the metal. This leads to the formation of cracks in the oxide layer and exposes fresh Al to the local environment [43]. Typically, O_2 and H_2O are in abundance so oxidation occurs along with the formation of a new, fresh, amorphous layer, which also converts over time. This cycle would continue in environments with unlimited O_2 through a process of breakaway oxidation and many extrudations of Al would be visible at the surface of a melt [44] [45].

Stephenson [46] showed that during the first 20 minutes of exposure to humid air, pure liquid Al rapidly absorbed H. This occurred because hydroxide ions were able to diffuse through the amorphous oxide layer at the melt surface and provided a source of hydrogen for the melt to absorb. The H content of the melt did not continue to increase after this time because of the crystalline γ-Al_2O_3 layer growing at the interface between the melt and the amorphous layer. This film grew and, once continuous across the melt surface, prevented hydrogen absorption. Absorption stopped because hydroxide ions could not diffuse through the γ-Al_2O_3 structure [18]. This continuous crystalline layer limits the absorption of H until the γ-Al_2O_3 transforms to α-Al_2O_3 during break-away oxidation, which cracks the oxide layer and allows water vapour to react with the surface again.

Imprey [42] demonstrated that in dry air, break away oxidation occurs rapidly, while the melt surface is protected for a prolonged period of time in humid air (although the exact moisture levels were not reported). This was reasoned to be because the hydroxide ions actually stabilise the γ-Al_2O_3 and prevent it from converting into α-Al_2O_3, for a prolonged period. Therefore maintaining a humid atmosphere would actually be beneficial in protecting against surface oxidation in commercial purity Al. The effects can be seen in Figure 2.11.

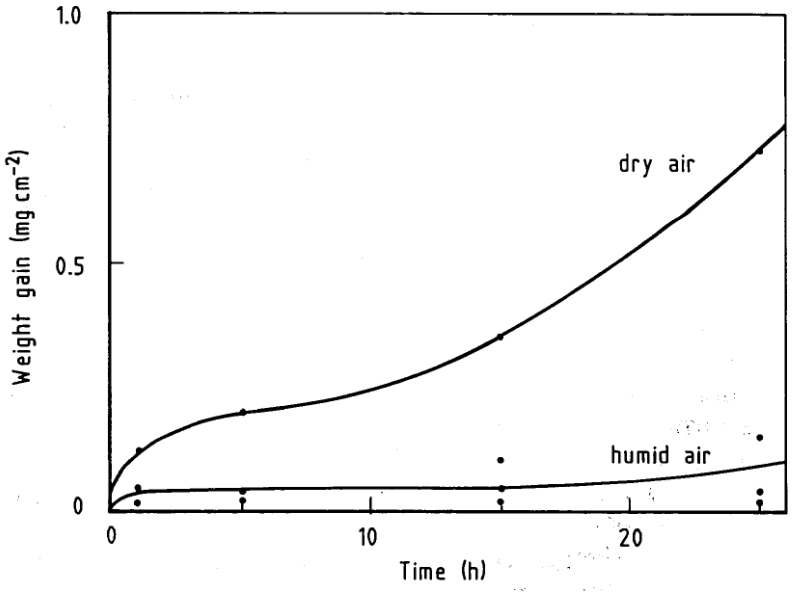

Figure 2.11 The oxidation of commercial purity Al in dry and humid air at 750^{o}C (35). Dry air allows rapid break away oxidation while the presence of hydroxide ions stabilises the protective oxide film for longer [42].

While γ-Al_2O_3 alumina is protective (at least for a time) Mg oxide is not. Mg oxide will allow further reaction between the melt and both O_2 and water vapour because unlike Al it does not form a continuous layer across the surface of the melt.

The Pilling-Bedworth ratio (PBR) describes this relationship:

$$\mathrm{PBR} = \frac{M_o \rho_m}{M_m \rho_o N_m} \quad \text{....Eq.6}$$

where M_o and M_m are molecular weights of oxide and metal layers respectively, ρ_o and ρ_m are the corresponding densities and N_m is the number of metal moles in the oxide. If the ratio is <1 the oxide is porous and not protective, >1 then the oxide is generally protective, >~2 the oxide spalls, falling away from the surface and is not protective (rusting of Fe is a common example). The PBR for some metals are shown in Table 2.2.2 [47].

Metals that oxidise to produce an oxide that is smaller in volume than the metal that is consumed in the reaction with O_2 remain vulnerable to oxidation as the oxide formed is porous. A porous oxide allows O_2 and water vapour to continue to react with the metal surface. If an oxide forms on a metal, and is greater in volume than the metal it consumes in the process, it will expand outwards, to an extent limited only by the strength of the oxide. Such oxides tend to seal the metal away from the reacting species by forming a continuous barrier across the surface of the melt, this is unless the volume of the oxide is so great that it cracks due to expansion and spalls away from the surface.

Metal	PBR	Metal	PBR
Al	1.28	Si	2.04
Ca	0.78	Mg	0.84
Cu	1.70	Zn	1.59
Li	0.60	Zr	1.55
K	0.51	Fe	2.06

Table 2.2 The Pilling-Bedworth ratio (PBR) for some common metals [47].

Al alloys containing Mg (or other elements that disrupt this surface oxide layer) will then continue to absorb H as this protective barrier does not form. In Al alloys containing approximately 0.005 wt% Mg, the surface oxide that forms is a mixture of MgO and Al_20_3, (spinel). As the melt Mg content increases, the levels of MgO at the surface scale with the increasing Mg content of the alloy [48]. When the Mg content of the alloy is raised above approximately 2% then the oxide film is expected to be pure magnesia, MgO from

thermodynamic estimates [49] [50]. Al alloys with high Mg contents can have especially high H content as the solubility of H within the alloy is also increased [18] [26].

Gaps in the oxide layer allow continued reactions with the environment and the melt surface as illustrated in Figure 2.12. In Figure 2.13 the porous oxide (MgO) formed on an Al 2.2% Mg alloy allows both absorption and desorption of H into and from the melt to the local environment. Elevated H levels are observed to first decrease rapidly (black dots) while lower H levels (white dots) increase rapidly so that the melt is in equilibrium with the local environment. Over time the H content is observed to increase by the continuous absorption of H through reaction with water vapour. A melt with a lower Mg content would presumably gain or lose hydrogen at a slower rate, dependant on the ratio of Al_2O_3 and MgO present at the surface.

Regardless of any protective films, disturbing the melt surface (such as metal splashing or rupture due to direct flame impingement in a gas fuelled furnace), will cause rupture of the oxide film. Increased melt turbulence which leads to surface disruption will increase the rate of H absorption as the protective oxide layer is disturbed, so more water vapour can react with the newly exposed Al surface.

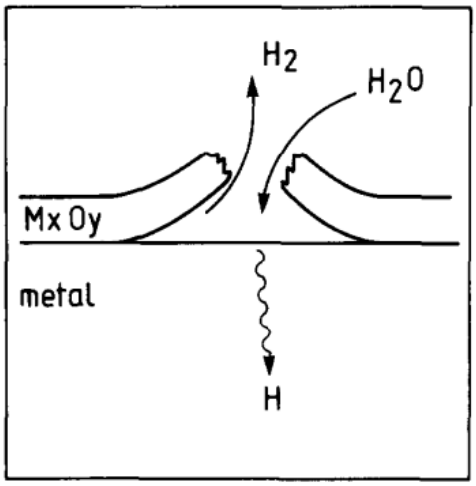

Figure 2.12 Gas absorption and desorption into and out of Al [20].

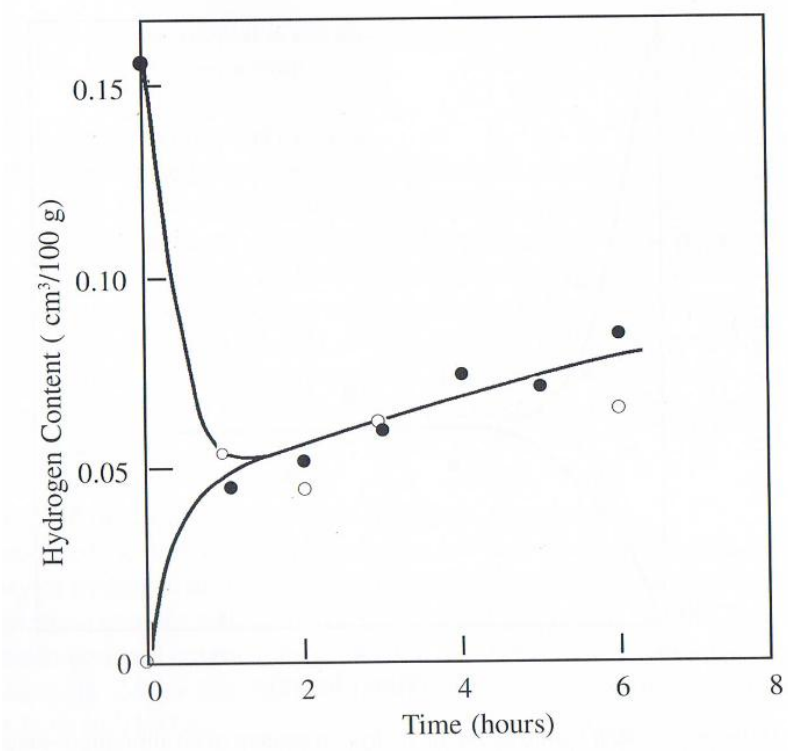

Figure 2.13 The influence of clean humid air on the H content of an Al – 2.2% Mg alloy at 550^{o}C. Oxidation continues and an increase in H content is observed over time because the Mg oxide film is not protective [18].

2.3 Porosity in aluminium castings

Porosity may form within Al castings for a variety of reasons. Primary or macroscopic shrinkage porosity occurs because Al alloys exhibit a relatively high shrinkage of between typically 3.5 and 8.5% [51] [52] that occurs during solidification (the figure varies depending on the alloy composition). Poorly fed castings might contain regions with gross porosity due to this decrease in volume, but generally good design and casting practices eliminate this type of porosity from modern casting processes, especially in direct chill (DC) casting, which directly feeds the area of primary shrinkage during casting.

Secondary or microporosity on the other hand is quite common in castings and is generally attributed to H_2 gas evolution during solidification or due to inter-dendritic solidification shrinkage, but most likely the overall microporosity in a casting is generated by a combination of these two mechanisms [10]. Interdendritic porosity results from the inability of the liquid to feed through interdendritic regions to compensate for the local volume shrinkage at solidification. Gas porosity arises due to the presence of H_2 gas within the metal, perhaps diffusing into interdendritic regions and expanding to create more significant defects.

2.3.1 Hydrogen gas porosity

H can have negative effects on a number of metallic systems, for example it is responsible for embrittlement of steel. In Al it has been linked to the presence of gas porosities in the casting and defects such as pores. Increasing the H content of the liquid metal leads to an increase in both number and the average size of the pores formed. Figure 2.14 shows how

the porosity of an Al-Cu alloy increases exponentially with increasing H content and Figure 2.15 demonstrates visually the effects of increasing H content on the porosity levels of small Al samples observed using the reduced pressure test method. Pores have obvious adverse effects on mechanical properties such as tensile and fatigue strength [53] [54] [55] as shown in Figure 2.16.

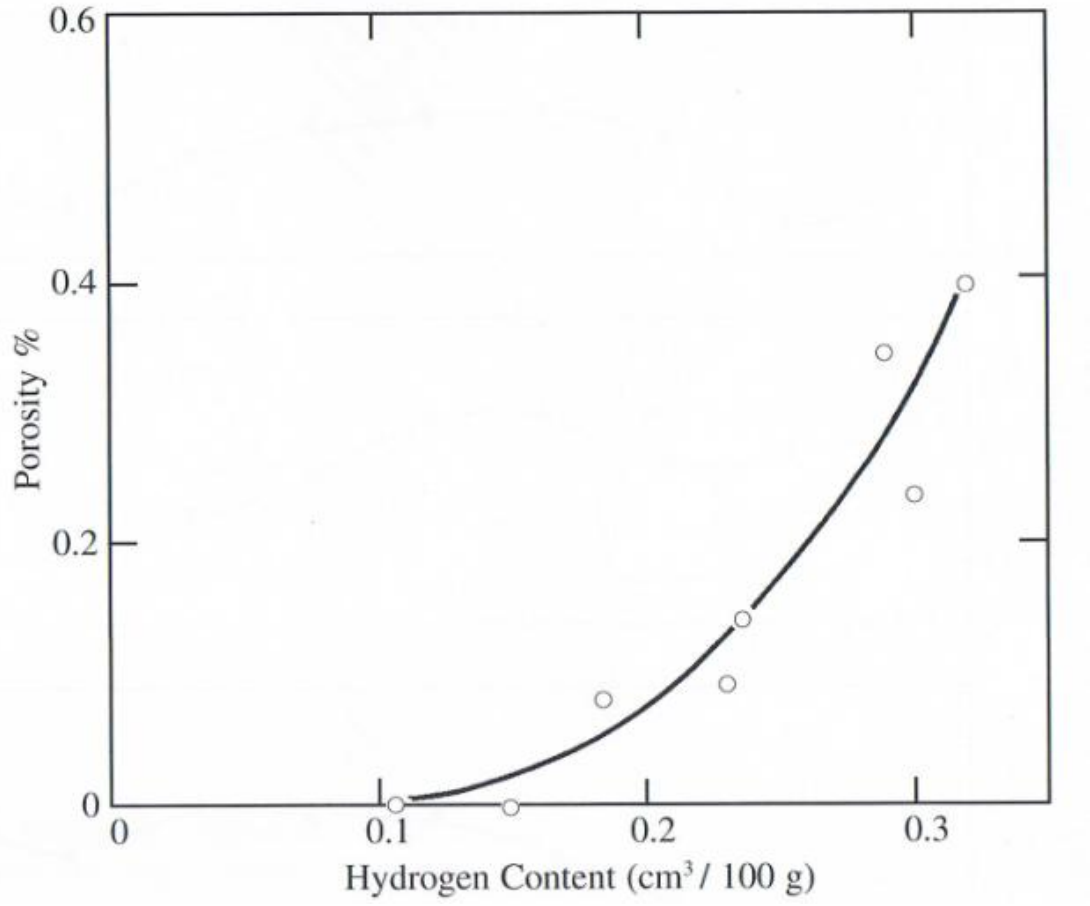

Figure 2.14 The relationship between average H content and average porosity found in industrial semi-continuously cast ingots of 2014 alloy (typically 4.5% Cu, 0.4% Mg, 0.8% Mn, 0.7% Si) [18].

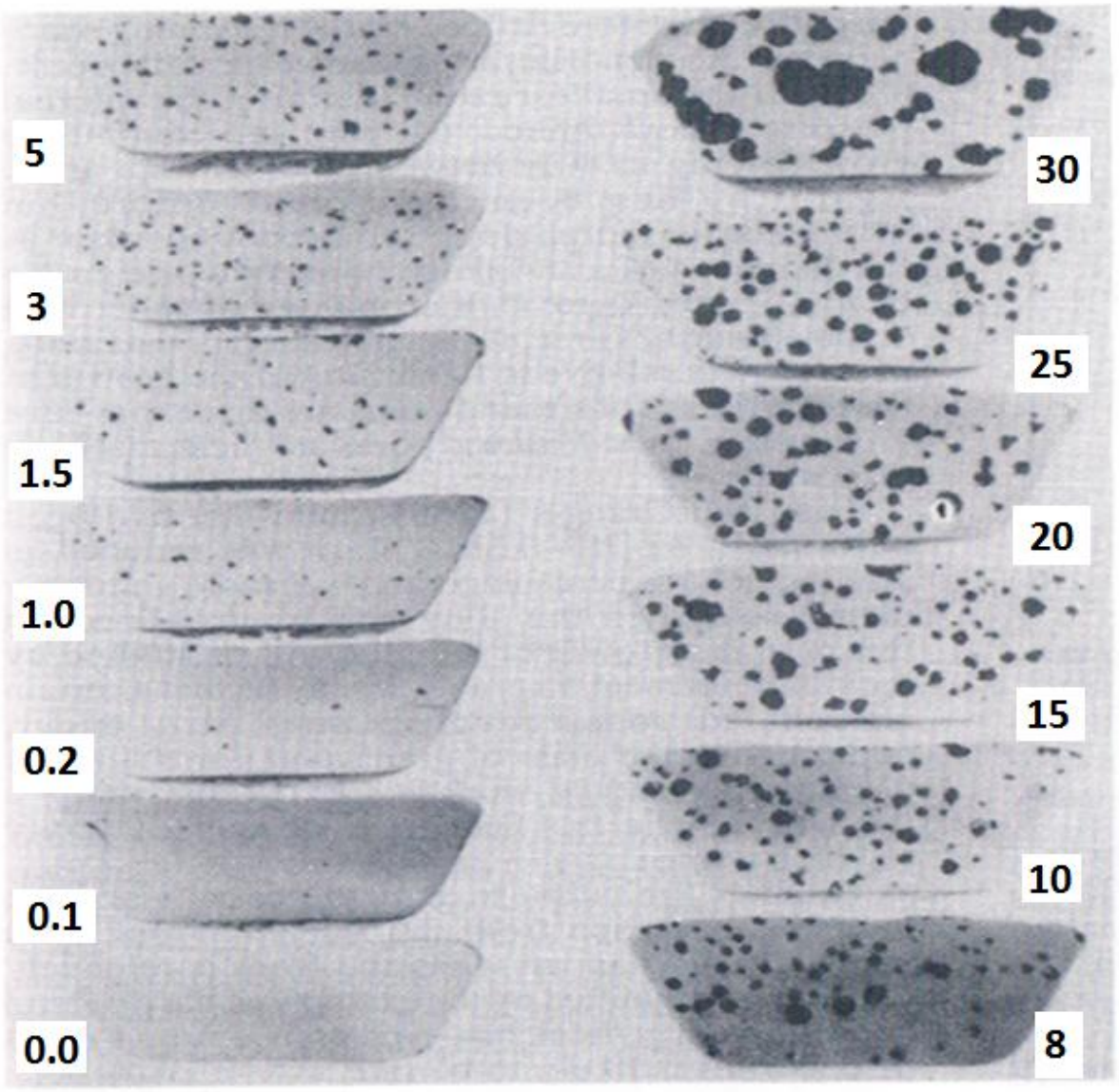

Figure 2.15 The H content (ppm) and corresponding porosity levels in pure Al samples. Produced using the reduced pressure test [30].

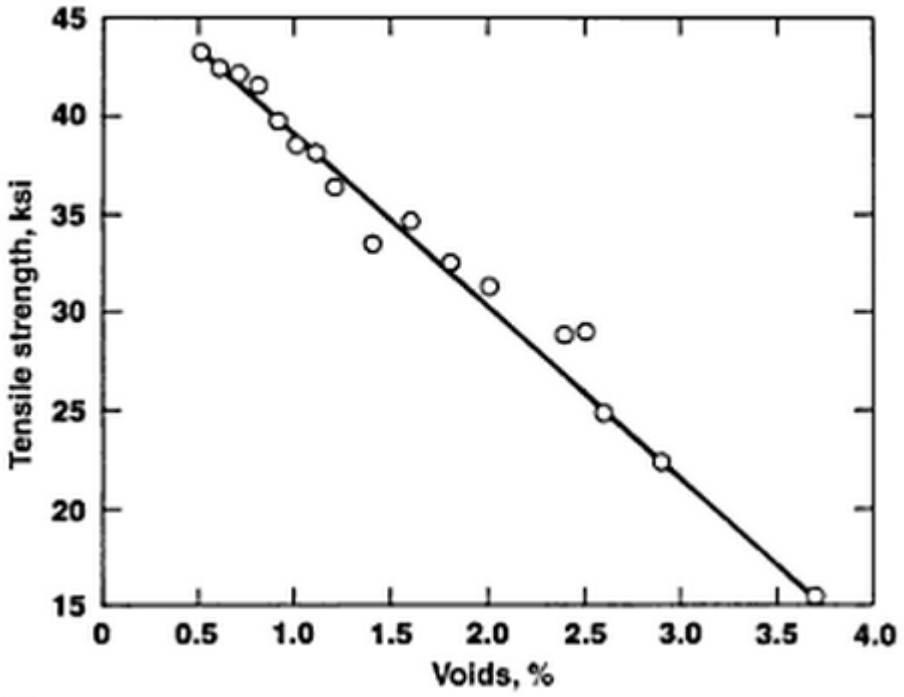

Figure 2.16 An example of the influence of voids on tensile strength, of alloy 355.0-T61 [56].

Gas porosity arises during solidification of the metal due to the large difference in solubility of H gas in the liquid compared to the solid Al, decreasing from (a maximum) of approximately 0.67 to 0.046 ml/100g [16] [57] during solidification; an order of magnitude. The decrease in solubility of H in Al and other alloys is shown in Figure 2.17.

The difference in solubility arises due to the decrease in volume and increase in density (solidification shrinkage) of the metal. The interstitial sites where H can reside are compressed and thus the H is forced out of the solid and into the liquid ahead of the solidification front. The H content of the liquid metal ahead of the solidification front increases as solidification proceeds until the metal is nearly entirely solid and the last remaining liquid is heavily enriched in H as shown in Figure 2.18. Due to this segregation effect the concentration of H at the centre of an Al casting just after solidification is

expected to be higher than the exterior. Over time the diffusion of H (from interior to exterior) would be expected to reduce this segregation.

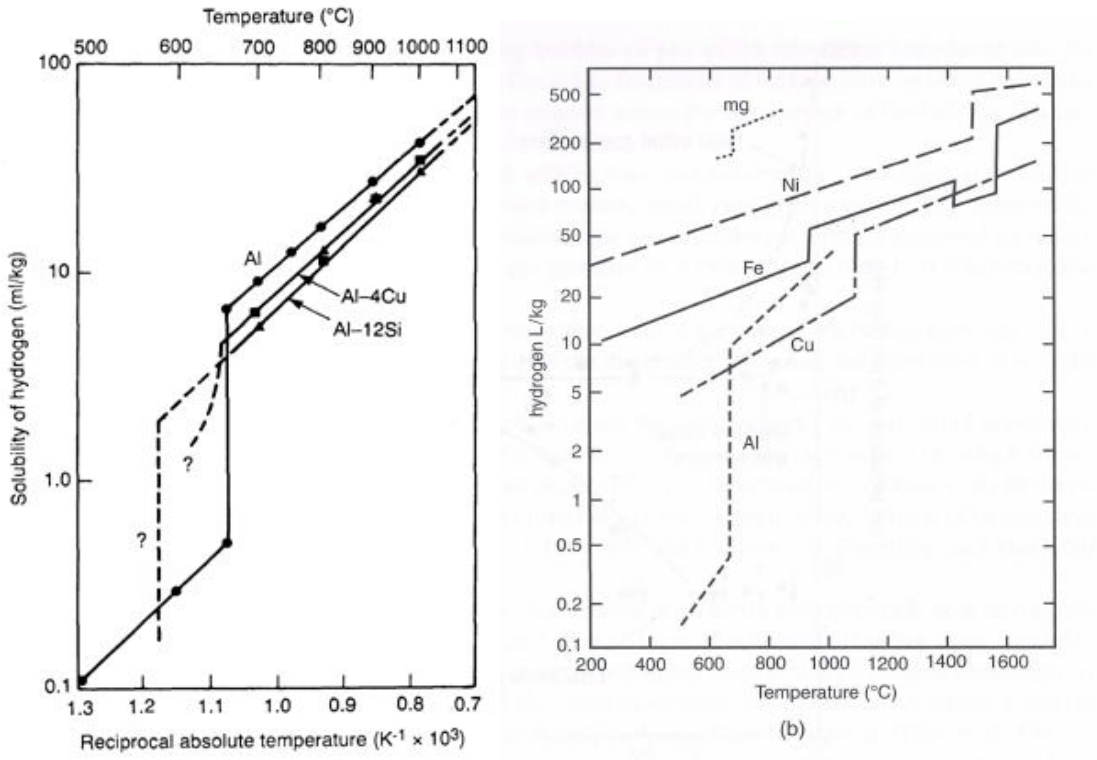

Figure 2.17 The solubility of H in Al and Al alloys containing Si and the solubility of Al compared to those of other metals. A marked decrease in solubility is observed during solidification [58].

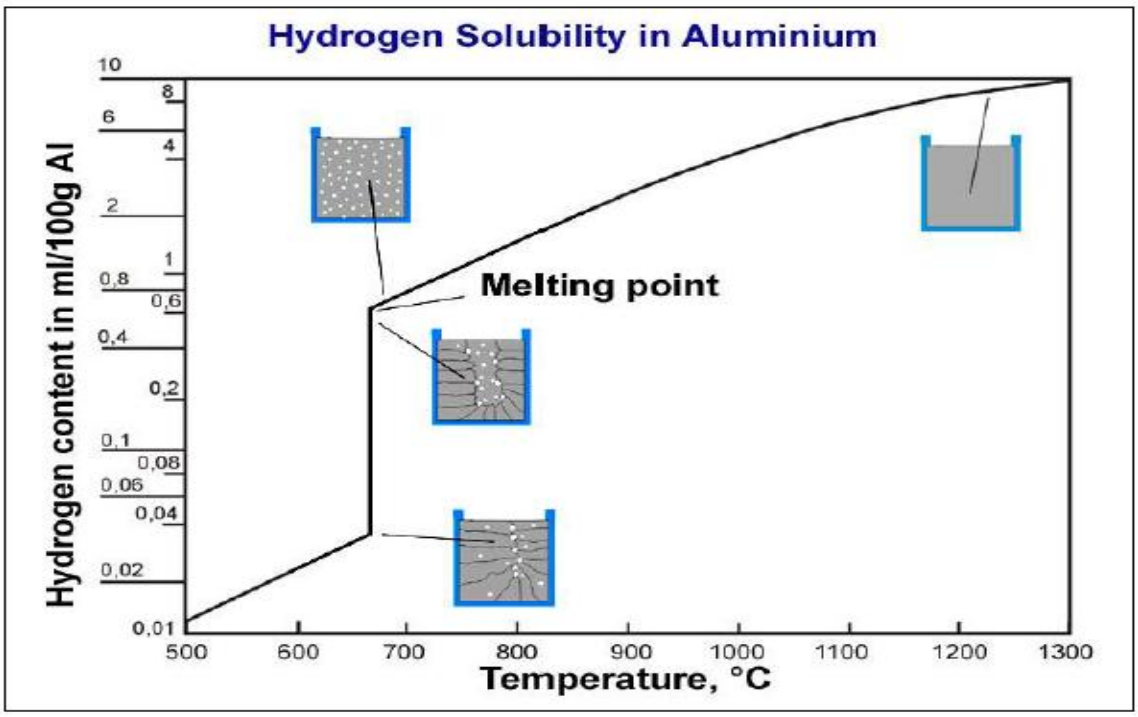

Figure 2.18: The solubility of H in Al decreases with temperature, resulting in Higher H_2 concentration levels at the centre of the ingot. This occurs because during solidification H is rejected from the growing solid and forced into the remaining liquid metal.

The conventional theory is that once sufficient H is present, the monatomic H nucleates into the diatomic H_2 molecule as a gas phase and grows by diffusion of additional H into the area. The homogeneous nucleation of gas porosity is however unlikely [30], but regardless of the nucleation process this gas phase survives as a H filled pore in the final casting. Zhao et al [59] observed gas pores within a low-freezing range alloy and pure Al castings (using X-ray) to float out of samples during rapid re-melting cycles as the gas within was buoyant and this eliminated porosity from small samples. Wider freezing range alloys tended to re-absorb the gas pores back into the eutectic composition phases as bubbles were trapped between the dendrites. This prevented them from floating out of the melt and so they were absorbed back into solution before the metal was entirely molten. The trapping of bubbles between growing dendrites during solidification is shown in Figure 2.18 [60].

The severity of the effect of porosity on mechanical properties depends on the amount of porosity, size and the distribution of pores formed during solidification, which in larger castings is typically towards the centre of the ingot. Porosity is usually found in quantities less than 1% by volume of castings under normal casting conditions, but it is suggested that, in the aerospace industry, levels less than 0.5% are required for good castings and superior mechanical properties [56].

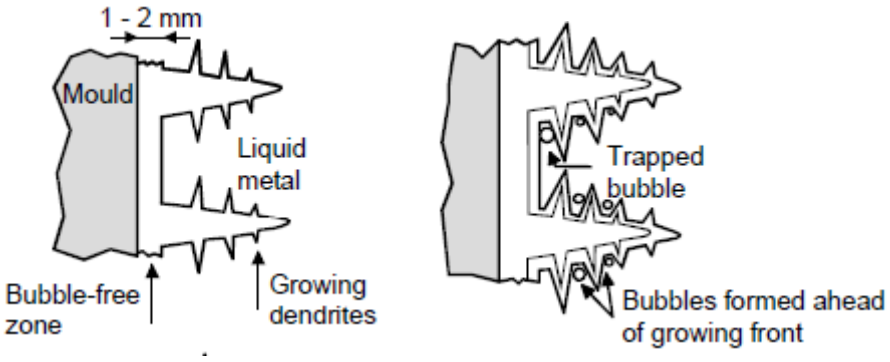

Figure 2.18 Nucleation of H_2 gas pores within the mushy zone, between secondary arm spacing [60].

Once pores have nucleated their growth is dependent on the diffusion of H from the bulk liquid and solid to the pore. Since this process is diffusion controlled, the final size of a gas pore is dependent on the amount of H in the melt and the time available for growth; that is the time between nucleation and the end of solidification. Faster rates of solidification retard growth by reducing the time available for H diffusion to the nucleated pore site. Faster rates of solidification will also lead to H retention in supersaturated solid solution and thus deprives the nucleated pores of the H they require for growth [21] [61]. Granger and co-workers [62] showed that cooling rate and H content reduce the severity of porosity by decreasing the average size and number of pores in A356 alloy and they also suggested that

grain refinement with inoculants further decreased the size and number of pores. This is explained by an increased number of nucleation points for the metal to solidify and consequently more grains develop in the casting and the average grain size is decreased, leading to an overall increase in grain boundary area. The H is then distributed along these boundaries over this increased area during solidification, reducing the pressure of segregated H in any one position along the boundary. Additionally the size of the spaces available for pores to grow between growing dendrites is reduced and this reduces the ability for H to segregate and accumulate within the liquid ahead of the solidification front during solidification.

As grain boundaries are trapping sites for H, Pedersen and Jonsson [63] discussed that (depending on the angle of the boundary) the diffusion of H could be inhibited along the boundaries, which would limit the diffusion of H into pores. Atwood et al suggested that grain refinement increased the overall fraction solid, affecting the rate at which H is rejected from the growing solid; increasing the H concentration in the surrounding melt whilst decreasing the effective diffusion coefficient [64]. The effects of rapid solidification, grain refinement and H levels are illustrated in Figures 2.19 and 2.20. In contrast, Anyalebechi [65] demonstrated that decreasing melt H content and increasing solidification rate decreased the number and size of pores, but found that additions of grain refiner slightly increased the average pore size and amount of porosity in a 4.5 wt% Cu 1.4 wt% Mg alloy at solidification rates above 1 K/s. It is unclear if the grain refining inoculants or oxide defects are responsible for this increase in porosity but it is suggested that this occurred due to earlier and increased pore nucleation at grain refiner related oxide nucleation sites which would of

been either entrained while adding refiner into the melt, or perhaps H within the grain refiner master alloy contributed to increase the H content of the melt.

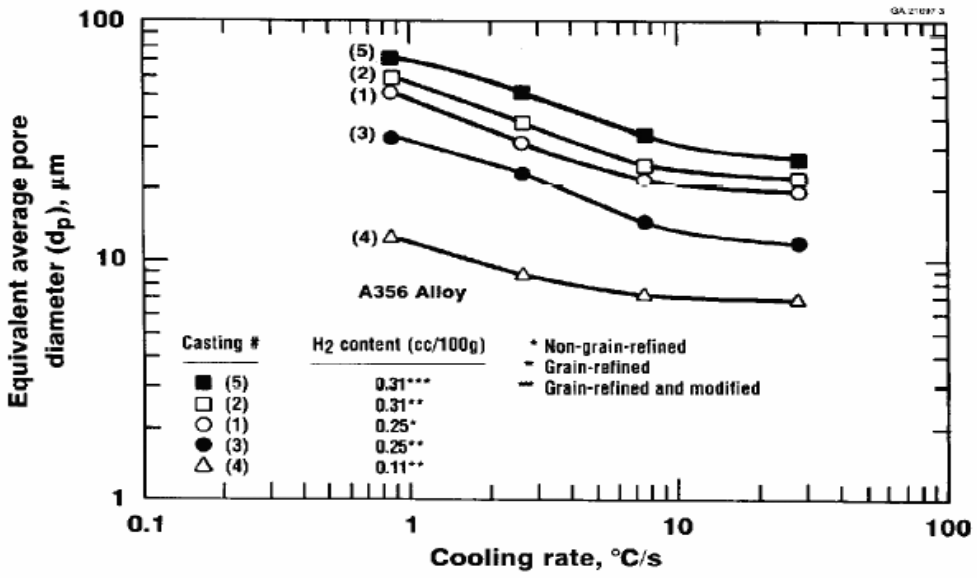

Figure 2.19 The influence of H gas content, cooling rate and grain refiner additions on the average pore size in A356 alloy castings [62].

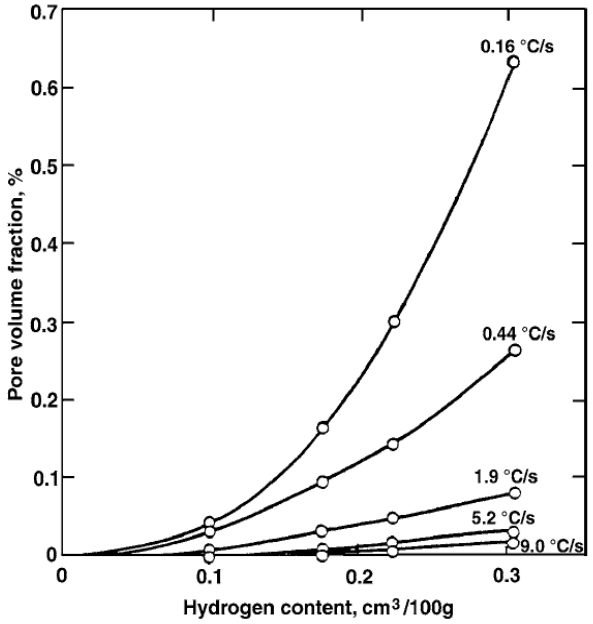

Figure 2.20 The effects of initial H content and cooling rate on pore formation [66].

Porosity has been linked to ultrasonic edge noise in flat rolled products at Alcoa Kitts Green; it has been responsible for the presence of ultrasonic indications close to the edges of rolled 7xxx plate [67] [68] [69]. Porosity that had formed during the casting of DC ingot has been shown to survive into the final product by Rudolph [69] who observed that DC cast and hot rolled plate that displayed ultrasonic edge noise contained significant levels of porosity in the edges when compared to the centre when examined using a microscope. The porosity was shown to be partly or completely healed (depending on the severity of the porosity and rolling parameters) when small samples were extracted and hot rolled in a subsequent process. In later, more detailed work, Rudolph [68] demonstrated that heavy rolling passes first make pores widen (attributed to tearing of pores due to local deformation processes) when the cross sectional area was reduced up to 60%. As rolling continued the pores were gradually compacted, forced and welded together so that at about 80% reduction very little porosity remains. These studies suggest that thick plate may still contain non-welded pores and ultrasonic defects. Also, due to the variations of stress across an ingot during rolling, pores at the edges of plate are exposed to lower levels of strain and so they do not always entirely close, like those in the centre of an ingot.

It is worth noting that hot rolling utilises water and oil lubricant to minimise contact stresses and the process is performed at an elevated temperature. The rolling process has been shown to increase the H content of the metal due to the process supplying heat, a local moisture source (from the lubricant) and damaging the surface oxide of the metal during deformation. This effect is demonstrated by Talbot [18] shown in Figure 2.21.

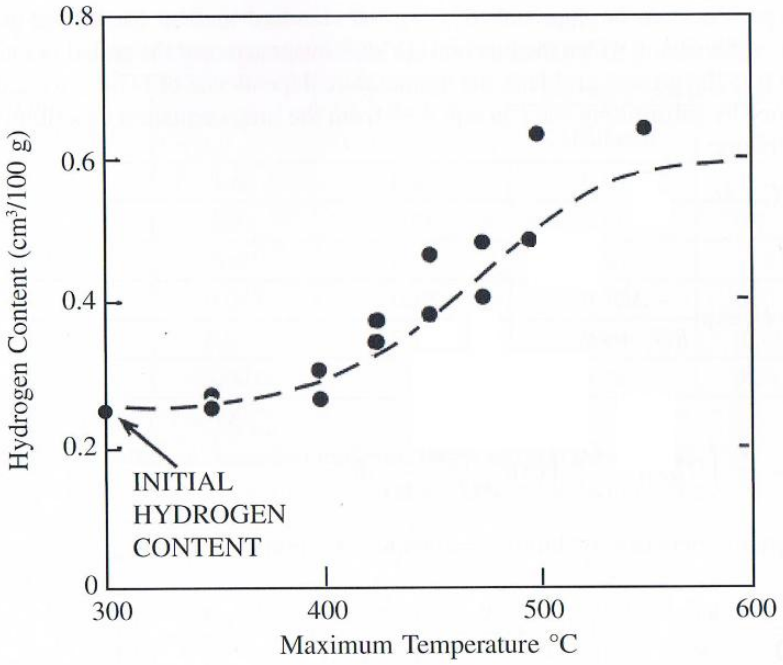

Figure 2.21 Effect of hot rolling on the H content of pure (99.2%) Al with a water vapour pressure of 3000 Pa [18].

2.3.2 Nucleation and growth of gas porosity

The amount of porosity in castings is influenced by the H content of the liquid metal, but the exact mechanism for nucleation of the gas phase within the melt has been a source of debate.

The conventional theory is that volumetric shrinkage and the change in H solubility during solidification causes porosity. The liquid that must flow towards the dendrites to feed the solidification shrinkage induces a pressure drop across the mushy zone and the liquid. As the metal solidifies H is rejected into the liquid which becomes increasingly rich in H. The dissolved H exerts a pressure (as given by Sievert's law) and a pore is formed when the H induced pressure in the melt is equal to the sum of the atmospheric, metallostatic and surface tension pressures in accordance with the Laplace equation:

$$P_{H2} = P_{ext} + P_m + P_s + \frac{2y_{1/g}}{r} \text{... Eq.7}$$

Where P_{H2} is the pressure of the gaseous H inside of the pore, P_{ext} is external or atmospheric pressure, P_m is metallostatic pressure $y_{1/g}$ is interfacial tension at the liquid/gas interface (surface tension of the melt) and r is the radius of the pore. For the gas phase to exist within the liquid there must be a nucleation event for the pore to form before its growth phase, which is not well understood.

Homogeneous nucleation is very difficult and typically requires significant under-cooling (when considering solidification of metals) and probably only occurs in laboratory conditions. For example, in the absence of nucleation sites it is possible for super-pure liquids to be cooled well below their solidification temperature because there are no suitable nucleation sites for the solid phase to grow from. Homogeneous nucleation of porosity requires the

initial formation of microscopic bubbles which would grow a few atoms at a time, by diffusion of H. These bubbles would be very small, only a few atoms across, and the surface tension pressure (which is inversely related to pore size) would be high. Campbell [58] calculated that the internal pressure within a pore in an Al melt would be approximately 30,000 atm. The magnitude of these pressures indicates the difficulty of homogeneous nucleation of porosity, and it can be reasonably assumed that homogeneous nucleation is very unlikely to occur [70].

The problem of pore nucleation can be greatly simplified if heterogeneous nucleation occurs on an exogeneous non-wetted substrate such as refractory particles, oxide films, inclusions or the mould wall [70]. Nucleation of gases on solid surfaces does not become favourable until the contact angle exceeds 65^{o} [71], this degree of wetting decreases the required internal pore pressure from approximately 30,000 atm to 1500 atm and the required pressures could be decreased even further if the bubble forms within in a crack [72], presumably to zero.

The work by Chen and Gruzleski [71] and Laslaz and Laty [73] have shown that with the same melt H content, the amount and size of pores was related to the amount of inclusions in A356 and A319 casting alloys, demonstrating that inclusions do have an effect of increasing porosity. This was achieved by comparing the porosity levels of filtered and non-filtered melts. Inclusions have been observed visually using scanning electron microscopy on the walls of pores [74]. Mohanty et al [75] observed that the addition of alumina to Al caused an overall increase in the volume percent porosity due to an increased pore density, but that the pores were smaller than when no addition of alumina was made. Smaller sized alumina additions had a more significant effect on porosity than relatively large ones, as

shown in Figure 2.22. This indicates that the surface area of the inclusion influences the porosity levels. A possible explanation for this behaviour is that with an increase in possible nucleation sites, pores form more readily, thus the H is distributed among more pores, resulting in a decrease of the average pore size. It is more likely that the addition of alumina into the melt entrained oxide films. The alumina particles would have passed through the surface oxide during addition, coating or enveloping the particle, consequently this created defects into which H could diffuse as shown in Figure 2.23.

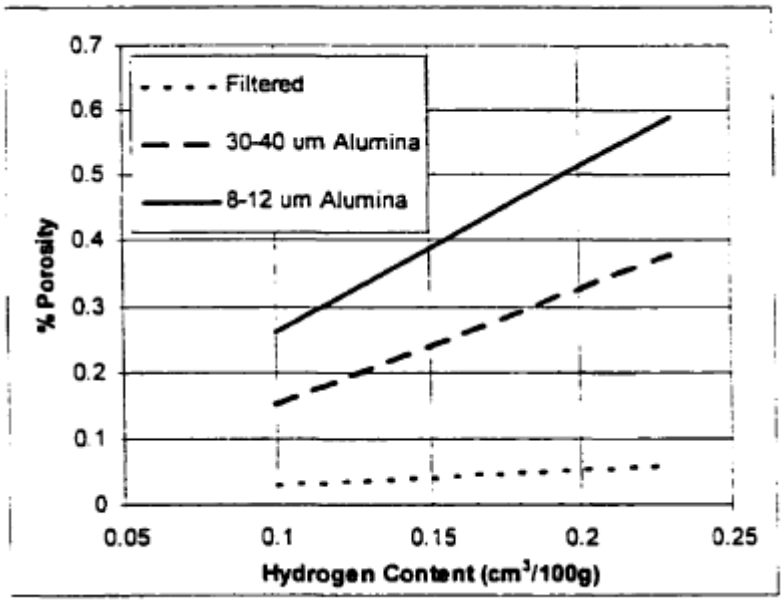

Figure 2.22 The effect of inclusions on the porosity levels for three samples of A356. Alumina particles of two different sizes were added to the melt to act as inclusions. The porosity levels are significantly lower in filtered metal [75].

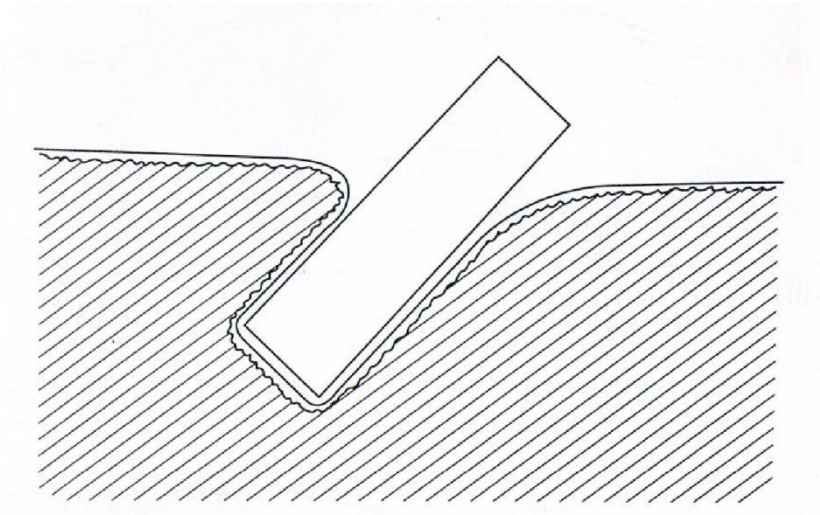

Figure 2.23 A particle (such as an inclusion or alloying addition) added into the melt will be encapsulated within an oxide - gas envelope during the entrainment event [30].

2.4 Inclusions in aluminium alloys

Inclusions are undesirable phases incorporated into the final casting which on the whole are detrimental to the required properties (be they mechanical, fatigue, electrical or thermal). Inclusions have been shown to degrade mechanical properties of castings, primarily fatigue and ductility [76] [77] [78] [79] [80] primarily because hard particles such as ceramics can fracture during forging processes or act as stress concentrators or crack initiators within the casting.

Brittle particles such as ceramics can lead to pinholes in rolled foil, breakage during wire drawing, tear-offs during can manufacture, they can lead to point defects (revealed using ultrasound) in plate, or surface defects in sheet or extruded products. They can range in size and composition, depending on the alloy composition or processing parameters and the

severity of their effects can range depending on the size and location of the inclusion and application of the end product.

Inclusions can be formed of macro-particles (such as large refractory ceramics), being many millimetres in size, to smaller micro-scale particles and phases such as intermetallics which may only be a few microns (typically 10-100 µm) in size [81]. General engineering parts may contain many of these features without great concern but safety critical or performance parts will necessarily be processed (at great expense) to ensure inclusions are kept to minimum levels, or removed from the metal before casting. Campbell [58] stated:

"Depending on the end goal of the product, inclusion concentrations can be anywhere between 10 $mm^2.kg^{-1}$ for general engineering to as low as 0.0001 $mm^2.kg^{-1}$ for more critical applications such as computer disks, with wrought alloys containing about 0.01 $mm^2.kg^{-1}$."

The unit $mm^2.kg^{-1}$ is taken from the analytical PoDFA process, which describes the area of inclusions present over a fixed area, when a known amount of metal has passed through a filter.

Inclusions can be listed in three main groups (adapted from Prillhofer et al, [82]):

- Nonmetallic inclusions:
    - Al_2O_3, MgO and spinel in compacts or clusters
    - Material from refractory lining
    - TiB_2 agglomerates
    - Salt (metal chlorides)
    - Carbides
- Metallic inclusions:
    - Cr, CrMn and $Zr(Ti)Al_3$
    - Fe-Si intermetallics
    - Incompletely dissolved alloying elements
- Oxide films:
    - Al_2O_3
    - MgO
    - Spinel

Indigenous or in-situ inclusions; are those inclusions formed by chemical reaction within the melt; e.g. the reaction between O_2 and Al Eq.8 or with Al and Mg to form spinel Eq.9.

$$3O_2 + 4Al \rightarrow 2Al_2O_3 \ldots \text{Eq.8}$$

$$Mg + 2Al + 4O \rightarrow MgAl_2O_4 \ldots \text{Eq.9}$$

Metallic and intermetallic inclusions such as Al_3Fe, $Al_6(Fe,Mn)$ (Figure 2.4.1) can come from contamination of the melt with Fe and are detrimental to corrosion resistance [83] decrease the toughness and fatigue properties [53] [84], as well as causing tearing during rolling [85]

and disrupting anodising processes. Intermetallics can also be sourced from poor melt control; for example TiBAl (Figure 2.24) is a grain refiner which is added to improve mechanical properties but can actually cause problems such as tearing during rolling if the TiB_2 particles are allowed to agglomerate [86] [87] because they are relatively hard compared to the surrounding Al matrix.

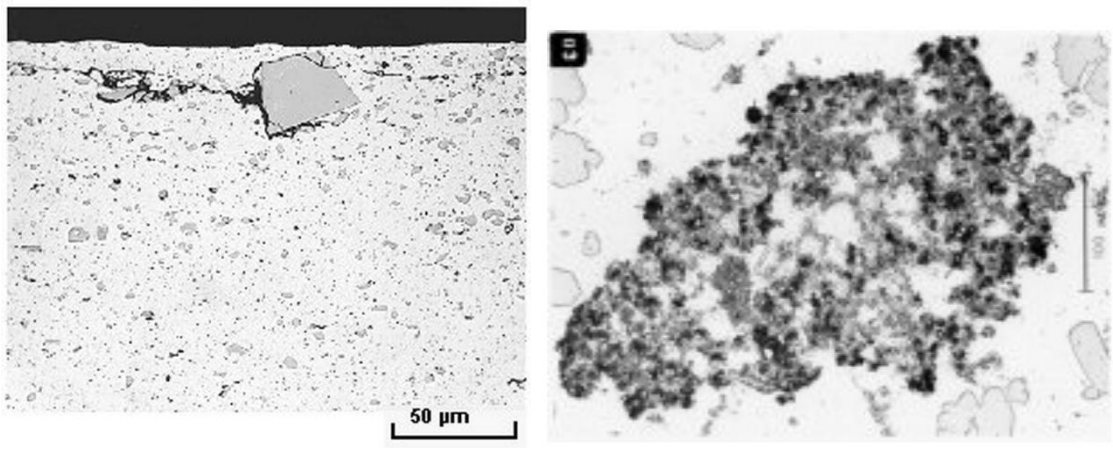

Figure 2.24 Inclusions found in Alcoa products a) coarse Al6(Fe,Mn) particles at the near surface of 3004 sheet (typically 1.25% Mn, 1% Mg), and b) an agglomerated boride inclusion in 3004 sheet [88].

Some alloys will have issues that arise specifically from their composition, such as the precipitation of phases from the melt such as $Zr(Ti)Al_3$ which can occur in high Zr content alloys (above 0.13 wt% Zr such as 7050). These phases can lead to ultrasonic rejection of plate products due to the response they cause during ultrasonic examination. Another example is the 5182 alloy which is expected to contain intermetallics such as $Al_x(Fe,Mn)_ySi$ and Mg_2Si after casting which have been shown to break up during hot rolling if they are >1 µm [89], so the development of these phases needs to be suppressed and reduced, typically by a combination of chemistry control, rapid cooling and homogenisation heat treatments.

Exogeneous inclusions; are those particles which already exist as a separate phase before melting or entering the melt, such as refractory ceramics from furnace insulation. Exogeneous inclusions are likely the most harmful to mechanical properties due to their large size, but are also easier to remove for the same reason.

By far the most common inclusion in Al alloys are oxides as they are produced as soon as the metal is molten. The reactions between metal and oxide are highly favoured thermodynamically and are limited only by the formation of the oxide skin on the melt surface. These oxides are Al_2O_3 but also MgO (magnesia) and mixed Al-Mg oxide structures (spinel) in those alloys containing Mg, such as the 5 and 7xxx series alloys. These oxides can be present as discrete compacts or clusters, or as an agglomerated cluster or films or they can be found within the metal using techniques such as PoDFA or may be found specifically at fracture surfaces. Inclusions such as exogeneous oxides have been shown to be deformed, crushed, elongated and flattened in the hot rolling of steel plate as well as causing void initiation between the inclusion and matrix [90] [91]. Similar mechanisms and effects are likely in the hot rolling of Al alloys because of the difference in hardness between the relatively soft and ductile Al matrix and the relatively hard and brittle ceramic oxide dispersions within. Metal that is poorly handled will contain oxides and form a dross at the surface of the melt (some 60-80% of dross from industrial applications can be Al encased in oxides) [92].

Examples of the Al and Mg oxides obtained through the microscopic evaluation of PoDFA samples are shown in Figures 2.25 - 2.27 [93].

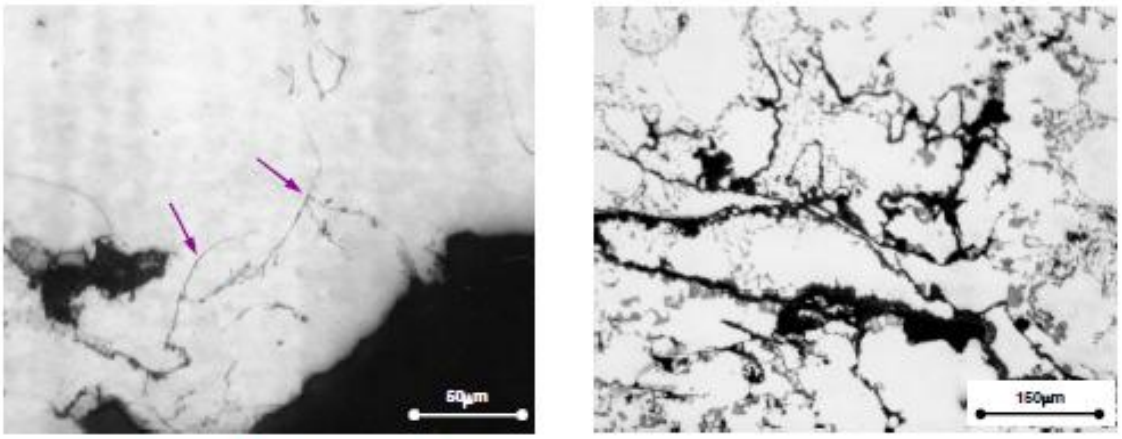

Figure 2.25 Examples of a) newly formed (thin) and b) old thickened oxide films found in Al using PoDFA [93].

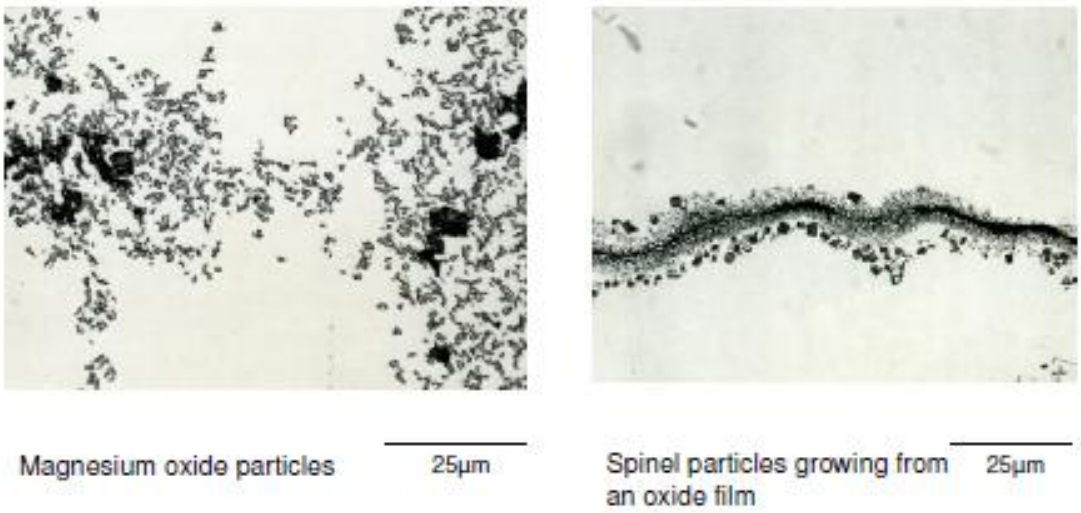

Figure 2.26 Examples of Mg oxide and spinel found in Al using PoDFA [93].

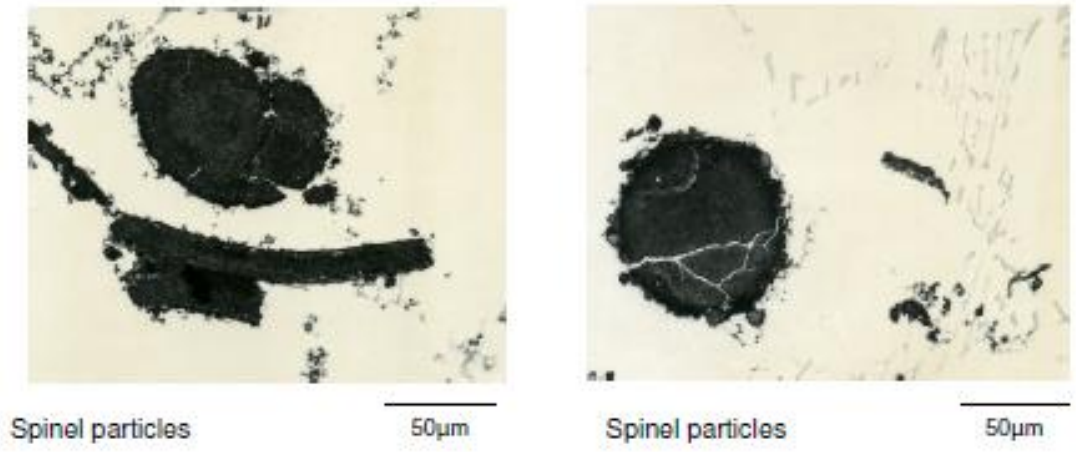

Figure 2.27 Spinel particles found in Al using PoDFA [93].

2.4.1 Double oxide film defects

Researchers have been focusing recently on a specific defect in Al and its alloys; the concept of double oxide film defects originally proposed by Campbell [58], with current literature summarised by Goplan [94]. These defects are thought to be responsible not only for limiting mechanical properties in castings but also provide a novel mechanism for promoting the formation of H gas porosity within castings during the final stages of solidification.

The molten metal surface is oxidised by the reaction of Al with atmospheric O_2 or water vapour, forming a thin film only a few nanometres thick on the surface of the melt within a few milliseconds. This film is from one point of view beneficial, because it protects the interior of the melt from significant further oxidation, and from corrosion once the metal becomes solid.

The oxide is flexible and tenacious and adheres tightly to the surface of the melt but if the surface is disturbed in any way - such as by the motion of splashing, melt additions, bulk turbulence or other forms of poor handling, then this oxide layer can be pushed under the surface of the metal, encapsulating local atmospheric gases (probably consisting principally of air) [95] within and transporting them underneath the surface of the melt, as outlined in Figure 2.28.

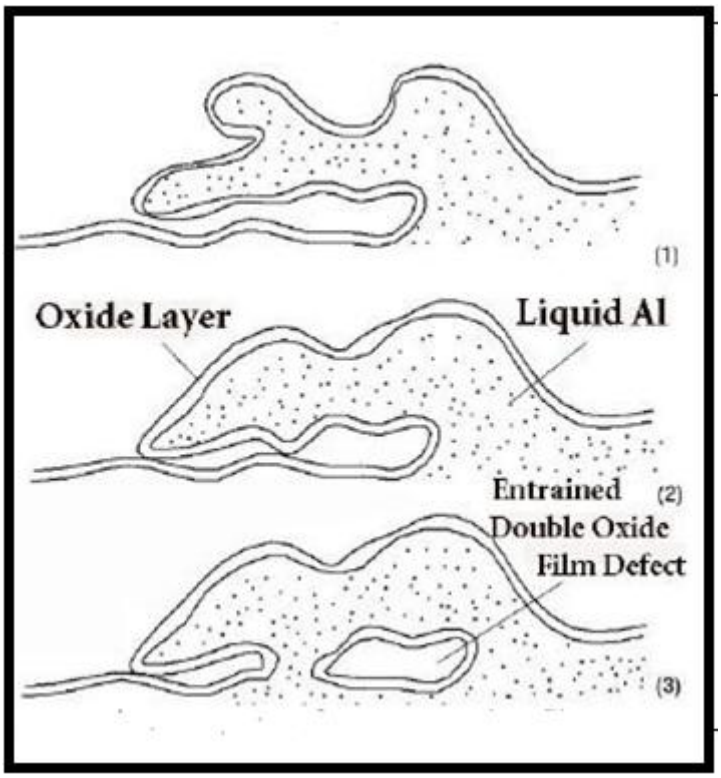

Figure 2.28 The formation of a double oxide film defect caused by splashing and folding of the metal surface. Atmospheric gases are encapsulated by the folding action [30].

Oxygen and alumina are completely insoluble in Al so they enter the liquid metal as a thin flexible ceramic with the atmospheric gases still inside. Alumina particles are typically 50 – 100 µm in size but Al_2O_3 films can be significantly larger, many 100's of µm in length but

being possibly only a few microns thick. They may coarsen over time due to the reaction of these entrained atmospheric gases with the melt [58] [96] so new oxides can be relatively thin whilst old oxides, which have reacted with the melt are thicker, (as shown in Figure 2.25).

The duration of the atmosphere within the double oxide film defect is relatively brief; first the O_2 reacts with the melt and later the N_2 [96] as shown in Figure 2.29 and it is suggested that the gases are consumed within about 3-5 minutes, depending on the size of that defect [97], after which the two opposing surfaces may come together.

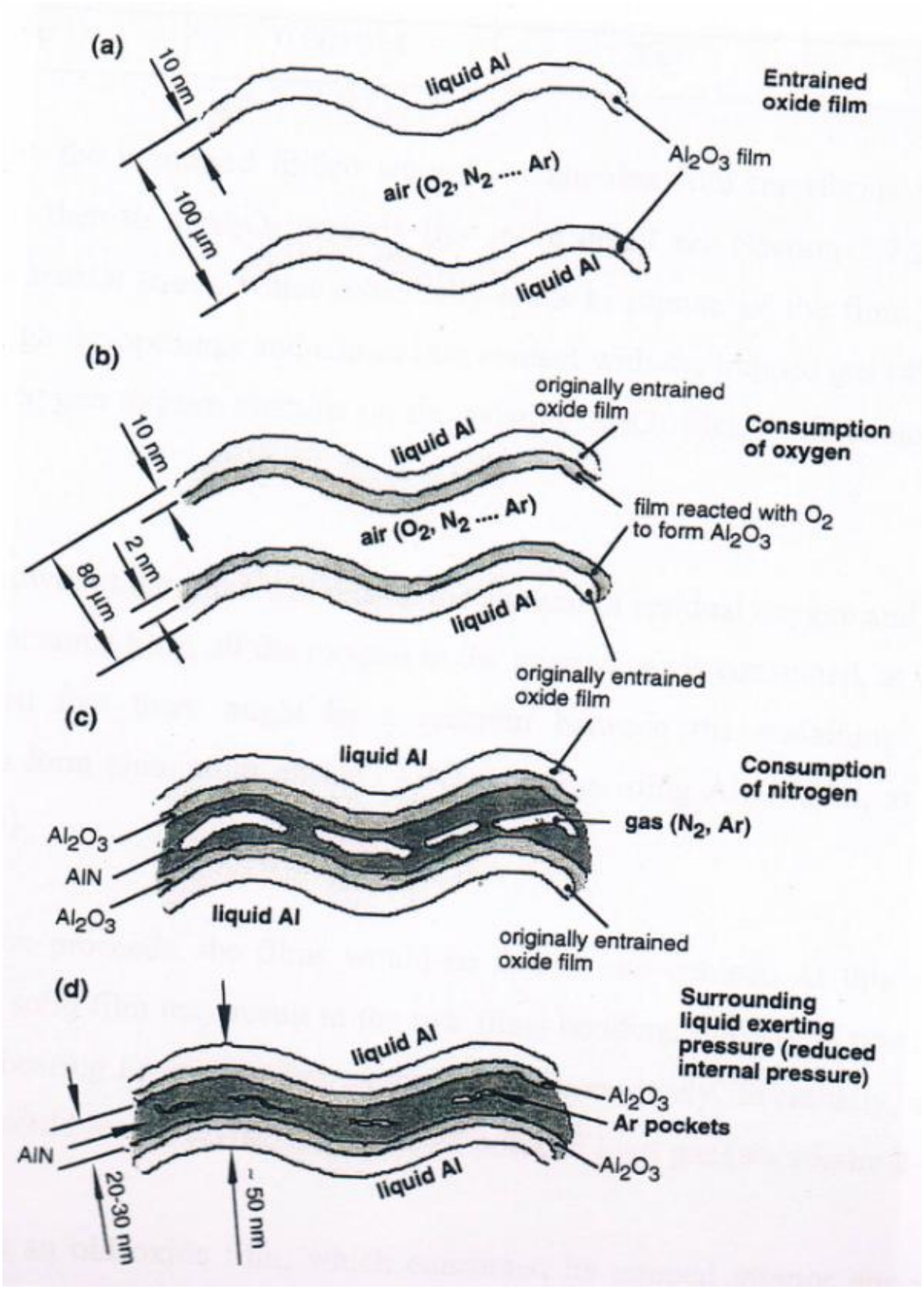

Figure 2.29 An illustration of the consumption of gases within an oxide film defect in Al as proposed by Nyahumwa et al [96].

Razideth and Griffiths [98] explored the reaction of air when held in contact with an Al melt for a prolonged period of time (up to 7 hours). The gases contained within an inert ceramic tube were observed to react with the melt causing a reduction in gas volume. First there was a reaction forming Al_2O_3 by consumption of the O_2, (and of course any water vapour), within the chamber and after about 5 hours the formation of nitrides on the Al was observed; the product of the reaction between N_2 and the melt [99]. The consumption of gases was observed to accelerate after about 5 hours (shown in Figure 2.30) which is likely attributed to break-away oxidation causing rupture of the oxide layer. The O_2 was eventually consumed and N_2 was allowed to react through cracks in the oxide, forming AlN instead. The nitrides formed were small (< 20 microns) in length, with a feather-like morphology as illustrated in Figure 2.31.

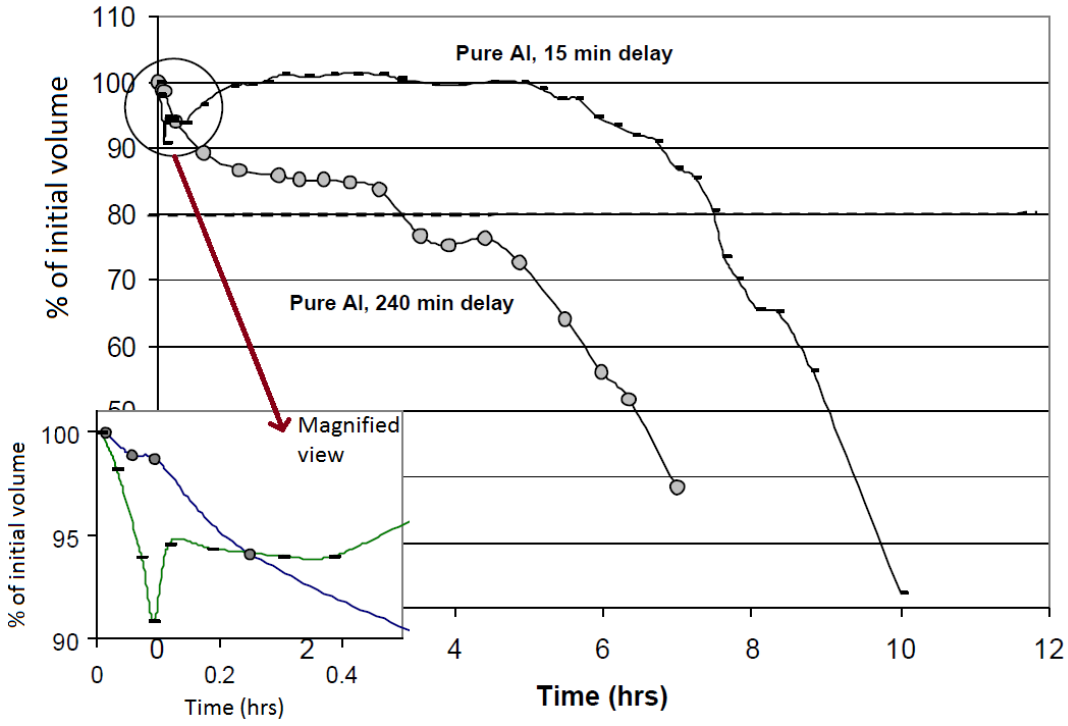

Figure 2.30 The change in trapped air volume when held in contact with an Al melt. After about 5 hours a rapid decrease in volume is observed due to break-away oxidation caused by conversion of γ to α alumina [97].

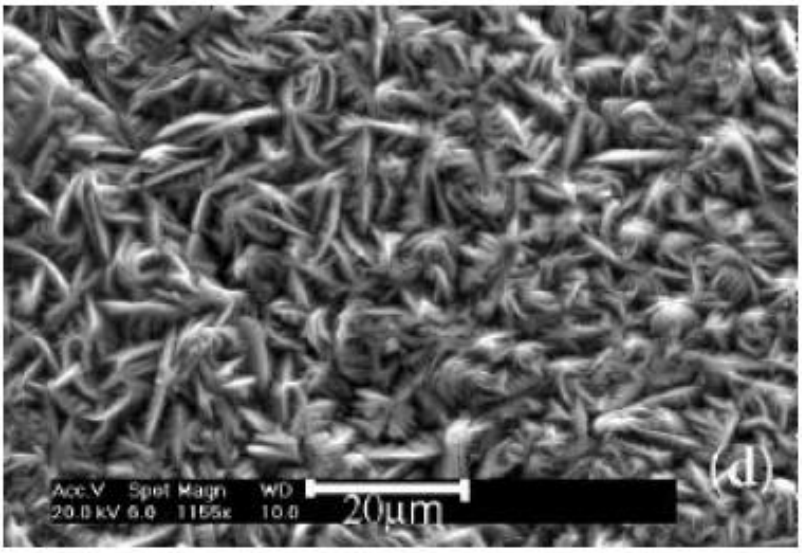

Figure 2.31 A dense layer of AlN crystals was found on an Al sample that was held while molten in contact with air for 10 hours, suggesting that N_2 reacted with the Al surface [100].

Double oxide film defects present an opportunity to explain how porosity can nucleate easily within Al melts, as an existing gas phase below the metal surface, into which H can diffuse and then expand and removes the necessity for a nucleation event [101]. Due to the presence of 1% Ar in air there will always be a gas phase present within the bi-film structure, regardless of the reactions of Al between O_2, water vapour, N_2 and H_2 within the envelope. This residual gas phase would act as a reservoir into which H can diffuse during the final stages of solidification. Diffusion of H into this gaseous envelope could cause expansion of the defect into spherical bubbles with dimensions far greater than the original bifilm [102].

H dissolved within the metal could conceivably enter the bi-film either by 1) diffusion across the Al_2O_3 and / or AlN layers, or 2) by entering the cavity directly by bypassing them completely (such an opportunity might be present if there are cracks in the double oxide film defect).

As previously discussed Mg containing oxides will form porous oxide films at the melt surface and below the surface of the melt the reactions with bi-films should be no different, so if an oxide film will form at the surface of the melt and become immersed during an entrainment event, it then reacts with the melt, the oxide cracks and allows further reactions between the melt and the gases within the bi-film. Following this mechanism H has an opportunity to diffuse into the feature at any time following the entrainment event and could be expanded easily during the final stages of solidification as the H content of the liquid increases due to changes in solubility.

In contrast, both Al_2O_3 and AlN are protective in nature so they will not crack immediately. Al_2O_3 has been shown to be an effective barrier to the diffusion of diatomic H [103] [104] to the extent that 20 nm thick films are being investigated as surface deposition barrier coatings in chemical engineering applications [105] and in electrical engineering applications, to minimise H diffusion. This also applies to the H proton diffusion across alumina, which has been measured to be as little as $6.5x10^{-18}$ cm^2s^{-1} at 25^oC [106] [107]. At this rate, even if the alumina surface of the bi-film was only 10 nm in thickness, it would take over 5,000 hours for H to permeate through the layer [106], (although the diffusion rate would be expected to increase at elevated temperatures).

Based on this it is therefore more likely that either bulk turbulence or the change in oxide morphology (from γ-Al_2O_3 into α-Al_2O_3) causes cracking of the bi-film surface and allows for H from within the melt to enter into the bi-film. If the oxide film cracks then the melt will interact with N_2 to form nitrides (if the atmosphere is free of O_2). Assuming that H does not enter the interior of the film during this event (although there is no reason why it could not enter at this point) the AlN layer will form and H will then only be able to enter the feature

by circumventing these films when cracks form in them, or if they are of a porous morphology.

It should be expected for bi-films to contain some H as well as Ar because air contains traces of water vapour which will also be incorporated into the oxide film defect. At the surface of the melt, moisture reacts with the melt to oxidise (by hydroxide ion diffusion through the alumina layer), and liberate H within the bi-film (and also coincidently increase the H content of the surrounding metal). H that enters into double oxide films directly from the metal will do so, however, as a number of discrete protons (H^+) as this is how the H exists in solution.

Protons are extremely reactive and as they enter the interior of the bi-film it is highly likely (given the temperatures involved) that they will bond with O_2 to form water vapour, with other protons to form diatomic H or even N_2 to form ammonia, and all of these reactions would immediately liberate energy within the bifilm envelope. Reactive by-products (water, ammonia) would also be able to react with the melt, liberating more energy and in both cases the end by-product would be H_2 gas that is released within the oxide film itself. Protons that do not have the opportunity to react with O_2 or N_2 will react with each other to form the covalent diatomic H molecule H_2, which is also a highly favourable and exothermic reaction. The formulas for these reactions are reported in equations 10 – 14 [18] [108]. The Gibb's Free Energy ΔG, (in kJ mol^{-1}) of a reaction is a measure of the thermodynamic driving force that makes a reaction occur. A negative ΔG indicates an exothermic reaction that can occur spontaneously while a positive value indicates and endothermic reaction that requires energy input to occur.

$$3H_2O + 2Al \rightarrow Al_2O_3 + 3H_2$$ (-958 kJ mol^{-1} H_2O)… Eq.10

$$O_2 + 2H_2 \rightarrow 2H_2O$$ (-498 kJ mol^{-1} H_2)… Eq.11

$$2H^+ \rightarrow H_2$$ (-436 kJ mol^{-1} H_2)… Eq.12

$$NH_3 + 2Al \rightarrow 2AlN + 3H_2$$ (-275 kJ mol^{-1} H_2)… Eq.13

$$N_2 + 3H_2 \rightarrow 2NH_3$$ (-105 kJ mol^{-1} H_2)… Eq.14

The local generation of energy and the associated production and formation of diatomic H_2 within the bi-film will lead to an increase in the internal gas pressure within the feature. The combination of increased pressure and heat would likely cause an expansion of the defect and cause failure of the surface film from within by inflating the pore. The failure of the oxide film due to the production of H is described indirectly by the work of Deng and Ferreira [109], who observed that pockets of H_2 formed between alumina and Al during reactions of Al particles with water, which led to fracture of the external alumina layer.

Campbell [58] discussed the possibility of “non-classical” methods of nucleation of porosity, for instance he suggested that trace radioactive elements in an alloy, (that would release high energy into the surrounding area), could create a small gas phase within Al by heating the surrounding Al during solidification. The H would then diffuse into this gas phase and develop into a pore. As H protons come together and react exothermically to form diatomic H_2 (or with other elements within the film such as O), they could theoretically release sufficient energy to create a gas phase by boiling the surrounding Al.

2.5 Hydrogen and inclusion removal from molten aluminium alloys

Foundries utilise a variety of methods to control H levels and inclusions in molten Al; they typical involve injecting gases directly into the melt, by lances, porous plugs or diffusers, or most effectively in-line rotary degassing units.

In each case an inert gas (typically Ar or N_2, with an addition of either Cl or a salt flux to remove inclusions) is bubbled up through the melt. H diffuses out of the melt and into the bubbles, which exit the metal at the surface and release the H into the environment as shown in Figure 2.32.

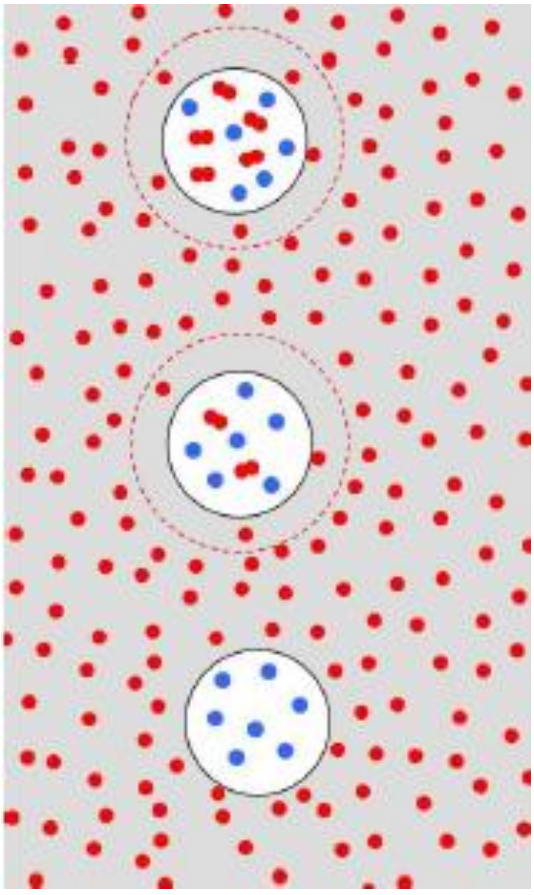

Figure 2.32 H dissolved in the molten Al diffuses into inert gas bubbles through a boundary layer. The bubble exits at the melt surface, reducing the melt H content [93].

2.5.1 Hydrogen removal

This degassing process occurs as a result of the partial pressure difference between H in the melt and in the bubbles. There is a driving force for transport of H into the bubbles, since equilibrium between the gas phase and melt demands that the H activity in the melt equilibrates with the partial pressure of H in the bubble (assuming that the pressure of H within the bubble is less than the surrounding melt). Within the melt the H is removed by a series of steps outlined by Sigworth & Engh [110];

1) H transport in the melt to the vicinity of an inert gas bubble (by diffusion).
2) Diffusive transport through a thin stagnant layer of fluid or 'boundary layer' surrounding the bubble.
3) Chemical adsorption onto and subsequent desorption from the bubble surface.
4) Diffusion of H as a gaseous species inside the bubble of the purge gas.

In their work they highlighted that step 2 was the limiting step in H removal so melts containing elevated levels of H will degas 'more efficiently' than melts with a lower H content (shown in Figure 2.33). This occurs as there is more of a diffusive driving force (greater diffusion gradient from melt to bubble) for H to enter the bubbles. In practise this will mean that a degassing procedure implemented on a fixed quantity of metal using a constant gas flow rate proceeds first quickly and then more slowly as the H levels within the melt decrease.

The interactions at the bubble – melt surface are critically important as the area over which diffusion can take place is also vital. Decreasing the bubble size will increase the efficiency of

degassing dramatically because the gas bubble / melt interaction area is increased. High degassing efficiency (> 80%) occurs when the gas bubbles are < 5mm in diameter. This is because when the bubble size is halved the surface area increases by a factor of four [25], increasing the degassing rate with decreasing bubble size (shown in Figure 2.33).

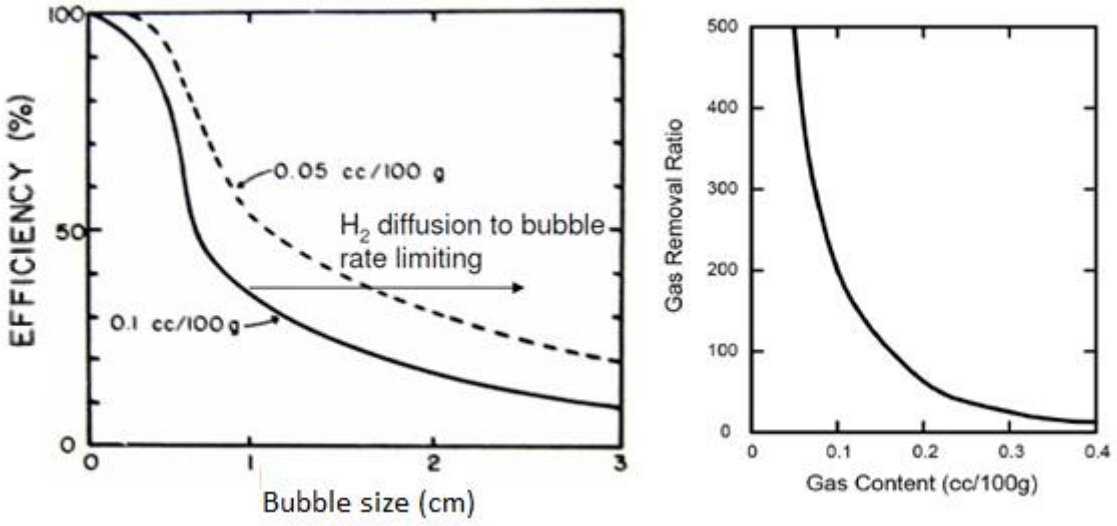

Figure 2.33 a) Degassing efficiency is limited primarily by H diffusion rates, decreasing with lower melt H levels and with larger bubble size b) The H removal ratio increases with melt H content (i.e. more pure gas is required to remove H when H levels within the melt are low) [25].

If the bubble size increases above about 15-20 mm, the bubble changes from an ideal spherical bubble to a less efficient ellipsoidal or spherical–capped shape. For this reason the choice of gas injection technology becomes very important. Lances for example are a crude poor design. Lances are reported as being as little as 1 – 20 % efficient at removing inclusions and H [18] [25] because of the large bubbles generated by this process (bubbles are many cm in diameter). Celik & Doutre [111] actually predicted that lance degassing will generate additional inclusions due to the large bubble size created using this process,

leading to splashing at the melt surface. Steel tubes can also corrode and introduce Fe (and Si if they are glass coated) into the metal, which is undesirable in most aerospace alloys.

Porous plugs are an improvement in design, showing a performance of around ~40 - 50%, but by far the best choice is to use rotary degassing units, which can remove 50 – 80% of the melt H in a relatively short time due to their design. The concept of in-line degassing units, which injects gases directly into the metal from below the metal surface using a spinning rotor, were first introduced into cast houses by Union Carbide in 1974. Modern degassing units such as SNIF (Spinning Nozzle Inert Floatation) or A622 reactors (differing by manufacturer and design) utilise two or four rotors within in separate chambers within the degassing unit. A schematic of a SNIF and the bubble distribution profile can be seen in Figures 2.34 and 2.35. The metal enters the unit (which is sealed and covered with an inert gas to prevent the metal surface being oxidised by interaction with the air) and gas mixture exits the underside of the rotor dispenser and the gas mixture is broken up into fine discrete bubbles as it passes up between the rotating vanes of the rotors. The metal then exits the reactor and towards the casting station.

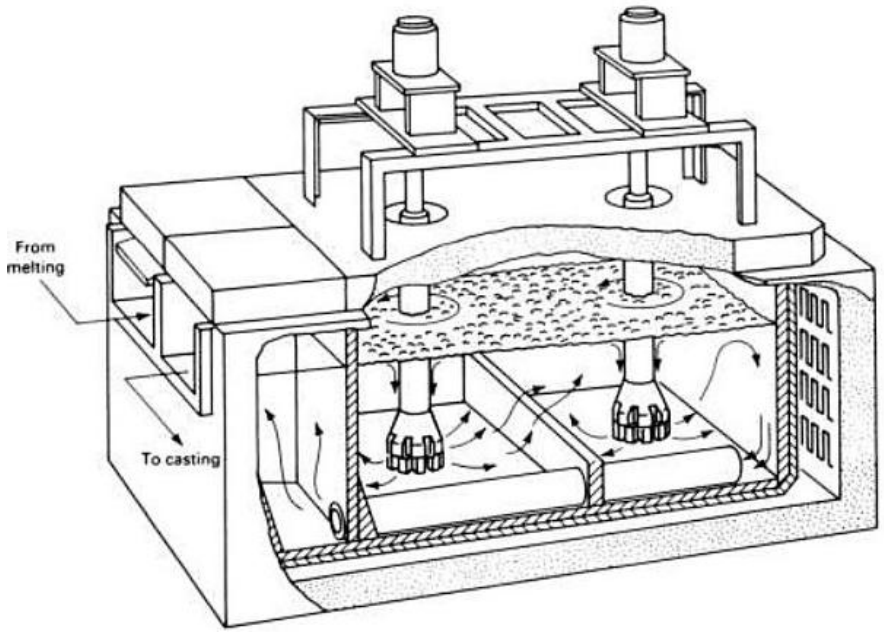

Figure 2.34 A schematical diagram of a SNIF (Spinning Nozzle Inert Floatation device) degassing unit used at Alcoa [93].

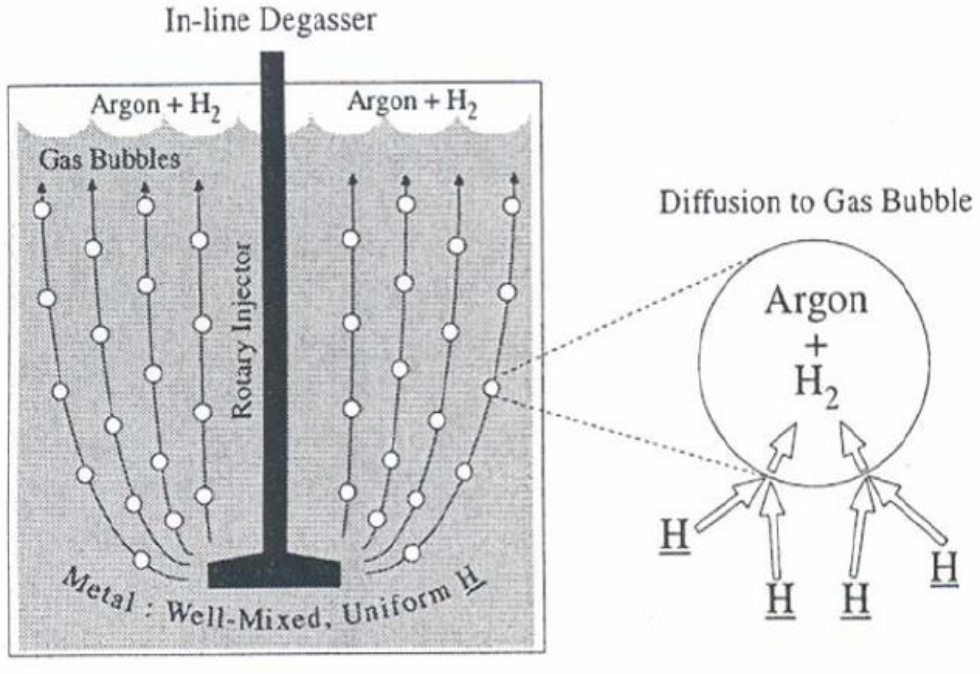

Figure 2.35 Visual interpretations of H pickup in Ar gas bubbles. Dissolved H will diffuse into the bubbles and exit the metal at the surface [93].

This type of degassing unit increases the effectiveness of H and inclusion removal, the reasons for this are as follows;

- Increased levels of bulk melt turbulence and stirring increases both particle - particle and bubble – particle collisions.
- Spinning rotors break up the gas stream into a fine dispersion of bubbles, which are spread uniformly throughout the reactor in a more efficient 'cloud' of bubbles (compared to a static lance).
- Fine bubbles have lower buoyancy in the molten metal, meaning they will rise more slowly up through the liquid and have longer time to interact with the metal.
- Smaller bubbles have a greater surface area which will increase the rate of surface controlled reactions (e.g. with inclusions) and diffusion of H into the bubbles.

2.5.2 Bubbles and solid phases in molten aluminium

As the bubble rises up through the metal the gas bubble interacts with solid particles and transports them to the free surface of melt. Floatation of discrete particles is described in similar mechanisms by Firouzi [112] and Wang et al [113] to consist of three basic sub processes; namely collision, attachment and detachment.

Collision involves the approach of a particle to a bubble in the field of flow and is governed by the liquid flow and the relative motion between bubbles and particles. The attachment involves three steps: (1) the thinning of the intervening liquid film between a bubble and a particle to a thickness of film rupture (2), the rupture of the liquid film and formation of a

three phase contact nucleus between the solid, liquid and gas (3) expansion and relaxation of the nucleus contact line from the critical radius to form a stable wetting perimeter.

The process of removal is influenced by factors including the liquid flow, properties of the inclusion (e.g. density, surface texture), bubble size and molten metal characteristics such as temperature, fluidity and depth. When particles do not wet the liquid phase the particles can be trapped by gas bubbles.

Attachment of inclusions to gas bubbles in steel is described in detail to occur in one of two mechanisms; (1) “Collision attachment”, where the inclusion approaches the gas bubble and a thin liquid film builds up between the inclusions and the bubble and the film drains until film rupture occurs. If the collision time is longer than the film drainage time the inclusion will be attached by collision but if the drainage time is greater the inclusion will be ‘bounced’ away from the bubble or it will slide on the surface of the bubble. (2) “sliding attachment”, where if the sliding time is greater than the drainage time then attachment will occur during sliding, but if the drainage time is greater, then the inclusion will not become attached at all to the bubble. Schematics of the interactions between bubbles and solid phases in molten metal are shown in Figure 2.36.

A water model [114] highlighted these steps using a 4mm diameter bubble and 100 µm inclusions made of copolyamide, shown in Figure 2.37. Inclusions were seen to collide and attach or leave the surface of the bubble around the equator of the bubble. Those inclusions that did attach existed in a ring around the bubble, the most likely explanation for which is that this location corresponded to the location where the force balance on the inclusions was a minimum.

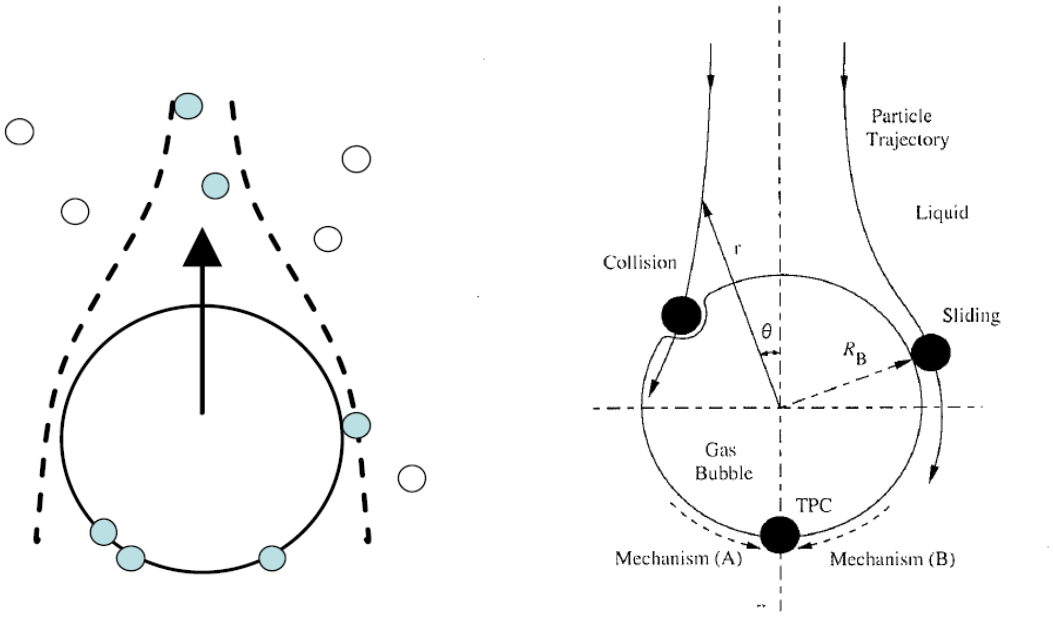

Figure 2.36 Visual interpretations of spherical inclusions interacting with particle like inclusions. Inclusions ahead of the bubble can either adhere with or flow around the gas bubble [113], [115].

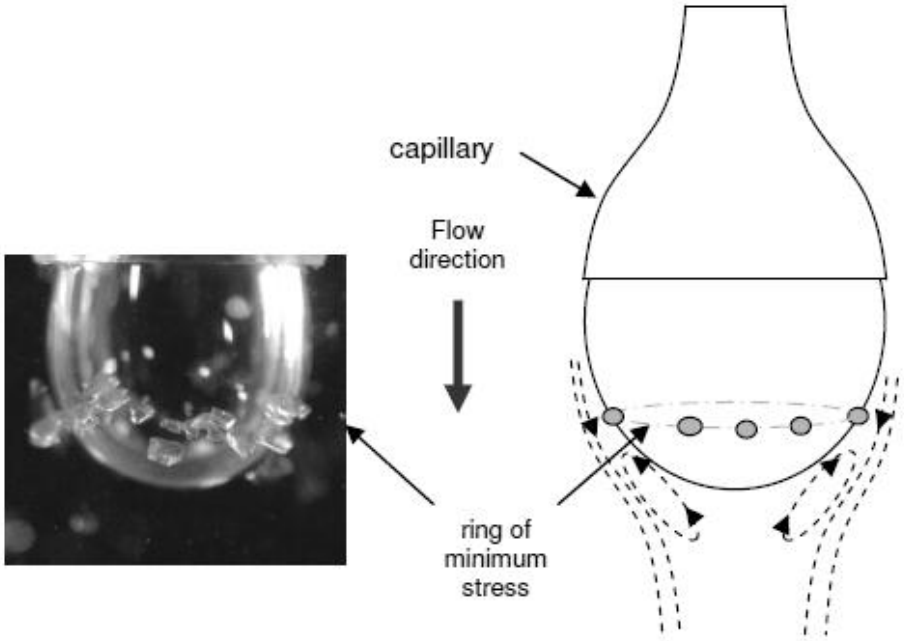

Figure 2.37 A cold water model demonstrating the collection of copolyamide inclusions on a gas bubble during flow [114].

Wang et al [113] described the probability of collision between a bubble and an inclusion (P_C) and the probability of adhesion of an inclusion to a bubble sliding (P_A) as being defined to describe the efficiency of inclusion attachment to a bubble. Small bubbles were demonstrated to have a high P_C while inclusions have a high P_A and a low P_C. The overall probability P (P_C x P_A) and the floatation time of the bubble suggested that the optimum bubble size for removal of fine non-wetted inclusions (inclusions of diameter 5 - 50 μm in size) was 0.5 – 2 mm in diameter. Calculations by Szekely [116] indicated that 95% of inclusions would be expected to be removed from molten Al within in a SNIF unit when using a bubble size <5 mm.

Inclusions that float to the surface of the melt are essentially removed and form part of the dross layer. Evidence has been presented in both steel [117], and water models [118] however that trapping of small bubbles within the melt can occur as they have insufficient buoyancy to exit the metal, or become trapped against a feature that prevents them from exiting the metal (e.g. a thick oxide or salt layer present at the surface of the melt). In steel for example this leads to development of line and internal defects in the product as the bubbles are held beneath the slag layer and cannot exit the melt. Zhao et al [59] also noted that H_2 bubbles were sometimes prevented from exiting Al melt during rapid re-melting of pure Al samples, presumably due to the presence of a surface oxide film that prevented them from escaping the melt.

2.5.3 Removal of inclusions and undesirable metallic elements from aluminium.

As inclusions and H can have detrimental effects on mechanical properties, methods are needed to remove them from the melt before casting. Historically inclusions were removed from the molten metal in the holding furnace by allowing the melt to stand un-touched for a few hours before casting. This practise was employed as it allows inclusions that are lighter or heavier than the liquid metal to separate out purely by density over time as shown in Figure 2.38 [119]. These natural processes are slow and extremely in-efficient (it requires holding the metal at temperature for a prolonged period, consuming energy and increasing production costs) so active methods are implemented to reduce the treatment time and increase the quality of molten metal. They are fluxing (using salt and/or Cl gas), and filtration.

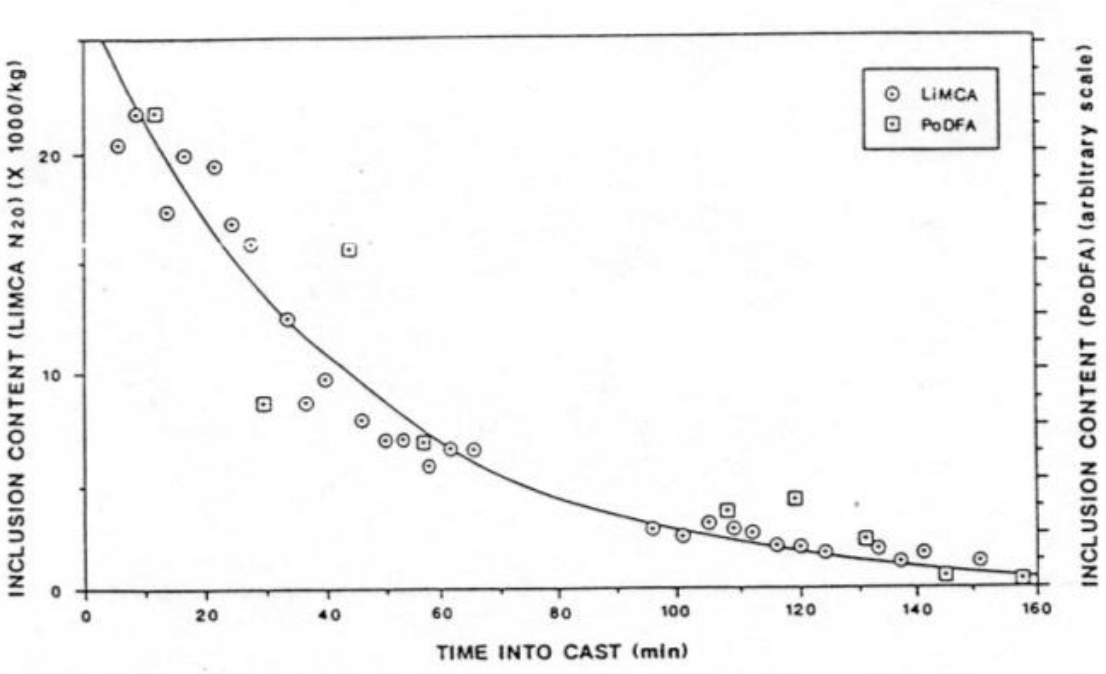

Figure 2.38 The effect of settling on inclusions concentration, measured using LiMCA and PoDFA [119].

2.5.4 Filtration

In-line ceramic foam filters (CFF) are commonly used to remove inclusions from molten metal as it flows through the filter pores. Solid inclusions with a size greater than the pore are trapped as they cannot flow through the network of pores. As the molten metal travels through the filter, smaller entrained particles collide with the filter media, or settle upon it by sedimentation. These small particles can begin to build a “cake” of bridged particles, which effectively reduce the effective pore size and increase the effectiveness of the CFF over time [93]. Traditional foam filters or glass fibrous web filters are reported to be good at removing large inclusions (100% of inclusions > 125 µm were removed using a 30 ppi filter), [120] but poor at removing small inclusions (<40 µm) unless coated with an active coating such as KCl – NaCl which form a layer of molten flux during casting [121]. Any inclusions which make contact with the wall adhere to this layer and are removed, although those which don’t make contact with the filter wall will remain in the metal [14]. An example of filtration performance of a deep bed filter is shown in Figure 2.39 [122]. The interactions of inclusions with filter materials are shown in Figure 2.40.

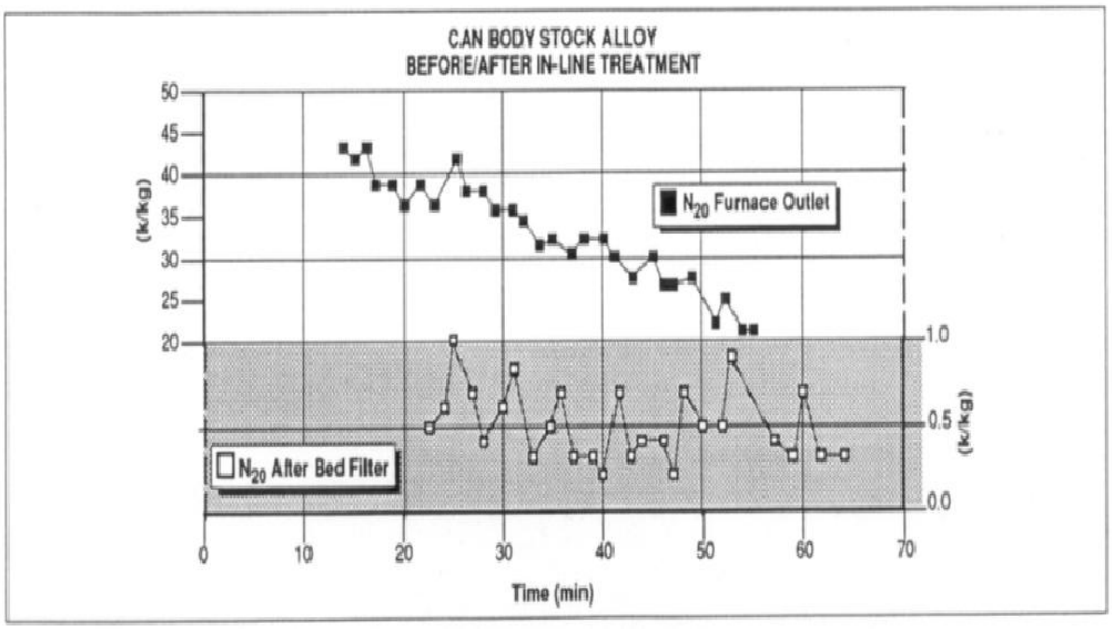

Figure 2.39 LiMCA II results in thousands of inclusions larger than 20 microns per kg of metal (N20). Measured for can stock alloy (AA3104). Natural settling occurs over an hour of LiMCA analysis whereas metal fed through an aluminia bed filter is cleaned to a higher standard over a shorter period of time [123].

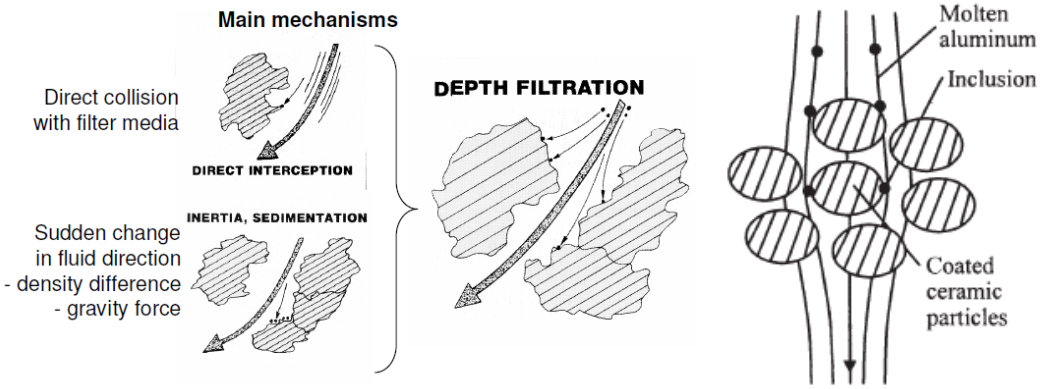

Figure 2.40 The mechanisms of removal of entrained inclusions by filtration [93], [121].

The erosion and corrosion effects on the filter surface can also generate inclusions as the filter material is attacked by the molten metal, with the reaction products and debris (filter material) entering into the melt over time. This is especially common in Li containing alloys

unless filter material is taken into consideration and they are coated with a protective substance such as boron nitride. Filters have no positive influence on the H content of the metal, alternatively if they are poorly stored and are allowed to absorb moisture they could provide a H source to the metal as the moisture reacts with the melt.

2.5.5 Removal of inclusions and alkali metals using chlorine

To non-metallic inclusions (such as oxides) Cl will act as a surfactant. The Cl or chloride reaction products wet or coat inclusions and particulates and decrease the surface tension between them and the melt [124]. Cl lowers the interfacial surface tension between gas bubbles and entrained particles, facilitating adsorption of the particle to the gas bubble surface [125] which causes the particle to be floated out of the melt along with the bubble. This is especially true for oxide films suspended in the melt [25], probably because of the large contact area presented by such features, making them easier and more likely to be lifted out of the metal. Smaller sub-micron inclusions are likely to collide and agglomerate in turbulent flow conditions leading to an increase in size across the inclusion size distribution [114] [126], yet still removing them from the metal. Coalescence and agglomeration of inclusions and de-wetting from the Al (with sufficient stirring) means that inclusions can be separated from the melt much easier.

Cl in both gaseous and solid (salt) form has been shown to be effective at removing inclusions and alkali metals from liquid Al [111] [114] [115] [127] [128] [129] [130] [131] [132]. Examples of Na and inclusion removal by Cl utilising degassing units are shown in Figure 2.41 and 2.42 [25] [124].

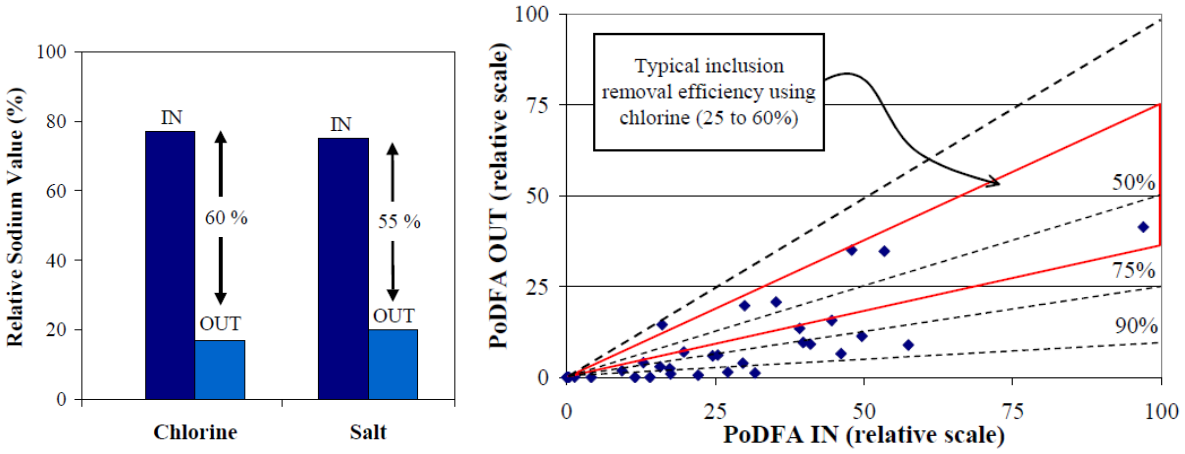

Figure 2.41 The removal of Na and inclusions from molten Al using Cl and salt fluxes using a rotary flux injector, adapted and modified from Leboeuf et al [124].

Sample Location	Taphole	After A622
Total Inclusions	0.132	0.008
TiB_2	0.087	0.003
Al_4C_3 (< 3 µm)	0.036	0.001
Al_4C_3 (> 3 µm)	0.007	0.004
MgO	0.003	---
$MgAl_2O_4$ (spinel)	---	---
Potential Chlorides	trace	trace
Oxide Films (#/kg)	3	0

Figure 2.42 The removal of inclusions from 8111 alloy using an A622 rotary degasser (using Ar and Cl). Results measured using PoDFA, values are mm^2/kg except for oxide films which have a unit value per kg. Approximately 90% of inclusions are removed during the process [133].

Celik and Doutre [111] found that fluxing with Ar or N_2 successfully removed dissolved H but was completely ineffective in removing inclusions, while fluxing with Cl and inert mixtures removed all types of inclusions and trace elements such as Ca. Chesonis and DeYoung [127] also found that Ar + Cl removed Ca from molten Al but Ar alone did not influence Ca removal. They found that it was actually likely that degassing with inert gases alone will

increase the inclusion content as disruption of the melt surface caused by bubbles exiting the metal will cause oxidation of the metal. The results of this experiment are shown in Figure 2.43; where LiMCA N_{20} counts were shown to increase with inert gas injection and decrease with Cl containing gas injection into pure Al.

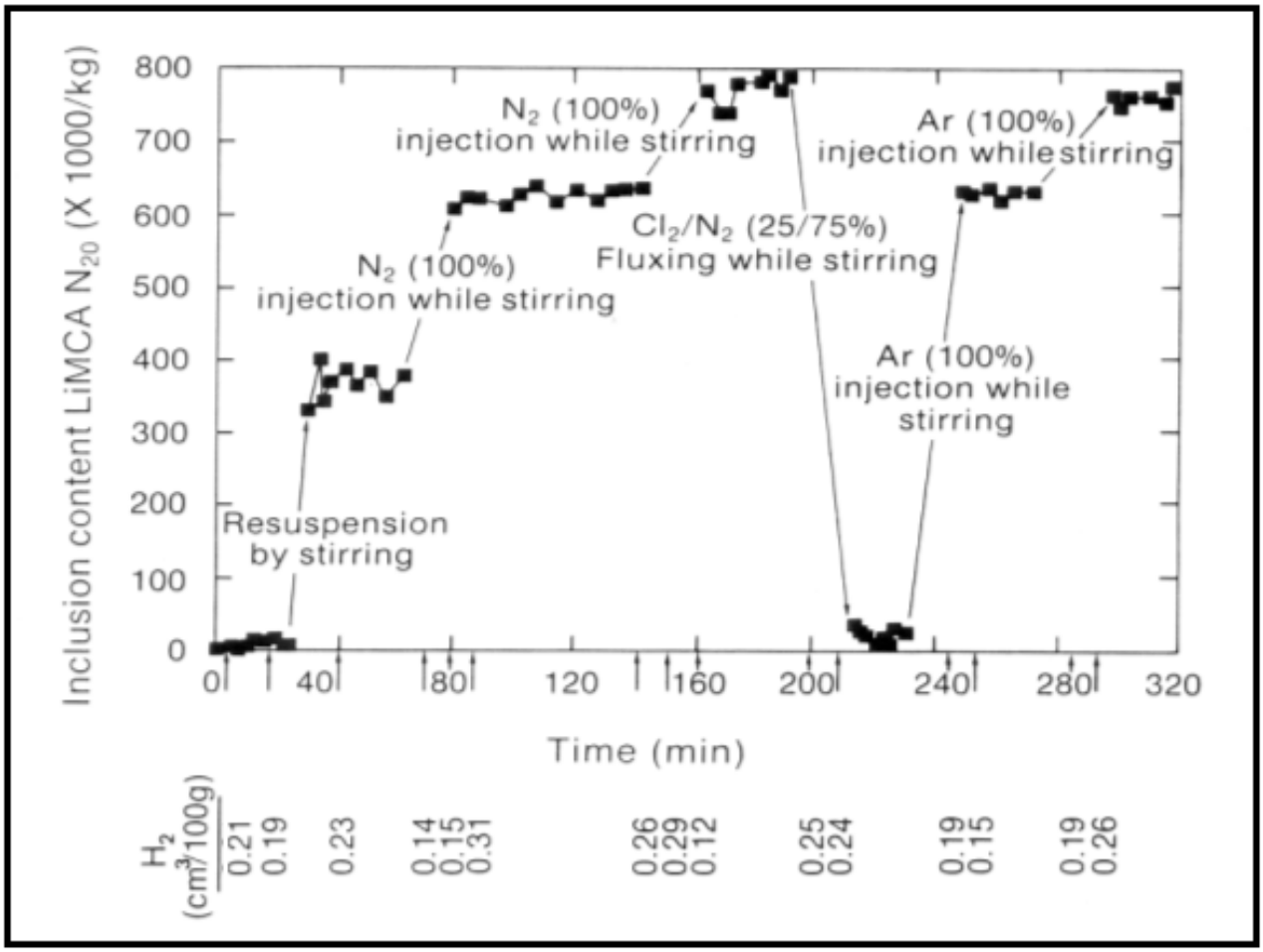

Figure 2.43 The generation of inclusions by injection of N_2 and Ar gases and removal of inclusions by injection of Cl containing gases, in Mg free Al. Melt stirring by impeller at 600 rpm. Gas injection by graphite lance (12.5 mm ID x 50 mm OD) [111].

Cl usage has become a focus of strict environmental regulations by government agencies [123], so the future use of Cl within industry is somewhat questionable. Many recent technologies [23] [124] [129] [134] have been designed around replacing Cl (gas) with chloride containing fluxes that are injected directly into the melt to reduce the

environmental and health and safety implications.. The injection of solid (e.g. powder or granular) fluxes has been shown to be effective at removing inclusions and reducing or eliminating chloride emissions [135] [136].

2.5.6 Removal of undesirable alloying elements from aluminium using chlorine gas

This group of impurities includes those elements from the first two columns of the periodic table; the alkali and alkaline earth metals, primarily Na, Ca, Li and Mg.

Mg and Li can be both deliberately made alloying additions or classed as impurities depending on the alloy design. Both elements are solid solution strengtheners, increasing the mechanical properties (e.g. increasing stiffness), but they also decrease ductility, increase the oxidation rate of the alloy by substituting for Al at the metal surface and can degrade the corrosion resistance (especially Li alloys). Both Na and Li have been known to degrade surface quality during hot rolling of Al alloys [23]. Na has been reported to cause hot shortness (a process where grains pull apart from one another during hot rolling, due to the presence of low melting point eutectics at grain boundaries). Manufacturers of can stock and foil may wish to control the amount of Mg in different parts of the Al container. The top and bottom of beverage cans contain ~4 wt.% Mg while the can body has less, ~1 wt.% Mg. Re-melt Al which has excessive Mg for purpose is often 'de-magged', lowering the Mg content of the alloy. This is typically achieved by salt fluxing or by injection of Cl gas into the melt [137].

Cl is very reactive and it had been thought by Botor [138] that Cl will react with H in the melt to form HCl, potentially enhancing the degassing rate, however the reaction between Al and

Cl is more thermodynamically stable, and so the latter reaction will occur preferentially [138] although it is possible for $AlCl_3$ that exits the melt at the surface to react with atmospheric water vapour to form HCl and Al_2O_3 dust which forms 'white smoke' in and around the degassing units [111].

As bubbles comprising a mixture of Cl and Ar rise up through the molten Al they react with the Al to form compounds of aluminium chloride (AlCl, $AlCl_2$, $AlCl_3$, Al_2Cl_6) depending on the concentration of Cl in the purge gas, but below 10% Cl the most favoured gas species to form are $AlCl_2$ and $AlCl_3$ [139].

The chlorides that form are then expected to be dispersed within the melt, depending on their state and physical characteristics. Relatively low melting point salts might be expected to reside as molten chloride droplets (e.g. $MgCl_2$), floating within the melt, while insoluble solid salts (such as NaCl) should be floated out of the melt and partitioned into the dross layer at the surface of the melt, [133] as shown in Figure 2.44.

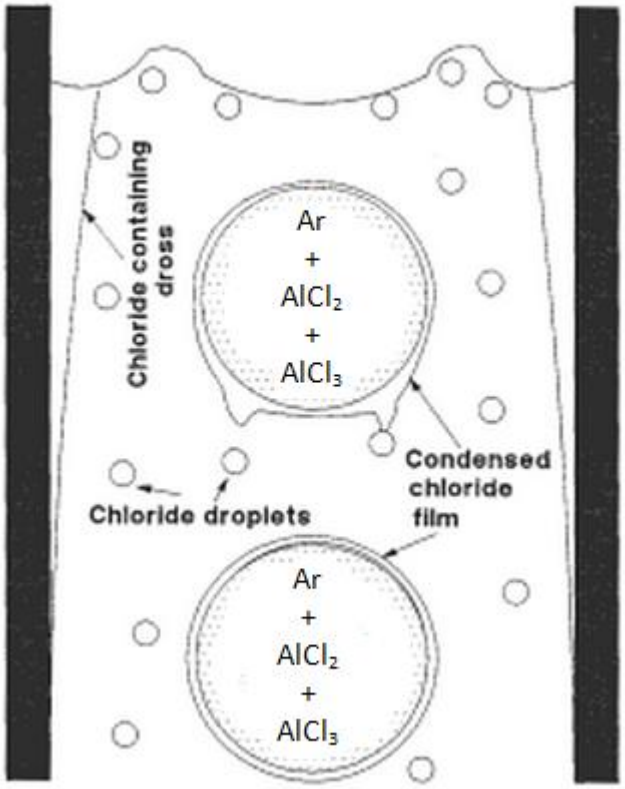

Figure 2.44 Gaseous Cl additions are proposed to react with the melt, dispersing reaction products between the surface of the bubble, within the melt as droplets and into the dross layer [139].

A variety of chlorides form during degassing and fluxing and this occurs because Cl reacts with the Al which then reacts with other elements such as Mg. Al reacts with Cl with a conversion efficiency > 98% [111] and as most wrought alloys are > 90% Al, $AlCl_x$ is likely to form first and serve as the dominant species for other reactions within the melt. I.e. it is $AlCl_x$ that reacts with other chloride forming elements to form other more thermodynamically favourable gaseous, liquid or solid reaction products within the melt, not Cl directly. As an example the reactions between Al, Mg, Ca and Cl are detailed in equations 15 – 18 [127] [124]. $AlCl_x$ will react with Mg within the melt to form $MgCl_2$,

liberating Al as shown in equation 17 [137]. $MgCl_2$ can then react with Ca in the same manner, substituting with Ca to form $CaCl_2$ and liberating Mg.

The reactions of Cl are greater with Ca, Li, Mg, Na, K (the most notable) than Al according to the Ellingham diagram [140] so these elements can be removed from the melt using Cl, but others (for example Fe and Si), cannot be removed by chlorination of the melt as reactions of Cl with these elements are less favourable and will not substitute with the $AlCl_x$. The reactions of O and Cl with various alloying elements are summarised in Figure 2.45. The reactions of Mg and Ca with Cl at the bubble interface are shown in Figure 2.46.

$$2Al + 3Cl_2 \rightarrow 2AlCl_3 \qquad (-354.5\ kJ/mol\ Cl_2) \ldots Eq.15$$

$$Mg + Cl_2 \rightarrow MgCl_2 \qquad (-481.7\ kJ/mol\ Cl_2) \ldots Eq.16$$

$$2/3\ AlCl_3 + Mg \rightarrow MgCl_2 + 2/3\ Al \qquad (-127.2\ kJ/mol\ Mg) \ldots Eq.17$$

$$Ca + MgCl_2 \rightarrow CaCl_2 + Mg \qquad (-157.1\ kJ/mol\ Mg) \ldots Eq.18$$

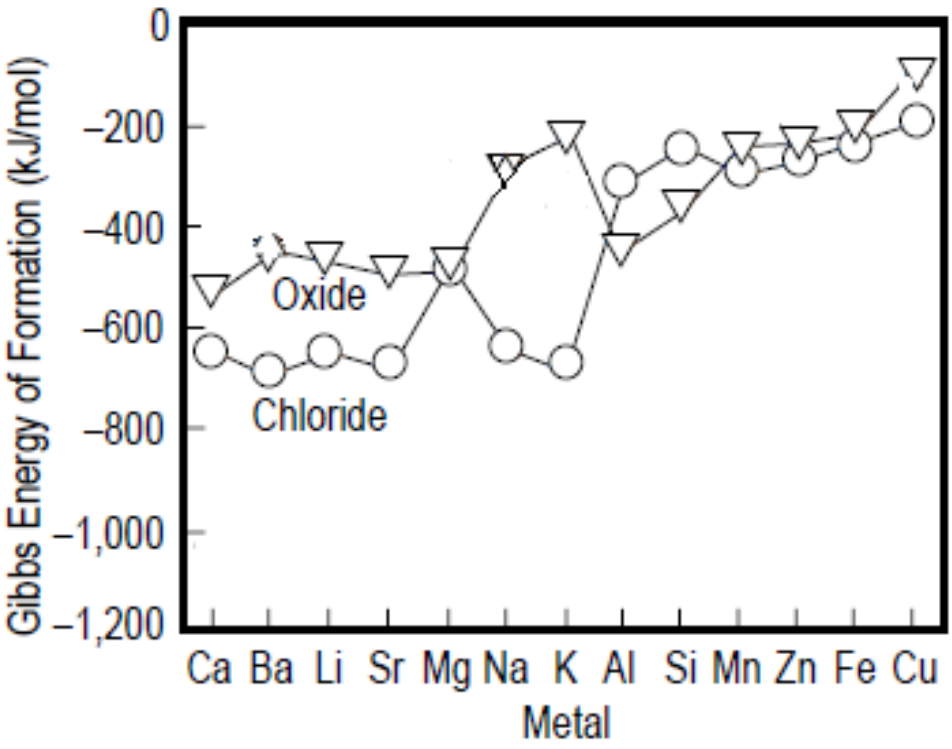

Figure 2.45 The reactions between common alloying elements reacting with oxygen and Cl from Utigard et al [92]. Graph modified to show only the energies of formation of oxides and chlorides of these common alloying elements.

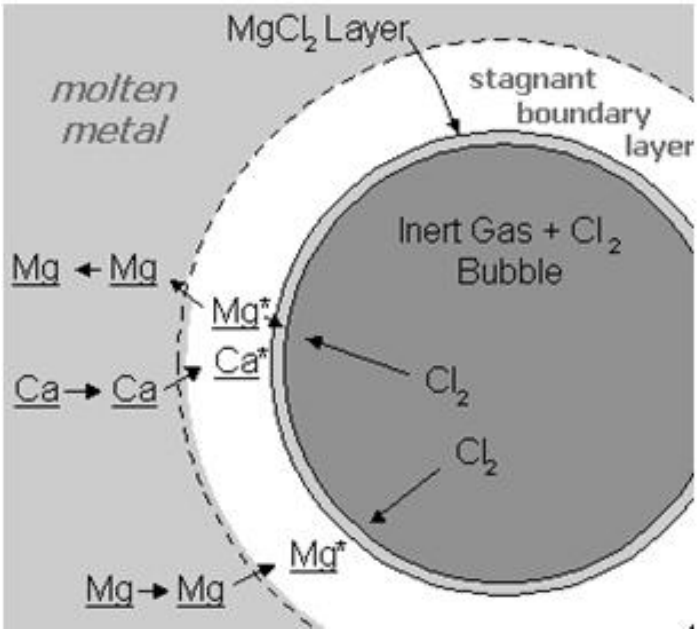

Figure 2.46 The interactions of Mg and Ca with a chlorinated gas bubble within Al [141].

Consumption of Mg by Cl to produce $MgCl_2$ was demonstrated by Qian et al [142] by reaction with Cl. The emissions of chlorides exiting a high Mg melt were shown to be much greater below the melting point of $MgCl_2$, 714^{o}C. Above this temperature low levels of Cl emissions persisted throughout a Mg removal experiment until nearly the end, at which point the emissions increased greatly. Qian suggested that below a critical concentration the reaction was first order, controlled by mass transport of Mg to the bubble surface and the transport of Mg to the bubble was insufficient for conversion of all Cl / $AlCl_3$ within the bubble to $MgCl_2$. Above the same critical Mg concentration the Mg removal rate was controlled purely by the rate at which Cl was supplied to the melt, and due to the low chloride emissions found above the melt it was concluded that above the melting point of 714^{o}C practically all Cl was converted to liquid $MgCl_2$.

It is therefore not Cl but $MgCl_2$ that is the most important compound for removing alkaline metals and inclusions from molten Al. Celik and Doutre [111] found that the rate of removal of Ca from pure Al remained constant regardless of increasing Cl content within a N_2 carrier gas (6.25 – 25% Cl in N_2). The same experiment performed with a 1% Mg addition increased the removal rate by 25 – 133% over the same range of gas flow rates (shown in Figure 2.47), this increase in Ca removal occurred because the rate of removal of Ca (which is initially controlled by the reaction between $AlCl_3$ and Ca), is enhanced as the liquid $MgCl_2$ salt formed at the bubble surface enters the melt and Ca is then removed by an additional substitution reaction with the liquid salt. This effect is demonstrated by the dependence of rate constant for Ca removal on both Mg and Cl contents. The rate constant depends on the availability of $MgCl_2$ (higher in a Mg containing alloy than in pure Al) and in the Mg containing alloy the rate constant for Ca removal also increases with increasing Cl_2, since

that too increases the availability of $MgCl_2$. The removal of Ca was shown to continue after the gas injection had stopped (as shown in 2.48) because previously formed $MgCl_2$ was still present in the melt and continued to react with the remaining Ca over time.

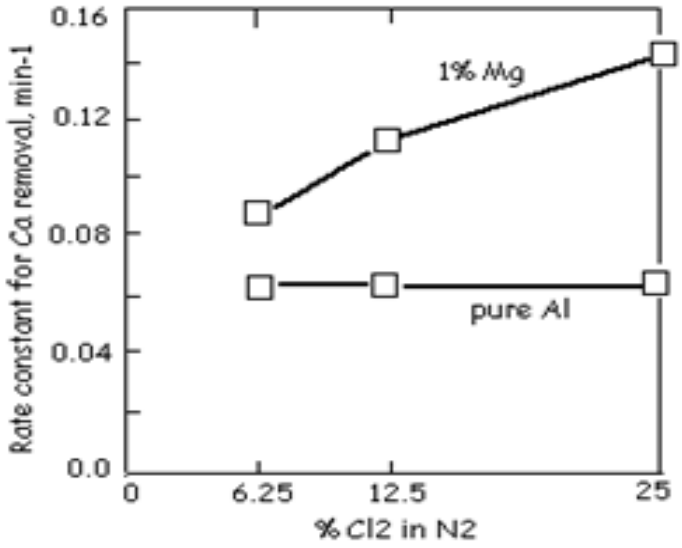

Figure 2.47 The removal of Ca by injection of Cl containing gases occurs faster in alloys containing Mg due to the formation of $MgCl_2$, which enhances the rate at which Cl can react with Ca [111].

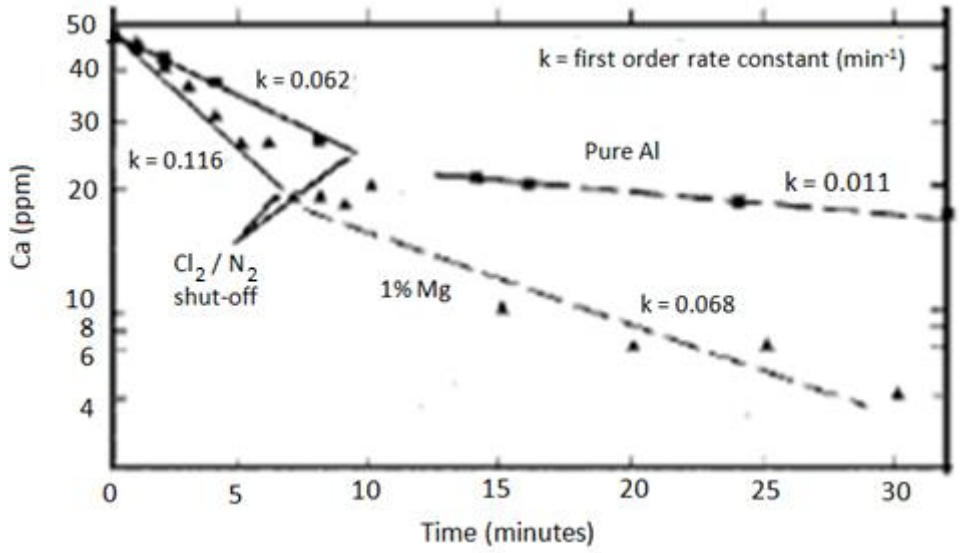

Figure 2.48 The removal of Ca from Al occurs even after the application of Cl gas has been halted. This occurs because molten $MgCl_2$ continues to react with Ca within the melt over time [111].

Roy et al [131] demonstrated that increasing levels of Cl (1, 2, 5, 10 and 20% Cl, in N_2), increasing gas flow rates (200, 500 and 1000 cc/min), and increasing rotor speeds for a rotary degassing system (100 – 500 rpm) all increased the rate of inclusion removal in an A356 alloy (0.20 – 0.45 wt.% Mg) at 740^{o}C when doped with SiC inclusions. The efficiency of inclusion removal increased as the probability of successful collisions between injected gas and those inclusions increased with increasing Cl and rotational speed (melt agitation), shown in Figures 2.49 and 2.50.

By reducing the bubble size and increasing the degree of melt turbulence (both increase the likelihood of collisions and successful adhesion of inclusions to the bubbles) and due to increased concentration of Cl at the bubble boundary layer, more successful collisions occurred. The inclusion removal rate was shown to be dependent on the number of collisions which occurred after an incubation period, during which inclusion removal was poor. The duration of incubation was the same regardless of flow rate and rotor speed but decreased with Cl concentration. This was reportedly to be because the wetting properties of the bubbles and inclusions became more favourable over time, although no mechanism is presented for this phenomenon within the work. The likelihood was that chlorination of the melt led to the development of liquid $MgCl_2$ salt droplets which increased the adhesion rate of the inclusions, making them agglomerate quicker with increasing Cl concentration. Additional Cl above a critical amount made little effect on inclusion rate removal, probably due to the consumption of all of the Mg within the alloy to form $MgCl_2$.

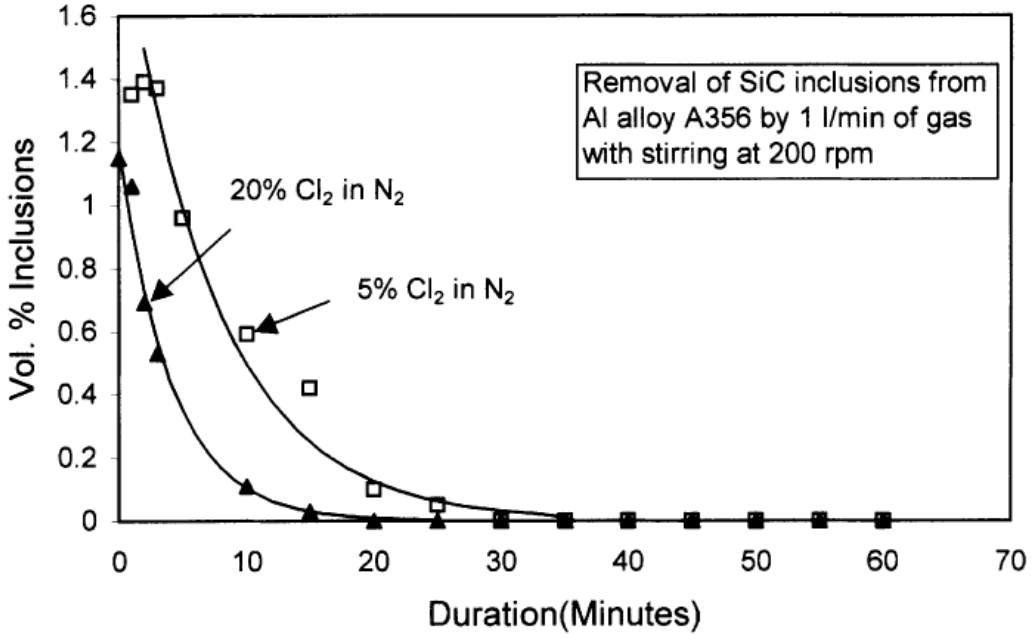

Figure 2.49 The effect of Cl content on inclusion removal while degassing with an N_2 and Cl_2 mixture [141].

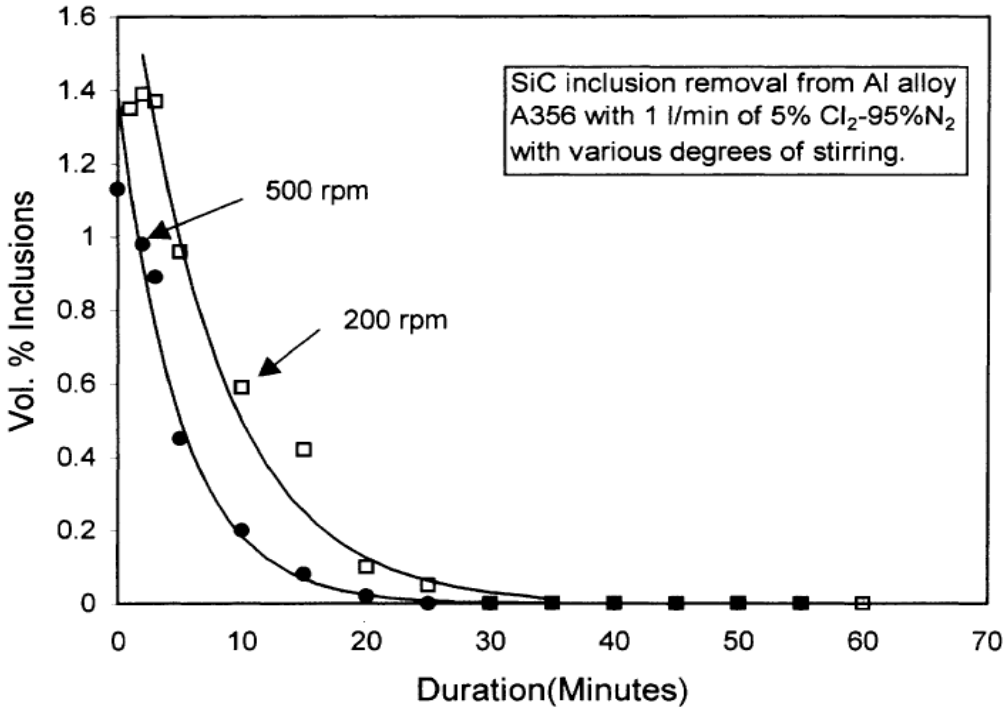

Figure 2.50 The effect of stirring on inclusion removal while degassing with an N_2 and Cl_2 mixture [141].

Stevens [132] investigated the removal of Ca, Na and H in various wrought Al alloys across ranges of 0 – 500 ppm of Ca and 0.02 – 1.0 ml/100g H (measured using LECO), using 0 and 5 % Vol.% Cl in Ar. She observed positive effects of Cl on Ca and Na removal, when Ca levels were above ~10 ppm the removal rate was observed to remain constant, indicating that Cl availability was the limiting factor and below this ~10 ppm level the Ca removal slowed down due to Ca availability becoming the limiting factor.

Stevens [132] reported a reduction in reactive metal removal rate constants when using elevated levels of Cl however, especially in Mg containing alloys, and clearly this contrasts the work of Celik and Doutre [111] described earlier. The rate of alkali metal removal was suggested to be dependent on transport of reactive elements to the bubble interface, on the transport of Cl to the interface and finally transport through the stagnant bubble – metal interface (in a similar mechanism to that of H). Instead of the Ca reacting with the $MgCl_2$ to increase the rate of Ca removal, it apparently slowed the removal process indicating saturation of the melt with $MgCl_2$ could occur. An interesting side note was that Na removal was always found to be higher compared to that of Ca, and this was reasoned to be due to the volatility of Na, causing it to diffuse into the gas bubbles and to be removed by this mechanism in addition to chemical reaction.

2.5.7 Fluxes

The term fluxing is used to represent additives and treatments of molten Al in which chemical compounds are used. Most fluxes are inorganic, based on salt (metal-chloride) systems but also include inert and reactive gases such as Cl and hexachloroethane (C_2Cl_6) to

remove H and alkaline metals. The most common chemical additives used in this function are listed in Figure 2.51.

Chemical	Molecular Mass (g/mol)	Solid Density (g/cm^3)	Melting Point (°C)	Boiling Point (°C)
LiCl	43.39	2.068	605	1,325
NaCl	58.44	2.165	801	1,413
KCl	74.56	1.984	770	1,500
$CaCl_2$	110.99	2.15	782	1,600
$MgCl_2$	95.22	2.32	714	1,412
$AlCl_3$	133.34	2.44	190	177.8
$BaCl_2$	208.25	3.92	963	1,560
LiF	25.94	2.635	845	1,676
NaF	41.99	2.558	993	1,695
KF	58.1	2.48	858	1,505
CaF_2	78.08	3.18	1,423	2,500
MgF_2	62.31	3.18	1,261	2,239
AlF_3	83.98	2.882	—	1,291*
Na_3AlF_6	209.94	2.9	1,010	—
$LiNO_3$	68.94	2.38	264	600†
$NaNO_3$	84.99	2.261	307	380†
KNO_3	101.11	2.109	339	400†
Li_2SO_4	109.94	2.221	859	high
Na_2SO_4	142.04	—	897	—
K_2SO_4	174.27	2.66	1,069	1,689
$CaSO_4$	136.14	2.61	1,450	high
$MgSO_4$	120.37	2.66	—	1,124†
Li_2CO_3	73.89	2.11	723	1,310
Na_2CO_3	105.99	2.532	851	high
K_2CO_3	138.21	2.42	894	high
$MgCO_3$	84.32	2.96	—	350†
$CaCO_3$	100.09	2.71	1339	850

* Sublimes
† Decomposes

Figure 2.51 Characteristics of materials used in fluxes from [92].

Fluxes form many functions including degassing, demagging, cleaning and alloying. For example fluxes based on KCl-NaCl may be used to cover and protect the metal from oxidation while fluoride-salt fluxes may be utilised to improve metal recovery from dross [92] by reducing the affinity between Al and Al_2O_3.

Fluxes for removing inclusions are generally based on KCl-NaCl and $MgCl_2$-KCl and form low temperature eutectics (dependant on composition, shown in Figure 2.52). These fluxes react

with other alkaline metals and also coat the surface of the metal with a thin liquid protective layer, and may be useful in protecting high Mg melts from excessive oxidation and H absorption [141]. An additional benefit of solid fluxing is that $MgCl_2$ is added into the melt as part of the salt and so compared to Cl there will be minimal Mg loss from the alloy during treatment.

Salt Composition	Approx. Melting Point
40% $MgCl_2$ – 60% KCl	430 °C
60% $MgCl_2$ – 40% KCl	485 °C
75% $MgCl_2$ – 25% KCl	570 °C
90% $MgCl_2$ – 10% KCl	660 °C
100% $MgCl_2$	714 °C

Figure 2.52 The approximate melting points for $MgCl_2$ based refining fluxes from Leboeuf et al [124].

Certain compounds will react or decompose beneath the Al surface releasing gases such as carbon-dioxide and Cl. Such compounds generate bubbles to form underneath the metal surface which are useful for removing dissolved H, alkaline metals and inclusions. H that is dissolved within the melt diffuses into the bubbles which then float out of the metal. The most notable gas-releasing compound is (C_2Cl_6) which generates Cl_2 and gaseous $AlCl_3$ [92].

2.5.8 Chlorides and degassing

The boundary layer between melt and gas bubble has been shown to be very important as it is the rate limiting step for H removal during degassing. The rate of reduction of H relies on H diffusing the gas bubble – metal interface and thus any films that may be present on the surface of the bubble could disrupt H transport. As Cl containing gas bubbles interact with the melt to form $MgCl_2$, the formation of this salt film could influence the potency of degassing.

The effects of Cl on degassing within the literature are conflicting. Some authors observed an increase in degassing efficiency when using Cl, other report that there should be no measureable effect on degassing rate, while others claim that salts have a potent negative influence on the H removal rate because of their influence on the boundary layer.

Williams [23] noted an improvement in degassing performance of a 1% Cu alloy when a 5% Cl (in Ar) mixture was used, compared to the use of Ar gas alone. On average the H removal rate was 32% using Ar + Cl, compared to just 17% using Ar only. The gas was injected using an in-line degassing system and the H content was established before and at two stages during degassing. It was also clear from the results that degassing using wands (lances) produced poor degassing results, actually increasing the H content of the metal by as much as 40%. These results are shown in Figure 2.53.

Furnace Flux Condition	H_2 at Flux Start	H_2 at 30 min	H_2 at 60 min	H_2 at Cast Start	% H_2 Reduction at 30 min
PHD-50 (Ar/Cl)	0.21	0.13	0.13	0.17	38%
PHD-50 (Ar/Cl)	0.21	0.18	0.17		14%
PHD-50 (Ar/Cl)	0.22	0.16	0.14		27%
PHD-50 (Ar/Cl)	0.30	0.15	0.16	0.23	50%
PHD-50 (Ar)	0.24	0.19	0.18		21%
PHD-50 (Ar)	0.31	0.27			13%

Figure 2.53 Williams results of an in-line degassing procedure on H content; using Ar 5% Cl and Ar only, and PHD-50 in line degasser using the same mixture. H removal is, on average, more efficient when utilising Cl additions [23].

Botor [138] reported that degassing proceeded far more intensively when using N_2 and Cl_2 compared to N_2 and Ar alone. Mixtures of N_2 and Cl_2 with Cl_2 contents of 4, 8, 12, 16, 20, 40, 60 and 80% Cl_2 were found to increase the mass transfer co-efficient to a peak around 10% Cl before decreasing and returning to a common value, shown in Figure 2.5.26. This was attributed to Cl increasing the metal-gas interfacial area due to an exothermic reaction between Al and Cl increasing the bubble volume. This is an unlikely explanation however as the positive effects of decreasing bubble size have already been reviewed. It is more likely that the Cl was having a chemical effect at the bubble surface / boundary layer, with an unknown beneficial reaction occurring at 10% Cl.

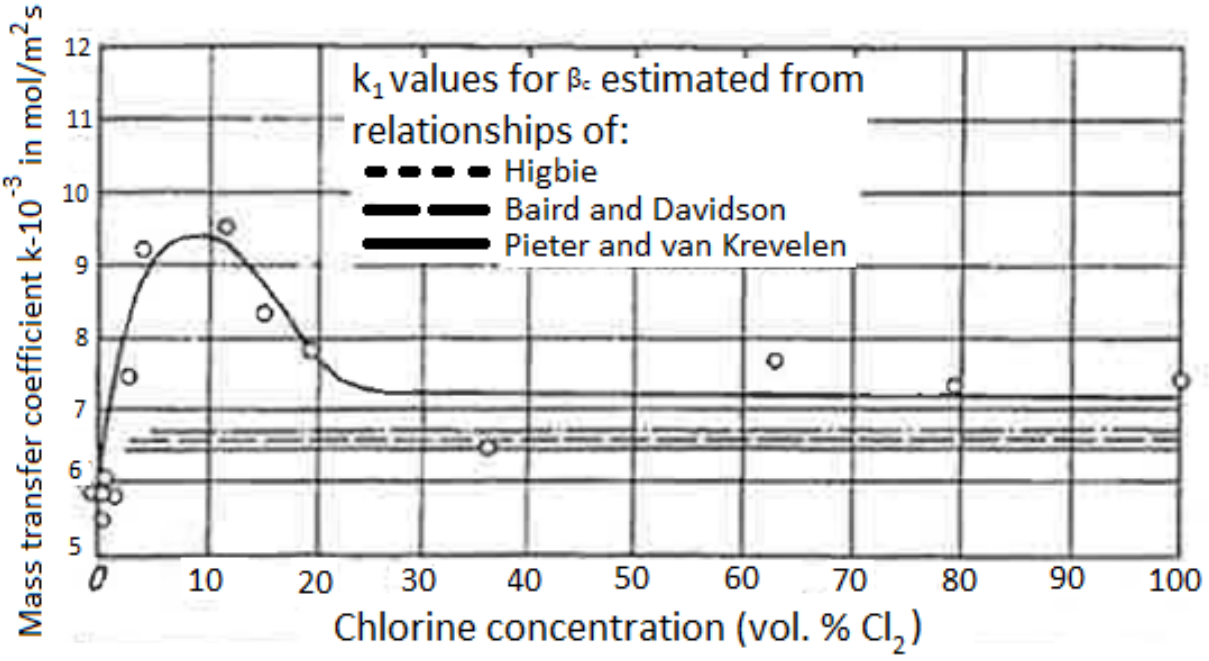

Figure 2.54: The mass transfer coefficient measured by Botor, was found to reach a maximum around 10% when using Cl_2 in N_2 [138].

Both Talbot [28] and Eister & Krumme [128] observed no significantly measureable difference in H removal when using stirred reactor vessels. Sigworth [110] and Engh [24] both comment that the removal rate could / should be improved by using Cl, but not by any measureable or significant amount. They provide no experimental data to support their claims however.

Chesonis & DeYoung [127] suggest that the H removal rate is reduced when using Ar + Cl compared to Ar alone in a 2.5 wt% Mg alloy, AA5052. The results compare degassing results (H values obtained using using LECO) from an A622 rotary degasser with a flux injector that forces solid $MgCl_2$ based flux and Ar in the melt. The results presented appear to be quite varied, with overall degassing efficiencies ranging from 29 to 67%, perhaps indicating that the degassing techniques were not truly comparable

Stevens [143] reports a negative impact on H removal, particularly in a 5083 high (4.5 wt%) Mg alloy, as did Stevens & Yu [132] reporting that the H removal rate was greater (when using an A622 degasser) with Ar alone compared to a mixture of Ar and Cl in a variety of alloys. The greatest impact was observed in alloys containing Mg and this was explained by the formation of $MgCl_2$ at the bubble boundary layer, which increased interface resistance at the bubble boundary layer and retarded H diffusion.

None of the reviews comprehensively evaluate the influences of Mg, Cl and temperature on the degassing efficiency in degassing units however, so the speculation and conflicting opinions on $MgCl_2$ and influence on degassing efficiency remains to be fully explained.

2.6 Methods of monitoring the hydrogen and inclusion content of aluminium

Determining the H content of the metal can be a difficult and expensive process and there are many techniques that have been developed, each with their own relative strengths and weaknesses [144]. The available techniques are discussed generally, relative to each other, and then in individual detail. To begin, they are grouped into liquid and solid techniques, reflecting the condition of the metal when the analysis takes place. The methods for evaluating the inclusion content of Al are also reviewed briefly.

2.6.1 Liquid metal hydrogen determination techniques:

Arguably the most useful H determination systems (from a practical point of view) take readings from the molten metal before casting. Techniques such as ALSCAN and ALSPEKH report the H content of the liquid metal to a reasonable accuracy (typically 0.01 ml/100g) [145] [146] and within a relatively short time period, typically less than about ten minutes. Such units represent a significant investment, costing tens of thousands of pounds to purchase run and maintain because the probes are consumable, lasting only a few hours during immersion or a few dozen dips in liquid metal. Probes are fragile and cost hundreds of pounds each.

Real-time reporting of data can then be used to assess the performance of a degassing unit during in-line casting or monitor the progress of a degassing process on a batch of metal. With these systems it would also be very apparent if there was a failure of the degassing system as the typical H content of the metal exiting the reactor would be observed to have increased. Such information is invaluable as it allows for immediate repair work to be

carried out and for affected material to be scrapped before entering the rest of the production system, preventing value from being added to an inferior product.

Monitoring the H content of the liquid metal may also be thought of 'perhaps a little further from the truth' as far as the casting quality is concerned because the actual porosity content of a casting depends also on the alloy composition and solidification conditions. Monitoring the H content of the liquid metal only provides opportunity to predict the quality of a casting.

2.6.1.1 ALSCAN

The ALSCAN utilises a porous ceramic probe which is inserted into the molten metal, which is connected to a gas circulation system. A nitrogen carrier gas is circulated within the unit, and the probe and H from the melt diffuses across the probe and into the gas supply. This gas is then evaluated by a thermal conductivity cell which evaluates the amount of H in the system. The probe and operation are shown in Figures 2.54 and 2.55.

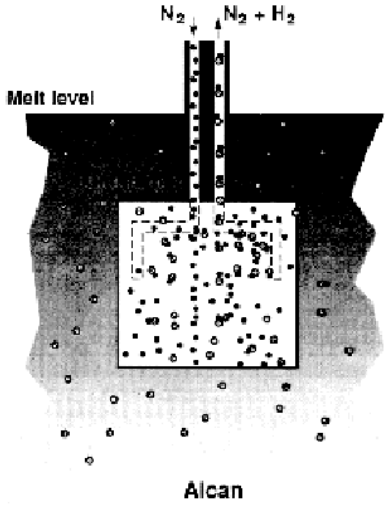

Figure 2.55 Diffusion of H through the porous ceramic probe on an ALSCAN unit.

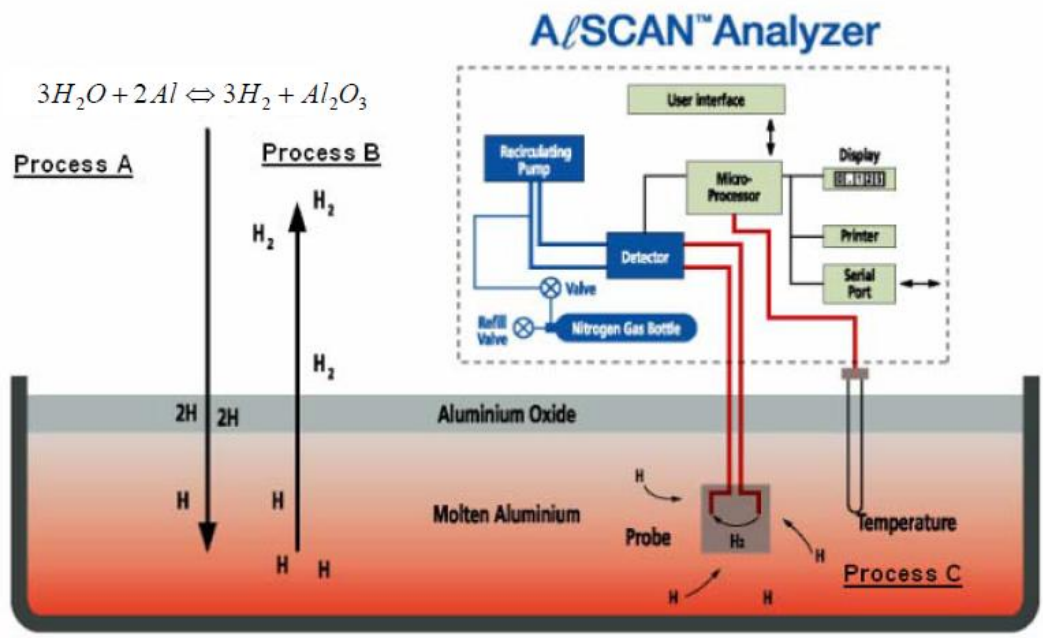

Figure 2.56 The operation of the ALSCAN unit and the probe interacting with H within the melt [147].

The unit uses alloy calibration factors and a thermocouple to refine the data and give more accurate readings dependant on the solubility of H in the melt (as described in section 2.2.1). The ALSCAN requires time for the gases within the unit to come to equilibrium with the melt, which becomes more accurate the longer the unit is instructed to sample from the melt (an analysis may take as little as three minutes but typically ten minutes or more).

2.6.1.2 ALSPEK H

The ALSPEK H unit utilises a ceramic ($CaZrO_3$-In) proton conductor imbedded within a probe which also houses a thermocouple, which is held in contact with the molten metal. The ceramic can absorb and conduct H ions from the melt which are exposed to a measuring

electrode, generating a voltage and this value is compared to a solid state reference electrode (which has a known H content) to calculate the H content of the melt. The value is also moderated by an alloy calibration factor and a built in thermocouple to factor the influence of alloy type and temperature on the solubility of the metal. A schematic of the probe tip is shown in Figure 2.56.

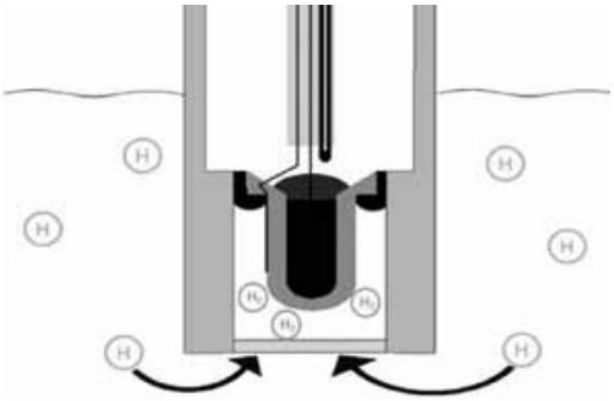

Figure 2.57 The interaction of H with the solid state proton conductor within the ALSPEK H probe tip.

The ALSCAN necessitates an inert gas to purge the probe and collect the H, which can degas small volume melts; it also collects H over a period of time, reporting the H content and temperature at the end of the cycle. In contrast the ALSPEK H takes a period of time to come to equilibrium with the melt, but then follows the H content (and temperature) in roughly real time. This maintains the H content of the melt and allows accurate tracing of the results over time.

2.6.1.3 Solid metal hydrogen determination techniques:

Examining the porosity within the ingot after casting directly is undoubtedly the most useful method of assessing metal quality but this is a destructive technique so not typically available outside of laboratory environments, so casting and analysing samples that represent the casting as closely as possible is the alternative. This is achieved through either vacuum degassing or hot extraction processes such as LECO.

The vacuum degassing technique works by inflating pores within a small metal sample, exaggerating the size of pores so that they can be visually assessed. Clearly this technique gives an impression of the porosity, but does not actually reflect the true structure of the ingot. The LECO analysis traditionally begins with the casting of a Ransley gas bar, which is machined to obtain a single sample (8 mm in diameter and 50 mm in length, weighing approximately 5 – 7 grams). This sample is heated during analysis and the H within enters a nitrogen carrier gas stream, into a thermal conductivity cell. This system can evaluate the H content of the metal to as little as 0.001 ppm of H. A schematic drawing of the key parts of the LECO is shown in Figure 2.57.

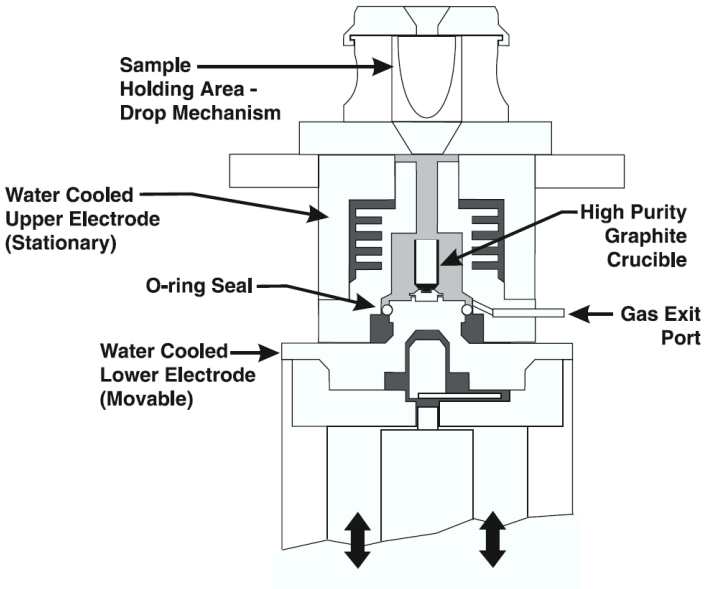

Figure 2.58 A schematic of the sample processing chamber in the LECO RH-402 H analyser [148].

The accuracy of such a technique is undoubtedly useful but it is worth noting that casting, preparing and analysing samples for LECO analysis takes a great deal of time which means the result of the analysis will not be known until after casting has been completed (perhaps for some weeks afterwards), clearly limiting its usefulness on commercial applications. Such an approach is also statistically vulnerable to error as the H content of the liquid metal can and will vary during a continuous casting process. It is not realistic to process dozens of LECO samples taken at regular intervals across an entire cast without a great deal of time and capital investment. Further to this a small number of samples will not accurately represent the overall H content across the casting. There are also potential sources of error from sampling, such as entrainment of dross during casting of the Ransley gas bar and absorption of H during machining processes using lubricants. It is the opinion of the author that the LECO is a relatively weak method for assessing the H content of Al in a high volume

industrial casting environment, but is useful for detailed investigations and quality assurance in specific applications.

2.6.2 Methods for monitoring molten metal cleanliness

2.6.2.1 PoDFA

The Porous disk filtration apparatus (PoDFA) is used to evaluate the quality of a known quantity of liquid Al by forcing the metal through a ceramic filter, which filters inclusions out of the metal. Typically 1.5 – 2.5 kg of metal is used in one sample. The metal is heated in a pan until molten or extracted in the pre-molten state, poured into a crucible and is passed through the filter either by pressure or vacuum. Inclusions within the metal are concentrated on the disk, which is later extracted and can be evaluated using microscopy. The consolidation of a volume of metal to an area across a filter leads to the unit mm^2/kg metal.

PoDFA samples can easily remove entrained oxides, spinel, borides, many coarse intermetallics and refractories which are visible and can be measured for size. Chlorides can be detected although not reliably using traditional cutting methods which utilise a coolant as they are water soluble and are pulled out of the sample before analysis. Holes in the preparation surface usually indicate the presence of chlorides.

The PoDFA process can give interesting insights into the quality of liquid metal but its greatest drawbacks are sample size and time or preparation. A PoDFA cannot give instant cleanliness data on a melt as sample preparation is required and it probably will not represent the true quality of a large semi-continuously cast product weighing a few tons or

more. A typical batch of 4 ingots will weigh approximately 8 tons and a single PoDFA utilises only 2 kg of metal, a sampling rate of 0.00025%. Obtaining a liberal amount of PoDFA samples (e.g. 10) from each cast, which represents a significant amount of sample preparation, would still analyse far less than 1% of the metal and is therefore (statistically) a weak analysis method.

2.6.2.2 Prefil

The Prefil process is very similar to the PoDFA process in that a known quantity of metal, (~2 kg), is forced through a filter to collect data on melt quality. As the metal is forced through the filter a weigh balance is used which records the weight of metal filtered over time, to represent the ease of which the melt passes through the filter. Clean melts will pass through relatively quickly whereas dirty melts will take longer to be filtered, as inclusions build up on the filter and restrict the flow of metal. The Prefil can then be used to gauge immediately the general cleanliness of the melt compared to other casts. The rate over time can also be associated with different types of inclusions found in the metal, borides for instance are known to immediately affect the flow and oxide film defects tend to slow down the end of the filtering process due to their size. The Prefil process then allows the extraction and analysis of the filter in order to evaluate the actual inclusions found within the melt.

2.6.2.3 LiMCA

The LiMCA process is an in-line method for assessing inclusions floating in the liquid metal. Metal passes through a small tube, which applies a voltage across it. The resistivity of the metal will change as inclusions pass through the tube. The LiMCA is useful because it provides instantaneous results, but it only measures a limited amount of metal, has a maximum inclusion size and is prone to blockages. It also does not directly confirm the species of inclusion within the tube so it cannot distinguish easily between a ceramic refractory an aluminium oxide defect or a gaseous bubble.

2.7 Hot rolling and grain mobility

Plastic deformation of DC ingot occurs during hot rolling and this achieves the desired shape and mechanical properties by work hardening the material. During rolling the grains morphology changes from an equiaxed structure to an elongated one after deformation. New grain boundaries are continually created during the working process, increasing dislocation density, entangling dislocations and orientating the grains in the direction of the applied stress. During rolling the material heats up and some of this energy is stored in the material in the form of crystal defects. Cold rolling material requires more strain to deform the material, generating more stresses within the bulk material.

There is a driving force to decrease the free energy arising from the reduction in elastically stored energy (dislocations), which occurs through recrystallisation, a process where nucleation and growth of a strain free grain microstructure occurs in certain areas of the

material. These grains grow to consume the deformed (or recovered) microstructure as shown in Figures 2.58 and 2.59. During recrystallisation the number of dislocations decreases, the average grain size increases and the material softens so there is a relative decrease in strength and increase in ductility during this process. After an incubation period the new grains begin as small nuclei within the parent structure at grain boundaries or second phase particles such as intermetallics. The rate of recrystallisation is alloy dependant and occurs more rapidly with increasing temperature. To initialise recrystallisation a critical deformation is required (stored energy) and a critical temperature to provide activation energy.

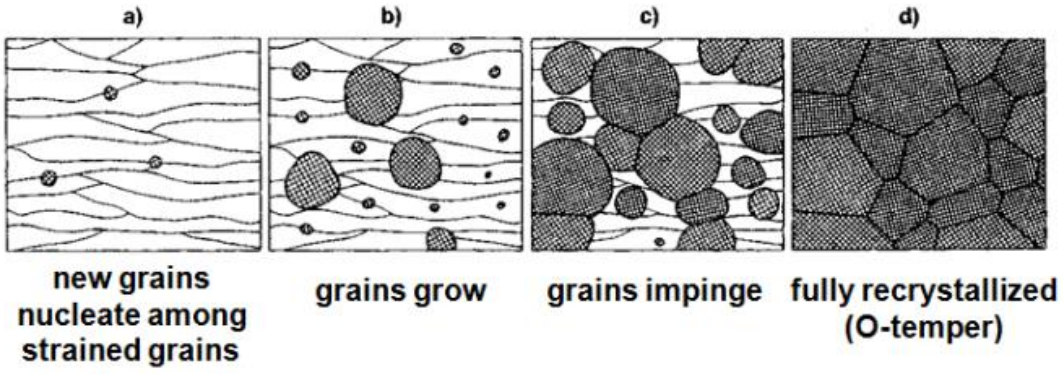

Figure 2.59 The stages of recrystallisation. The deformed microstructure is replaced by equiaxed grains that nucleate from the grain boundaries of existing grains [149].

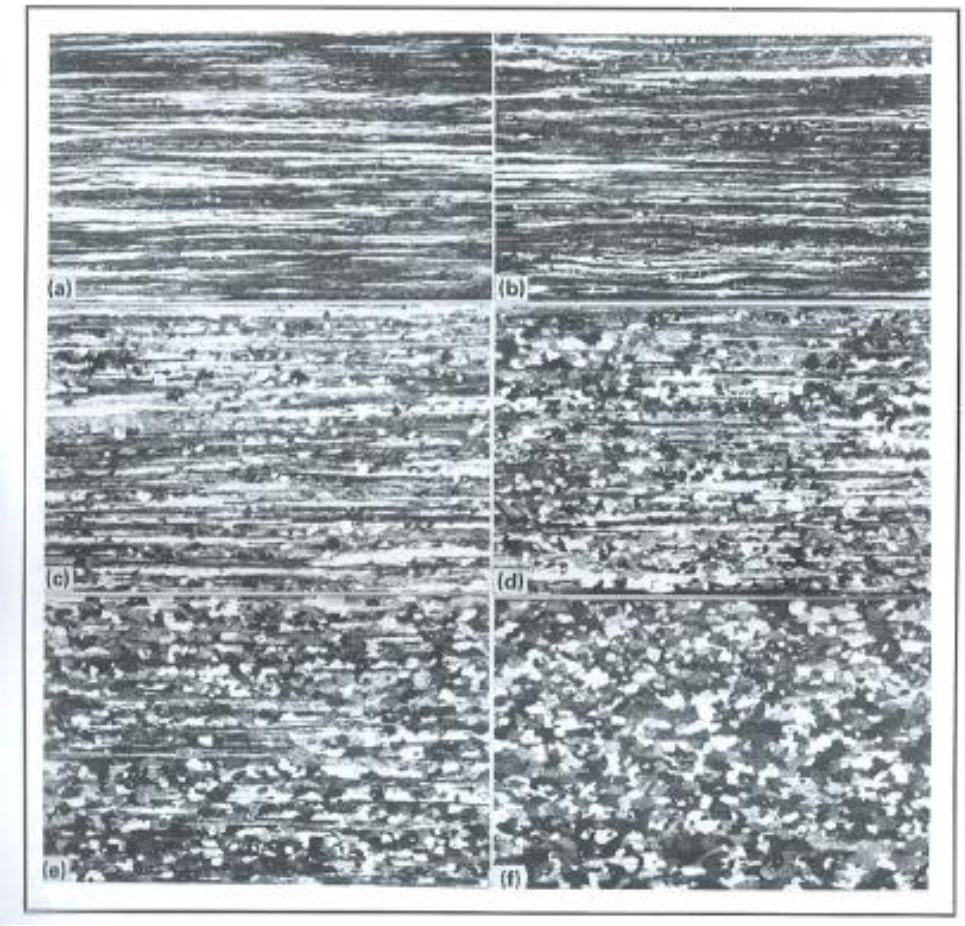

Figure 2.60 Polarised light micrographs showing the progress of recrystallisation in 5182-H19 sheet annealed at 245 ^{o}C; a) as rolled, b) 1h c) 2h d) 3h e) 4h f) 7h. Barkers Etch, 120x [149].

Dispersed phases can act to accelerate or retard recrystallisation, depending on their spacing and size. Fe for example has been used as an example by Callister [150], to show how alloying can dramatically inhibit recrystallisation in 1xxx aluminium in increasing concentrations up to ~0.01wt% Fe, see Figure 2.61. Above this concentration the trend is reversed. It is unclear here if Fe in solid solution (Fe solubility is only 0.04 wt% in Al) or Fe intermetallic precipitates are influencing recrystallisation temperature. Coarse Fe containing intermetallics could enhance the process, lowering the required recrystallisation temperature as they act as nucleation points.

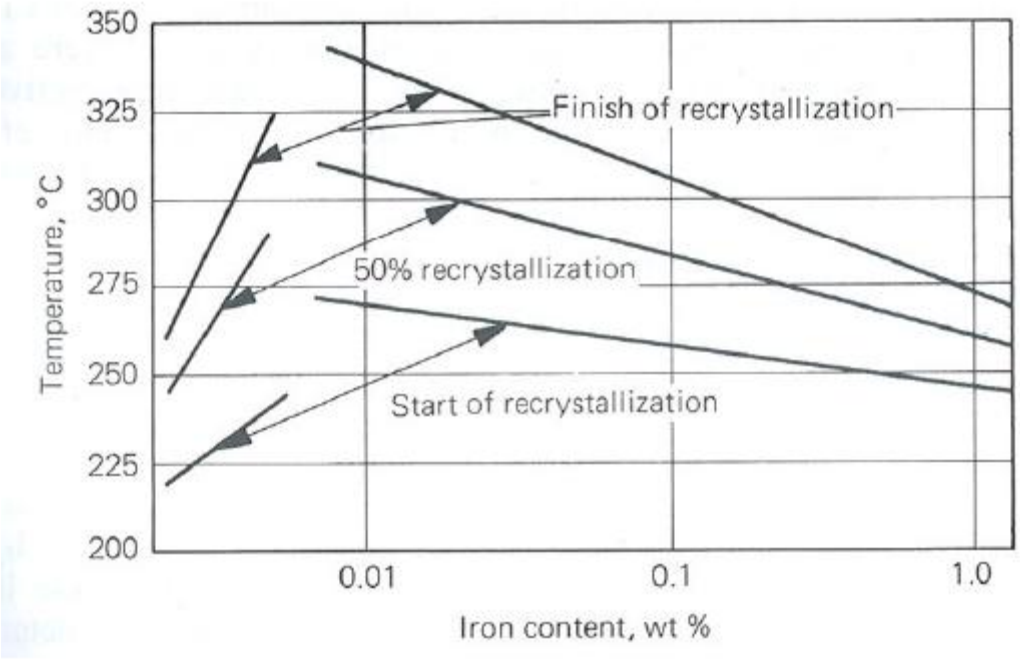

Figure 2.61 Recrystallisation versus Fe content in high purity Al alloys (cold rolled 60%) [150].

Sanders et al showed by SEM investigation that Fe-Al-Cu precipitates are expected to be present in 7075 and 7475 alloys, although no data on average size or distribution is recorded in the work. It is predicted such precipitates could form phases which play a role in accelerating or retarding recrystallisation [151]. Small particles that are coherent with the microstructure (such as Zr and Cr) can be used to control recrystallisation as they pin grain boundaries, preventing them from migrating through a process called Zener pinning. 7xxx alloys contain Cr and / or Zr, which precipitate from supersaturated solid solution as $Al_{12}Mg_2Cr$, and Al_3Zr phases respectively, ranging in size from about 0.02 to 0.5 µm [152], [153].

2.7.1 Grain size and ultrasonic response

The sensitivity of ultrasonic detection is primarily determined by the ultrasonic wave frequency, relative to grain size of the material being evaluated. If the grains are fine and the wavelength long then the wave will pass through the material without any scatter. As the grain size becomes greater then scatter will become significant, causing attenuation or loss of signal during wave propagation. Coarse grain material causes an ultrasonic response while relatively fine grains do not [154].

A temporary jam of the reel that feeds grain refiner rod into the molten metal was found to be the cause of an ultrasonic failure in 7050 alloy plate (see Figure 2.62). This type of diagram, referred to as a C-scan, shows a plane view of the plate and displays the features detected by ultrasound. The defect was shown to be a series of indications in a band across the central portion of the plate [2]. This type of defect occurred because the metal was not supplied with grain refiner for a period of time. This caused a portion of the ingot to have a coarse grain structure which was revealed by the ultrasonic scan after the material was hot rolled.

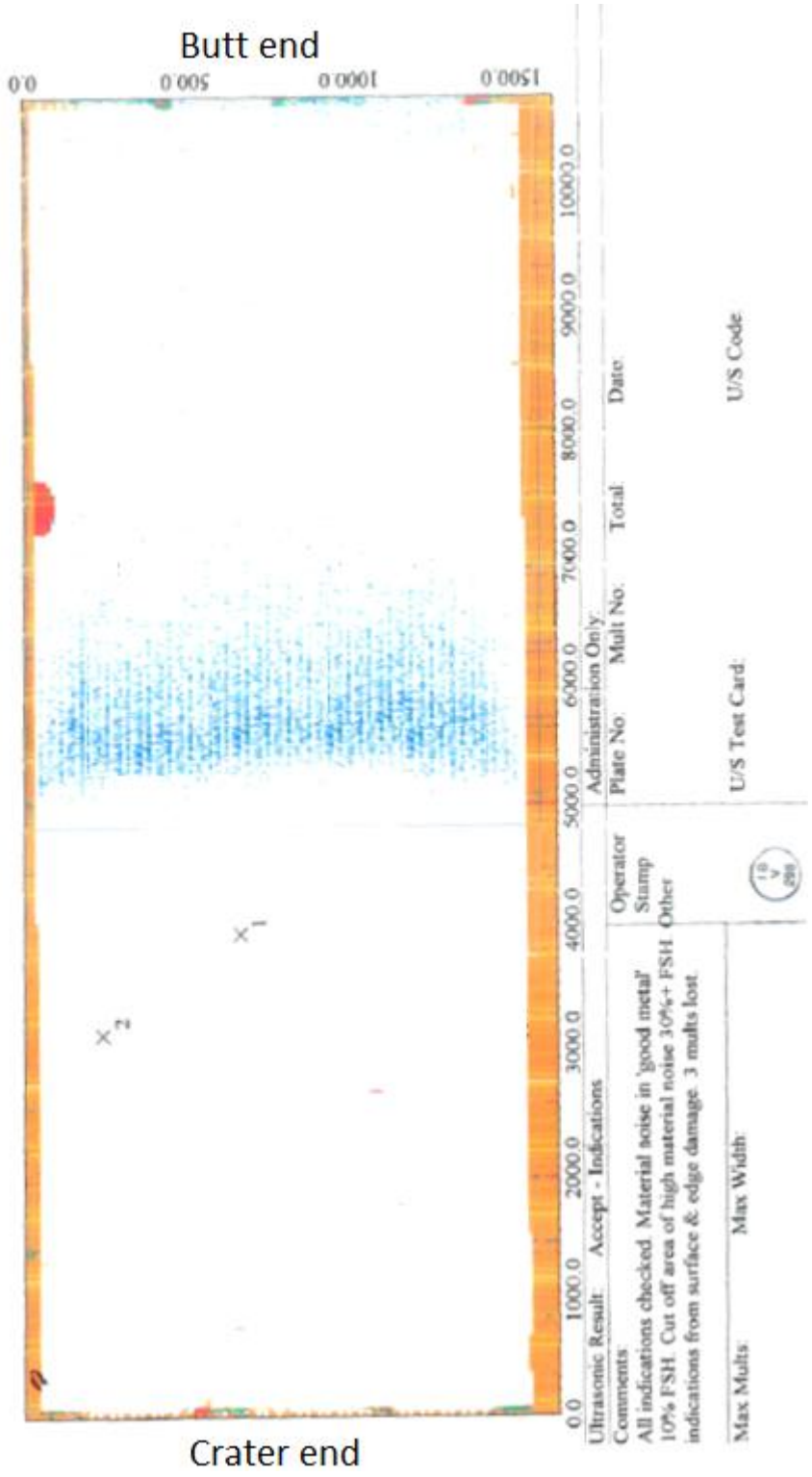

Figure 2.62 A plan view of a plate after ultrasonic examination. The effect of grain refiner failure during casting on the ultrasonic scan of a 7050 alloy plate (1073 mm wide, 1638 mm long, 90.9 mm thick) is shown. The lack of refiner causes coarse grain to develop over the entire width of the plate, which is shown in blue on the scan.

2.8 Statistical analysis

Independent samples t-test is used regularly throughout this work to determine if different data sets are significantly different from one another. In each instance the standard t-test function within Excel was used. Essentially it establishes if two means (averages) are reliably different from each other. It determines how likely that the difference between two groups is reliable, or whether it is just due to chance. It does this by calculating the variance between the groups and the variance within the group.

A standard critical probability (p) value of 0.05 (5%) was chosen, so that any p value above 0.05 suggests there is no statistical significance between any two data sets (i.e. the 95% confidence level). It is useful to decide upon a null hypothesis in each instance, for example "Cl has no effect on degassing efficiency". If a value greater than 0.05 is obtained, for instance 0.60, this would represent a 60% chance that the null hypothesis it true and we would fail to reject it. If the p value is below 0.05 then the null hypothesis is rejected and it would be concluded (with 95% confidence) that Cl does in fact influence the degassing efficiency.

Chapter 3 Experimental procedure

A number of experiments are described in this section. The first two are focused on eliminating defects which were found in rolled plate products that were manufactured at Alcoa and were detected using ultrasound. These investigations aimed to better understand the aetiology of these particular defects, how and why they occur, and to find ways to eliminate them from production, resulting in a cost saving for Alcoa.

The third experiment describes attempts to capture gas bubbles in molten Al and to examine changes in gas composition using a mass spectrometer and to examine the reaction products at the metal-gas interface using SEM. The aim of the experiment was to give better understanding to the reactions between Cl and the various alloying elements present in different alloys (2L99, 5083 and 7010). The compounds formed at the metal - gas interface may influence the diffusion of H into the bubbles, so it was hoped to observe differing levels of hydrogen within gas bubbles that were processed with and without Cl additions. These gas levels could be linked to the different compounds at the gas - metal interface and this would help to clarify the conflicting findings presented in the literature (see section 2.5.8).

The fourth experiment explores how Cl gas additions affect the efficiency of degassing Al alloys using a SNIF unit. Three commercial alloys (7010, 7050 and 7075) were treated in an industrial setting; the degassing performance of the SNIF unit was assessed using ALSCAN technology, when the degassing procedure was implemented both with and without Cl additions. The aim was to observe an increase or decrease in degassing rate when Cl was used in the degassing unit, to better understand the effects of Cl on degassing of 7xxx alloys.

The fifth experiment examines the influence of Mg and Cl on the degassing efficiency of small Al melts. Three different Al alloys (pure Al, 5083 and 7010) at different temperatures with different gas compositions were degassed using custom built apparatus and the H removal rate was monitored using ALSPEK H. These experiments would show how degassing rates varied with alloy composition, melt temperature and gas Cl content. $MgCl_2$ salt has been proposed to retard the diffusion of hydrogen into gas bubbles above its melting point (714^{o}C, see section 2.5.8). These experiments would clarify the role of $MgCl_2$ on the degassing performance of commercial alloys by evaluating the rate of degassing above and below 714^{o}C.

The sixth experiment investigates both the effectiveness of the LECO H determination device, (the aim of these experiments was to gauge the effectiveness of the LECO as a degassing tool for small samples), and absorption of H into Al alloys over time and in different atmospheric conditions.

The seventh and final experiment investigates the diffusion of H across AlN and Al_2O_3 films that were formed on the surface of different Al alloys. Al_2O_3 has been suggested to be a barrier to H diffusion (see section 2.4.1), but AlN has been proposed to form by reaction between the melt and air entrained / encapsulated within bifilms after any O_2 within the bifilm has been consumed by reaction with the melt. H may be able to diffuse through AlN more easily than through Al_2O_3, and would explain part of the mechanism that allows bifilms to facilitate H gas porosity within castings.

3.1 Alloys

Six alloys were used in different aspects of this study; 7010, 7475, 7050 (AE and AT variants), 7075, 5083 and 2L99. The first five are commercially available wrought alloys and their compositions are given in Table 3.1. These alloys feature good strength, fracture toughness and fatigue performance, and they are amongst standard production material at Alcoa Kitts Green and are widely used in the aerospace and marine industries. 2L99 is a casting alloy which is often found in automotive parts and contains a relatively high amount of Si, which increases the fluidity of the melt and therefore the ease of mould filling.

Alloy	Mg	Cu	Zn	Si	Fe	Ti	Zr	Cr	Mn
5083	4.0–4.9	<0.10	<0.25	<0.40	<0.40	<0.15	<0.05	0.05–0.25	0.4–1.0
7010	2.1–2.6	1.5–2.0	5.7–6.7	<0.12	<0.15	<0.06	0.10–0.16	<0.05	<0.10
7050 AE (typical)	2.4	2.3	6.2	<0.12	<0.15	0.03	0.11–0.15	<0.04	<0.10
7050 AT (typical)	2.4	2.3	6.2	<0.12	<0.15	0.03	0.11–0.14	<0.04	<0.10
7050 (generic)	1.9–2.6	2.0–2.6	5.7–6.7	<0.12	<0.15	<0.06	0.08–0.15	<0.04	<0.10
7075	2.1–2.9	1.2–2.0	5.1–6.1	<0.40	<0.50	<0.20	<0.25	0.18–0.28	<0.30
7475	1.9–2.6	1.2–1.9	5.2–6.2	<0.1	<0.12	<0.06	<0.05	0.18–0.25	<0.06
2L99	0.20–0.45	<0.10	<0.10	6.5–7.5	<0.20	<0.05	<0.05	<0.05	<0.10

Table 3.1 Specifications for alloys used in this investigation. All values are wt.%, balance Al. Valid 2009 [155].

3.2 Plate quality assessment

At the beginning of this study two specific types of defect were selected for detailed investigation. The aim was to research and investigating their causes and, if possible, to modify the production process or chemistry to eliminate them from future production. In both cases plate that was produced through the standard production processes at Alcoa (casting, hot rolling, etc.) was ultrasonically scanned. The scan revealed indications that suggested the plates were of inferior quality.

The ultrasonic scan is applied as one of the final quality checks before the plate is released to the customer. During the scan the plate is immersed in water, which acts as an acoustic medium for the passage of ultrasound from the probes and into the plate. Ultrasound is emitted by probes into the plate, which is reflected by the metal surfaces and any features within the bulk of the material that can reflect sound waves. The plate is scanned and the result is displayed on a “C-scan”, which details the size, depth and location of these features. An example of a C-scan containing no notable features is shown in Figure 3.1.

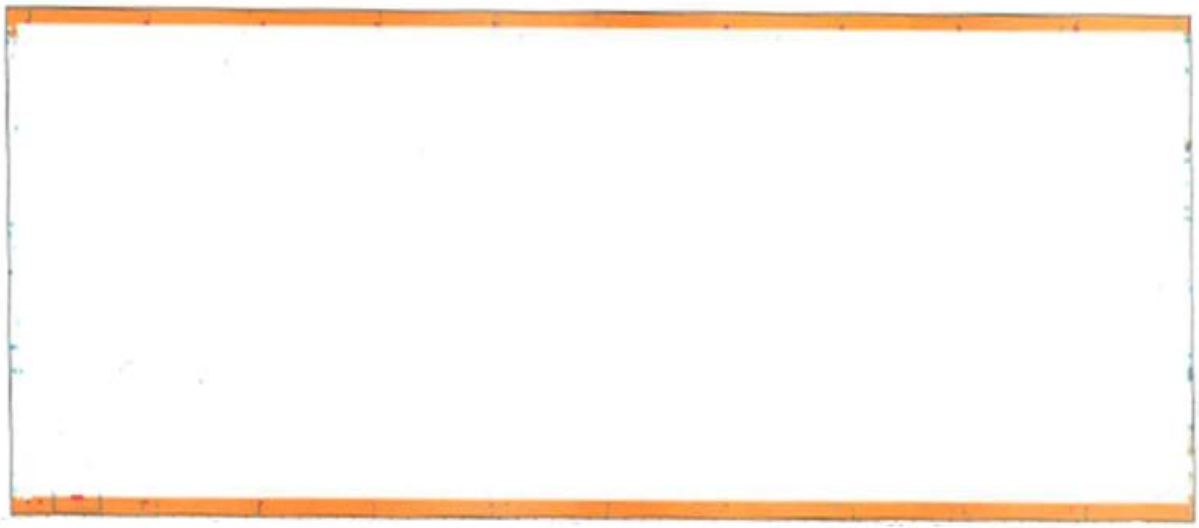

Figure 3.1 A plan view C-scan of an Al plate. The orange area represents the periphery of the plate. This particular example is free from defects and thus the scan appears white / blank.

The first defect selected for investigation was found to occur in a specific sub-type of the 7050 alloy series referred to as 'AE' within Alcoa, the composition of which is in Table 3.1. Point defect type indications were observed throughout plates of this alloy which led to either the entire plate or part of a plate being scrapped (see Figures 4.1 - 4.3). The specifications for both AE and AT alloys are within the generic 7050 alloy specification, but have far tighter internal composition specifications to achieve the desired mechanical properties in the final product.

The second defect investigated was observed to occur only within thin gauge (<45mm) 7475 alloy plates. During ultrasonic evaluation areas of 'high noise' were detected along the long edges of the plates and these areas had to be cut away and scrapped. High noise refers to a specific type of ultrasonic response which is characterised by an elevated background noise across the entirety of the time scale of the pulse-echo scan, and is generally associated with presence of porosity within the plate.

3.2.1 Point defect indications in 7050 alloy plate

To examine any defect in detail a section containing an ultrasonic feature is cut from the larger plate (which could be many meters in both length and width) to a more manageable size and weight, to an approximate maximum of 0.5 m^2. These plates were then stamped with alloy type and plate number of origin at that time. Unfortunately this type of sample collection prevented any reliable traceability so that the inclusions found could not be linked to their exact position on a particular C-scan.

The plates were first examined in laboratory conditions using portable ultrasonic scanning equipment. The equipment used was an EZ Avenger Pro with a twin crystal probe running at a frequency of 5 MHz and a velocity of 6300 m/s^{-1} resulting in a wavelength of 1.26 mm. The device was calibrated using standard drilled flat bottom-hole depth calibration blocks and was capable of detecting features greater than about 0.8 mm in diameter. The range was determined by the plate thickness and the gain was set within the range of 79-81 dB. A chlorinated gel was applied to the plate for acoustic transmission and the probe was coupled with the plate. The plate was then scanned slowly by hand and any inclusions contained within the plate were revealed by the device, as shown in Figure 3.2. Inclusions were clear, presenting as a definitive peak, typically above 80% full screen height (FSH). It was generally quite obvious if an inclusion was present within the plate because the ultrasonic response was clear and large. When a defect was detected its location was marked using an indenting tool.

Figure 3.2 The ultrasonic probe set up. The presence of an inclusion is marked by the response on the screen of the ultrasound unit.

After being scanned the plate was cut using a band saw into smaller sections containing the inclusions. Blocks were approximately 20 x 20 x plate thickness (mm), examples are shown in Figure 3.3.

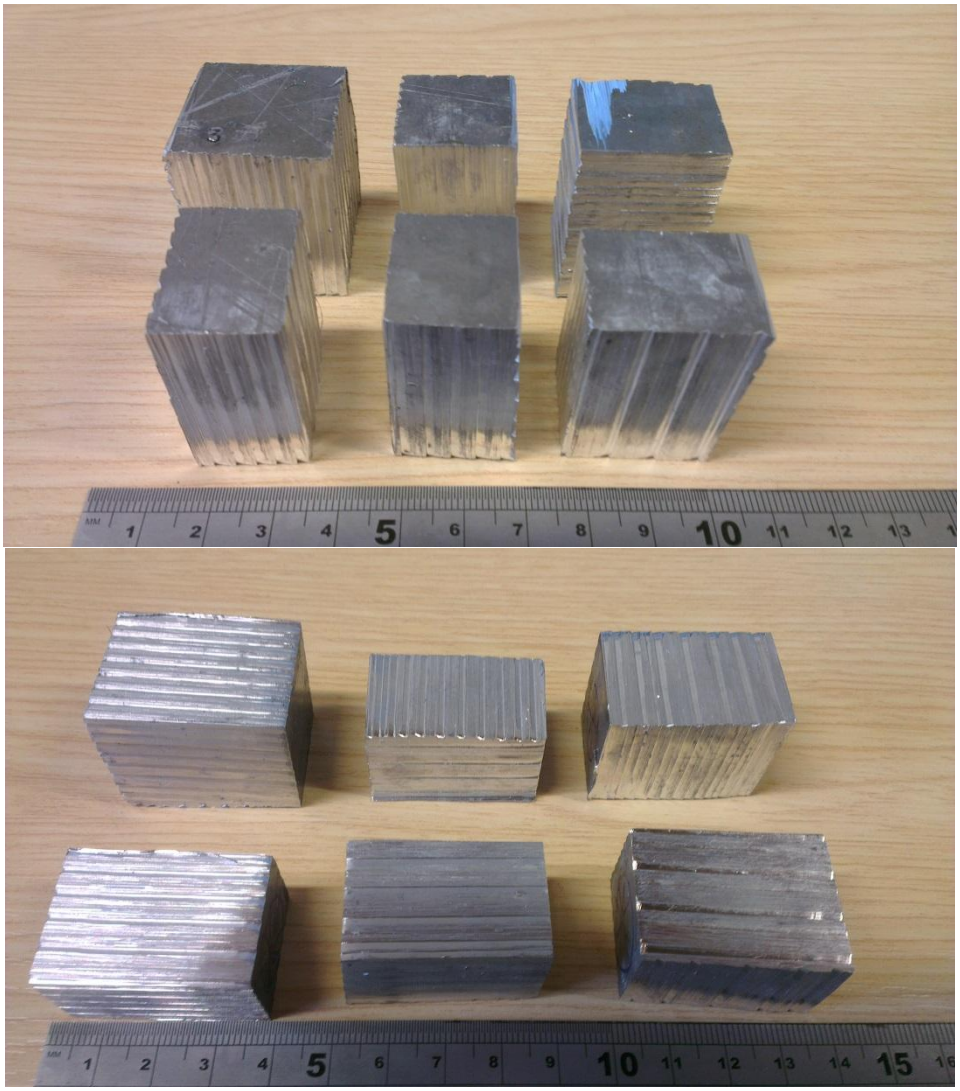

Figure 3.3 Plate sections containing inclusions were marked with a scribe and cut out of the plate into small blocks, approximately 20 x 20 x plate thickness (mm), in this instance 40 mm.

The depth and location of the indication within each block was then more accurately assessed by re-scanning the plate with the ultrasonic probe. The exact depth of the inclusion was easy to establish but due to the size of the probe the exact position of the inclusion in

the X – Y axis was less accurate, but estimated to be within +/- 5 mm. The position of the inclusion was marked on the top and side of the block and the side of the block notched using a band saw, achieved by cutting towards the inclusion, but not into or across the inclusion itself. The block was then fractured with a blow, which revealed the inclusion on the fracture surface. A sketch of this procedure is shown in Figures 3.4 and 3.5. Both JEOL 6060 and Phillips 7000 SEM with EDX attachments were used to examine the inclusions. A total of 20 samples were extracted from three separate plates using this process.

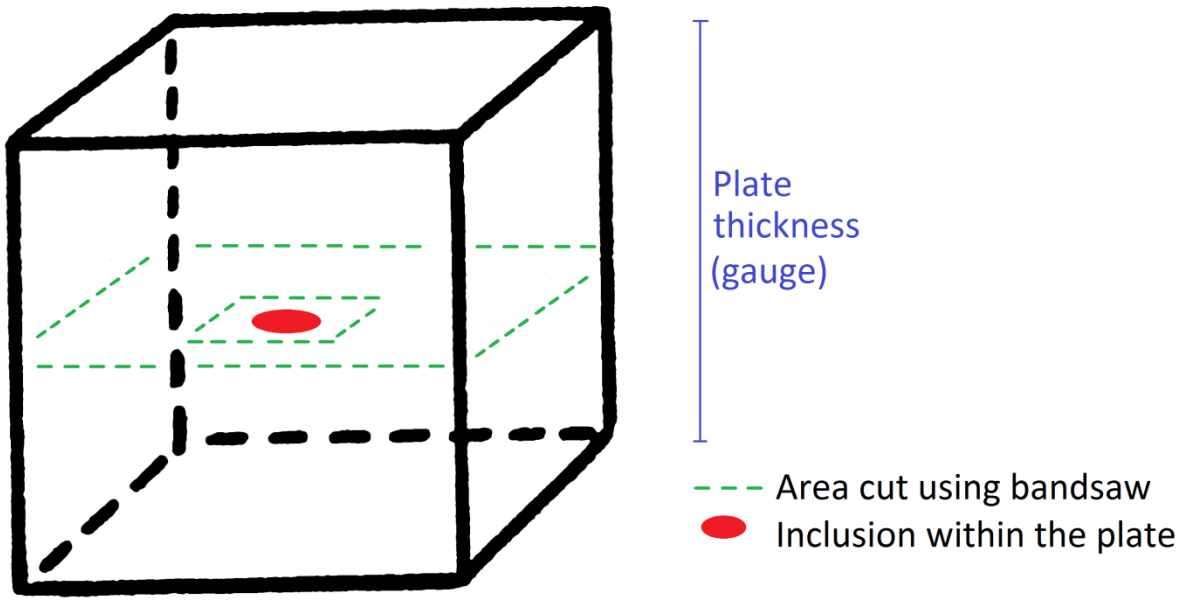

Figure 3.4 Plate samples containing inclusions were first cut using a band-saw along the centre of the thickness and then fractured. This was the standard method for assessing the composition of inclusions.

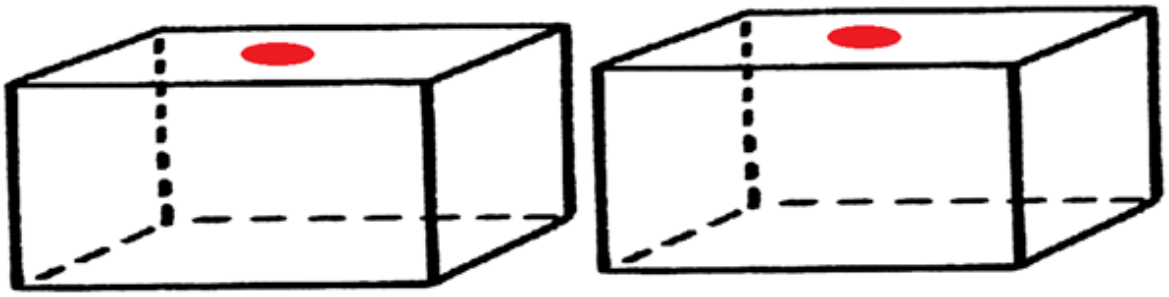

Figure 3.5 The specimens are fractured to reveal the inclusion, split equally across both fracture surfaces.

3.2.2 Near surface indications at the edges of thin gauge (<45mm) 7475 alloy plate

The investigation into the cause of the indications in the 7475 alloy plate began by cutting a sample block from the defect containing area (approximate dimensions of the sample were 200 x 150 x 38 mm). A sample slice (dimensions 10 x 150 x 38 mm) was removed from one end of this block for optical examination. The slice was ground to achieve a smooth surface finish using Si carbide paper (grit sizes 200, 500, 1000, 2000 and 4000) to prepare it for dye penetrant inspection (DPI) detailed in section 3.2.3.

Smaller samples were also cut from the block in order to evaluate the grain size. Specimens were approximately 15mm^2, cut so that the short transverse (ST) direction was visible, (see Figure 3.6 for clarification), and then mounted in conducting Bakelite using a hot press. These samples were ground with SiC paper (grit sizes 200, 500, 1000, 2000 and 4000), and then polished using 5 and 3 µm diamond suspension and an OP Chem suspension. Water was removed from the surface using a hot air blower, where heat was applied for about 30 seconds. These samples were then anodised as detailed in section 3.2.4.

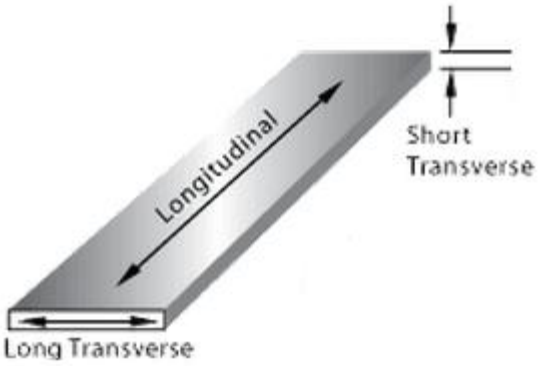

Figure 3.6 A schematic of rolled plate. The rolling direction is called the longitudinal direction, the width of the product is called the long transverse direction, and the thickness is called the short transverse (ST) direction.

3.3.3 Dye-penetrant inspection (DPI)

Checks for visible porosity within the plate edge were made using DPI. The slice was polished using SiC paper before being painted with a photo-reactive dye (Britemor 4455). The excess dye was washed away with water and the plate examined under ultraviolet light. Pores were highlighted by the reactive dye (which was not washed out of the pores as it is retained within by capillary action). The size and number of pores was measured by eye against a standard scale to determine the typical size and distribution of pores, as described in Alcoa work instruction WI-EN-203-I4 (see section 4.21 for detail of this instruction).

3.3.4 Polishing and anodising

Samples were anodised by immersion in Barkers reagent (5ml HBF_4, 200ml H_2O) for 40 – 80 seconds using the Al sample as an anode in a powered electrical circuit (20V DC) [156]. The sample was then flushed with water and observed using a polarised lens in an optical microscope. The sizes of the grains were measured by use of a 1 cm graticule, with minimum spacings of 100 µm.

3.3 The influence of chlorine on hydrogen removal and degasser performance in liquid aluminium

Cl is thought to affect the degassing efficiency of Al and its alloys by influencing the kinetics at the bubble boundary layer. In the literature it has been stated that Cl may either enhance or retard or have no effect at all on the diffusion of H through the boundary layer by different authors. The retardation is thought to be especially true in the case of Mg containing alloys as $MgCl_2$ forms around the bubble, having a negative effect on the removal of H.

The first study aimed to evaluate the bubble - metal interface formed between gaseous bubbles and liquid Al during degassing. This was to be achieved by capturing bubbles in the melt and subsequently extracting them using a pore gas analyser and analysing the interface between bubble and gas using SEM.

The second study took place in an industrial setting. Two ALSCAN units were used to observe the performance of a SNIF degassing unit on a casting unit at Alcoa Kitts Green. This was achieved by placing an ALSCAN before and after the SNIF reactor on DC (Direct Chill) casting unit 'DC3'. The incoming (pre degassing) and outgoing (post degassing) H contents were measured using this technique, with readings being taken over a period of weeks when suitable alloys and casting conditions became available. The aim was to evaluate the performance of the SNIF unit when it was operating using two different gas compositions; 1) using Ar gas only and 2) using an Ar and Cl gas mixture. These two gas compositions were used to treat three commercial alloy systems (namely 7010, 7050 and 7075 alloys) produced using standard casting practices.

The third study took place in a laboratory and utilised the ALSPEK H unit to observe the degassing progress of small Al melts in 'real time'. These experiments were performed to fully evaluate the effects of Mg and Cl and temperature on the degassing efficiency of three commercial alloys (pure Al, 7010 and 5083 alloy). The experiments were carried out to determine the effects of temperature, alloy Mg content and the presence of Cl on degassing performance.

3.3.1 Bubble trapping in liquid aluminium alloys

In this experiment Ar and Ar-Cl gas bubbles were caught in solidifying Al alloys placed in a real time X-ray machine. It was intended to capture and analyse the gases within the bubbles, to investigate the consumption of Cl during the degassing process. It was also hoped to observe $MgCl_2$ formed on the interior of the bubble and to observe any other chemical products occurring at the bubble – metal interface.

Early attempts at this experiment showed that it was extremely difficult to capture bubbles in pure Al, due to its negligible solidification range. 2L99 is a casting alloy with a relatively long solidification range (approximately 550 – 615^{o}C) and so this was chosen to improve the success rate of capturing bubbles. A 5083 alloy was selected as it contained high levels of Mg (~4.5 wt% Mg) and it was desired to observe the occurrence of $MgCl_2$ at the bubble interface. Finally a 7010 alloy was chosen as it is used in other experiments (detailed in section 3.3.2 and 3.3.3).

In each experiment a stainless steel tube (316 L) of 8 mm OD and 6mm ID is first turned into a 'needle tip' by machining. This reduced the cross-sectional area of the tube from 6mm to approximately 0.2 mm, allowing small bubbles to be pushed out, up through the liquid metal, while preventing metal ingress into the tube. A sketch is shown in Figure 3.7.

The needle was inserted into the base of a ceramic fibre crucible which was impregnated with alumina-sol (200 mm x 65mm od, internal diameter 52 mm) and fixed in place using a stainless steel washer and FiberFrax40 ceramic cement. The length of the needle tip inside the crucible protruding from the insertion point ranged from 10 - 50 mm, and was coated with boron nitride to protect it from reacting with the melt. In early experiments a

thermocouple was glued against the side of the crucible to monitor the melt temperature as it cooled, but this was removed as gas bubbles sometimes became trapped around it. An X-ray picture of the crucible and needle can be seen in Figure 3.8.

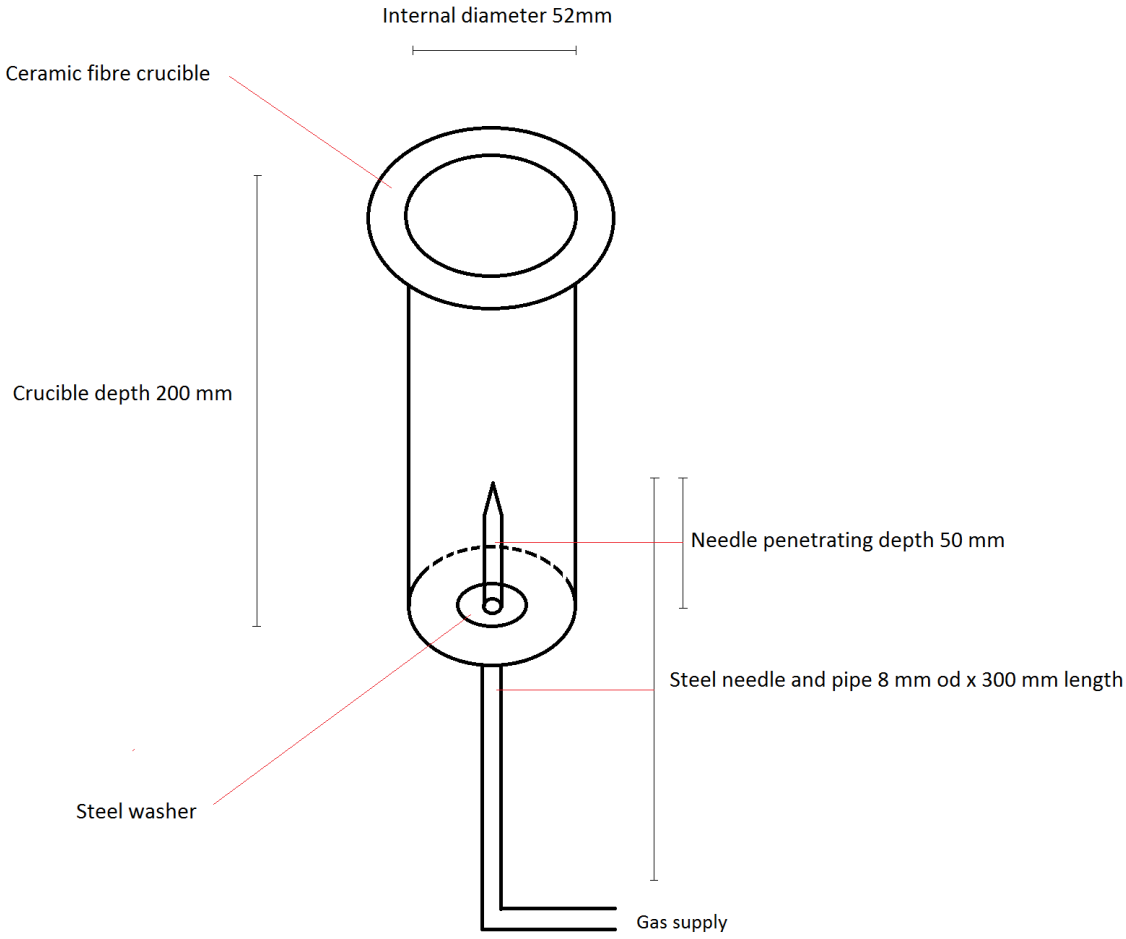

Figure 3.7 A schematic of the bubble capture set up.

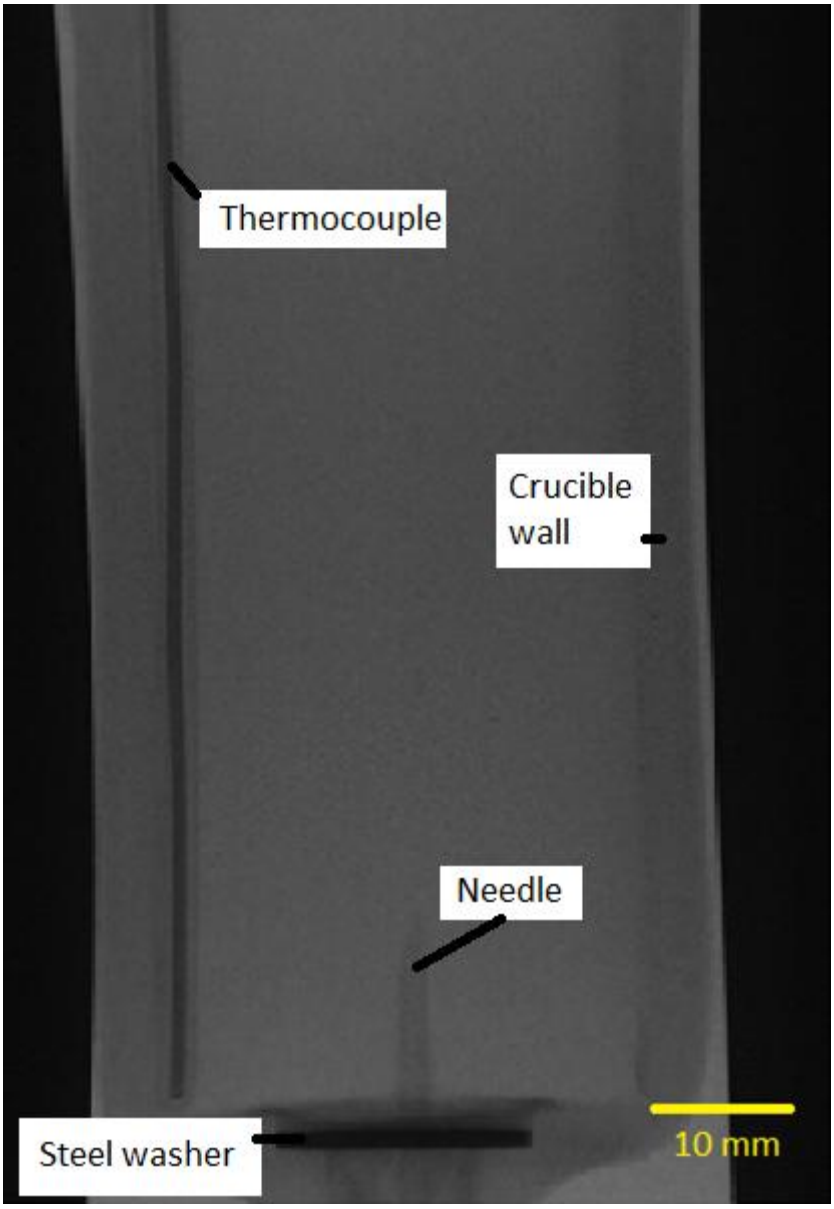

Figure 3.8 An x-ray image of the bubble capture set up.

The opposite end of the steel tube was connected by flexible PVC tubing to a flow gauge (range 0 – 300 cc/min Ar) and finally to the gas supply, controlled by standard bottle regulators. The gases used were PureShield Ar (99.999% purity) and an Ar/Cl gas mixture (8000 ppm, 0.8 % Cl in Pureshield Ar).

Ar gas was first purged through the system for 20 minutes to remove any excess residual air and moisture from the gas lines. The system was not heated, so some residual moisture was expected to remain inside the tubing. Approximately 2 - 3 kg of Al alloy was melted in an induction furnace and poured into the top of the crucible. The doors of the X-ray unit (manufactured by Xylon Internaltional, X-ray at 100 – 225 keV), were then closed and the unit activated. The bubbles were observed to flow up through the melt, at a rate controlled by the flow gauge, releasing a single bubble approximately 1-2 cm^3 in volume, every two seconds at a minimum flow rate of 5 cc/min. It was difficult to maintain a steady gas flow rate for long as the metal began to cool it became more difficult to release bubbles and it was necessary to increase the pressure to maintain the bubble flow. In many cases the bubble flow rate was either too high, so that multiple bubbles were forced out in 'pulses' of two to four bubbles, or the metal entered the steel tube and solidified. In experiments where the size of the needle aperture was decreased to below 0.2 mm, the pressure of the gas in the line caused a constant release of dozens of tiny bubbles (< 0.25 cm^3) into the metal which could not be trapped within the melt.

In a few successful experiments bubbles were caught, because as the alloy began to solidify the bubbles became trapped against the solidification front. At a point where a bubble was trapped and did not leak away the gas supply was isolated so that no more bubbles were produced and the ingot was allowed to cool in air. After cooling the crucible was broken open and the cylindrical ingot was extracted. The ingot was then sectioned and blocks containing bubbles were produced of maximum height 23 mm and circumference 22 mm, in order to fit inside a Pore Gas Analyser (PGA) sample chamber. In order to puncture the bubble inside the analyser the samples needed to have only a thin barrier between the

bubble and the external surface. Finally, samples were ground using SiC paper so that only about 1 mm of material separated the bubble from the surface, which was thin enough to puncture.

Pore Gas Analysis

The Pore Gas Analyser is a device which was originally designed to test the gas content of welds, but was adapted easily to puncture cast samples containing bubbles of gas. The PGA utilises a HAL RC-100 mass spectrometer and control unit manufactured by Hiden Analytical (Warrington, UK).

The sample was first placed within the analyser, which was then sealed and a primary vacuum pump was activated to remove atmospheric gases from within the sample chamber. The system pressure was then reduced to about $1x10^{-6}$ Pa using a secondary diffusion pump between the specimen chamber and mass spectrometer.

Once this vacuum was achieved, the chamber was isolated away from the primary vacuum pump and a Ti tipped needle screwed down to puncture the surface of the specimen. The gas contained within the bubble was drawn through the mass spectrometer and the composition and quantity of the gas is established. A picture and simplified sketch of the PGA can be seen in Figure 3.9.

The sensitivity of the mass spectrometer to different elements was quoted to be not equal by the manufacture, and a sensitivity factor was required to normalise the reading. The measured values were corrected by dividing the recorded result by the sensitivity factor for

that element, which were: H_2 = 0.44, N = 1, H_2O = 1, O_2 = 0.86 and Ar = 1.2. This meant, for example, that the equipment was more sensitive to H_2 and less sensitive to Ar.

After the contained gases (if any) were extracted from the bubble containing samples they were removed from the analyser, cut in half and examined using a JEOL 6060 SEM with EDX attachment.

PGA accuracy and qualification:

The ability of the PGA to detect gases was determined by Mahmoud [157] by using an air reference sample made from Cu. The Cu sample had a diameter of 6mm and was 5mm in height. A thin Cu plate (1mm thick) was placed on top of this and soldered in place. This trapped 141mm^3 of air within the sample, which was then placed inside the analyser. The needle was used to puncture the top of the Cu sample and the gases within were processed by the mass spectrometer. The analyser reported for an average of three samples, a composition of 79% N_2, 18% O_2, 1% Ar, and 0.6% water vapour, accurate with the composition of air.

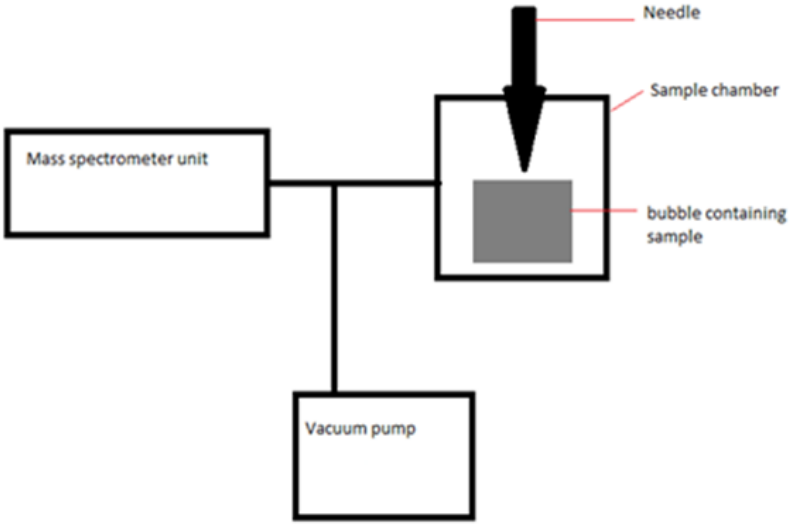

Figure 3.9 A picture of the pore gas analyser and a simplified illustration of the working of the unit.

3.3.2 Hydrogen removal from 7xxx aluminium alloys using a SNIF reactor with and without chlorine gas additions, measured using ALSCAN.

The aim of this study was to obtain data on degassing efficiencies from a commercial casting process. Since the material was destined for release to customers there were restrictions to the changes that could be made to casting parameters. The operating conditions could not be altered as modifications could potentially have had a negative and costly impact on the quality of castings, and clearly this had to be avoided. As such the study was designed to extract information without interfering with the production process.

The three alloys; 7010, 7050 and 7075 are common production alloys on DC3, with casting campaigns for each alloy type occurring approximately monthly, varying by schedule and customer demand. These alloys were cast using the same degassing procedure in that the SNIF unit uses an identical gas flow rate, gas composition and rotor speed within the unit to treat these alloys. These parameters are outlined in Table 3.2. Less commonly, castings are made on DC3 using those same SNIF parameters but without any Cl additions. These castings are cleaned instead by the use of ceramic foam filter (CFF), which is situated downstream from the SNIF unit. The CFF removes inclusions by de-wetting them from the Al and has no impact on the degassing performance of the SNIF unit. These parameters are outlined in Table 3.3.

This presented an opportunity to compare the performance of the degasser when operating under two different conditions; with and without Cl additions. The operating temperature and Cl contents of the SNIF could not be adjusted.

	Rotor one	Rotor two
Gas composition	Ar with 1.5% Cl	Ar with 0.8% Cl
Gas flow rate	1.5m^3 /hour	1.5m^3/hour
Rotor speed	450 rpm	430 rpm
SNIF temperature	Typically 700^oC	Typically 700^oC

Table 3.2 The (standard) operating conditions for the SNIF unit operating with Cl.

	Rotor one	Rotor two
Gas composition	Ar only	Ar only
Gas flow rate	1.5m^3 /hour	1.5m^3/hour
Rotor speed	450 rpm	430 rpm
SNIF temperature	Typically 700^oC	Typically 700^oC

Table 3.3 The operating conditions for the SNIF unit operating without Cl.

ALSCAN preparation:

Prior to the experiments both ALSCAN units were fitted with new HME3000D probes for wrought alloys, supplied by ABB Bomem, and standard Inconel sheathed K-type thermocouples, and were filled with low oxygen nitrogen (99.998% pure) from the same cylinder. Both units were set to operate with a calibration factor of 1.00 for all experiments so that the alloy specific correction factor CF(A) could be factored into the results post-analysis.

The units were set to purge the probes with N_2 3 times for 30 seconds before commencing a 10 minute analysis cycle, which recorded the H content in ml/100g as a function of the metal temperature which was also recorded. If, during an analysis, the probe (or

thermocouple) failed the measurement was ended and the result was removed from the data. Probes (or thermocouples) were then replaced on both units simultaneously to eliminate any variation in sensitivity over time from the results.

Accuracy of readings and drift of measurement:

Before and after these primary experiments took place the variation in the measurements of the two ALSCAN units was examined by placing them side by side before the SNIF unit in a long launder section of the same casting station, positioned so that the probes and thermocouples were approximately 10 cm away from one other. A sketch of this arrangement is shown in Figure 3.10. The units were then activated at the same time so that they analysed approximately the same section of the launder. The results can be observed in Tables 3.4 (before the experiments) and 3.5 (after the experiments). The H content of the metal during these experiments was observed to vary by a maximum of +/- 0.009 ml/100g slightly less than the reproducibility Figure quoted for the ALSCAN unit, (0.01 ml/100g). The conclusion was that there was no significant difference in measurement between the two units, either before or after the experiments took place.

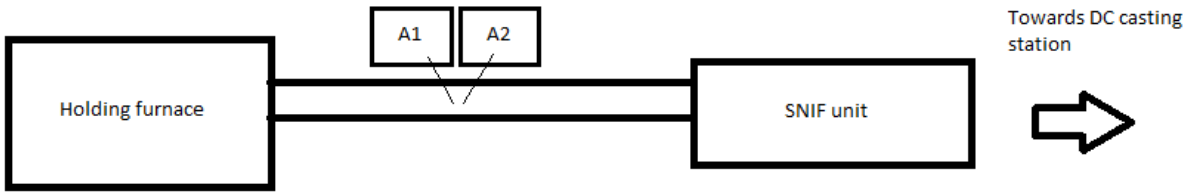

Figure 3.10 The Two ALSCAN units (A1, A2) were first set to run next to each other on the same length of launder during a casting to assess the variation in measurements.

Analysis cycle	A1: Melt H content (ml/100g)	A2: Melt H content (ml/100g)	Variance at the end of analysis (ml/100g)
#1	0.349	0.351	0.002
#2	0.344	0.339	0.009
#3	0.316	0.313	0.003

Table 3.3 The measured H content of the two ALSCAN units on the same cast and the variation in H content. These measurements were taken before the primary experiments took place.

Analysis cycle	A1: Melt H content (ml/100g)	A2: Melt H content (ml/100g)	Variance at the end of analysis (ml/100g)
#1	0.323	0.319	0.004
#2	0.327	0.320	0.007
#3	0.326	0.319	0.007

Table 3.4 The measured H content of the two ALSCAN units on the same cast and the variation in H content. These measurements were taken after the primary experiments took place.

During the experiments the two ALSCAN units were positioned so that one was on either side of the SNIF degassing unit, as shown in Figure 3.11. The same unit was placed in the same position each time to eliminate any unnecessary measurement variations.

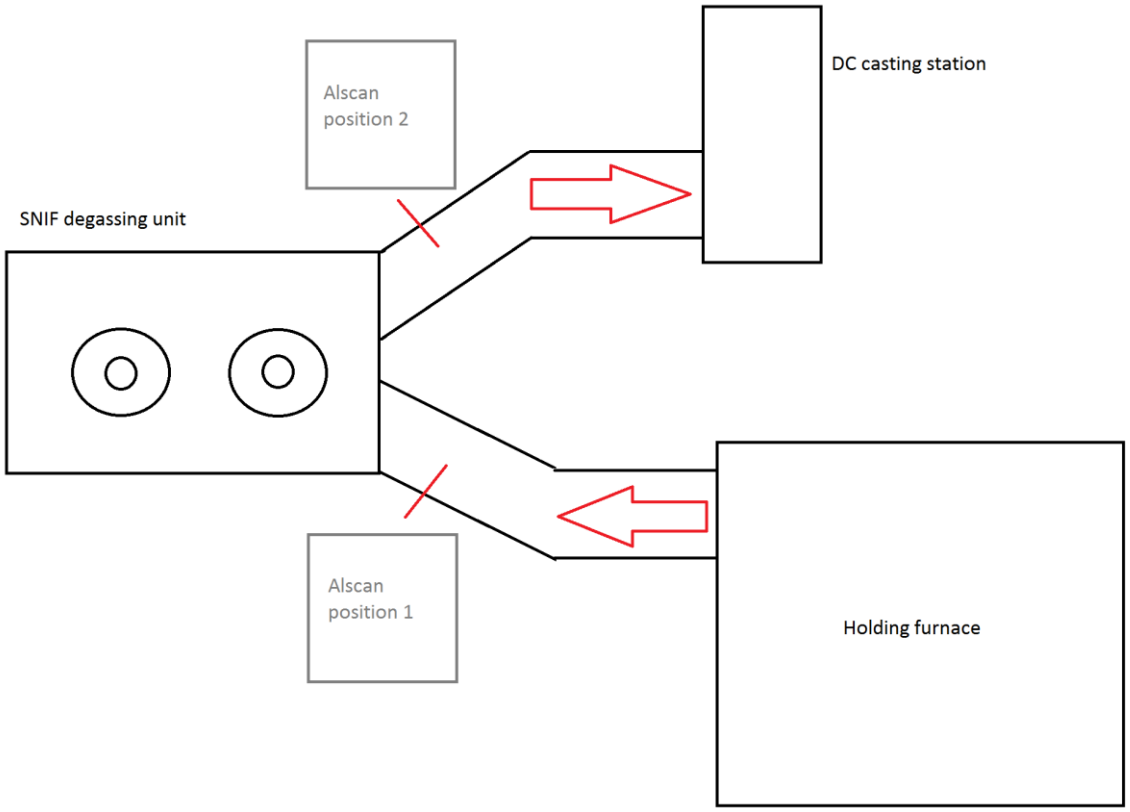

Figure 3.11 A plan view of the experimental setup. One ALSCAN unit is placed before and the other after the SNIF degassing unit. The red arrows indicate the direction of metal flow.

So as not to interfere with the potentially dangerous start of casting, the units were moved into their respective positions but were only activated once the casting had entered steady state conditions, so that readings began typically when the ingot was at a length of about 300 - 400 mm and the metal in the launders was at a constant depth. The probe and thermocouple were allowed to pre-heat above the surface of the melt during this period (which is essential to minimise thermal shock on the ceramic probes).

The unit in the pre-SNIF position (position one in Figure 3.11) was activated so that gas was flowing out of the probe for a few seconds before the probe and thermocouple were pushed under the metal surface to a distance of 2 cm from the bottom of the launder. The

total metal depth in the launder varied from cast to cast and during each individual casting (this occurs naturally and could not be accurately controlled) but is estimated to have varied from about 12.5 – 17.5 cm during any one measurement. Approximately 15 seconds elapsed before the post-SNIF position unit (position 2 in Figure 3.11) could be activated and immersed in the same manner. Depending on the planned cast length typically 2 – 4 readings were taken during each cast.

The ingot size and number of ingots produced during each cast was recorded, as was the ambient humidity and local temperature, using a LASCAR - EL-2-LCD USB data logger, which was placed approximately 2 meters away from the SNIF unit. The alloy composition of each cast was established by taking three OES samples; one at the start, middle and end of the cast, and averaging the results.

Processing data: the elimination of influences of temperature and alloy composition on measurements.

The H measurements made by the ALSCAN in both pre and post SNIF positions are a product of the equation in Equation 19;

$$S = \sqrt{PH_2}\ x\ CF(A)\ x\ S_o\ x\ CF(T_{melt}) \ldots\ldots \text{Eq.15}$$

where S is the solubility factor, PH_2 is the partial pressure of the H_2 in the closed loop (measured in atmospheres, multiplied by 1 $atm^{-0.5}$), S_o is the solubility of H in pure Al at 700^{o}C (0.92 ml/100g), CF(T_{melt}) is the measured metal temperature (and takes into account the increasing H solubility with temperature) and CF(A) is the alloy correction factor (which takes into account the variation of solubility according to the chemical composition of the alloy).

The S value is a product of these variables, as an example;

$$S = \sqrt{PH_2} \text{ x } 0.95 \text{ (alloy calibration factor) x } 0.92 \text{ (H solubility 700 Celcius) x } 710 \text{ (the measured melt temperature).}$$

Before the data could be accurately compared it was necessary to normalise the data so that the influence of measured metal temperature and the alloy composition could be removed. Each measured value obtained during the casting was divided by the recorded metal temperature and then multiplied by 700, thus removing the influence of melt temperature. Once the exact alloy calibration factor CF(A) was calculated from the average chemistry data obtained using OES, each measured value was then multiplied by the correction factor to eliminate the influence of the alloy H solubility from the results.

The latter was done because the chemistry of the alloy directly influences the H solubility and the generic alloy calibration factors recommended in the ALSCAN manual [147] are not precise. The average chemistry of each casting was obtained using optical emission spectroscopy (OES) and the information was used to determine a specific CF-A for each casting using a calculator that was designed to incorporate the influences of Cu, Mg, Zr, Zn, Ti, Fe and Si on the H solubility of the alloy, refining the accuracy of the measured results. CF(A) is calculated using the equation in Eq.20.

$$\log CF(A) = k_{Mg}Wt_{Mg} + k_{Si}Wt_{Si} + k_{Fe}Wt_{Fe} + k_{Cu}Wt_{Cu} + k_{Zn}Wt_{Zn} + k_{Zr}Wt_{Zr} + k_{Ti}Wt_{Ti} \quad \text{.... Eq.20}$$

where k_x represents the influence of the alloying element on the solubility of H and Wt_x is the weight percentage addition of that element in the alloy. An example of the calculator that was set up within Excel based on the work by Sigworth [158] can be seen in Figure 3.6. It should be noted that there appears to be a decimal point error for k Zr (k Zr is reported as

0.808) in this work, which is much higher than [159] so the value was reduced by a factor of 10 in Table 3.6.

Wt % element		k	Sub total
2.4	Mg	0.066	0.15906
0.06	Si	-0.0119	-0.00071
0.135	Fe	-0.0659	-0.0089
1.8	Cu	-0.0334	-0.05979
6.5	Zn	-0.016	-0.1032
0.10	Zr	0.0808	0.009696
0.04	Ti	0.0205	0.00082
		Total	-0.00302
		Factor	0.99

Table 3.5 An example of the alloy calculator employed to generate the alloy calibration factor CF(A) in Excel. The final alloy factor is achieved by applying a power10 function to the total.

So, as a general example, a measured S value of 0.350 ml/100g at 690^{o}C is first standardised to 0.355 ml/100g at 700 ^{o}C and the final S_i value of 0.348 ml/100g is obtained by multiplication of the alloy calibration factor, which is 0.98.

After refining the raw data, the measured incoming and outgoing H levels were used to calculate efficiency values as per Eq.21.

$$\frac{H_i - H_o}{H_i} \times 100 \quad \text{... Eq.17}$$

Where H_i is the H content of the metal entering into the SNIF unit (pre SNIF, position 1), and H_o is the H content of the metal exiting the SNIF unit (post SNIF, position 2). The equation describes the amount of H removed from the metal during the degassing process and is expressed as a percentage.

3.3.3 The degassing efficiency of aluminium alloys, achieved with and without chlorine, measured using ALSPEK H.

In these experiments the ALSPEK H was used to monitor the degassing rates of small batches of Al melts, specifically with the aim of evaluating the influence of Mg and Cl on degassing efficiency.

Choice of alloys and test conditions

Commercial purity Al (99.98%) and two Al alloys with varying Mg contents (7010 alloy containing 2.1 – 2.5 wt% Mg and a 5083 containing 4.0 – 4.9 wt % Mg) were chosen in this study as they were expected to influence the amount of $MgCl_2$ formed during the degassing procedure. These melts were heated so that they were either above or below 714^{o}C (the melting point of $MgCl_2$), to target temperatures of 680 - 695^{o}C and 730 - 750^{o}C respectively. A listing of the experiments can be seen in Table 3.7.

20 kg of metal was melted in a standard Salamander super A60 crucible (340 mm internal depth by 230mm internal diameter) using an induction furnace. This crucible was then transferred into a custom built resistance-heated furnace and kept at a steady temperature using a control system which held the furnace and metal temperature constant during the experiments. There was typically a 20^{o}C difference between the furnace and metal temperature (the furnace was always hotter).

Experiment number	Composition	Target minimum temperature	Gas
1	Pure Al	730^{o}C	Ar only
2	Pure Al	730^{o}C	Ar & Cl
3	7010 alloy	730^{o}C	Ar only
4	7010 alloy	730^{o}C	Ar & Cl
5	7010 alloy	680^{o}C	Ar only
6	7010 alloy	680^{o}C	Ar & Cl
7	5083 alloy	730^{o}C	Ar only
8	5083 alloy	730^{o}C	Ar & Cl
9	5083 alloy	680^{o}C	Ar only
10	5083 alloy	680^{o}C	Ar & Cl

Table 3.6 The experiments performed using the ALSPEK H.

The crucible was partitioned into two by the use of a ceramic baffle (approximate dimension 360 mm height x 220 mm width x 20 mm thickness), which was added to allow metal to circulate within the crucible (and H to diffuse), but to prevent bubbles from the ceramic lance interfering with or damaging the ALSPEK H probe tip. The baffle was held in position by a ceramic top plate and furnace lid that both contained two holes, through one hole the ALSPEK H probe was inserted and through the other, a ceramic tube used for degassing. A schematic of the experimental setup can be seen in Figure 3.12.

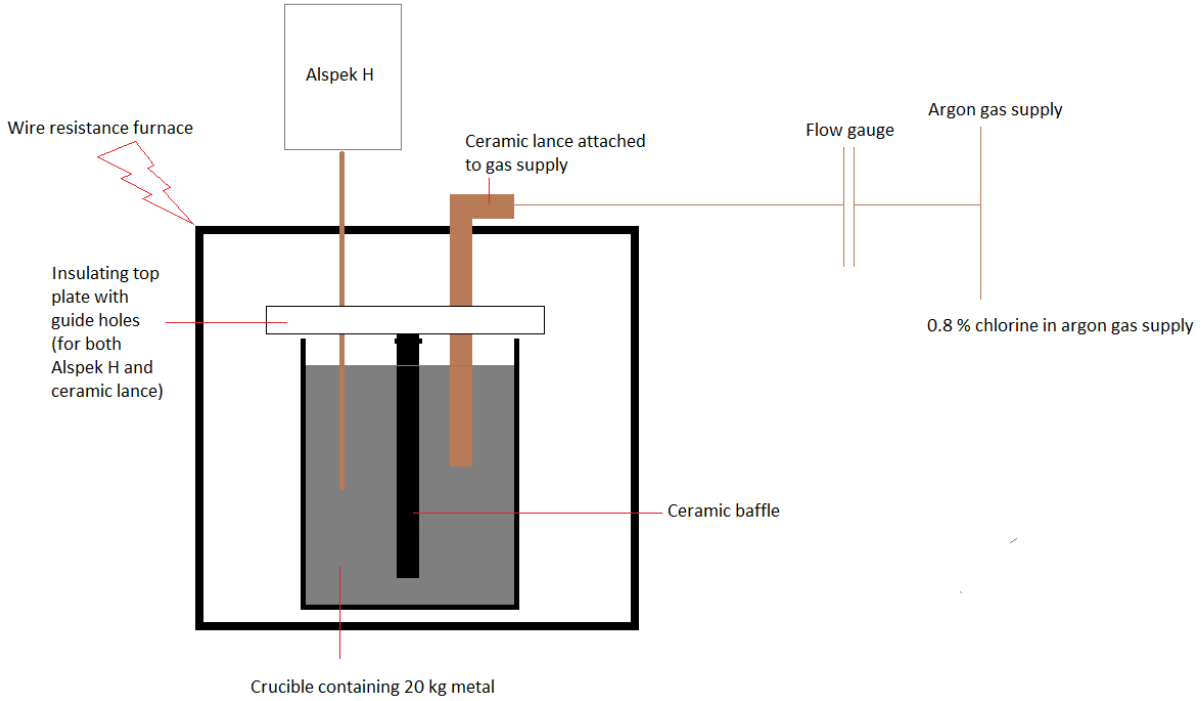

Figure 3.12 A schematic of the ALSPEK H experiments.

The ALSPEK H probe was inserted into the melt at a constant metal depth of 150 mm by the use of a supporting arm and laboratory clap stand attached to the side of the furnace. The ALSPEK H unit was observed to take approximately 5 – 10 minutes to reach stable readings within the melt. Once the measurements were stable the H content of the melt was increased by adding 75g of moist organic material (apple) to the top of the melt. This decomposed and provided moisture (steam) and thus H for the metal to absorb.

The H content of the melt was observed to increase a few minutes after the organic material was added, and within typically 10 – 15 minutes the H readings had stabilised at a higher value, between which the readings were noted to 'overshoot' and then reduce quickly to a steady value as the H within the melt equilibrated with the atmosphere in the furnace.

The elevated and stable H levels were then reduced by degassing, by purging Ar or Ar and Cl through the ceramic tube, (which was made of SiAlON 101). The lance (250 mm in length, external diameter 23 mm, internal diameter 11 mm) was submerged so that the tip of the lance was as a constant metal depth of 150 mm, controlled by the ceramic insulating top plate that was placed on top of the crucible. Although lances are a poor tool for degassing they are simple in design, relatively cheap and require minimal engineering to fit into position. The lance was connected to a gas supply via stainless steel compression fittings and tubing to a mass flow controller with a range of 0 – 300 cc/min, and then by flexible PVC tubing to the Ar and Ar-Cl gas bottles.

The melt was degassed by injecting either a) Pureshield Ar (99.999% Ar) or b) Pureshield Ar with 8000 ppm (0.8%) Cl gas, which was supplied in a pre-mixed cylinder produced and supplied by BOC Special Gases. Both gases were forced through the melt at 300 cc/min.

If, for example, the steady initial H content was observed to be in the region of 0.45 ml/100g, the melt was degassed but the measurements were not made until the melt H content decreased to 0.35 ml/100g, and recordings were made until the melt reached 0.15 ml/100g, over a range of 0.2 ml/100g.

This range was chosen because it represents the typical range of pre and post degasser readings commonly observed at Alcoa. It was also reasoned to limit the minimum H content to 0.15 ml/100g, as below this level it becomes significantly harder to degas the metal, and prolonging the ALSPEK H probe life and minimising the amount of Cl used was felt to be important for reasons of both cost and safety.

Response of the ALSPEK H to changes in H content and drift of measurement.

Before the main experiments, the ALSPEK H was used to monitor the increase and decrease in H in pure Al, to gauge the units' responsiveness to changes in melt H content. A 20 kg melt of pure Al was first allowed to stand for an hour after melting and transferring into the resistance-heated furnace so that any moisture sources were consumed and the metal would be in equilibrium with the crucible and ambient atmosphere. The Alspek H probe was inserted and allowed to come to equilibrium with the melt for another 20 minutes. The readings were then recorded and observed to vary by +/- 0.01 ml/100g over 40 minutes. The metal H content was then lowered by purging Ar gas up through the metal, (although the gas flow rate was not recorded in this trial).

The melt H content was observed to decrease to 0.1 ml/100g H, over about 50 minutes, when the degassing procedure was stopped. The furnace lid was then removed and approximately 5 minutes elapsed before a small amount of organic matter was added to the surface of the melt. The H content of the melt was observed to increase over the next twenty minutes as the H was absorbed by the metal and diffused towards the probe. Once the H content was similar to the original H content a second degassing procedure was implemented. After a period of time when the melt H content appeared to be balanced, (by the simultaneous absorption and floatation of H into and out of the melt), the H content of the melt was observed again to be reduced by the degassing process. The results of the trial are shown in Figure 3.13.

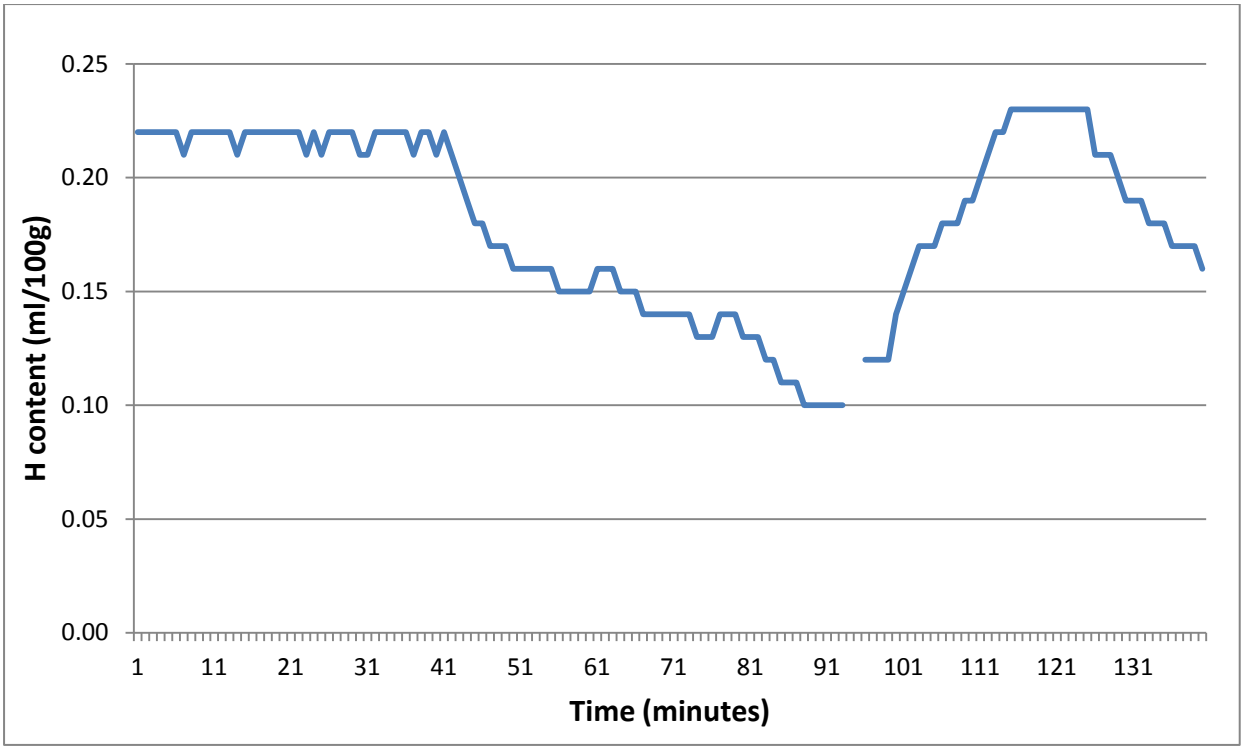

Figure 3.13 The H content of a pure Al melt measured using the ALSPEK H. a) degassing using Ar gas b) exposure to a H source and c) degassing using Ar gas.

3.4 LECO degassing and hydrogen analysis experiments

The LECO H determination device is used to evaluate the H content of solid Al samples. The LECO device measures the H content (in ppm) of cylindrical samples 8 mm OD x 50 mm length. It does this by heating them with the H passing into a closed loop nitrogen gas carrier stream, which passes through a thermal conductivity cell to give the H_2 content of the mixture. The analysis is non-repeatable as H within the sample is removed during this process.

This work began as an investigation into the accuracy of the LECO device, as there were concerns that the device was reporting un-reproducible measurements, and there were no commercially available Al standards to which results could be compared. Initial experiments assessed the capability of the LECO device to detect changes in the H content of Al samples over time, which revealed that the device could also be used as a tool for degassing the solid samples. Degassed samples could be exposed to different environments and the H absorption measured over time. The experiments are described in section 3.4.1.

The literature states that H diffuses into double oxide film defects, inflating them into pores during solidification. H, however, exists as protons in the melt which must diffuse across Al_2O_3 and AlN layers before it can re-combine to form a diatomic molecule (gas phase) within the double oxide film. As these layers have been shown to be inhibitors to proton diffusion, the LECO was adapted in a novel way to measure the H content of surface modified Al samples.

Samples that had been degassed using the LECO technique were placed inside a furnace and then exposed to different gaseous environments (specifically, air and N_2) and heated until

molten. The gas influenced the formation of different films on the surface of the samples (Al_2O_3 or AlN, respectively) as they melted. Samples were then exposed to H_2, which would have to diffuse across or migrate around these films in order to enter the Al samples. Finally, the H absorbed into the samples was measured by inserting it back into the LECO. The hydrogen furnace and LECO experiments are described in detail in section 3.4.2.

The following applies to both sets of experiments detailed in sections 3.4.1 and 3.4.2.

Before any experiments took place the Cu turnings and the incoming gas and furnace cleaning reagents within the LECO were replaced using the recommended LECO procedures detailed in the manual. The reagents were monitored electronically so that they were used for no more than 200 analyses before being changed. If the Schultz reagent (which is used to absorb carbon dioxide in the system, which can influence the results of an analysis) was degraded (changing colour from yellow to black with exposure to CO_2 or moisture) before this limit, then it was replaced immediately so that it did add error into the measurements.

The LECO was prepared first by heating it five times using a high temperature out-gassing procedure (>700^{o}C) that drives any moisture from the furnace and the graphite crucible that is used in the process. The unit is then calibrated by dosing the thermal conductivity cell with pure H_2 (99.9995%) six times. The first reading is discarded and an average of the remaining five readings provides a calibration factor to be applied to future readings. The reference point for accurate dose calibration is 3.01 ppm H and under this low sensitivity mode the accuracy of the unit is +/- 0.01 ppm.

A sample is inserted into the unit, heated and then exposed to a commercial purity N_2 cover gas (99.998%). The H within the sample flows into the N_2 and the H + N_2 mixture travels

through the thermal conductivity cell where the amount of H is established. This process has a higher reported accuracy of +/- 0.005 ppm. The LECO reports both surface and bulk H contents for a sample and also a total of these two values. In this report only the total H content was used as the surface readings were always small compared to the bulk readings. For example a typical surface value of 0.001 ppm would be added to a bulk reading of 0.15 ppm.

LECO sample production procedure:

32 Al LECO samples were machined from pure Al (99.98%) and 5083 alloy plate, as detailed below. These samples were then used as stock material for the experiments detailed in sections 3.5.1 and 3.5.2.

- A section of DC cast and hot rolled 5083 alloy plate with the approximate dimensions of 150 x 150 x 10 mm was cut into 20 bars approximately 50 x 10 x 10 mm in size.
- A block of commercially pure extruded (99.98%) Al with the approximate dimensions 100 x 80 x 60 mm was cut into 12 bars approximately 50 x 10 x 10 mm in size.
- These individual 50 x 10 x 10 mm bars were then machined into rods with final dimensions of 8 mm OD x 50 mm length using a lathe without any liquid coolant. An example of a LECO sample is shown in Figure 3.14.

Figure 3.14 An Al sample used in the LECO H determination process, dimensions 8mm OD x 50 mm length.

3.4.1. Hydrogen absorption measured using the LECO.

It was desirable to observe the variation of the H content in cast and wrought products and how the samples responded when exposed to different atmospheric conditions, so the performance of the LECO was first evaluated using the high Mg (4.5 wt.% Mg) alloy 5083.

Two 5083 samples were processed in the LECO ten times to evaluate how much H was removed during each analysis. This was done because the samples do not melt during the LECO analysis cycle, and it was felt that H may be retained within the sample, with only one analysis cycle being used. The repeated degassing of these two samples can be seen in Figure 3.15.

It was established that the LECO removed about 85% of the H from within a sample during the first analysis, with any significant levels of H being removed from the samples in the first three analyses. Typically after this third degassing process only values close to the error

levels of the LECO device (+/- 0.005 ppm) were observable. The LECO was deemed to be capable of reporting accurate H levels as long as each analysis was above 0.01 ppm, but once a value below this 0.01 ppm limit was obtained the analysis was stopped.

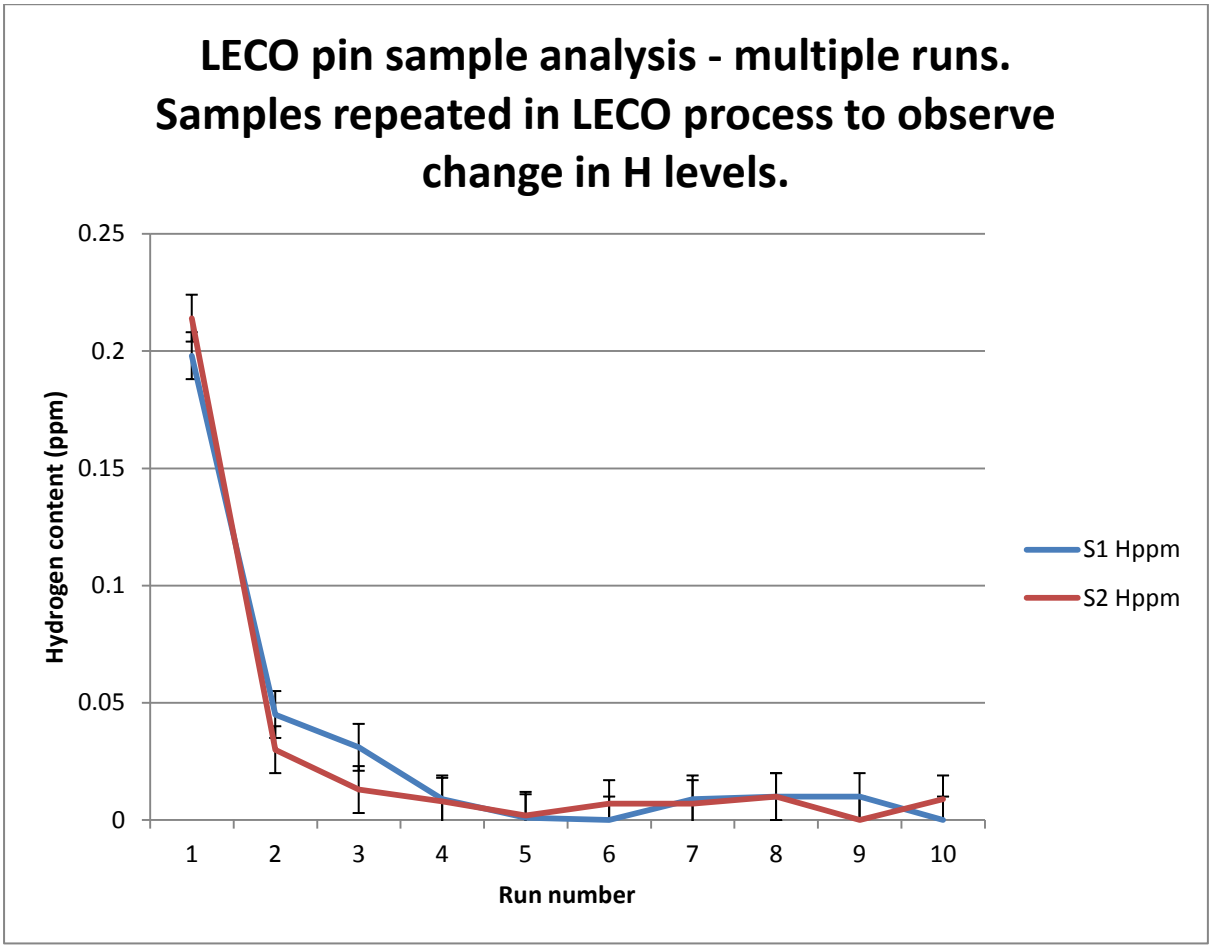

Figure 3.15 The degassing of two LECO samples. Any significant H within the samples was observed to have been removed during the first three analyses. Error bars of +/- 0.01 ppm are added to each value.

A number of experiments were carried out to test how the Al pin samples responded when they were exposed to different environmental conditions after being degassed. As noted in the literature, Al_2O_3 formed on pure Al should be protective, minimising H absorption over time, whereas spinel and MgO formed on alloys containing Mg that are not protective, and

so these alloys should absorb H over time. Acetone is used routinely at Alcoa to dissolve any grease from the surface of the Al pins, but it was unclear if exposure to hydrocarbons had any effect on H absorption. Three experiments were carried out to test these various points:

1) The two 5083 samples degassed in Figure 3.15 were allowed to sit in the laboratory near an open window for ten weeks before being re-analysed in the LECO. H was expected to be absorbed into the samples over this period.
2) Ten 5083 samples had their H content removed by degassing 3 times using the LECO device and were then left standing in the laboratory along with a LASCAR - EL-2-LCD USB data logger that monitored the local ambient temperature and humidity. One sample was re-analysed every 24 hours for 96 hours, and then every seven days after that to observe the H absorption into the 5083 alloy samples over time.
3) Four 5083 samples were degassed three times and one of each was immediately inserted into a glass jar containing a specific atmosphere;
    a. Sample resting in a glass jar that contained de-ionised water.
    b. Sample resting in a glass jar that contained acetone.
    c. Sample placed in an open top glass jar near an open window.
    d. Sample sealed in a glass jar with only air.

    Samples were left in these conditions for four days, before being tested again in the LECO.

3.4.2 Hydrogen diffusion across aluminium oxide and aluminium nitride experiments:

Double oxide film defects are thought to trap air and bring it beneath the surface of the melt where it can react further; perhaps producing a feature into which H can diffuse and expand to produce gas pores in castings. The Al_2O_3 film is known to coarsen and crack over time which will allow N_2 to react with the melt to form AlN beneath the pre-existing oxide layer. It is unclear if H can preferentially pass through or around this nitride film, however. The experiment below was designed to better understand the absorption of H through these films.

Eight pure Al, four 2L99 alloy and two 5083 alloy samples, (all 8 mm OD x 50 mm length), were degassed three times using the LECO, then immediately sealed in glass jars with screw top lids and transported to the furnace. In total seven separate experiments were performed using the furnace; four using pure Al, two using 2L99 alloy and one using 5083 alloy. Each experiment used two samples, processed simultaneously, and the experiments are summarised in Table 3.8.

Experiment number	Alloy / Heating atmosphere
1	Pure Al /Air
2	Pure Al /Air
3	Pure Al / N_2
4	Pure Al / N_2
5	5083 alloy / Air
6	2L99 alloy / Air
7	2L99 alloy / N_2

Table 3.7 The list of experiments used to assess the H absorption into Al samples.

Each sample was placed within its own cylindrical alumina crucible with dimensions of 9mm ID and 100 mm length. These crucible dimensions were chosen as the crucible needed to be large enough to accommodate the thermal expansion of the Al during the test, but also small enough to ensure that the metal did not dramatically change shape when molten so that it could be put back into the LECO to measure the H absorption after being in the furnace. Alumina was chosen as it was inert and non-wetting to Al, allowing the crucibles to be re-used, and also would not contribute to the H absorption.

These crucibles were placed on a holder that was then inserted into the tube furnace. A standardK-type thermocouple was then inserted so that it rested between the two approximately 5 mm away from both samples to provide accurate and repeatable temperature measurement. A sketch of the setup is shown in Figure 3.16. The procedure for each experiment is detailed below:

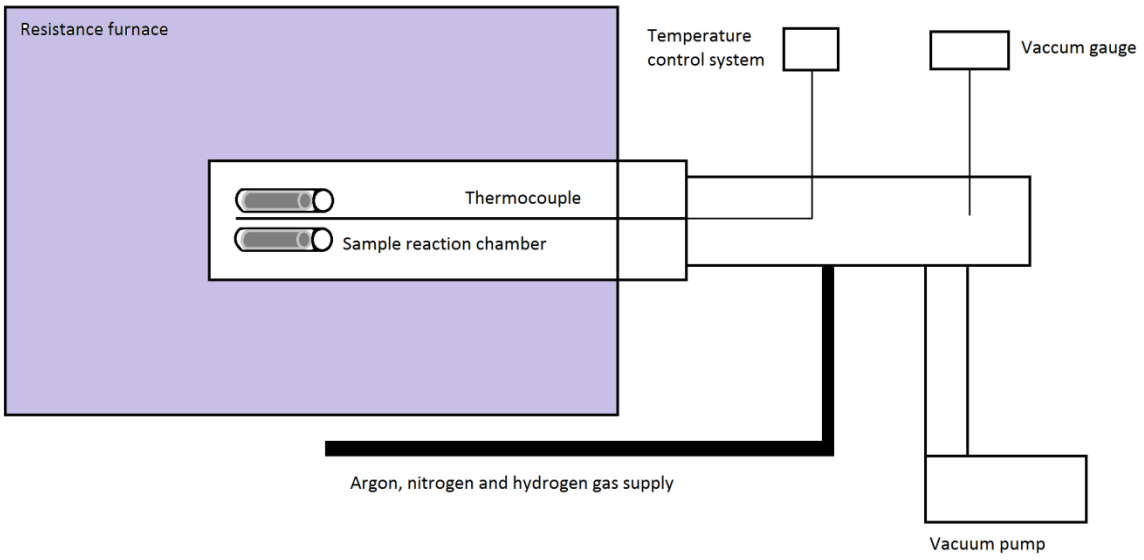

Figure 3.16 A schematic of the hydrogen furnace.

The samples are contained within alumina crucibles which are inside a steel furnace tube. The tube is connected to both the vacuum and gas supplies. The furnace tube is surrounded by a tubular resistance furnace that heats the samples. In the experiments using N_2 a small ceramic tray loaded with 50g hafnium is inserted in front of the samples in order to absorb any residual oxygen.

Experiments one and two:

Two pure Al samples were inserted into the furnace, which was then sealed. The furnace was then heated to 700^{o}C at a rate of 40^{o}C per minute so that the samples first expanded and then melted in air. They were allowed to stand at this temperature for 15 minutes, after which the air was removed to a vacuum pressure of 1 Pa. The furnace was then immediately filled with H_2 to a pressure of 150 kPa and held at this temperature and pressure for one

hour. The furnace was then cooled at a rate of 20^{o}C per minute to 50^{o}C before the H was removed and the samples extracted.

Experiments three and four:

Two pure Al samples were inserted into the furnace with a ceramic dish that contained approximately 50g of Hf turnings. The furnace was then sealed and air was removed to a pressure of 1 Pa, the furnace was then filled with Ar gas to a pressure of 100 kPa. The Ar was then removed by vacuum until a residual pressure of 1 Pa remained within the furnace. This Ar pressurising to 100,000 Pa and removal by vacuum to 1 Pa cycle was repeated a total of five times to ensure that no atmospheric oxygen remained within the furnace.

The furnace was evacuated and then filled with N_2 (99.998%) to a pressure of 150 kPa before being heated to 700^{o}C at a rate of 40^{o}C per minute and allowed to stand for 15 minutes in a N_2 atmosphere. This slightly increased pressure was chosen to encourage the reaction of N_2 with the Al surface. The furnace was then evacuated, removing the N_2 gas, and filled immediately with H_2 to a pressure of 150 kPa and held at this temperature and pressure for one hour. The furnace was then cooled at a rate of 20^{o}C per minute to 50^{o}C before the H was removed by vacuum and the samples were extracted.

After the Ar/vacuum cycling procedure the furnace was calculated to contain about $2x10^{-21}$ Pa of O_2 from the air so the main source of background O_2 contamination would be from the oxygen free N_2 gas used in the experiment. The oxygen free N_2 gas was 99.998% pure so would contribute an additional 0.002 Pa of O_2 into the system, or $4x10^{-09}$ Pa O_2 once the N_2 gas was removed by vacuum to a pressure of 1 Pa. Any residual O_2 within the system was expected to react preferentially with the hafnium turnings placed in front of the

samples, acting as an O_2 scavenger. With such low levels of O_2, the formation of AlN was theoretically possible, based on the work by Swaminathan et al. [160] [161] who estimated that an O_2 impurity threshold of 10^{-6} Pa O_2 would prevent AlN formation.

Experiment five:

This was identical to experiments one and two but used 5083 alloy samples instead of pure Al. The Mg content of this alloy (~4.5 wt.% Mg) was expected to change the surface oxide formed during melting to Mg oxide and was expected to absorb excess H.

Experiment six:

Was identical to experiments one and two but used 2L99 alloy instead of pure Al. 2L99 alloy contains a small amount of Mg (0.2 - 0.3 wt.% Mg) so would be expected to form spinel at the sample surface.

Experiment seven:

Was identical to experiments three and four but used 2L99 alloy instead of pure Al. 2L99 alloy contains a small amount of Mg (0.2 - 0.3 wt.% Mg) so would be expected to form spinel or nitride at the sample surface.

Post hydrogen furnace treatment:

Following each experiment the specimen obtained was removed from the furnace and placed immediately into a glass jar and sealed with a screw top lid to minimise H pick-up from the atmosphere. The samples had their H content measured three times. Those samples processed in N_2 atmosphere were then inspected using SEM in order to evaluate the surface. The H contents of the pure Al samples heated in air and N_2 were then compared

using the Student's t-test that was described earlier in this report (see section 2.8). In this instance the null hypothesis is defined "Al_2O_3 and AlN are both equal barriers to H absorption".

Chapter 4 Results

4.1 Point defect indications within the 7050 alloy plate

The ultrasonic C-scan for plates containing point defects can be observed in Figures 4.1 - 4.3. Indications which are assumed to be inclusions were scattered across the scan, visible as green and red dots or lines on the white background, (which indicates defect free Al). The edges of the plates in the scan were represented by the orange border; red, green and orange markings at the opposite long ends of the plate are surface defects created by clamping during the stretching process. The plate number, temper and other details were given at the top of the scan. Hand written notes, detailing the type of ultrasonic response, defects and comments such as 'reject' are made by the operator running the ultrasonic equipment.

In Figure 4.1 defects within the 7050 plate (those which are so large they require the plate to be scrapped) are circled in blue and identified with an R. There were five such inclusions within this particular plate and due to their locations it had to be completely scrapped. There were so many inclusions in Figures 4.2 and 4.3 that these plates were also scrapped. Inclusions were also observed to make up a 'V' shape profile on the scan. This profile resembled the liquid-solid profile of the sump which forms naturally within the ingot during the DC casting process. The sump is formed by the combination of heat input, from fresh metal entering the top of the ingot, and heat extraction, by application of water sprayed onto the surface of the ingot underneath the water cooled mould. From this observation it was reasonable to assume that these inclusions were released in a flush of material, either

out of the launder or distribution bag (which is situated on top of the casting between the downspout and the solidifying ingot) into the metal stream during casting, see Figure 2.1.

Inclusions were successfully extracted from the plate for examination (as detailed in section 3.1.1) about 70% of the time, dependant on the size and location of the inclusion within the plate. In general the larger and more central the inclusion within the thickness of the plate, then the more successful the extraction process became. The inclusions weakened the specimens and facilitated the fracture of the plate when notched and impacted, but very small inclusions, and those near the surface of the plate or found in thin gauge plate, were more difficult to extract, because the length of the specimens was reduced, making them more difficult to break.

A total of 20 inclusions were surveyed from these three plates (shown in Figures 4.1– 4.3). Both larger and smaller defects were evaluated and were found to be identical in composition, varying only in size. Examples of inclusions are shown in Figure 4.4. These images were chosen as they represent the largest, typical and the smallest size of inclusions found in the survey, and their size ranged from over 15 mm^2 to as little as about 1mm^2 in size.

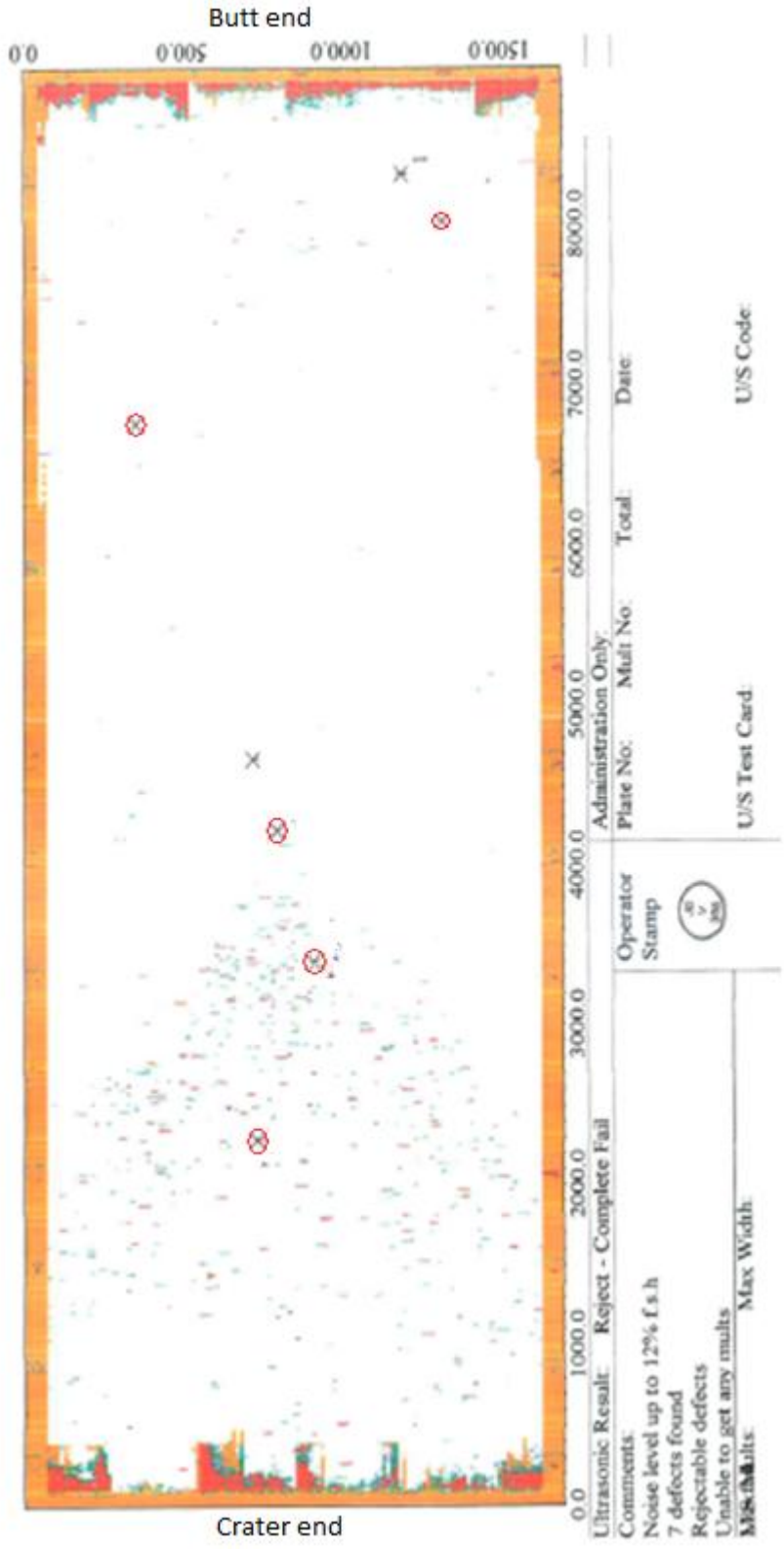

Figure 4.1 Plan view ultrasonic C-scan for 7050 alloy plate (length 8989 mm, width 1701 mm, thickness 60 mm). A characteristic 'v' shape of inclusions can be observed from the crater end pointing towards the centre of the plate.

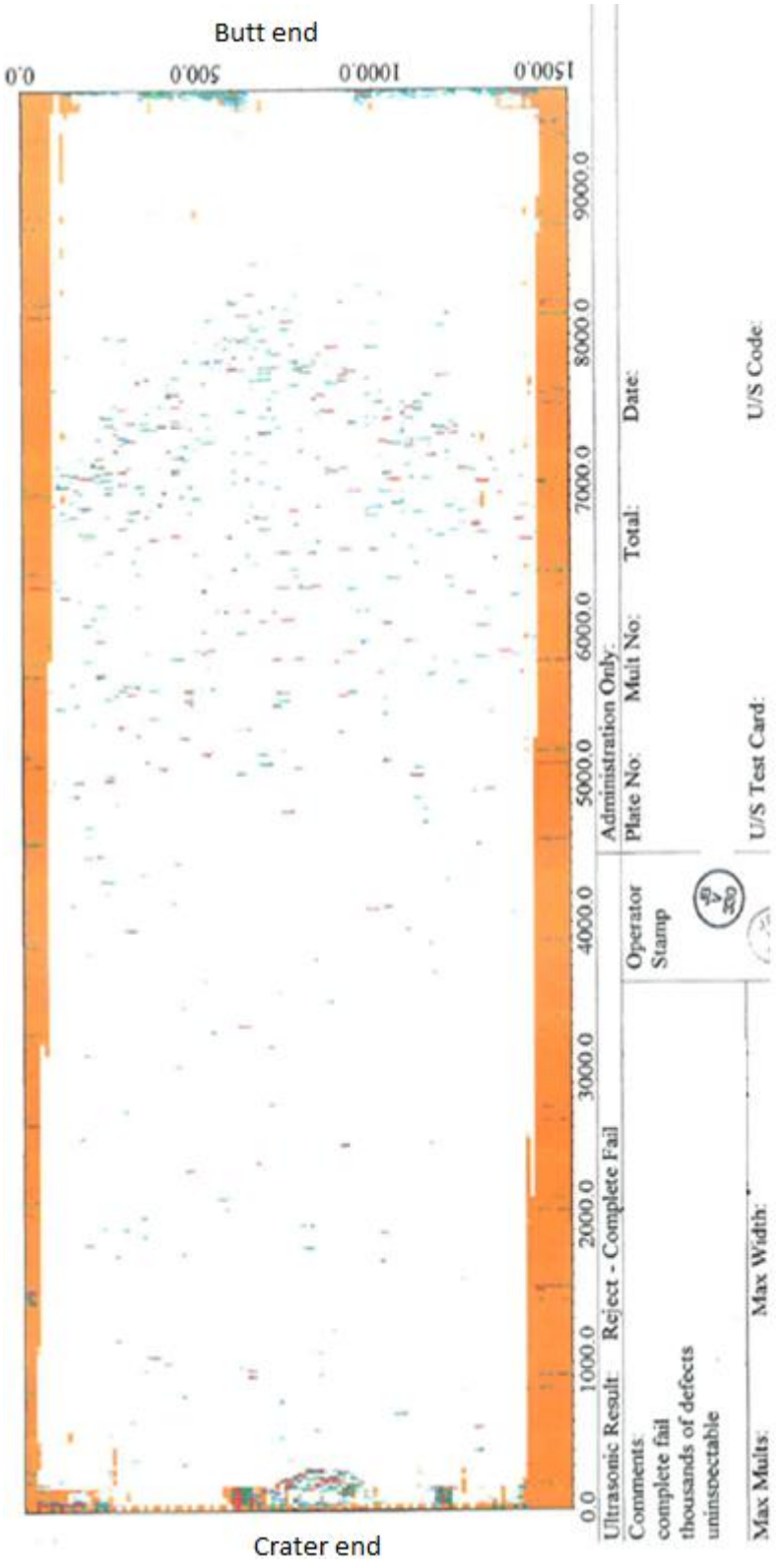

Figure 4.2 Plan view ultrasonic C-scan for 7050 alloy plate (length 9678 mm, width 1575 mm, thickness 70.6 mm). A characteristic ‘v’ shape of inclusions can be observed from the crater end pointing towards the butt end of the plate.

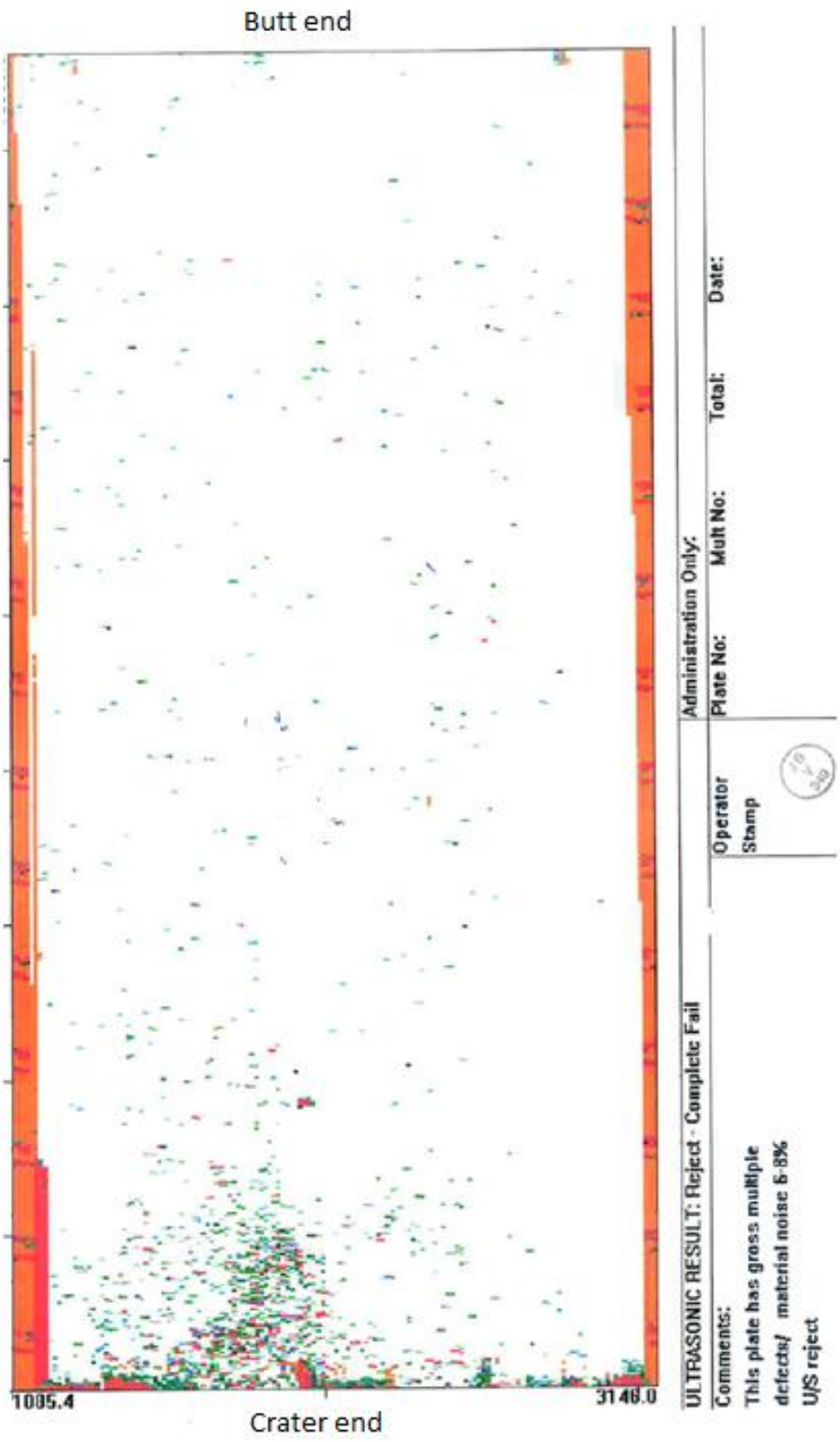

Figure 4.3 Plan view ultrasonic C-scan for 7050 alloy plate (8645 mm length, 2257 mm width, thickness 51.4 mm). A characteristic 'v' shape of inclusions can be observed from the crater end towards pointing the centre of the plate.

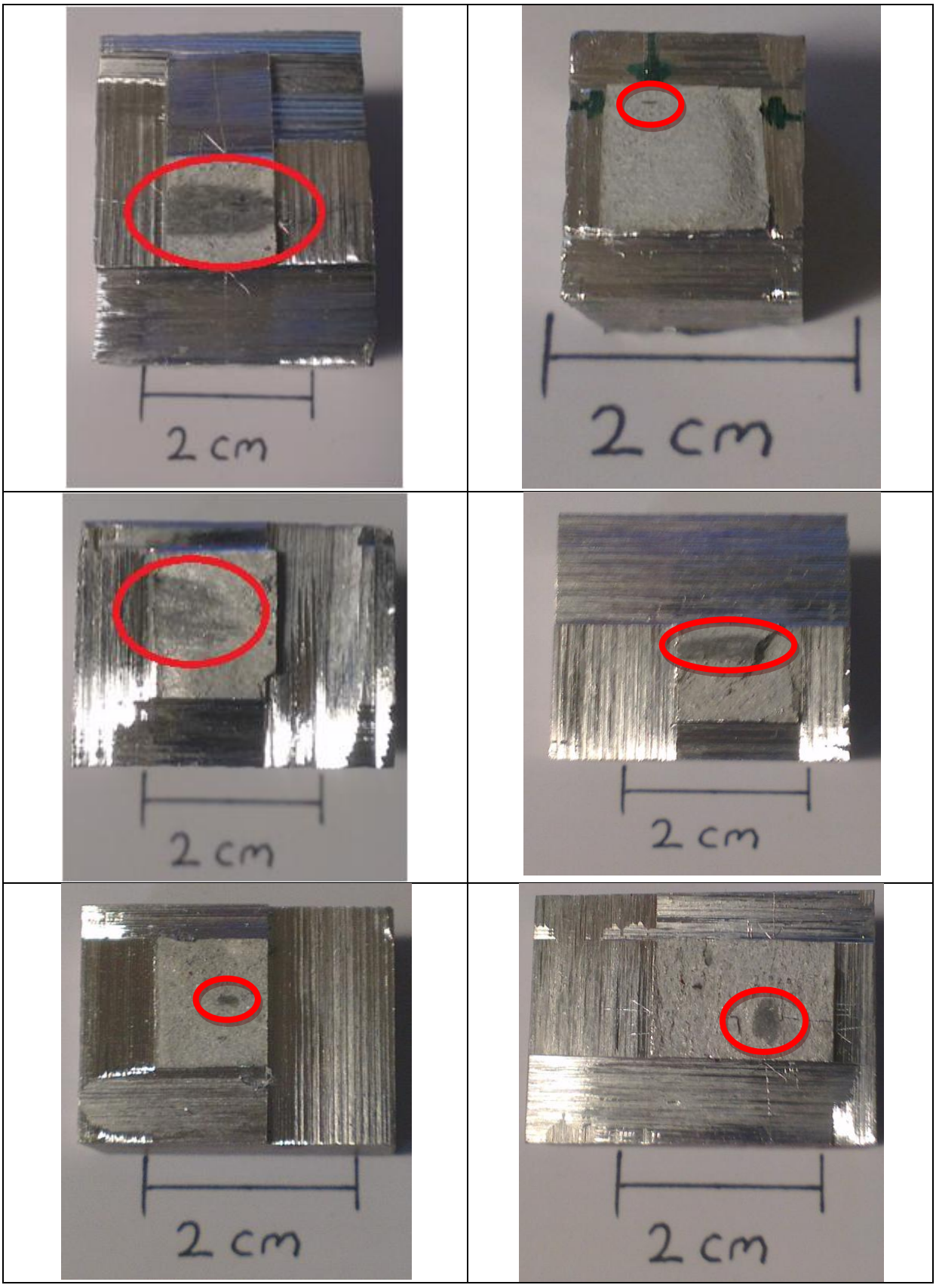

Figure 4.4 Examples of the inclusions found in 7050 plate samples.

The inclusions appeared to be plane (there were no protrusions from the surface of the defect and no fragments came loose from the surface of the inclusion during the extraction process) and were primarily grey or grey - black in colour. Inclusions were not soft, did not rub away when touched or dissolve in water and appeared to be well adhered to the surface of the Al, presumably because of wetting during solidification or the heat and deformation during the hot rolling process.

Inclusions were found to be made up of two different phases when examined using backscattered imaging in the SEM. One phase appeared light and the other dark, when compared to the Al matrix. The phases were contrasted in this manner because one was made up of heavier elements that reflected more electrons and thus appeared brighter compared to the Al matrix, the other was made up of lighter elements, reflecting fewer electrons and thus appearing darker than the surrounding matrix.

Figure 4.5 shows the chemical analysis of the Al matrix and an inclusion using Energy Dispersive X-ray spectrometry (EDX). The matrix was composed primarily of Al, Zn, Cu and Mg, the inclusion was composed of O, Cl, Ca, Ti and Zr.

Figures 4.6 – 4.9 shows examples of inclusions found in four separate specimens. The light and dark phases are found to be interlaced across the fracture surfaces of all inclusions. Images in each instance are labelled by area: 1) Al matrix (the composition of which is omitted) 2) light phase 3) dark phase. The EDX chemical analysis of each analysis is presented below each image.

It should be noted that carbon was not present within the alloy but it is a known artefact of the SEM and has been discounted from the analyses.

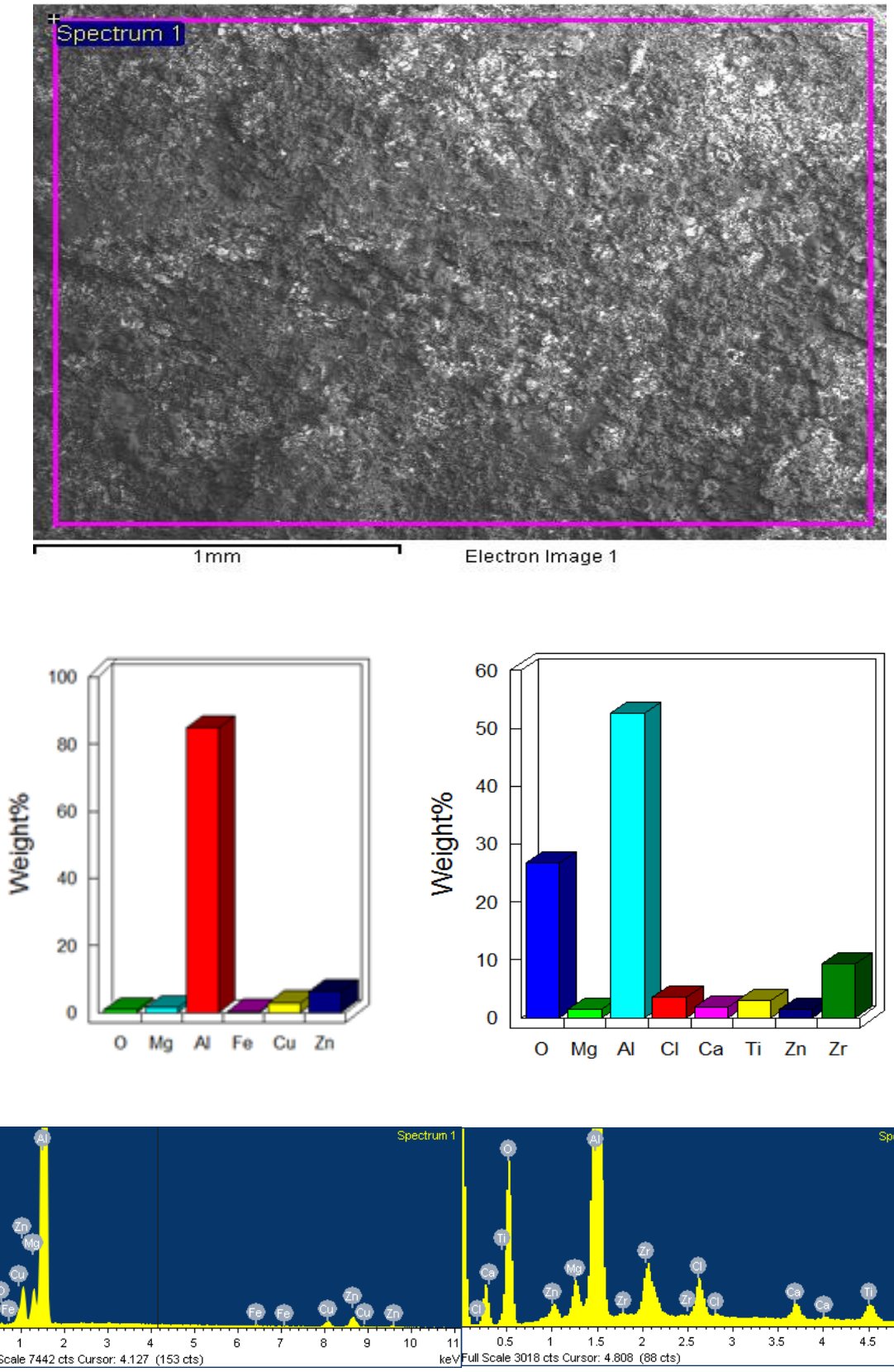

Figure 4.5 BSE image of an inclusion found in 7050 plate. The first EDX spectra shows the matrix of the surrounding alloy (primarily Mg, Cu and Zn). The second EDX shows an overview of the entire inclusion surface (notable quantities of O, Cl, Ca, Ti and Zr).

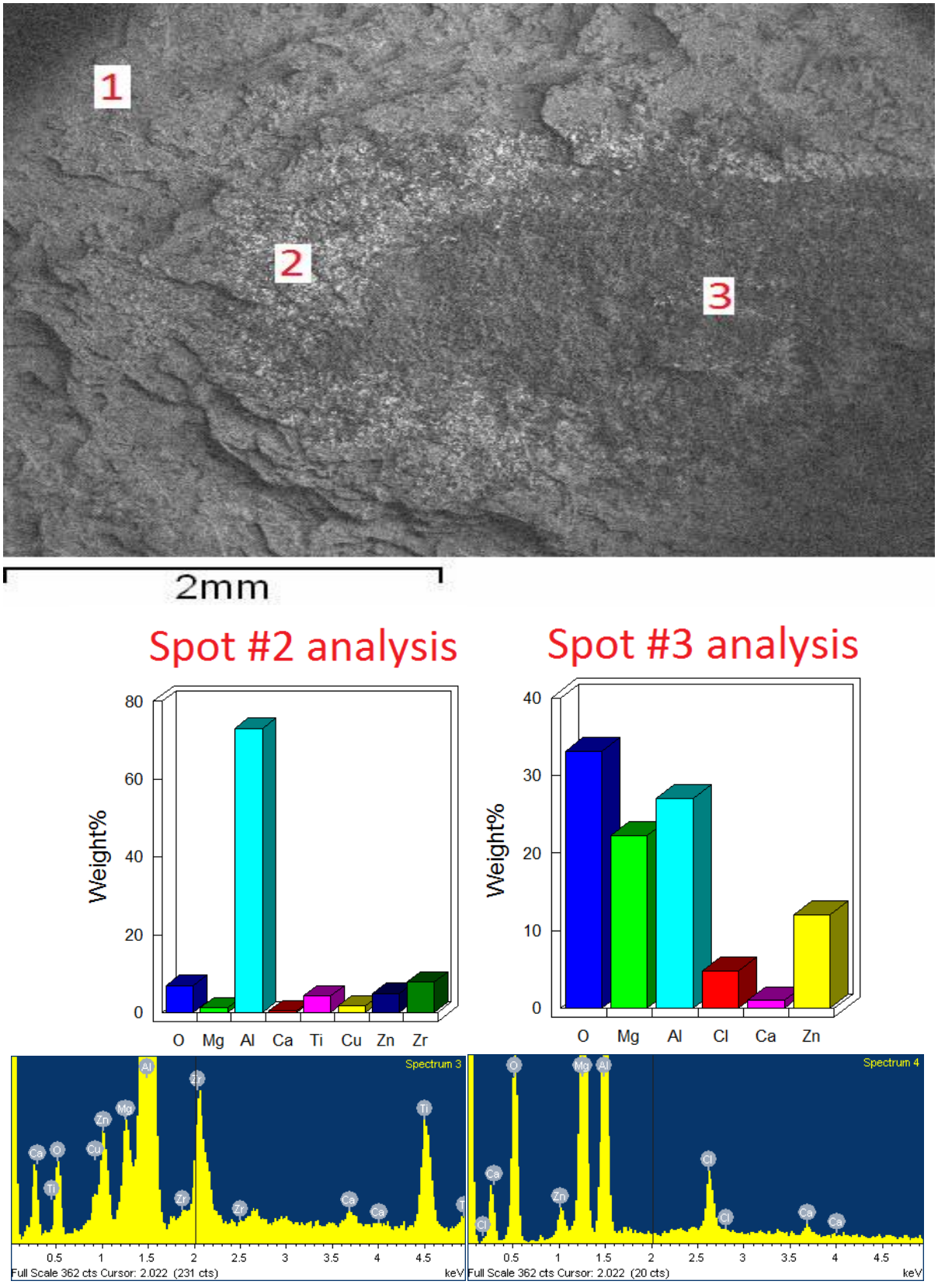

Figure 4.6 BSE image of an inclusion found in 7050 alloy plate. Spot labelled; 1) Al matrix / fracture surface 2) part of the inclusion that is composed primarily of the light phase 3) part of the inclusion that is composed primarily of the dark phase.

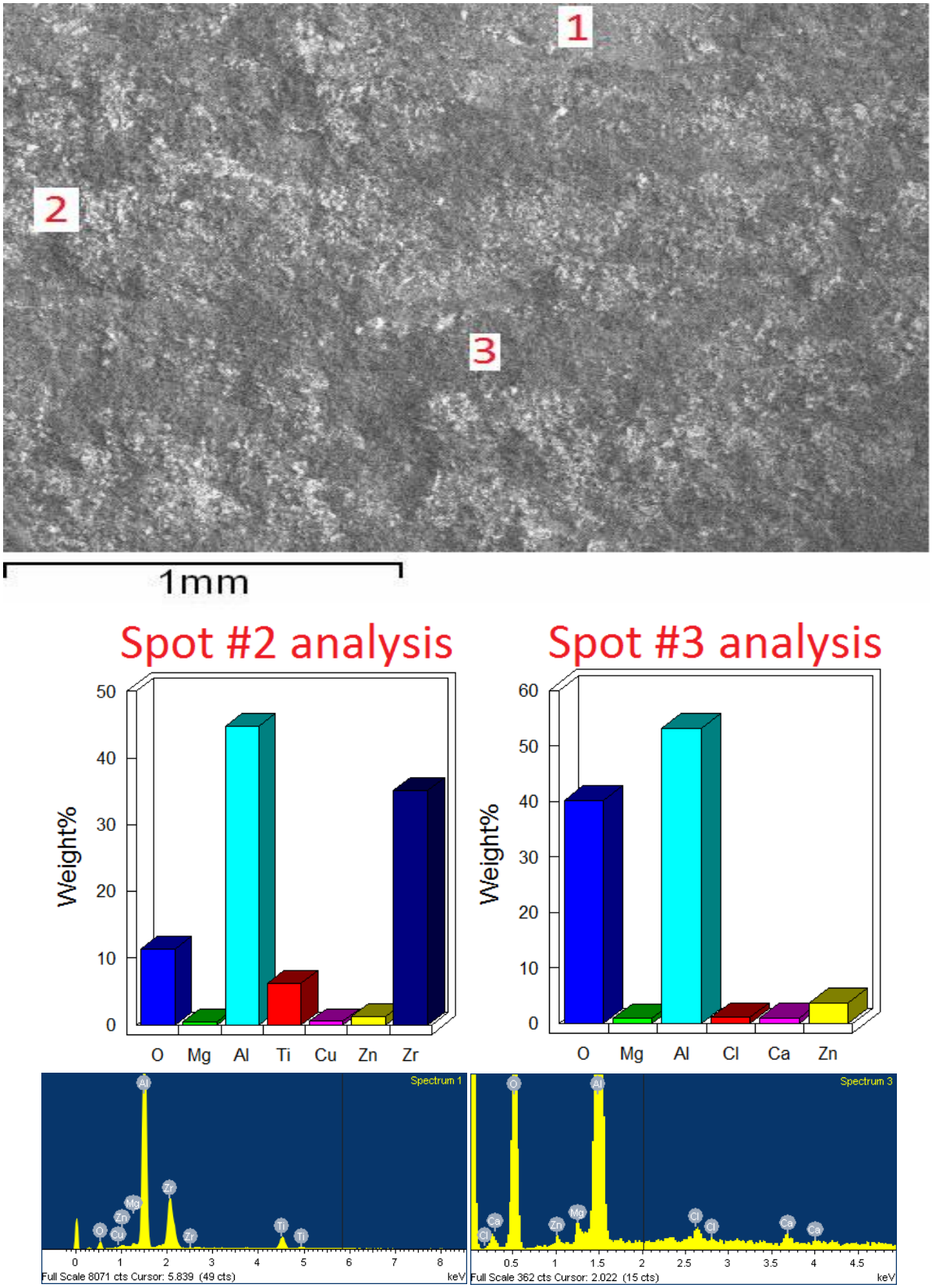

Figure 4.7 BSE image of an inclusion found in 7050 alloy plate. Spot labelled; 1) Al matrix / fracture surface 2) part of the inclusion that is composed primarily of the light phase 3) part of the inclusion that is composed primarily of the dark phase.

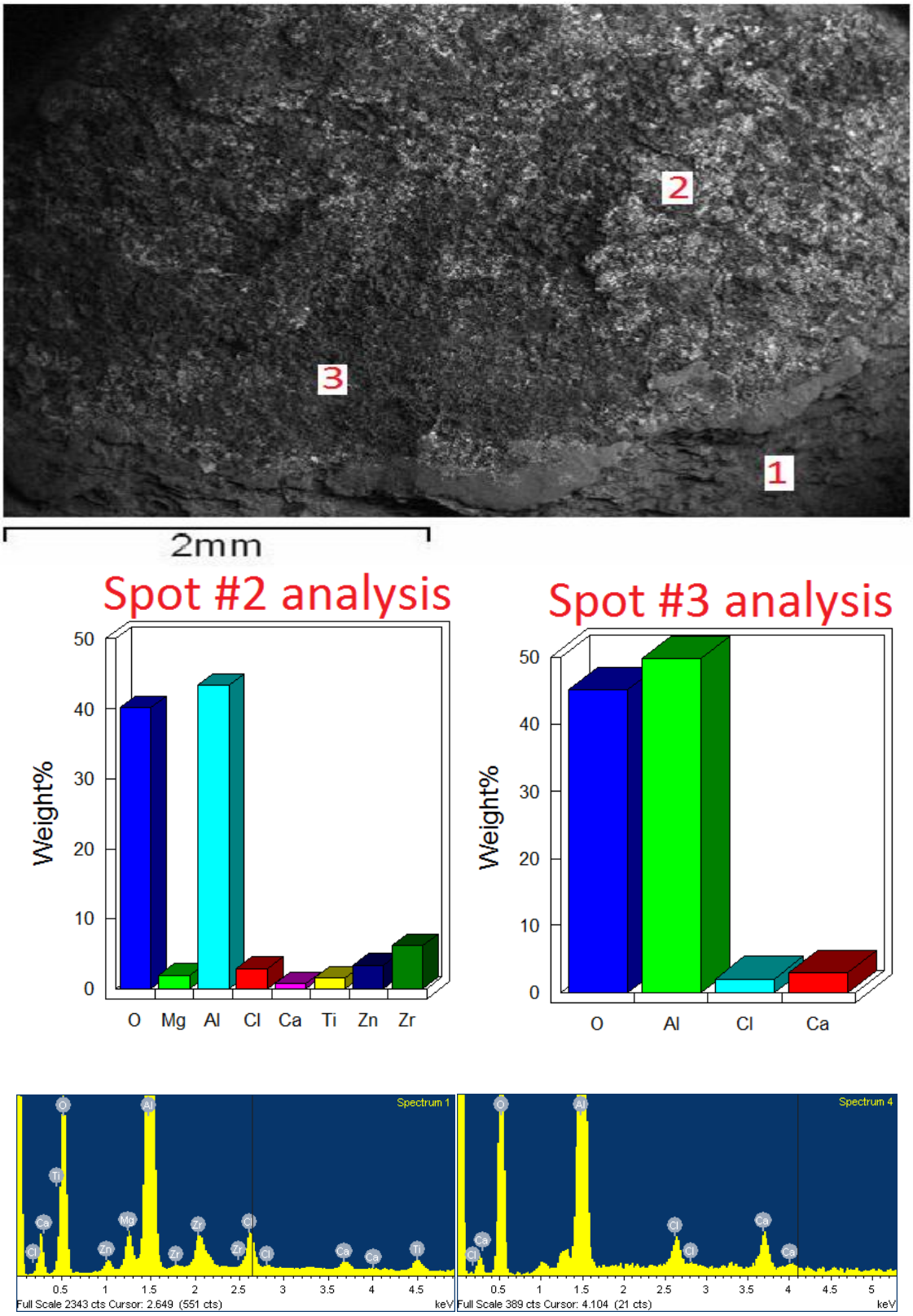

Figure 4.8 BSE image of an inclusion found in 7050 alloy plate. Spot labelled; 1) Al matrix / fracture surface 2) part of the inclusion that is composed primarily of the light phase 3) part of the inclusion that is composed primarily of the dark phase.

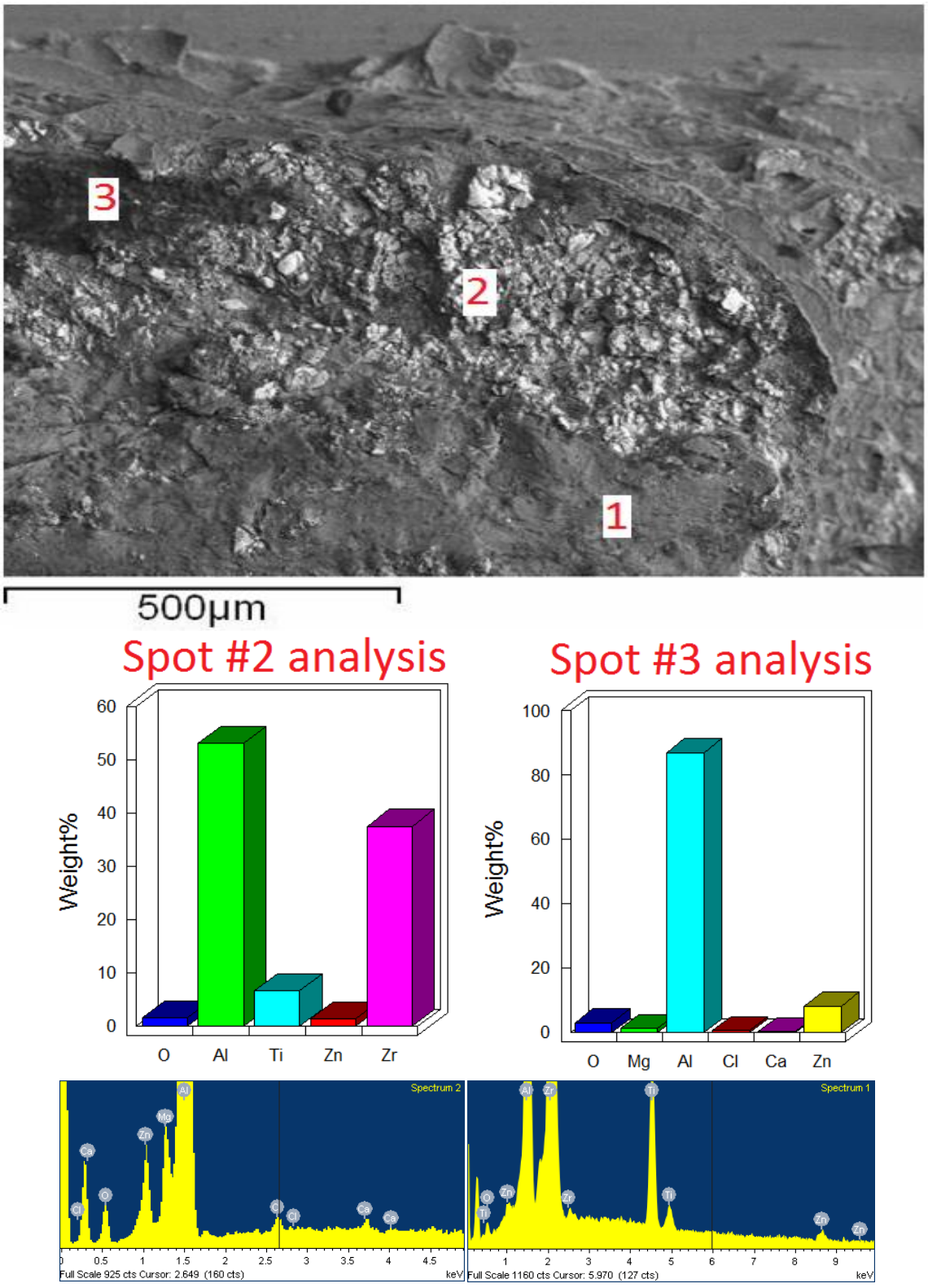

Figure 4.9 BSE image of an inclusion found in 7050 alloy plate. Spot labelled; 1) Al matrix / fracture surface 2) part of the inclusion that is composed primarily of the light phase 3) part of the inclusion that is composed primarily of the dark phase.

4.1.1 The dark phase

The dark phase was observed to possess a topography that resembled dried and cracked mud; at greater magnification nodular protrusions were also evident (shown in Figures 4.10 and 4.11). The composition suggests that the phase was made of metal oxides (primarily Al_2O_3 with traces of MgO and CaO) and metal chlorides, $MgCl_2$ and $CaCl_2$.

This phase was found to be composed primarily of Al and O, with as much as 60 wt% of the phase being made up of O. Mg and Ca were present, and the oxides formed with Ca and Mg are more stable than with Al so these compounds are likely also present. Cl was most likely present in the form of metal - chlorides (solid salts). $CaCl_2$ is the most stable Cl containing compound and found exclusively with Al_2O_3 in Figure 4.8. $MgCl_2$ reacts with Cl to form $CaCl_2$ (see section 2.5) and it is proposed that this phase is typically composed of Al_2O_3 and Ca and $MgCl_2$.

Traces of Zn, ranging from ~2 – 10 wt.% were also found, but given the composition of the alloy (6.0 – 6.4 wt.% Zn) it is difficult to establish if these contribute towards the salt portion of the composition of the inclusion or if they are only present due to the interaction volume of the electron beam interacting with the alloy beneath the inclusion.

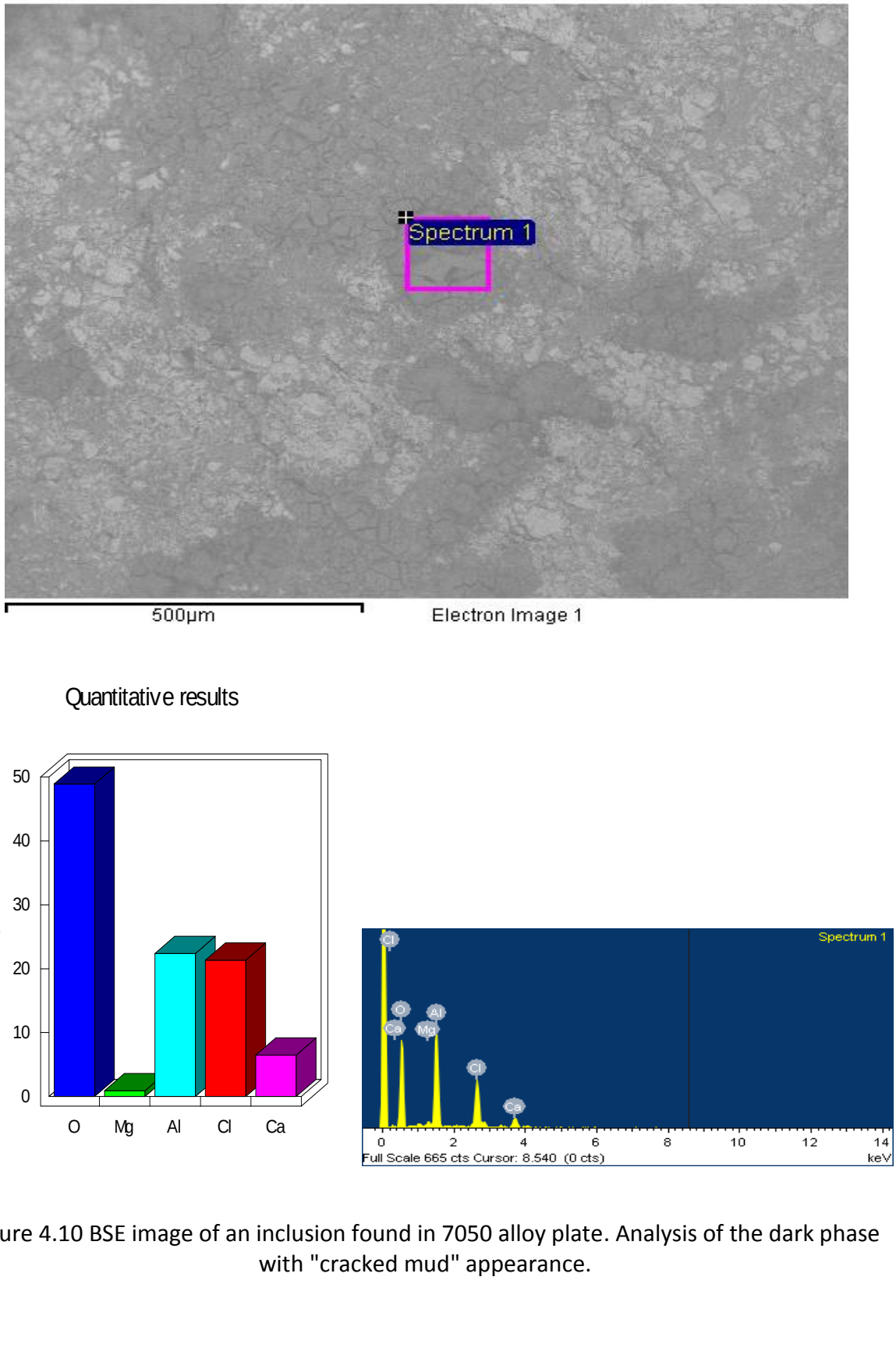

Figure 4.10 BSE image of an inclusion found in 7050 alloy plate. Analysis of the dark phase with "cracked mud" appearance.

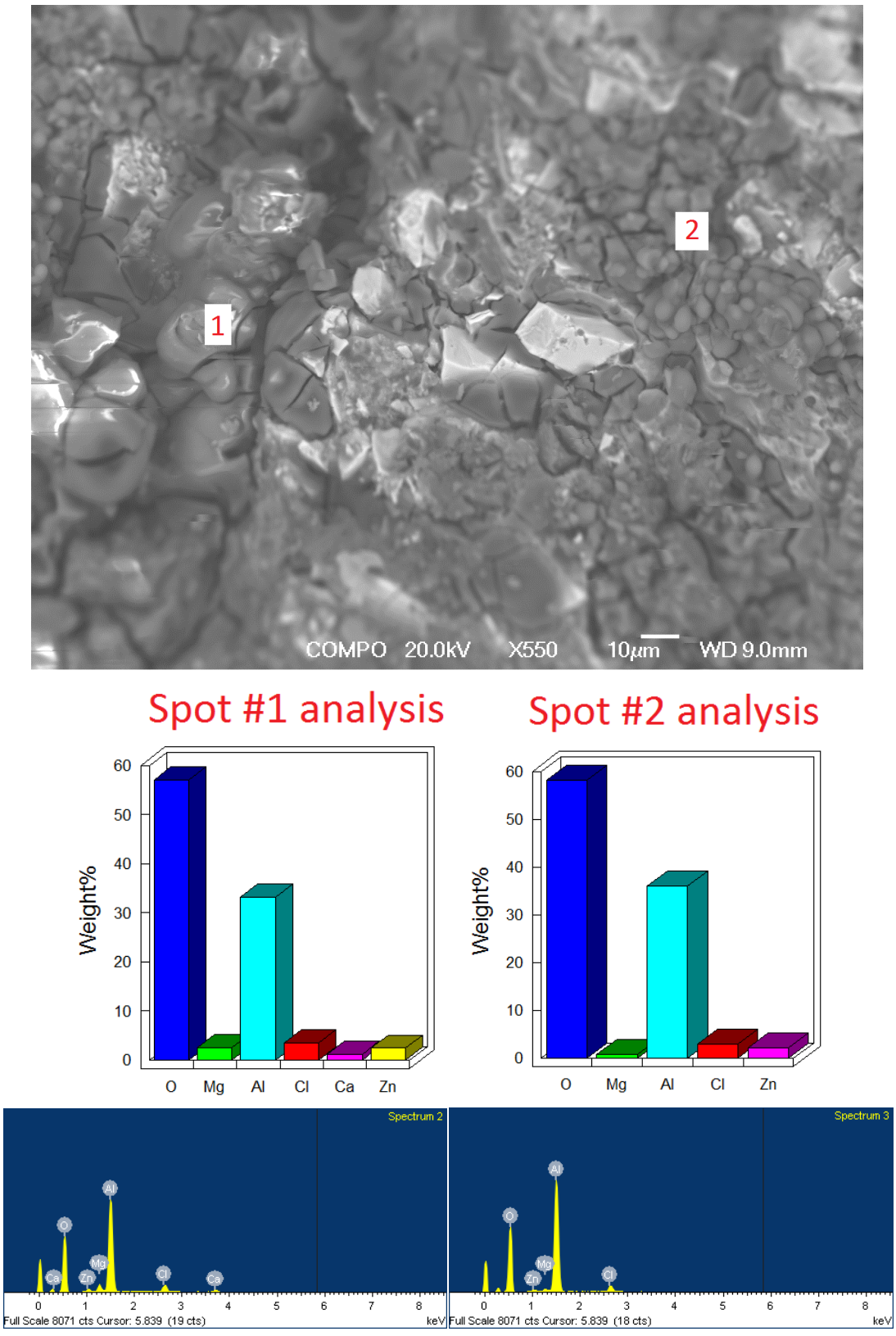

Figure 4.11 SE image and compositional analysis of the 'dark phase' was found to be made up primarily of Al_2O_3 and salts.

4.1.2 The light phase

The lighter phase (indicating that it was composed of elements heavier than the matrix) was found to be composed of $Zr(Ti)Al_{3,}$ a mixture of $ZrAl_3$ and $TiAl_3$ intermetallics which were found to exist as crystals deposited in clusters both across and within the dark phase, as shown in Figure 4.12. Each crystal was typically less than 100 μm in size, (an example of which is shown in Figure 4.13) but were observed to be agglomerated.

It was not clear from the SEM images if there was any repetitive / consistent layering of these two phases from sample to sample. It was not possible to conclude that (for example) the $Zr(Ti)Al_3$ was always deposited on top of the oxide layer.

In summary, the inclusions found in 7050 AE alloy plate were found to be composed of Zr and Ti aluminide intermetallics, oxides of Al, Mg and Ca and salts of Mg and Ca.

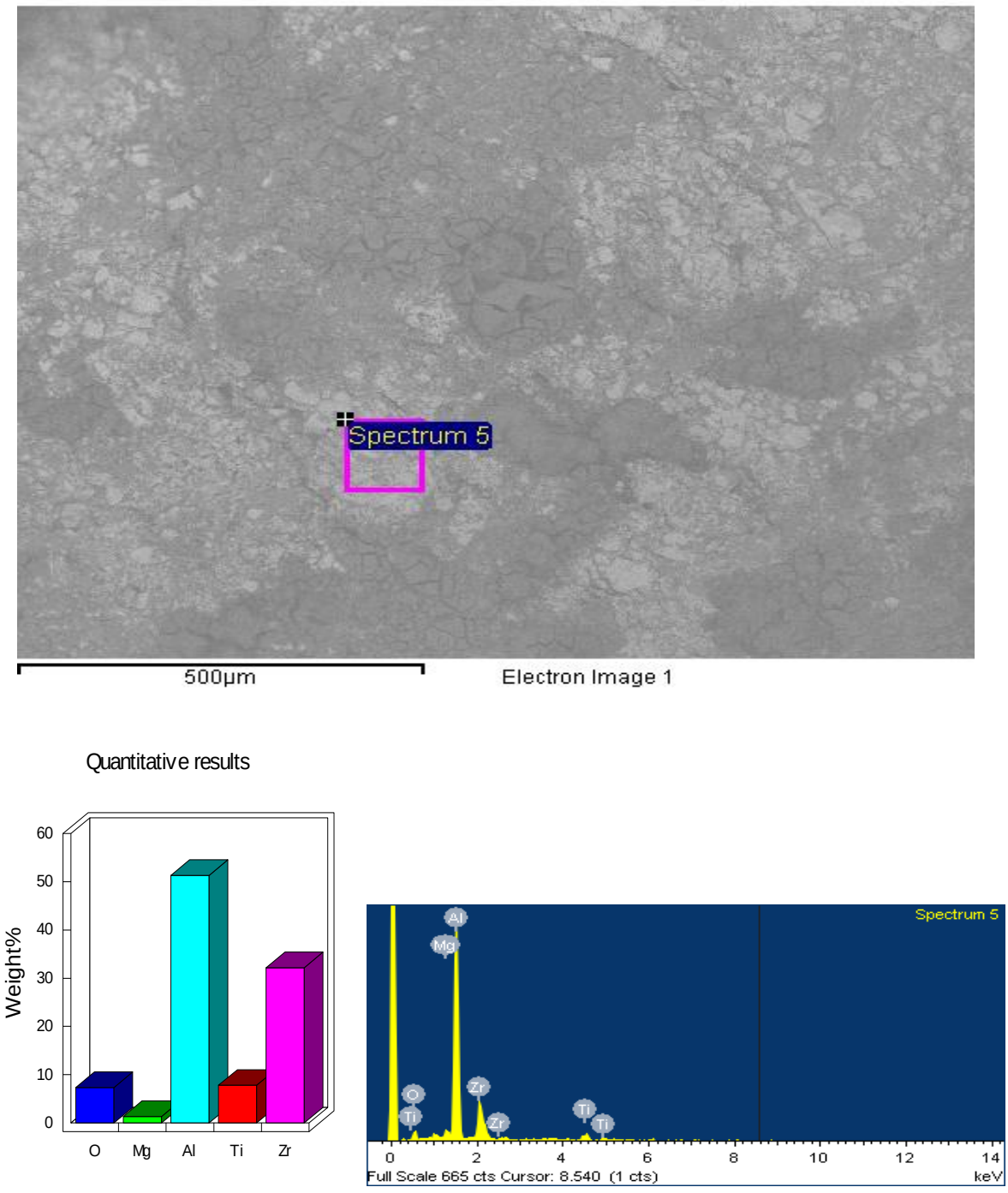

Figure 4.12 BSE image of an inclusion found in 7050 alloy plate. The light phase is composed primarily of Zr and Ti intermetallics.

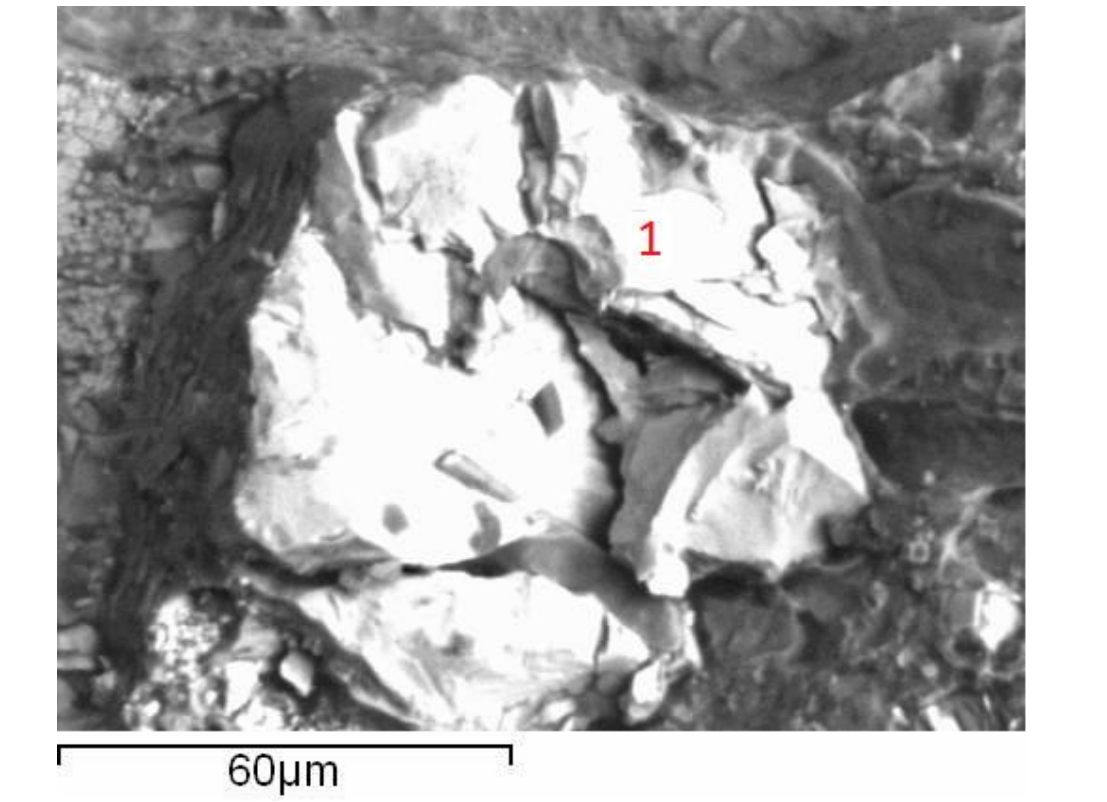

Figure 4.13 BSE image of an inclusion found in 7050 alloy plate. An Al-Zr-Ti aluminide intermetallic found at the surface of the inclusion.

4.2 Near surface indications at the edges of thin gauge (<45mm) 7475 alloy plate

The ultrasonic C-scan for a plate containing indications along the edges of the plate is shown in Figure 4.14. The comments made by the operator are recorded upon it and suggest that the ultrasonic response was interpreted as caused by porosity, and that the defective area was closer to the surfaces of the plate than the centre. The operators comment in each of these scans all reveal that the signal response was elevated in these near surface areas. In each case they suggest that the defect being observed was sub-surface porosity. Examples of other defective 7475 plates are shown in Figures 4.15 – 4.17.

The ultrasonic indications were concentrated in the first and final quarter of the thickness (a sketch for clarification is shown in Figure 4.18). The signal in these surface regions ranged from 18 – 30% full screen height (FSH), compared to the centre of the plate that displayed a signal that was low, < 10% FSH. Acceptable quality material from the centre of the plate also displayed a signal with < 10% FSH. The increased signal response led the operators to issue recommendations that the areas with elevated noise were cut off and scrapped, reducing the yield of useful material that could be obtained from each plate.

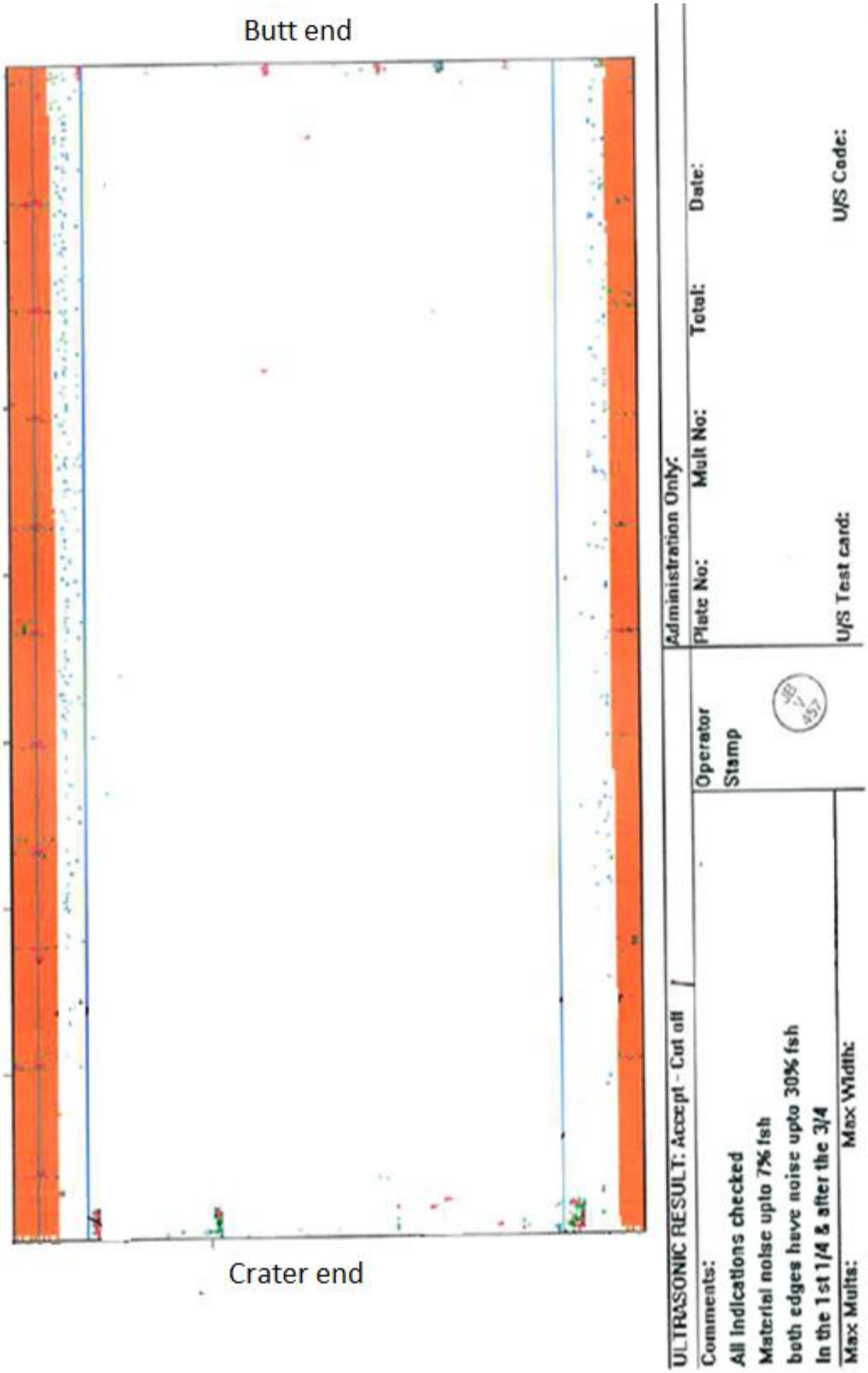

Figure 4.14 Plan view ultrasonic C-scan of a 7475 alloy plate (length 7046 mm, width 3192 mm, thickness 38 mm) exhibiting high edge noise defect (example one).

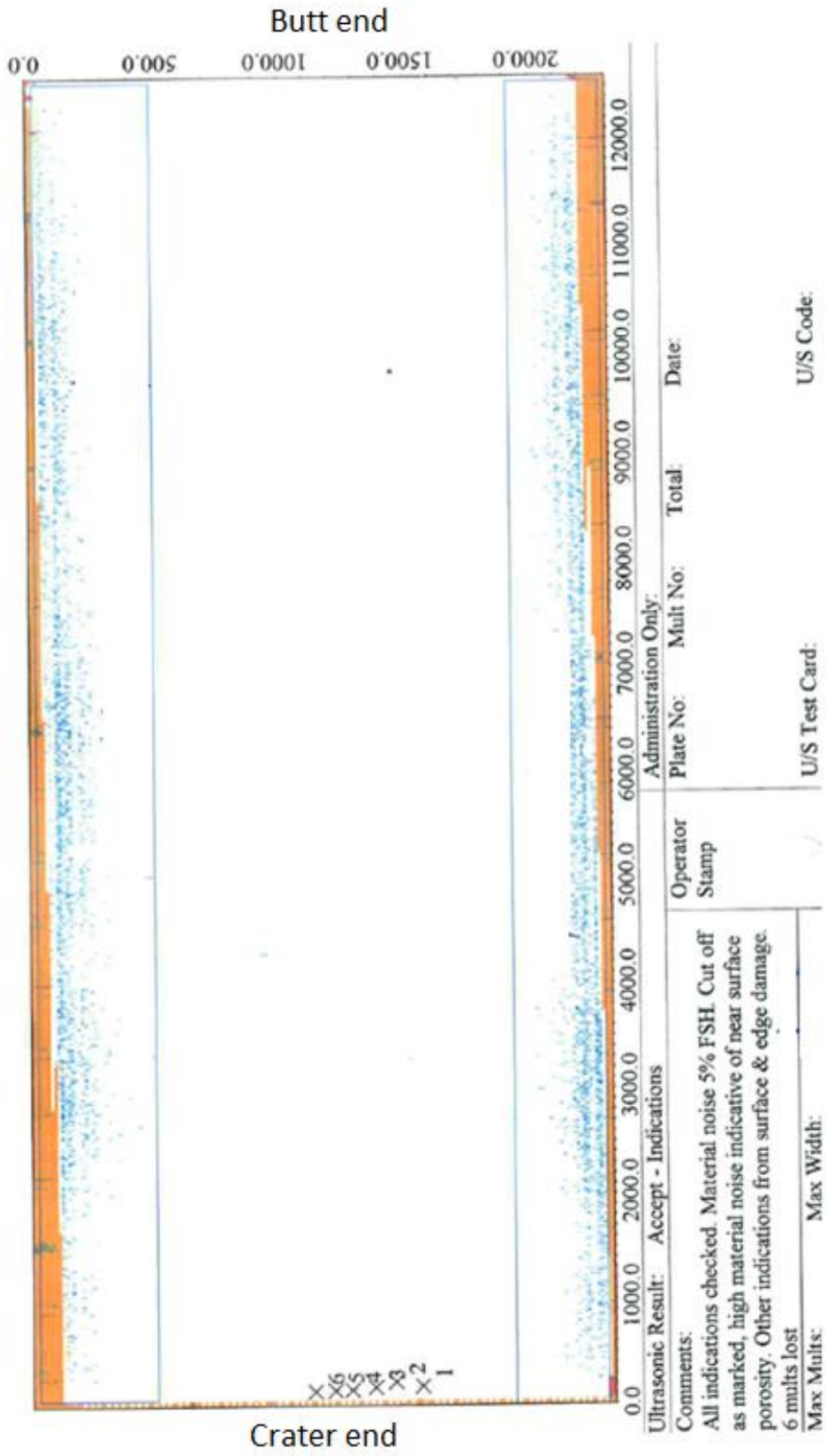

Figure 4.15 Plan view ultrasonic C-scan of a 7475 alloy plate (length 12598 mm, width 2325 mm, thickness 32.7 mm) exhibiting high edge noise defect (example two).

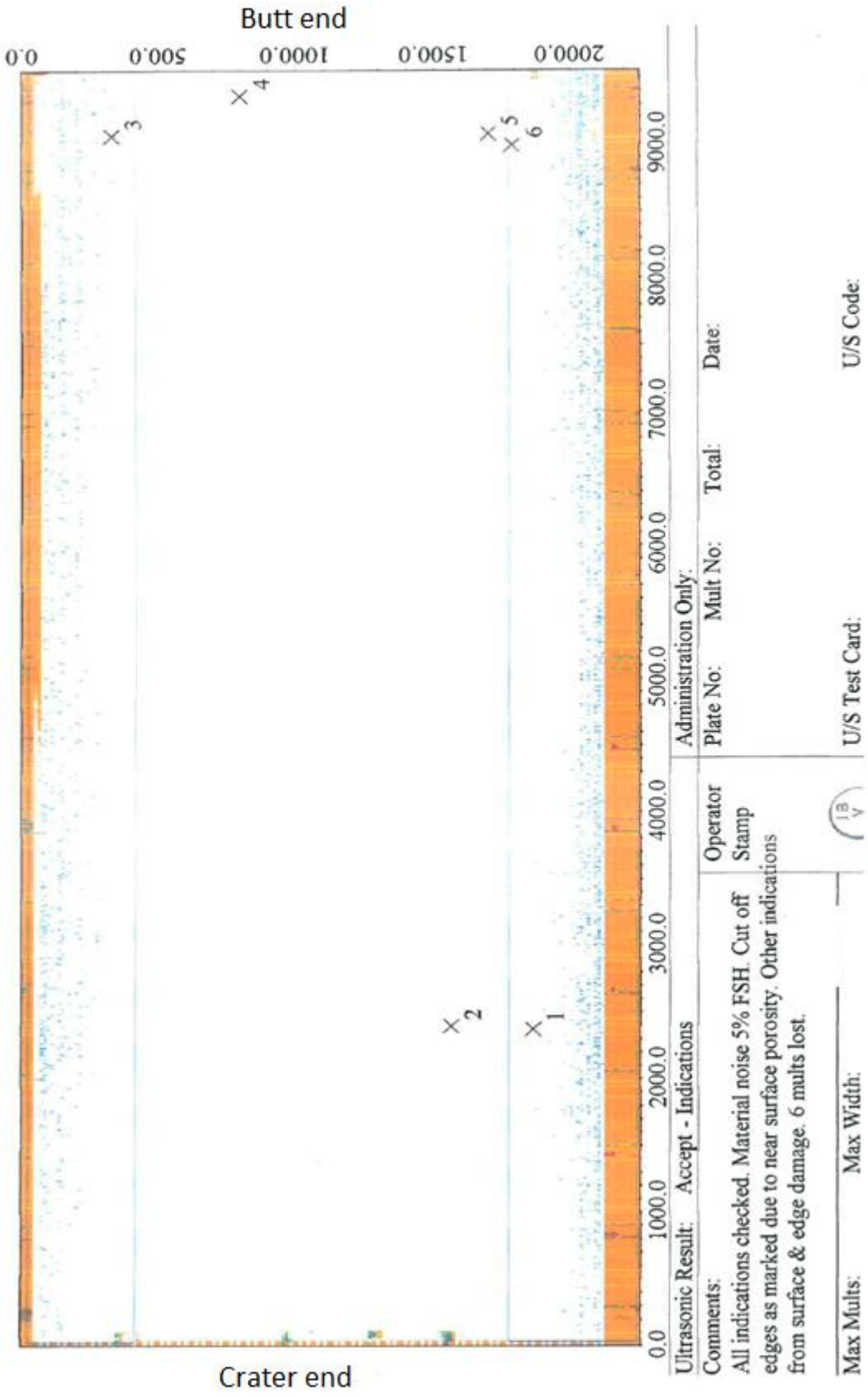

Figure 4.16 Plan view ultrasonic C-scan of a 7475 alloy plate (length 9558, width 2268, thickness 42.4 mm) exhibiting high edge noise defect (example three).

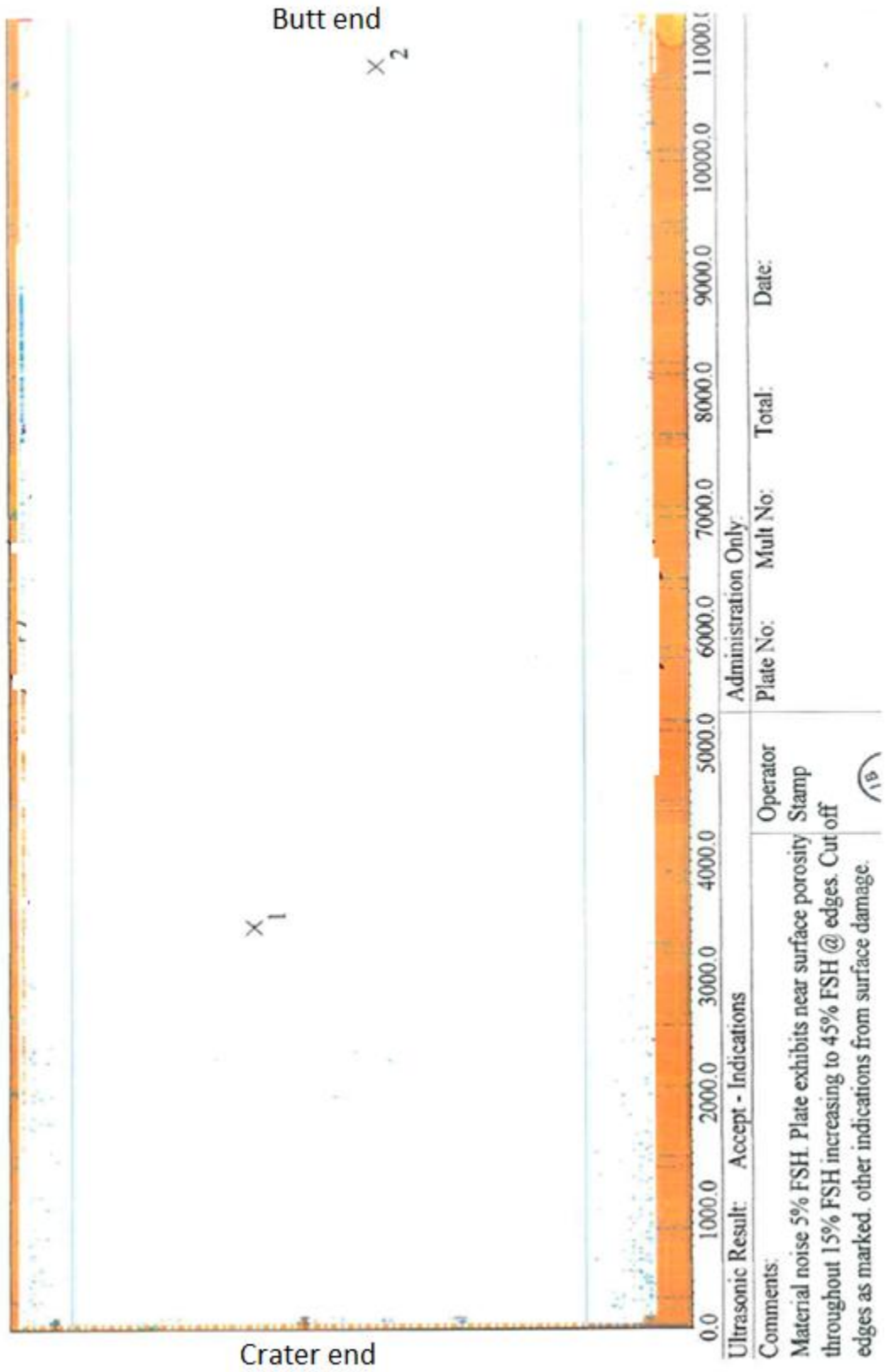

Figure 4.17 Plan view ultrasonic C-scan of a 7475 alloy plate (length 11432, width 2520, thickness 44.9 mm) exhibiting high edge noise defect (example four).

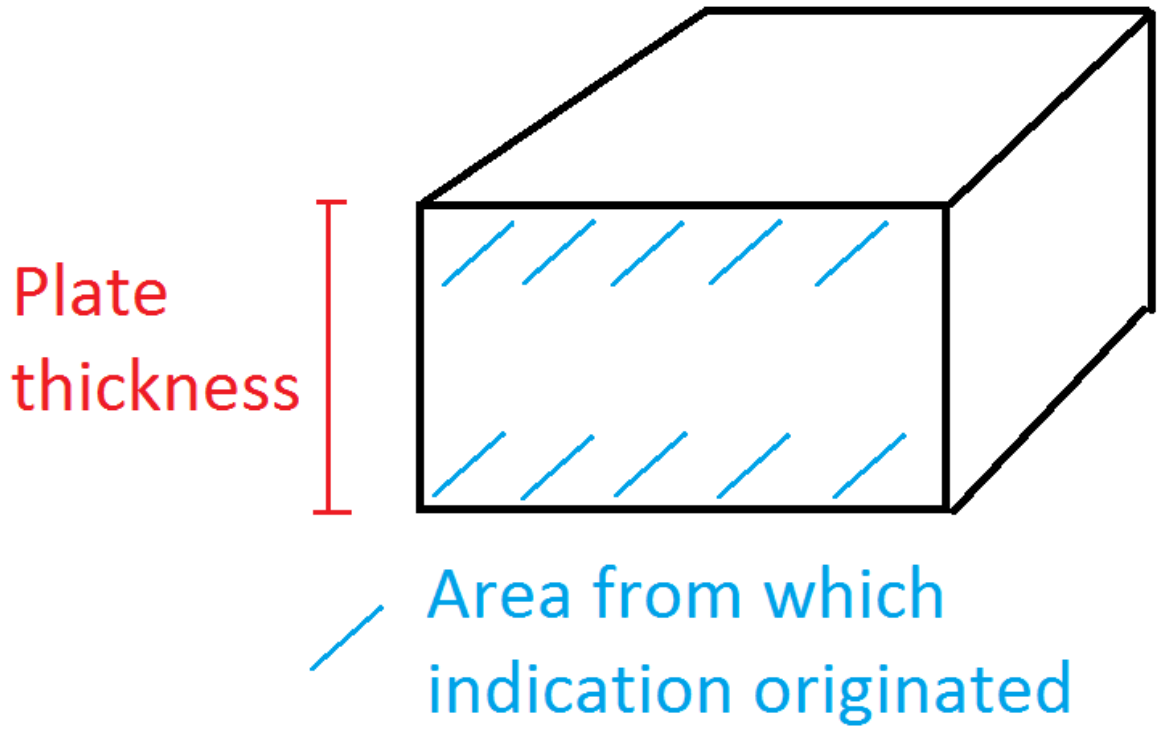

4.18 A sketch of the location of the ultrasonic response

4.2.1 Assessment of the porosity in 7475 plate:

Pore size measurements were made on the plate samples using the DPI technique outlined in section 3.2.3. The pores retain the dye (through capillary action) and highlight the pores in these areas under the UV light. The size and number of pores can be measured against a scale. The results were compared to the size and distribution pore evaluation as described in the Alcoa work instruction and summarised here:

- Maximum pore size (diameter):
    - Small <0.381mm (<0.015 inches)
    - Average 0.381mm to 0.635mm (0.015 – 0.025 inches)
    - Large >0.635mm (>0.025 inches)
- Typical pore size distribution:
    - 0-20 pores per (25.4 mm)^2 (inch^2) is deemed acceptable quality.

The evaluated sections were observed to contain a maximum pore size of 0.127mm, with 3 - 4 pores per (25.4mm)^2. The size and distribution of pores were well within acceptable levels. The maximum pore size was found to be in the 'small, less than 0.381mm' band, and the distribution was well within the typical 0 – 20mm^2 range. Figure 4.19(a) shows the porosity assessment of the plate rolled surface under ultraviolet light (the scale used to evaluate the porosity is placed on top of the plate) and Figure 4.19(b) shows the short transverse direction. Both were observed to contain negligible levels of porosity. To contrast this, Figure 4.20 shows an example of extensive centre band porosity (found in a series of 2xxx alloy plates). These particular plates contained porosity ranging from about 40 – 80 pores per (25.4 mm)^2, with a typical pore size of about 0.318 mm. It was concluded that porosity

was not the cause of the near surface ultrasonic response in the 7475 alloy plate, and that there was another cause for the indications observed in the ultrasonic scan.

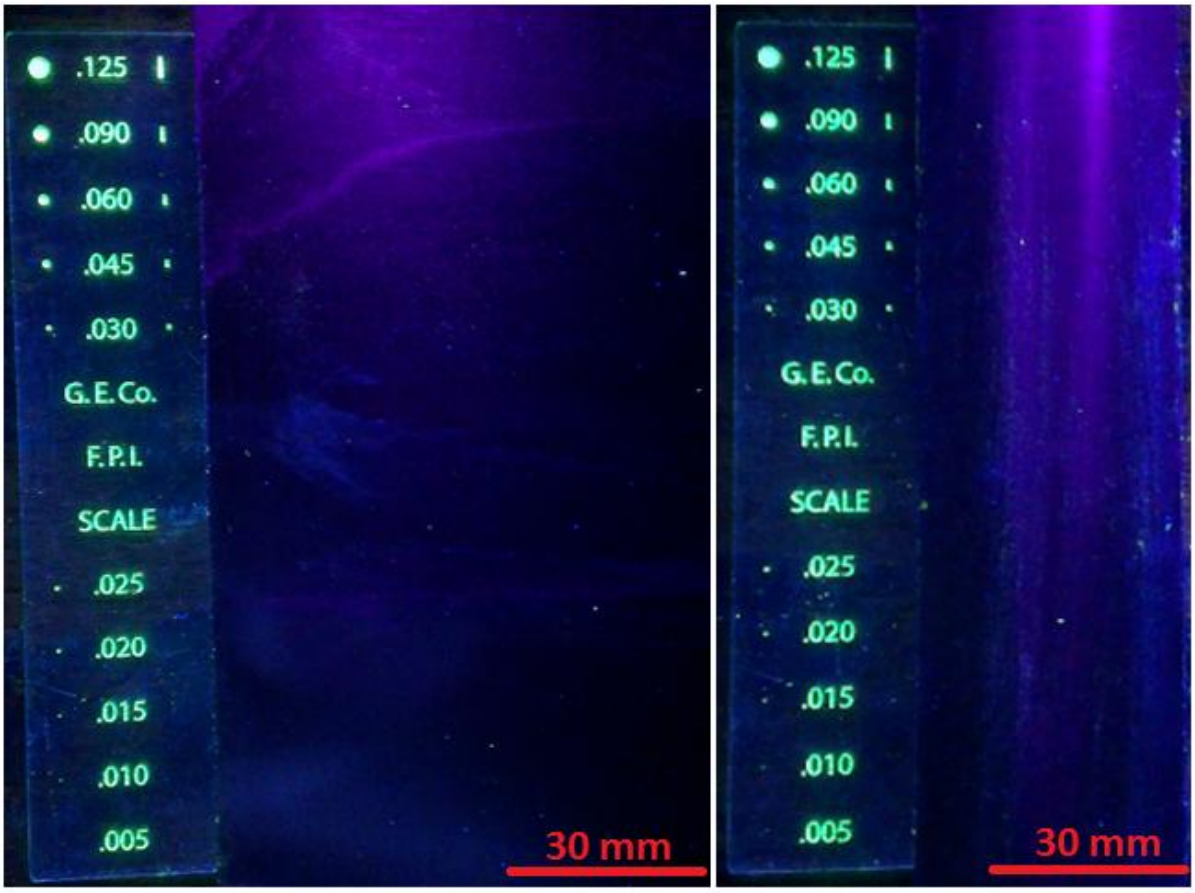

Figure 4.19 The DPI examination that highlights the size and number of pores revealed that porosity levels in the "high noise" 7475 plate were insignificant. a) Rolled surface and b) short transverse direction.

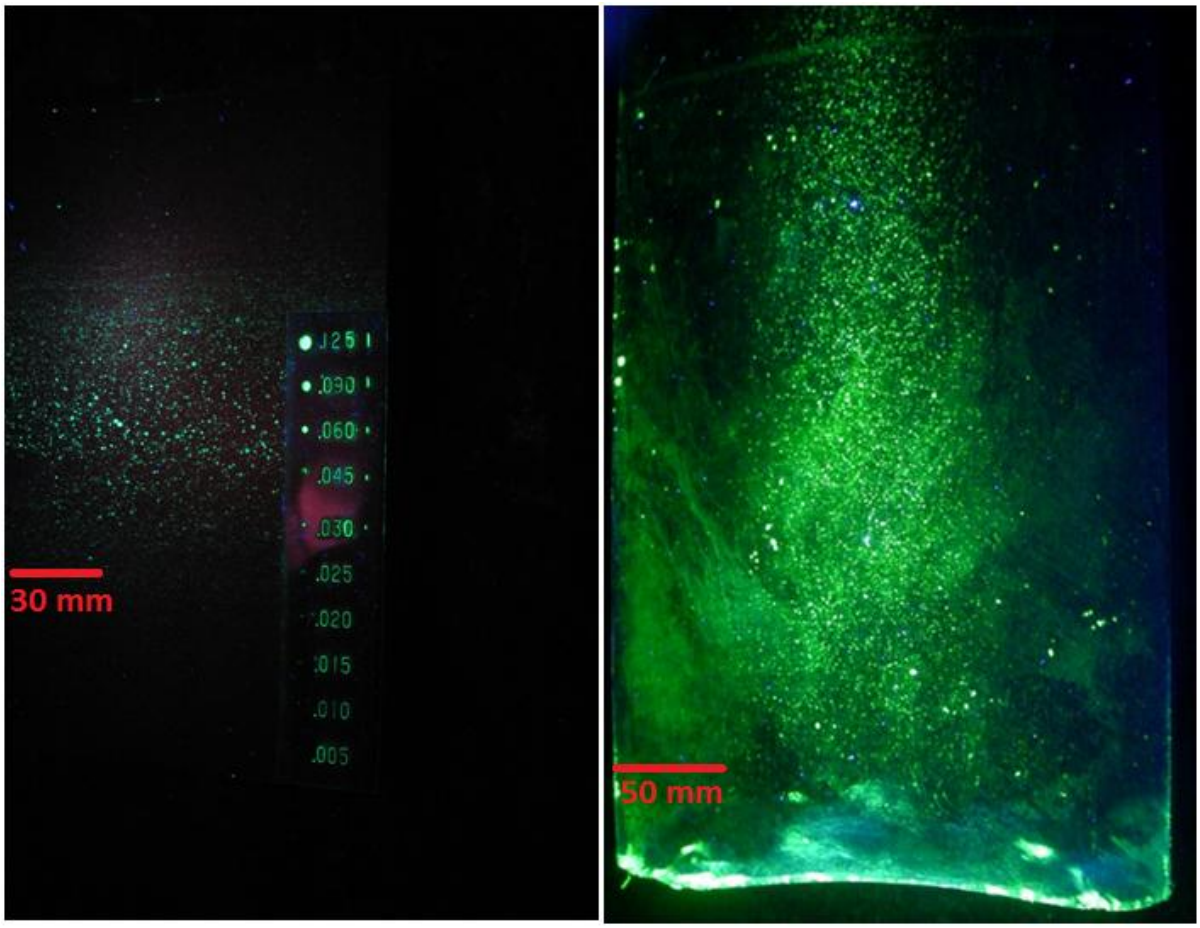

Figure 4.20 Examples of severe centre band porosity found in 2xxx alloy plates, highlighted using the DPI technique.

4.2.2 Grain structure:

The grain size of the material is known to cause indications across areas in ultrasonic scans [154]. A fine grain structure does not impede ultrasound, but a large grain structure does, as large grains cause attenuation of the signal as the sound propagates through the material [154]. If the grains are fine and the wavelength long then the wave will pass through the material without any scatter. As the grain size becomes greater then scatter will become significant, causing attenuation. This starts to manifest itself when grain size becomes greater than a tenth to a hundredth of a wavelength in size.

The grain size of the near surface areas that contained an elevated signal (approximately the first and last 10 mm of the thickness of the sample) was compared to the centre of the plate that had a 'normal' ultrasonic signal (as in the sketch shown in 4.18).

The grains were found to be of a typical morphology; elongated in the direction of rolling and thinner in the short – transverse direction, (see Figures 3.6), however the grain size in the rolling direction in the near surface regions was found to be significantly larger when compared to the centre of the plate, by about an order of magnitude. The near surface grain size in low ultrasonic response 7475 alloy plate was of approximate length of 150 – 250 µm (from left to right in Figure 4.21) compared to about 1,500 – 2,000 µm (from left to right in Figure 4.22) in the high ultrasonic response plate. (Note that the circular 'bubbles' observable in these images are water droplets that have seeped out of the Bakelite-metal interface that have been compressed by the graticule, and are not part of the microstructure). The ultrasonic wave passes through the width of the grains, (i.e. from top to bottom in Figures 4.21 and 4.22). The grains in this direction are estimated to be approximately 1 - 20 µm in the low ultrasonic response 7475 (see Figure 4.21), and 50 - 300 µm in the high ultrasonic response 7475. The wavelength of the ultrasound is estimated to be approximately 1.26 mm at 5 MHz, which would explain why the signal is attenuated in the coarse grain regions of the 7475 plate (see section 2.7.1).

BSE SEM analysis of the surface of the coarse grain sample confirmed that Fe based intermetallics (Al_7Cu_2Fe) were present, and these were in the region of 2 - 50 µm in length, shown in Figure 4.23.

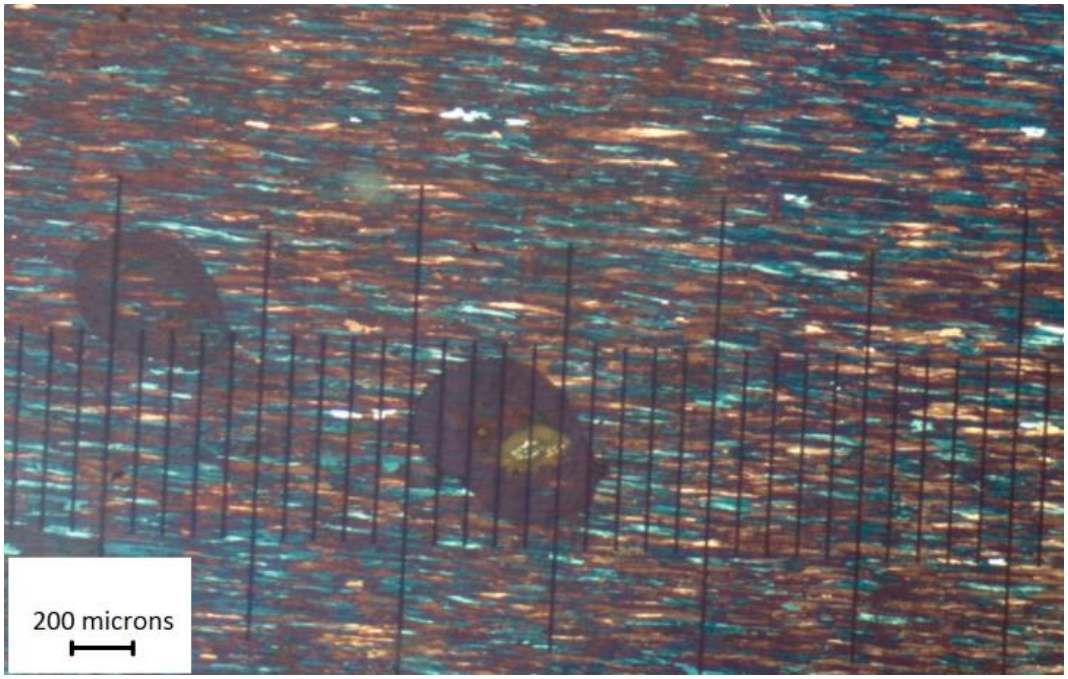

Figure 4.21 The near surface grain size of an anodised 7475 alloy plate from 'defect free' material. Grains were observed to be typically 150 - 250 µm in length.

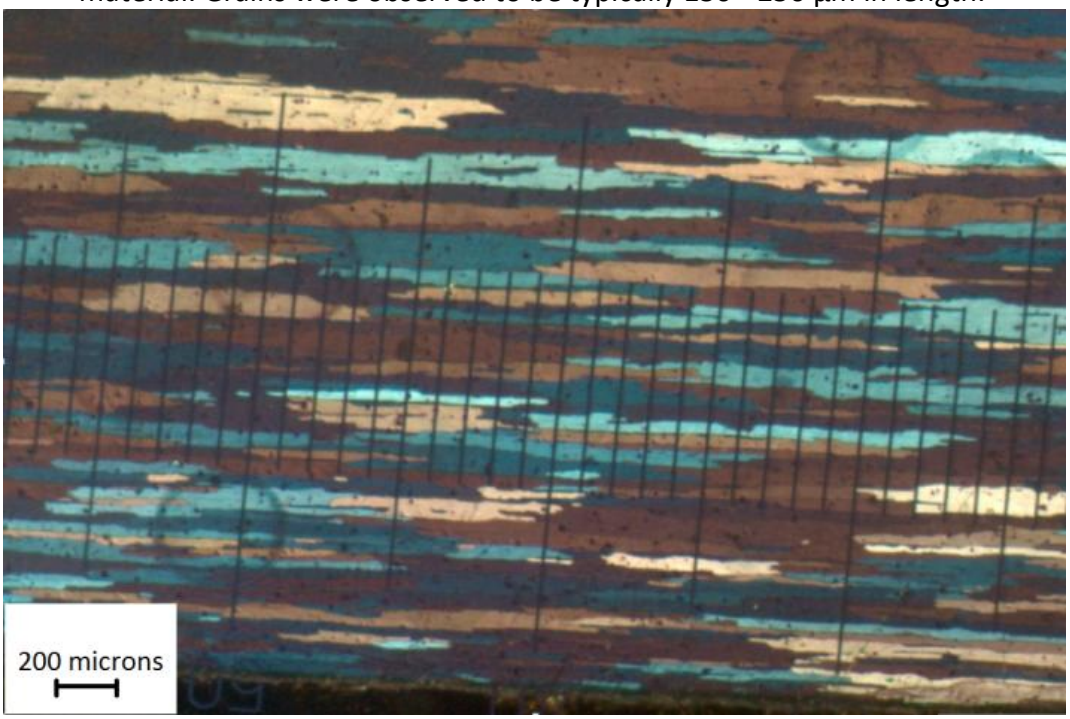

Figure 4.22 The near surface grain size of an anodised 7475 alloy plate from the edge of plate 1016502. Grains were observed to be typically 1000 - 2500 µm in length.

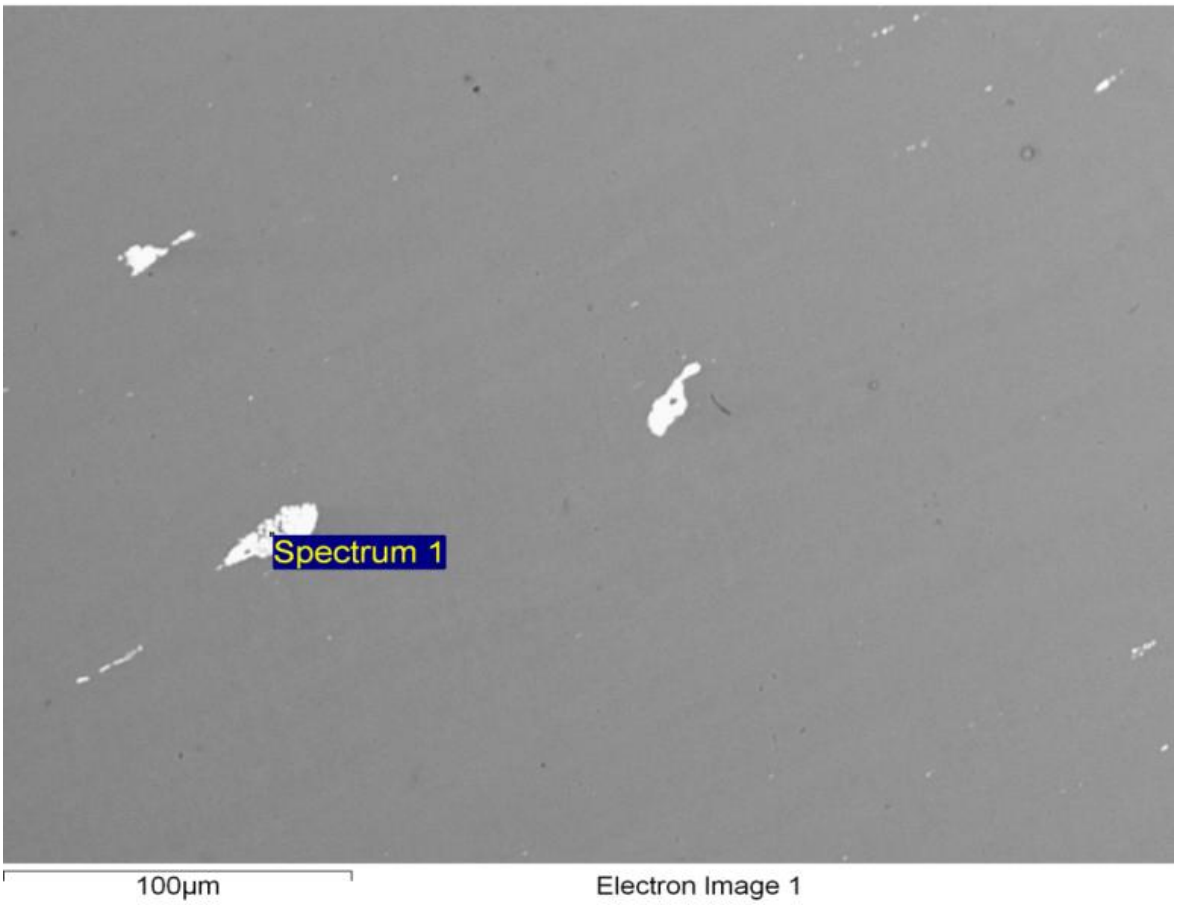

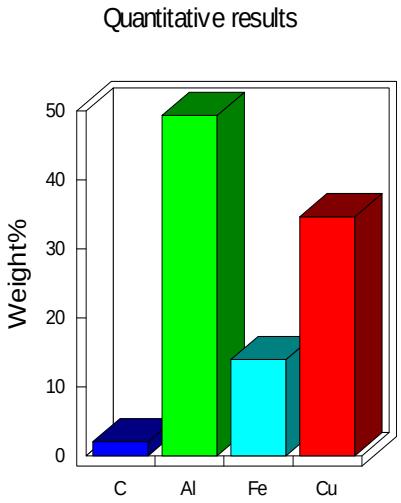

Figure 4.23 BSE image of Al_7Cu_2Fe particles identified in 7475 alloy exhibiting coarse grain microstructure.

4.2.3 Aetiology of coarse grain structure in 7475 alloy plate:

Relationships between the chemistry and processing (in particular rolling profiles) were obtained from Alcoa internal production databases, focusing on thin gauge 7475 plate which had been rolled to <45 mm in thickness, in particular,

A) Chemical analysis; and the presence of Fe, Si and Cr within these plates (note Zr is not added into this particular alloy).
B) Processing parameters; namely starting ingot size and the degree of rolling.

Figures 4.24 and 4.25 show comparisons of the chemistries of 7475 plates that exhibited high noise at the edges of plates against those that did not. The graphs compare distribution curves of combined Fe and Si contents (Figure 4.24) and Cr levels (Figure 4.25) for all of the plates produced during this period (2009). Within this survey 5.7% of the plates were found to have possessed this specific 'high surface noise' edge defect. The differences between the data sets were checked for statistical significance using a Student's t-test.

The majority of plates (94.3%) contained no edge defects. The mean combined Fe and Si content for these plates was 0.081 wt%. 5.7% of these plates contained edge defects, and although they contained a slightly higher combined Fe and Si content of 0.084 wt% (as shown in Figure 4.24), the values were not found to be significantly different using a Student's t-test, where P was calculated to be 0.18.

Figure 4.25 shows the Cr content of the same plates. Plates that had no edge defects contained a mean value of 0.196 wt% Cr while plates that did contain edge defects contained a mean value of 0.193 wt% Cr. The data sets were shown to be significantly

different using a t-test where $p = 0.03$, revealing a trend for plates with reported edge defects to have lower Cr content.

Figure 4.26 shows a simple frequency chart of the amount of plates produced from the three ingot thicknesses, 325, 440 and 525 mm. The plates that contained no defects are represented in blue and the plates that contained edge defects are additionally added in red on top of the same column. More thin gauge plate products were produced from 325 mm ingots (48% of total) than both the 440 mm (27%) and 525 mm (25%) ingots, and no plates that were produced from this smallest cross section exhibited this edge defect. 5.7% of the plates were defective; 1.3% of the defective plates were produced from 440 mm ingot and 4.4% were produced from 525 mm ingots. There was a clear trend that increasing ingot thickness increased the occurrence of the reported defect.

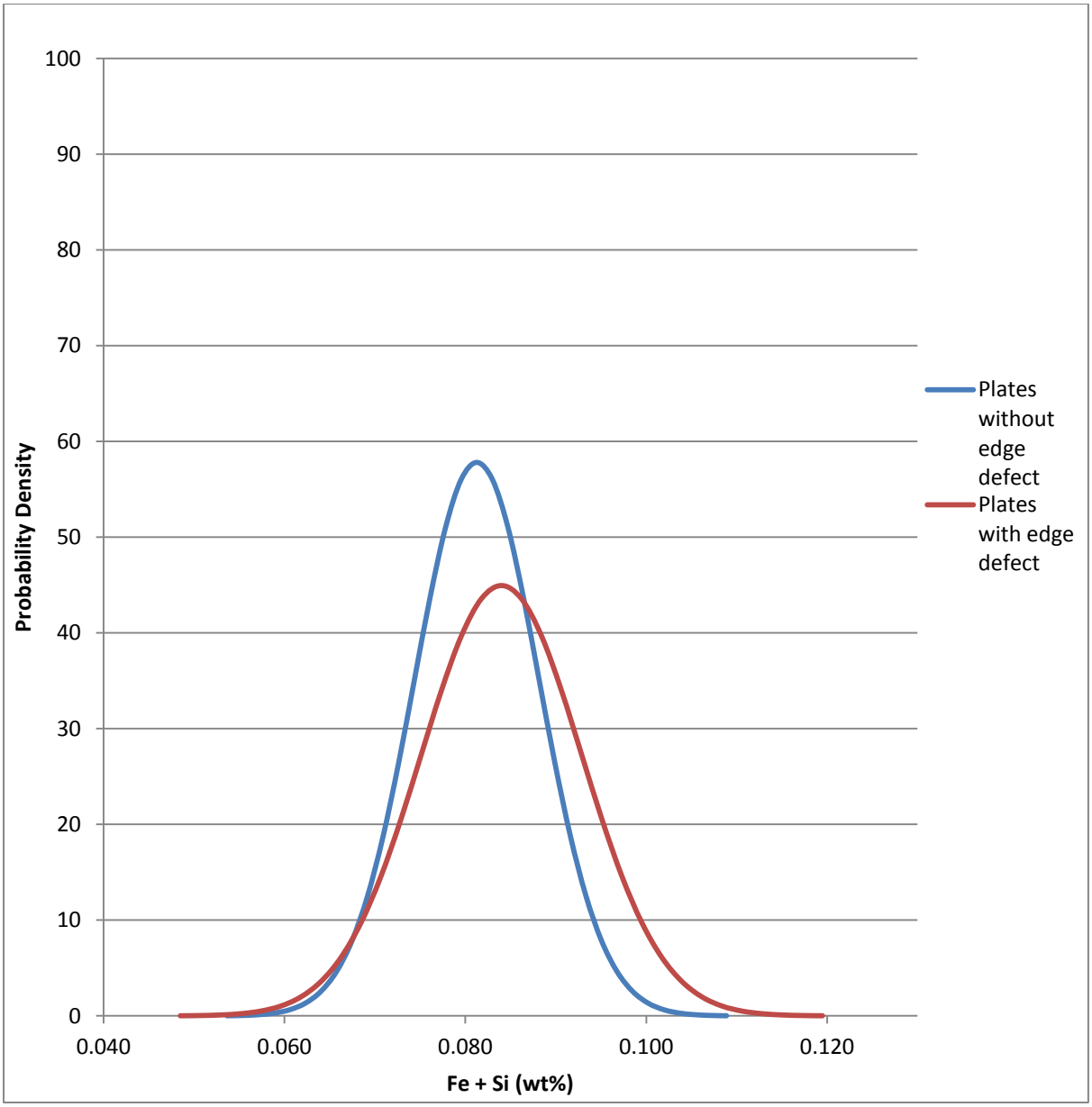

Description	Mean	Standard deviation	t-test (p)
Plates without edge defects	0.081	0.007	0.18
Plates with edge defects	0.084	0.009	

Figure 4.24 the average combined Fe and Si contents in 7475 alloy plates rolled to <45 mm thickness. There is a slight but not statistically different correlation between increasing combined Fe and Si content and edge defects.

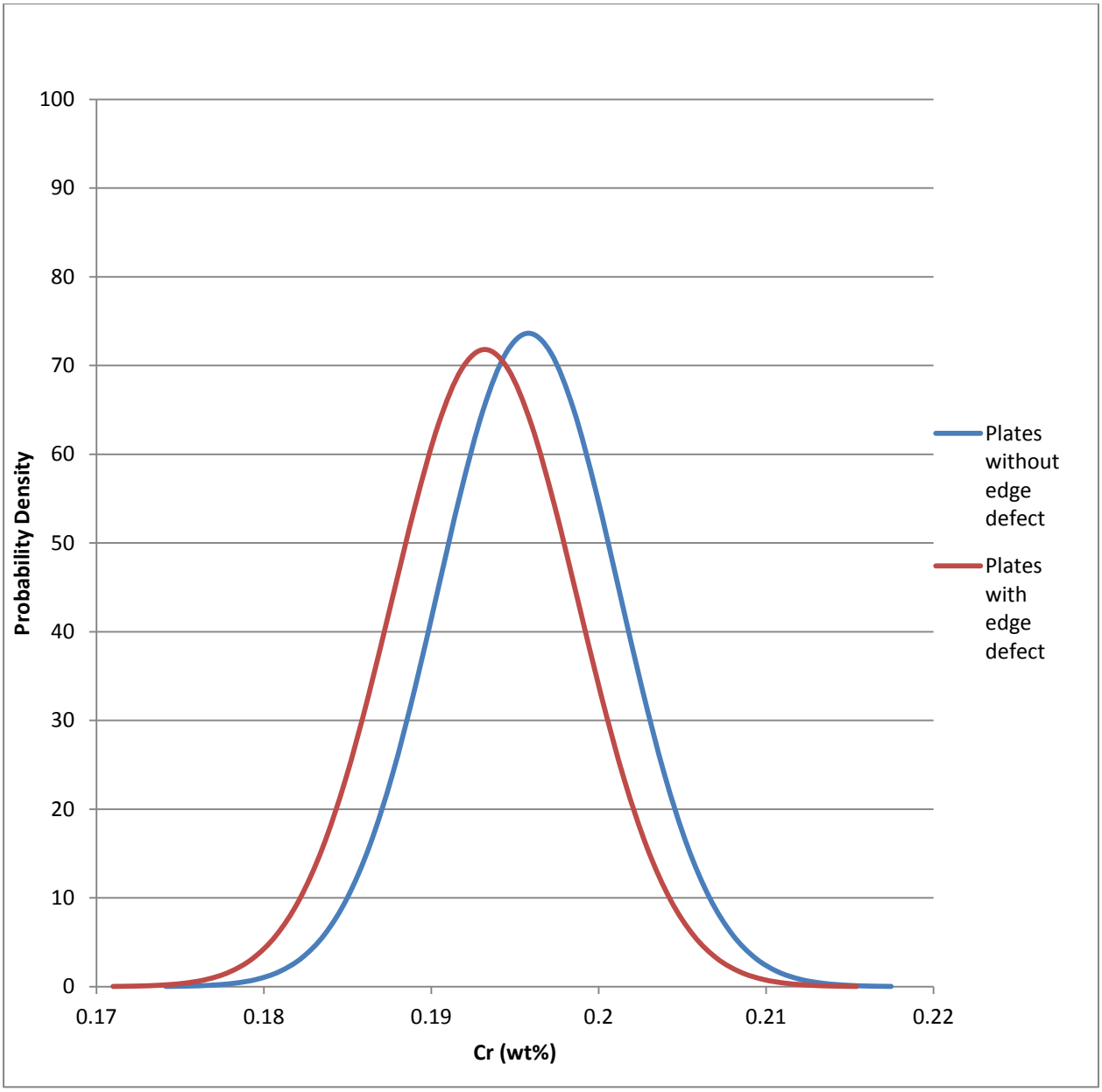

Description	Mean	Standard deviation	t-test (p)
Plates without edge defects	0.196	0.006	0.03
Plates with edge defects	0.193	0.006	

Figure 4.25 The average Cr content in 7475 alloy plates rolled to <45 mm thickness. There is a positive correlation between the presence of edge defects and plates that were lower in Cr content.

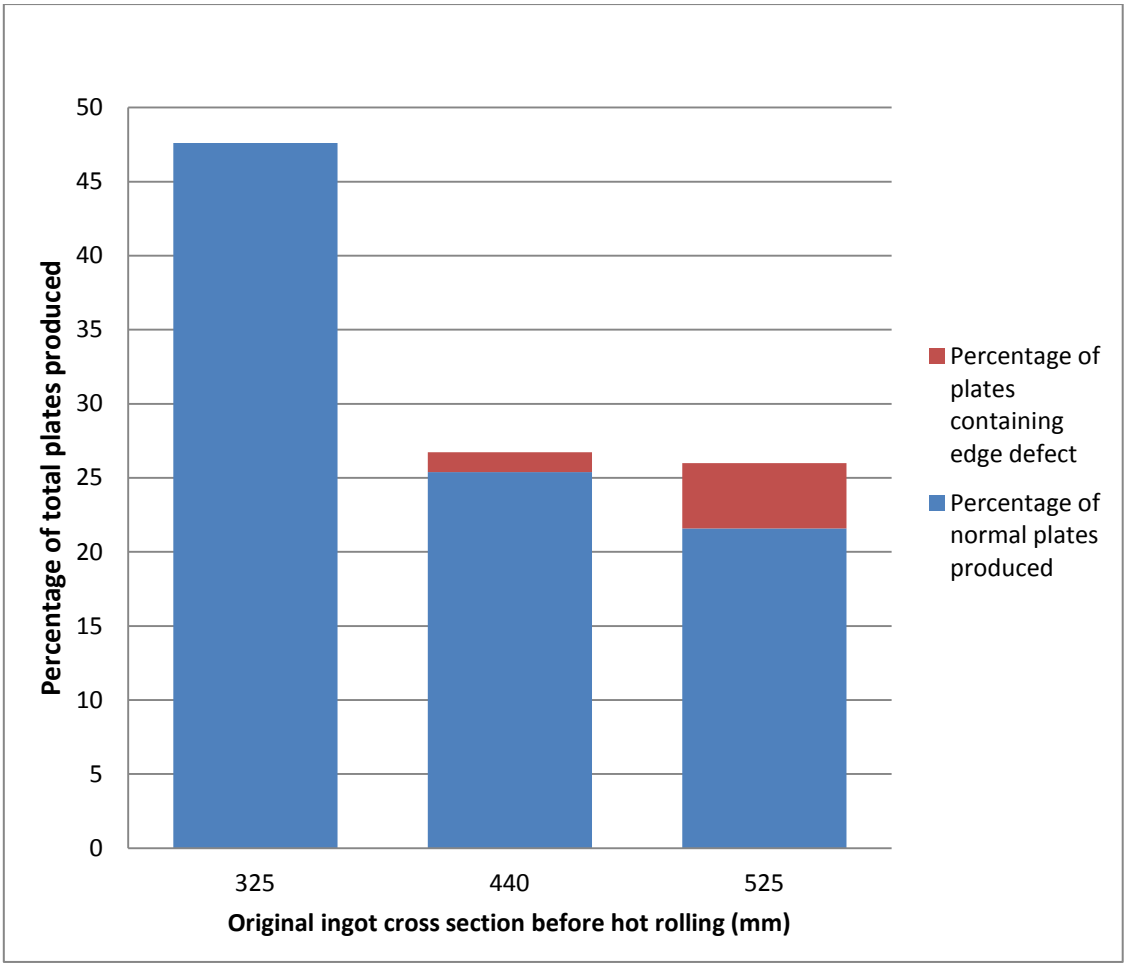

Figure 4.26 The percentage of edge defects increases directly with increasing ingot size. No defective plates were sourced from 325 mm ingots. Defective plates originated from 440 mm ingots (1.3% of total production) and 525 mm ingots (4.4% of total production).

Each plate was produced first by direct chill casting of an ingot of a certain size which was then rolled down into the desired gauge plate. Ingots that were larger required more rolling passes, i.e., received more strain, to reduce the cross-section to the same gauge when compared to thinner ingots. As an ingot is rolled it becomes steadily longer but also wider. Larger ingots will also have increased levels of widening compared to thinner ingots when they are rolled to the same gauge.

Plates that were produced from 440 and 525 mm thick ingots were found to have a significant variation in the amount of widening that occurred during rolling as shown in Figure 4.27. Plates that contained edge defects were far more likely to of come from ingots that received excessive widening during rolling.

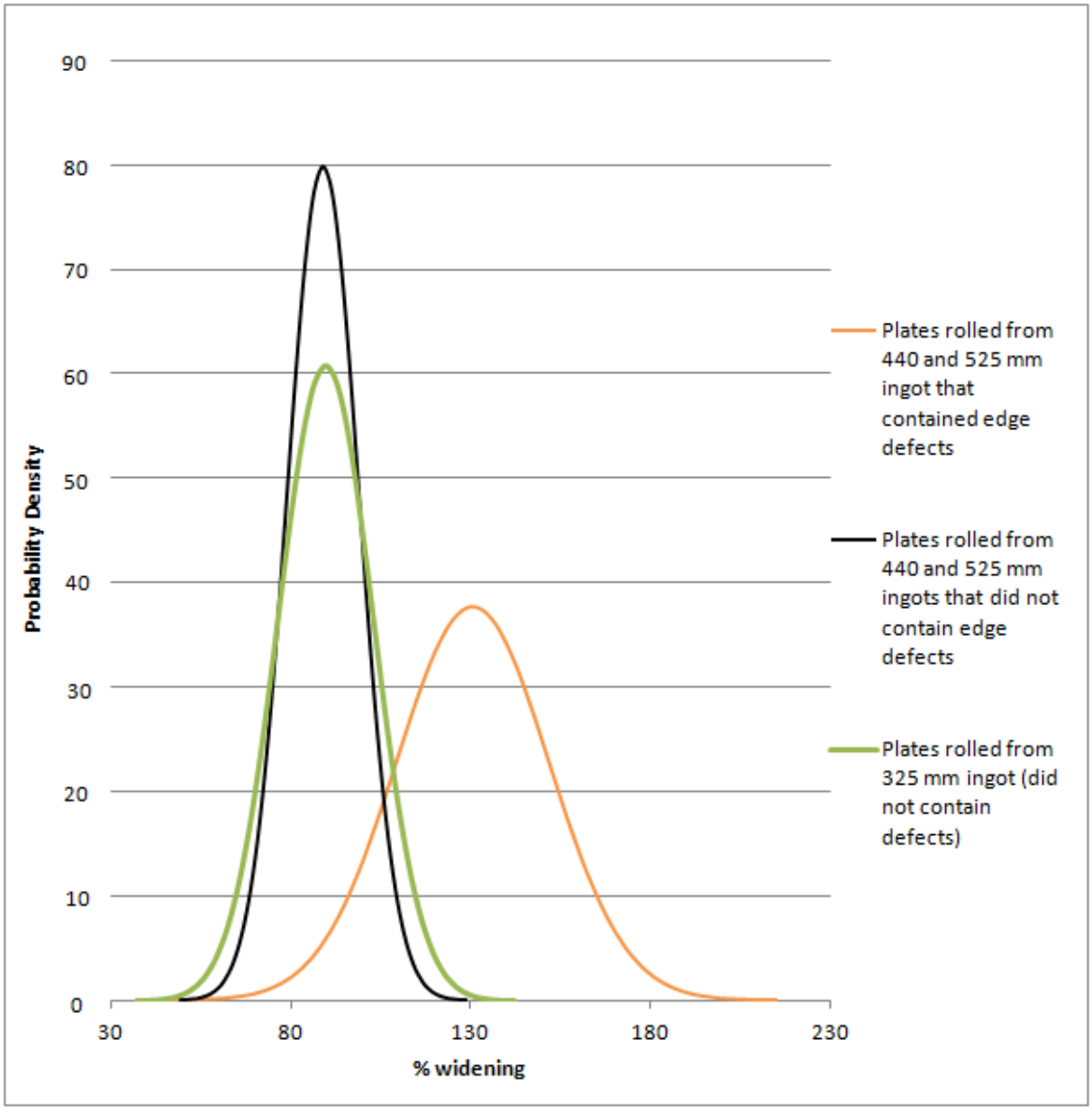

Figure 4.27 The influence of ingot widening during hot rolling on the defect occurrence.

In summary the ultrasonic “high noise” defects were found to be caused by a coarse grain structure that was localised near the surface of the plate. The defect occurred more often when larger ingots were rolled to thinner gauges and with a relatively large degree of widening. The plates that contained this type of defect were found to contain statistically lower amounts of Cr.

4.3 Bubble trapping in liquid aluminium alloys.

The interactions between Cl and the melt were investigated by trapping gaseous bubbles within molten metal. The change in gas composition was evaluated using the Pore Gas Analyser and the metal – gas interface was examined using SEM and EDX. This was done in an in an effort to increase the understanding of the effects of Cl on degassing of Al alloys.

During the experiment, bubbles typically followed the same path through the metal once injected; directly up through the central portion of the crucible. Occasionally bubbles were observed to divert from this path (left or right along the X-axis) suddenly, towards the crucible wall, before exiting the melt. As the X-ray camera only looks from one plane through the metal / crucible it was not possible to determine the bubble movement in the radial–axis (towards or away from the camera) during the experiments.

When the metal began to solidify the bubbles would become temporarily stationary near the melt surface due to presence of semi-solid metal. If the gas flow was interrupted at this point then any bubbles would eventually exit the melt, slowly decreasing in size as the gas leaked out through the melt surface. If the gas flow was allowed to continue, however, approaching bubbles would collide, agglomerate and subsequently the combined gas contents of both bubbles would be forced out of the surface of the melt.

It was only possible to capture bubbles by either a) temporarily stopping the gas flow rate and restarting it at a later point in time (typically a few minutes) as this allowed the metal surface to completely solidify to provide a physical barrier to the bubble escape or b) reducing the gas flow rate to such a low level that a bubble was held temporarily within the melt at the tip of the needle, which could then be released a few minutes later after surface

solidification had occurred, by carefully increasing the pressure. These techniques allowed the surface to completely solidify and form a barrier through which the bubbles could not escape. By repeating this technique it was often possible to emit and capture a single bubble and wait for the ingot to partially solidify, and then repeat the process. This allowed multiple bubbles to be caught within a single ingot.

4.3.1 X-ray analysis:

Figure 4.28 shows two Ar gas bubbles caught in a 2L99 Al melt using the bubbling technique. The bubbles are held within the centre of the solidified Al ingot. One bubble was relatively large, with a diameter of approximately 20 mm and was oval in shape (labelled A). The second (B) was roughly spherical and is slightly smaller, approximately 15 mm in diameter. Both bubbles in this image are surrounded by “clouds” of gas that are not of a typical bubble size or shape. It is thought that these are formed by Ar gas trapped within interdendritic regions during solidification (C). The bubble labelled A was too large to fit in the analyser, but the bubble labelled B was cut out successfully and processed.

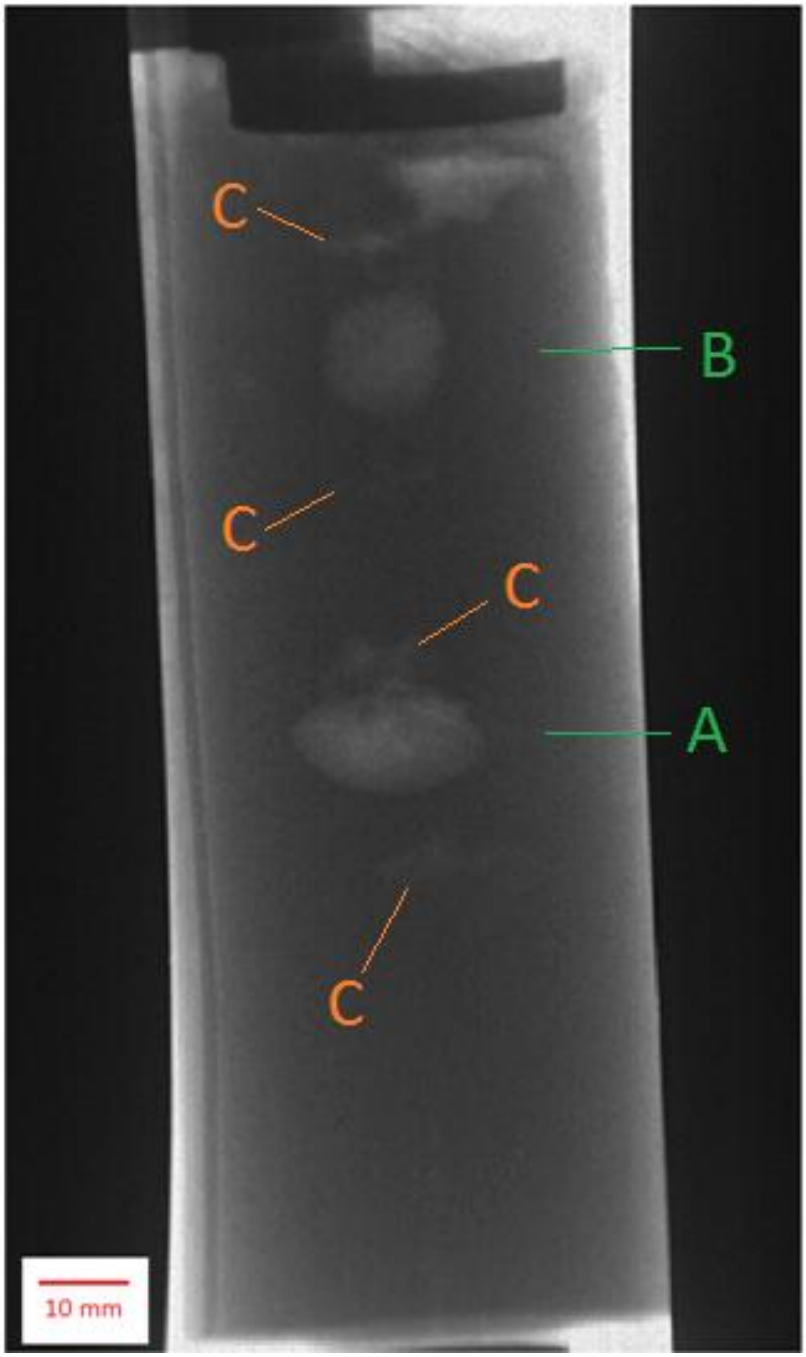

Figure 4.28 An example of Ar bubbles caught in an Al melt (A and B). Gas has forced itself into interdendritic spaces forming “clouds” around the bubbles (C).

Bubbles were cut from the solidified ingots and machined into small 20 (diameter) x 20 (height) mm cylindrical blocks as shown in Figure 4.29. The cylinders in each case were clearly porous, being pitted by numbers of pores, suggesting that the bubbles and pores

were connected to the interdendritic shrinkage. Figure 4.30 shows the cross section of a bubble caught in Al using this technique, it is clear that the pores are in contact with the bubble. In Figure 4.31 (a) a gas bubble tapped underneath solid metal is shown, below the bubble the metal was still liquid. In Figure 4.31 (b) after complete solidification a dense network of interdendritic porosity has formed throughout the casting and surrounds the bubble.

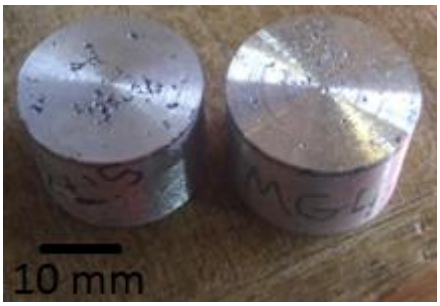

Figure 4.29 Images of a 2L99 sample from experiment #3 (left) and 5083 alloy from experiment #4 (right) samples before analysis in the pore gas analyser. Porosity is visible across the surface of both samples.

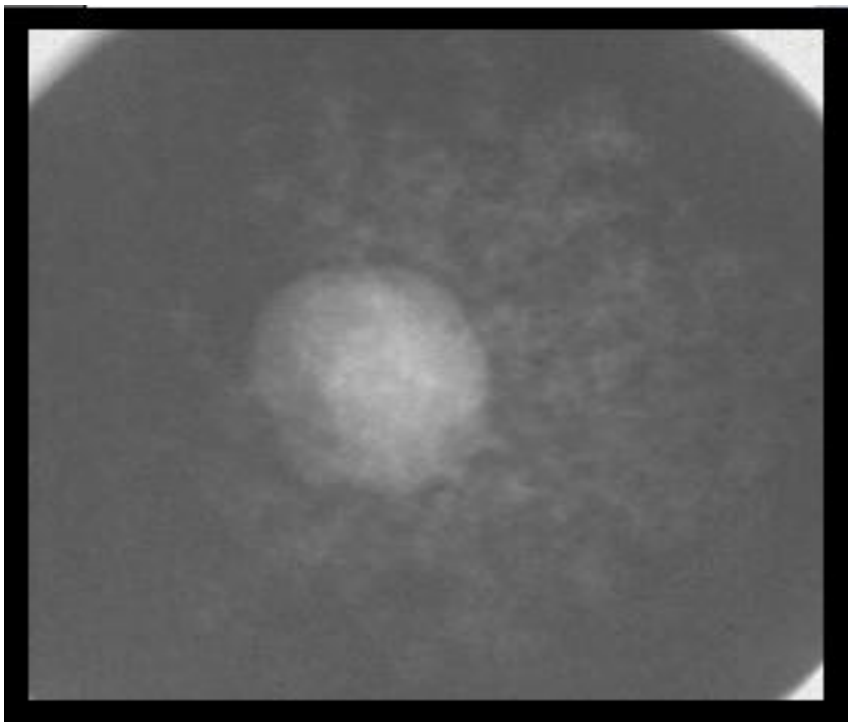

Figure 4.30 A trapped bubble surrounded by porosity (a cross section from the solid ingot).

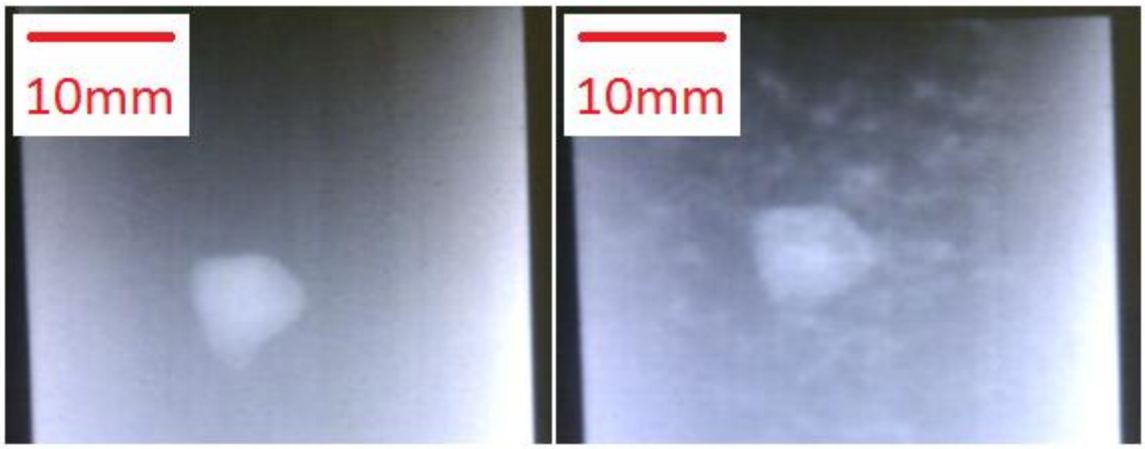

Figure 4.31 (a) An Ar gas bubble caught in 2L99 alloy just after capture (left), and (b) 12 hours later (right) after complete solidification has occurred. A network of porosity has developed in the solidified metal and surrounds the primary bubble.

This capture and cutting procedure was successfully implemented for 4 different bubbles generated using Ar gas; 3 trapped in 2L99 alloy, one in 5083 alloy (samples 1 – 4 respectively). Two bubbles were also caught using an Ar & Cl gas mixture (0.8% Cl in Ar), one in 5083 alloy (sample #5) the other in 7010 alloy (sample #6). All of these samples were individually examined using the Pore Gas Analyser. They were then sectioned and the internal bubble surface examined in the SEM. The results are summarised below in Table 4.1.

Sample number	Alloy	Gas composition	Pore gas analyzer summary	SEM / EDX summary
#1	2L99	Ar	H_2, N_2, H_2O	Al oxide coating
#2	2L99	Ar	No gas detected	Metallic interface
#3	2L99	Ar	H_2, N_2, Ar, H_2O	Al oxide coating
#4	5083	Ar	No gas detected	Metallic interface
#5	5083	Ar + Cl	No gas detected	Al and Mg oxides, traces of CaO and $CaCl_2$
#6	7010	Ar + Cl	No gas detected	Al and Mg oxides, $MgCl_2$

Table 4.1 Summary of bubble capture experiments

4.3.2 Interior of bubble samples and gas compositional analysis using SEM and the PGA:

Only two of the six bubble samples contained any detectable gases (samples #1 and #3). Both of the samples were 2L99 alloy obtained using Ar gas. The other four samples yielded no results. The gas containing specimens were found to have heavily oxidised interiors when examined in the SEM, those that didn't contain gases generally had insignificant or no oxidation.

The SEM analysis of the interior of the bubble of 2L99 alloy (samples #1 and #3), the two bubbles that were found to contain gas using the Pore Gas Analyser, is shown in Figures 4.32 – 4.37. The interior of both of these bubbles was covered with spinel. This is deduced because the Al peaks were not symmetrical, having a 'shoulder' around 1.4 keV, where Mg is present (this is because the 2L99 alloy contains 0.2 – 0.45 wt.% Mg). At increased magnification the spinel was found to be fragmented, as shown in Figures 4.33 - 4.34. The

spinel is shown to be lighter in colour, and is disrupted by the darker Si rich eutectic protrusions (see Figure 4.35). The presence of the eutectic pushing up through the spinel layer suggested that O_2 or water vapour within the gas bubble had reacted with the liquid metal. As solidification has taken place, Si rich eutectic has grown in towards the centre of the bubble, causing stress and fracture of the spinel layer. The result is a series of Si rich protrusions into the interior of the bubble, surrounded by plate – like spinel fragments. Images are secondary electron, (SE), showing the topography of the specimen, or back-scattered electron, (BSE), showing the contrast between phases (composed of heavier or lighter elements).

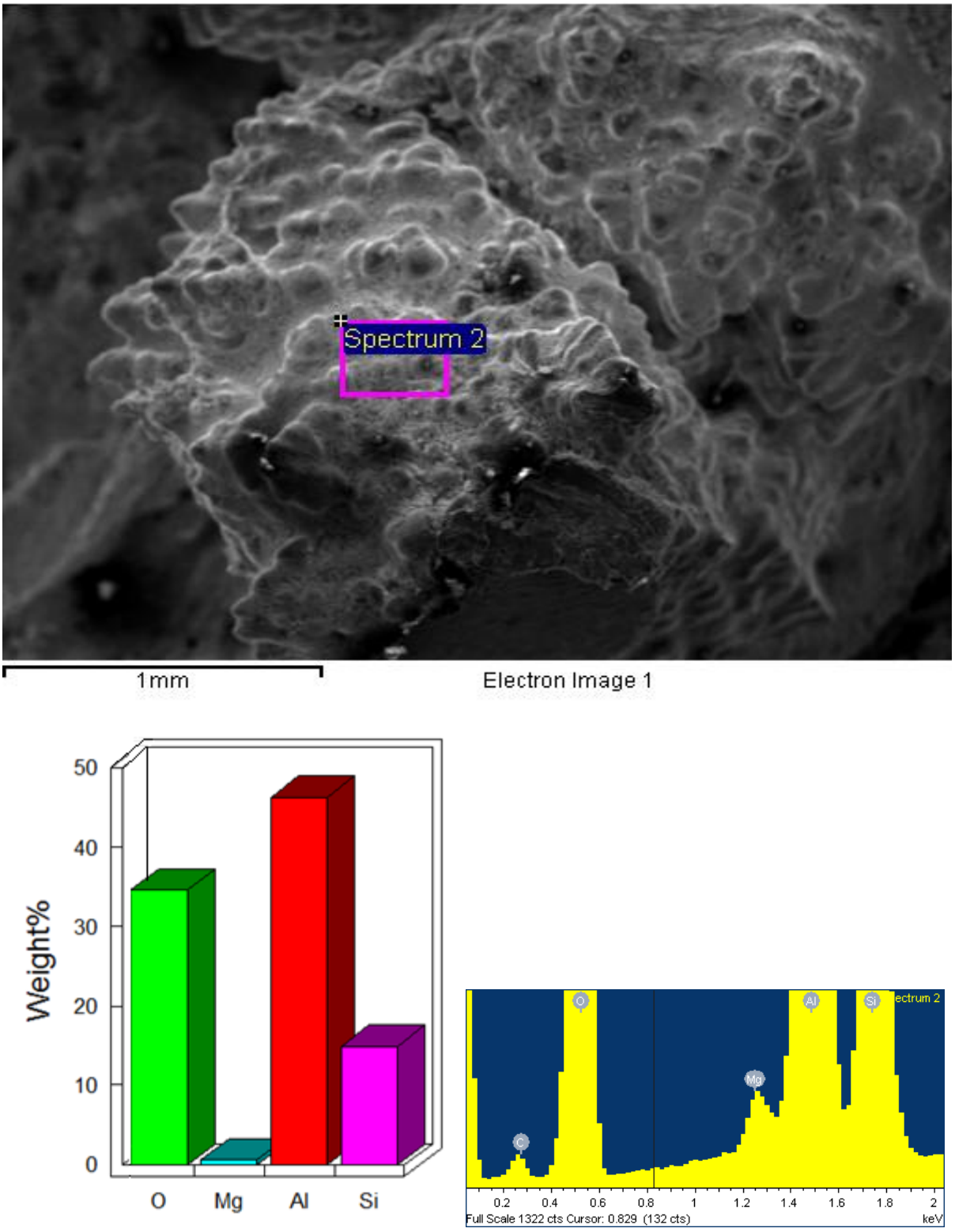

Figure 4.32 Sample #1. SE image of 2L99 alloy with oxidised interior following the bubble trap experiment with Ar, after gas removal using the Pore Gas Analyser.

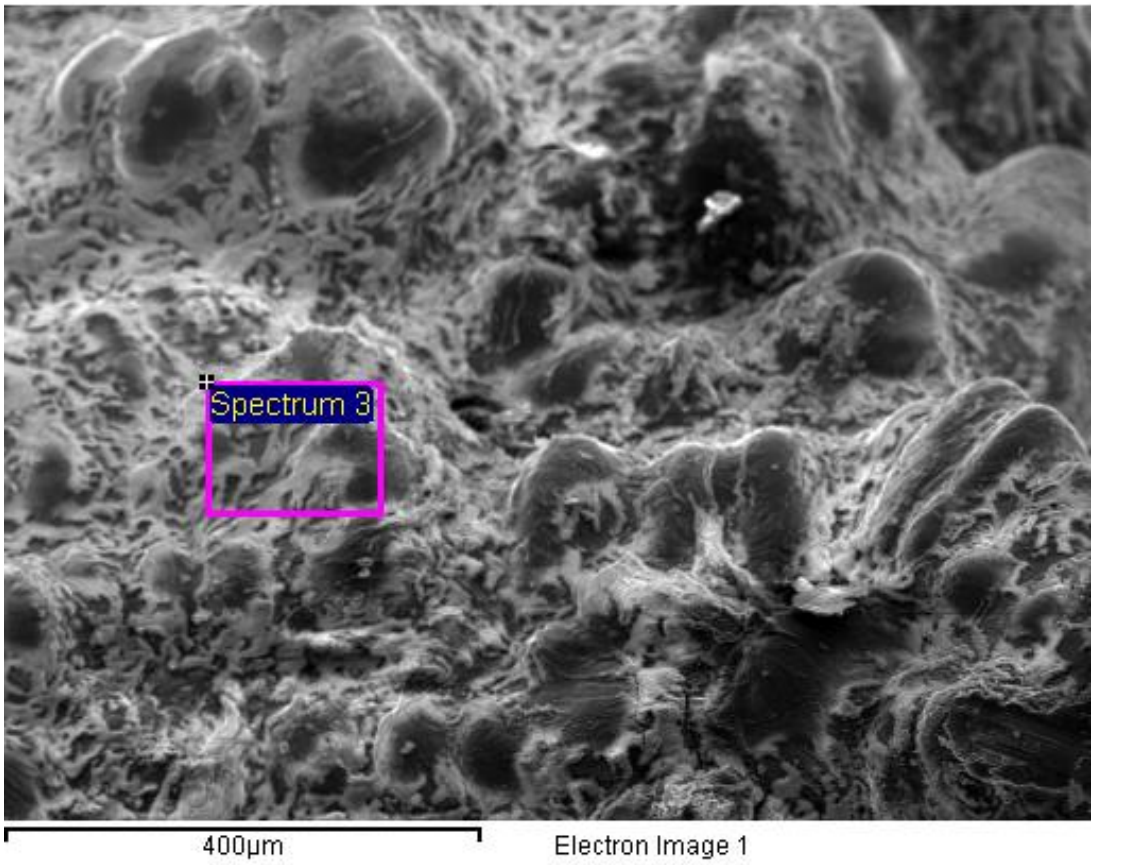

Figure 4.33 Sample #1. BSE image of 2L99 alloy with oxidised interior following the bubble trap experiment with Ar, after gas removal using the Pore Gas Analyser.

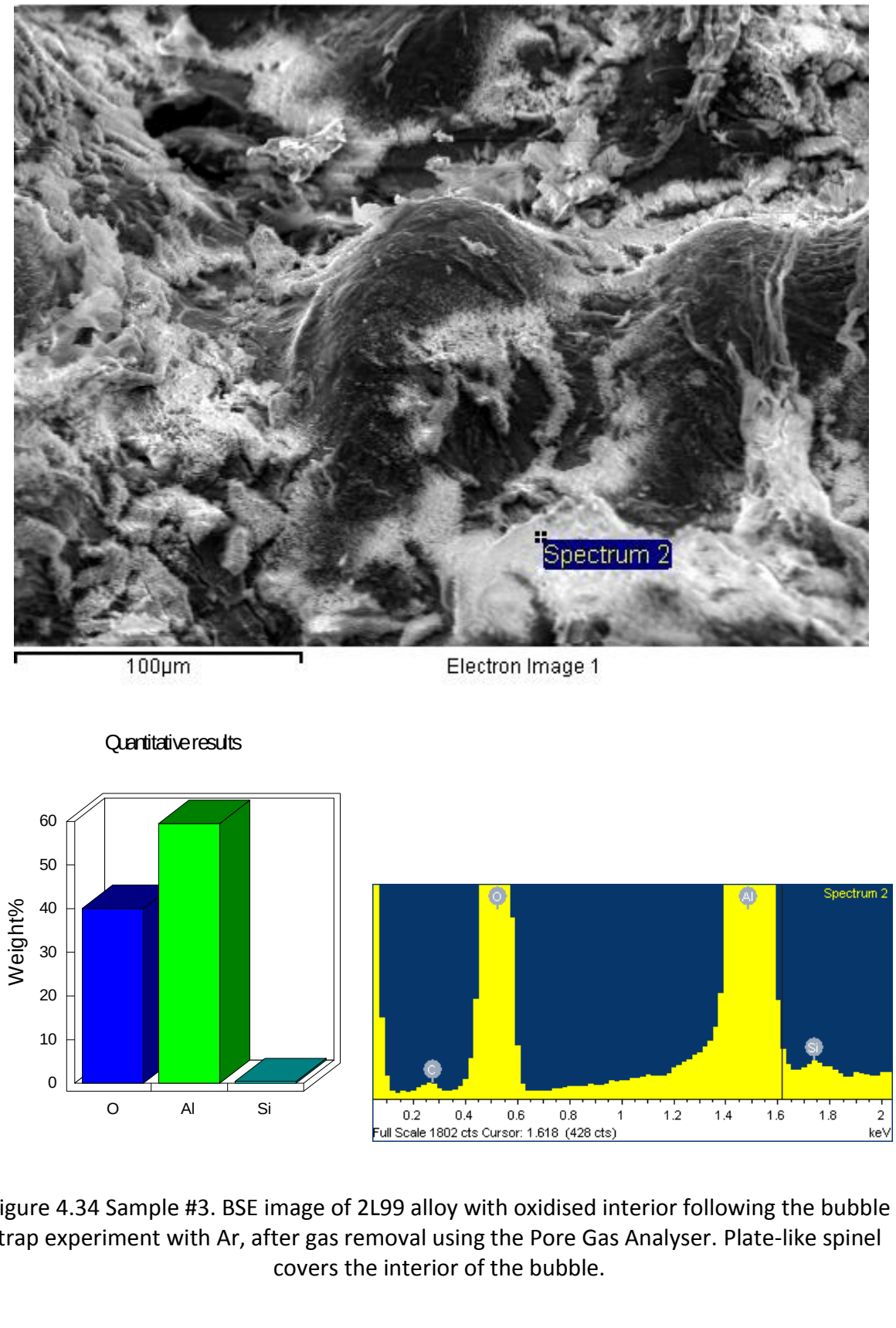

Figure 4.34 Sample #3. BSE image of 2L99 alloy with oxidised interior following the bubble trap experiment with Ar, after gas removal using the Pore Gas Analyser. Plate-like spinel covers the interior of the bubble.

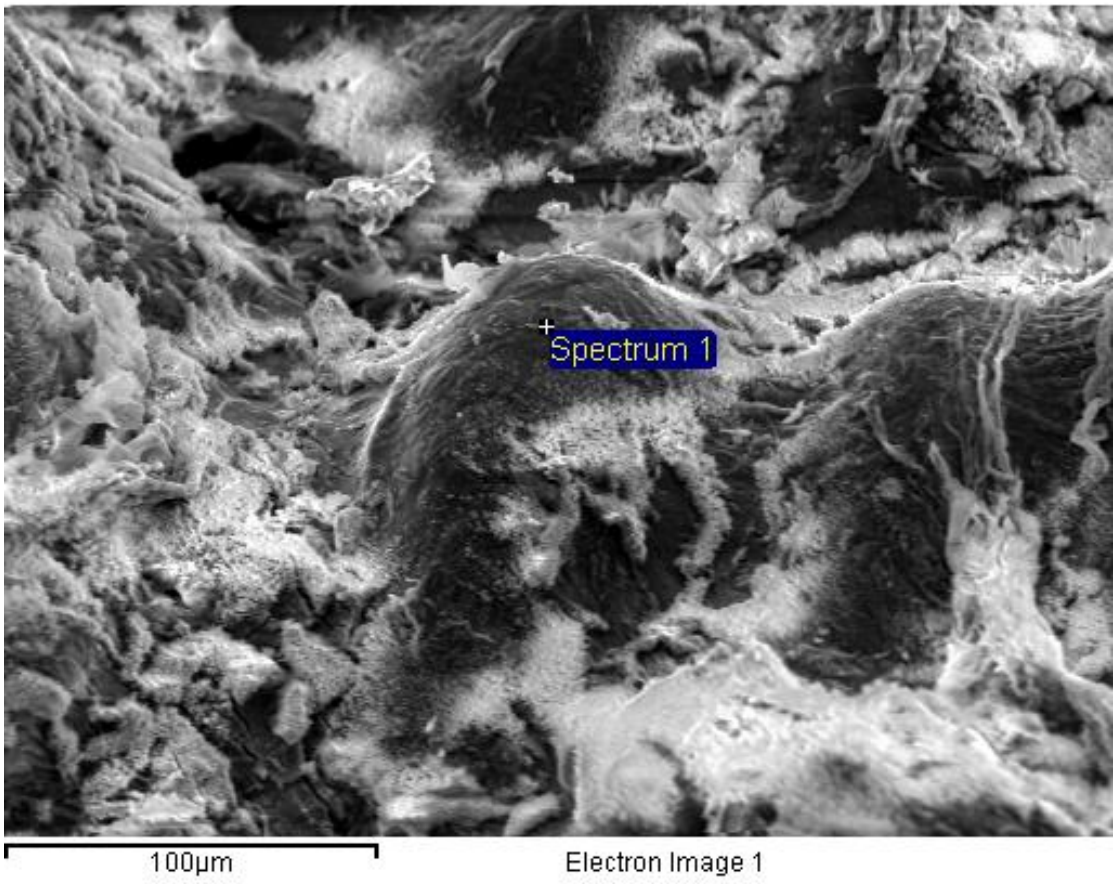

Figure 4.35 Sample #3. BSE image of 2L99 alloy with oxidised interior following the bubble trap experiment with Ar, after gas removal using the Pore Gas Analyser. Si rich eutectic is found to protrude into the gas bubble, through the spinel layer.

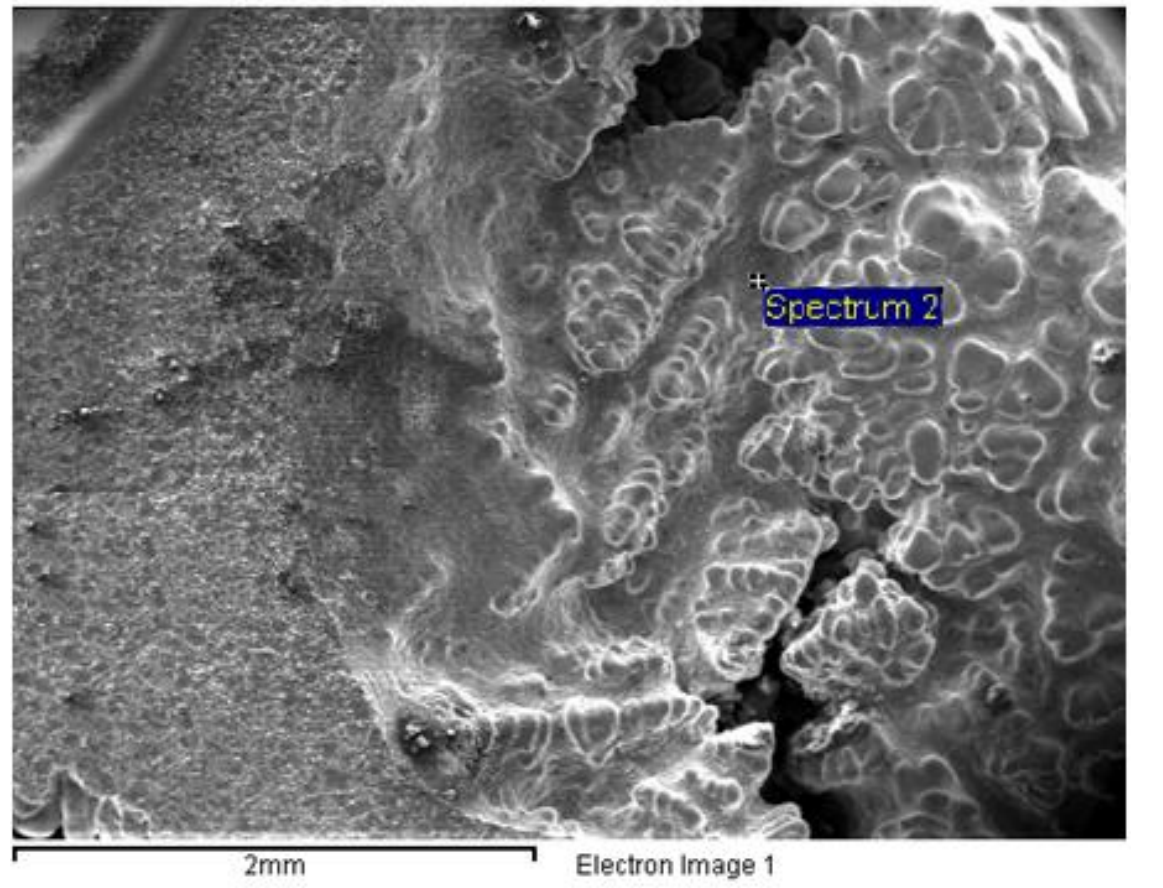

Figure 4.36 Sample #3. SE image of 2L99 alloy with oxidised interior following the bubble trap experiment with Ar, after gas removal using the Pore Gas Analyser.

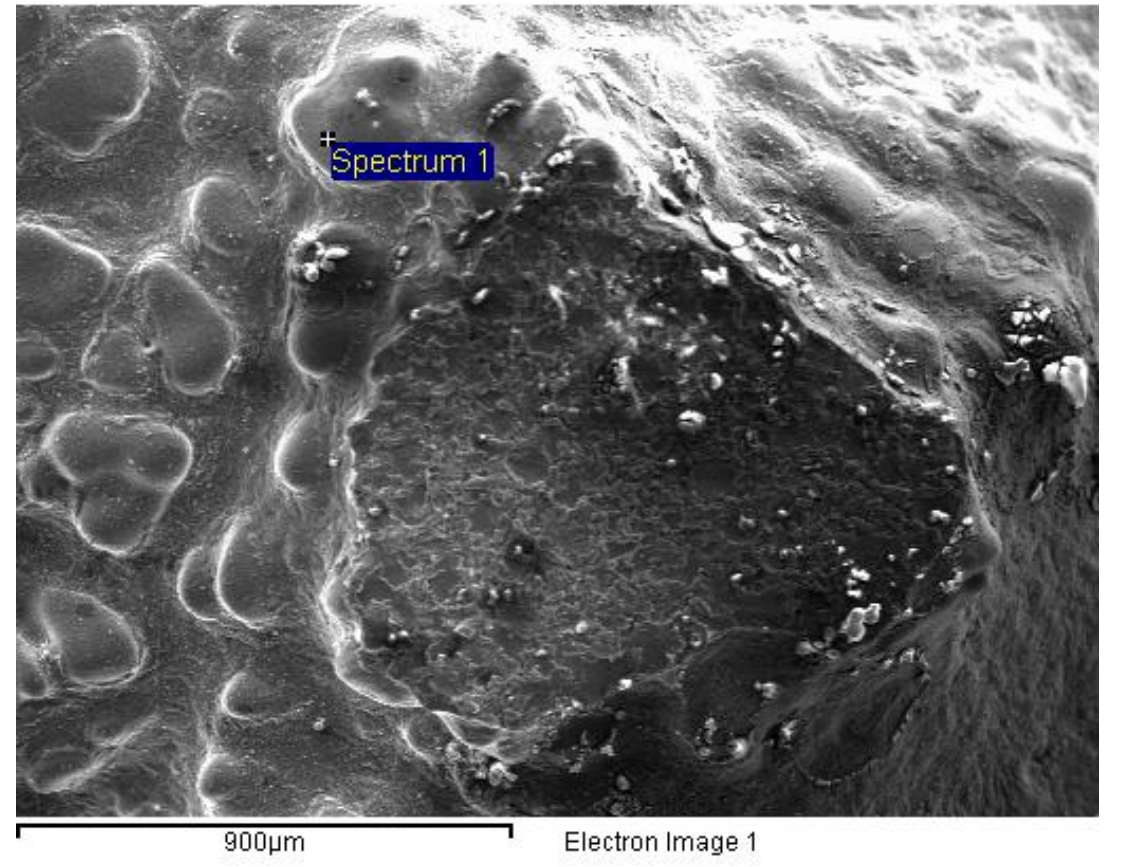

Figure 4.37 Sample #3. SE image of 2L99 alloy with oxidised interior following the bubble trap experiment with Ar, after gas removal using the Pore Gas Analyser.

The SEM analysis of the interior of the 5083 alloy (sample #4), produced using Ar, is shown in Figures 4.38 - 4.40. The surface of the bubble was clearly dendritic in structure. Only a trace (<1 wt.%) of oxygen was found during the analysis indicating that oxidation of the surface was minimal when compared to sample #1 and #3 that contained gas. Clearly no significant O_2 or water vapour was present in the Ar gas. Analysis of the central portion of the bubble was not possible in this instance due to the geometry of the sample (the depth of the bubble blocked the electrons reaching the detector).

The analysis of the 5083 alloy processed with Ar + Cl (sample #5) is shown in Figures 4.41 – 4.43. Although no gases were detected when this sample was processed in the Pore Gas Analyser, the interior surface of the bubble was found to be oxidised. Particulates were found between dendrites, which were mostly Al_2O_3 and MgO with traces of Ca, Na and Cl. This suggests that in this sample the Mg in the alloy reacted with O_2 (or water vapour) to form Mg oxide around the interior of the bubble, rather than Cl to form $MgCl_2$. This is because the reaction of Mg with O is more thermodynamically preferred to the reaction of Mg with Cl [140]. The Cl apparently reacted with traces of Ca and Na within the melt to form salts, formed at the interface of the bubble.

The analysis of the 7010 alloy processed with Ar + Cl (sample #6) is shown in Figures 4.44 - 4.47. The interior of the bubble was found to be covered with a relatively thin layer of oxide, presumably MgO, due to the Mg content of the alloy being 2.1 – 2.6 wt.%. The sample resembled sample #4, having a metallic appearance. Traces of Cl were detected by EDX analysis but were present at <0.5 wt.%. There did not appear to be any particles on the bubble surface, and no evidence of Ca, Na, potassium, Zr or Ti was found. The Cl was therefore presumed indicative of $MgCl_2$ as this is the most stable compound. Cl did not

appear to be concentrated as part of the intermetallics compared to the rest of the Al matrix, shown in Figures 4.46 and 4.47.

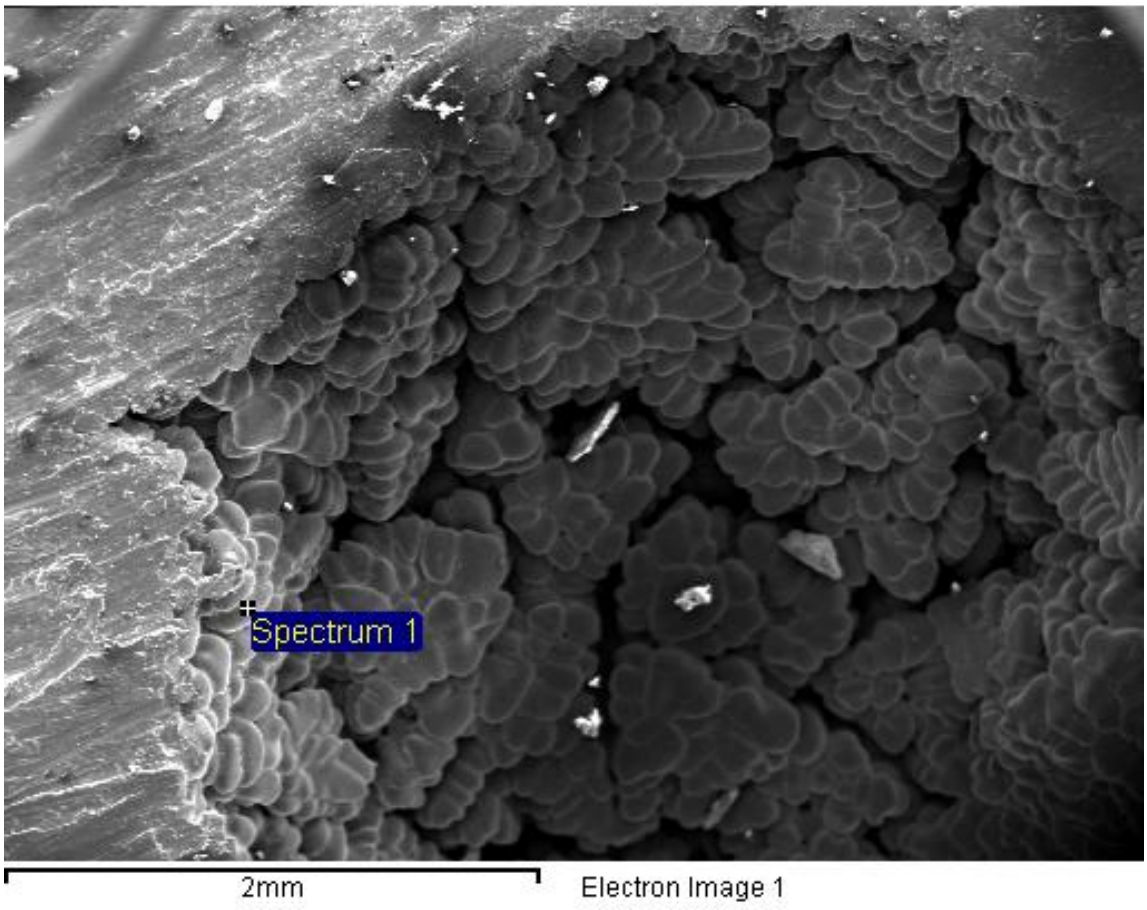

Figure 4.38 Sample #4. SE image of 5083 alloy with metallic interior following the bubble capture experiment with Ar. No gas detected using the Pore Gas Analyser.

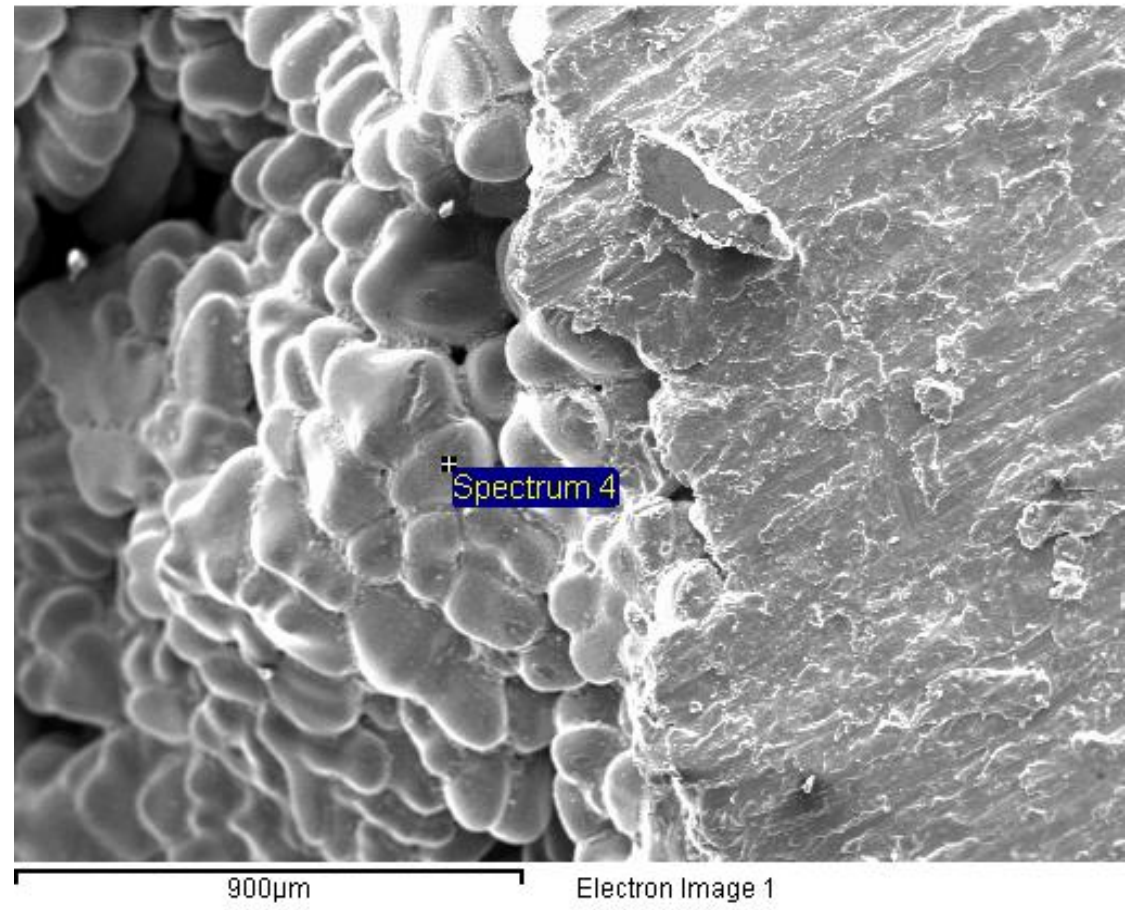

Figure 4.39 Sample #4. SE image of 5083 alloy with metallic interior following the bubble capture experiment with Ar. No gas detected using the Pore Gas Analyser.

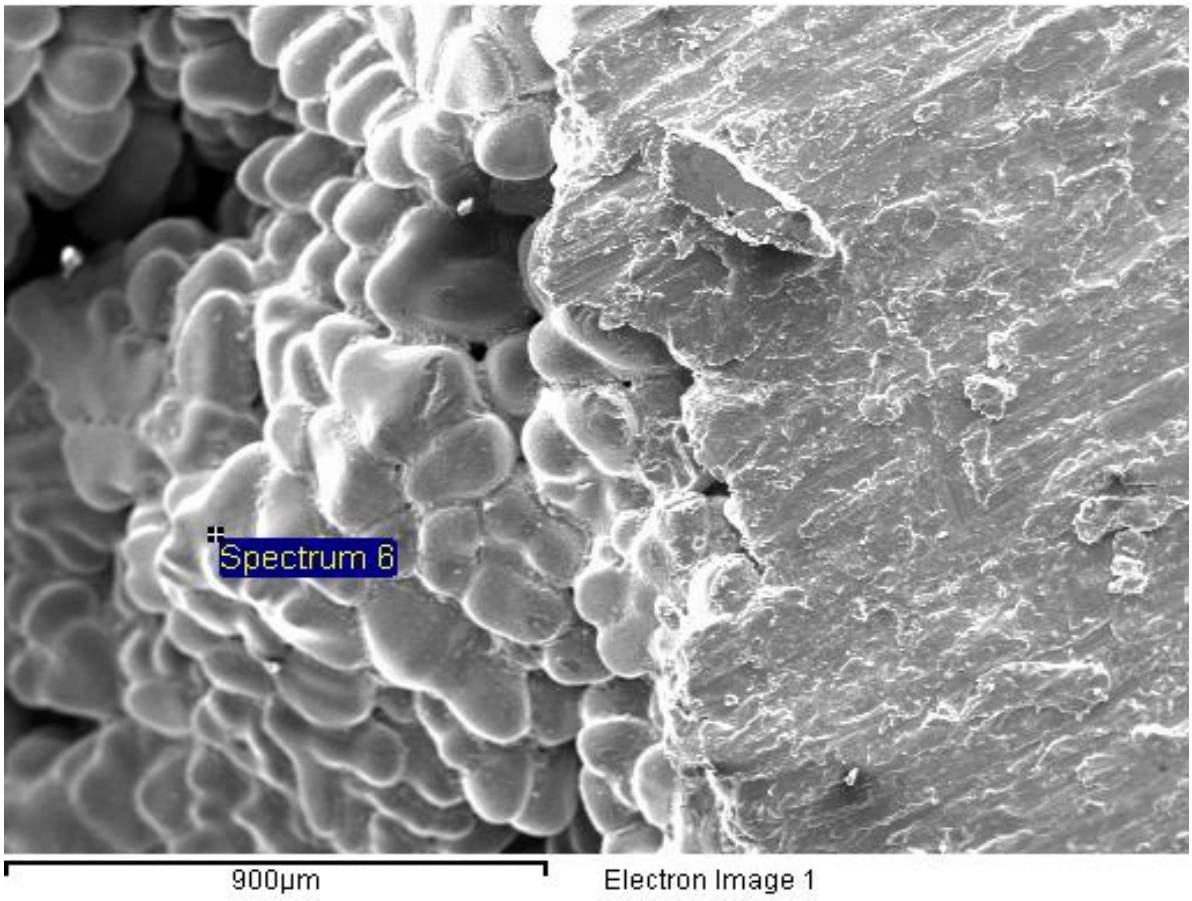

Figure 4.40 Sample #4. SE image of 5083 alloy with metallic interior following the bubble capture experiment with Ar. No gas detected using the Pore Gas Analyser.

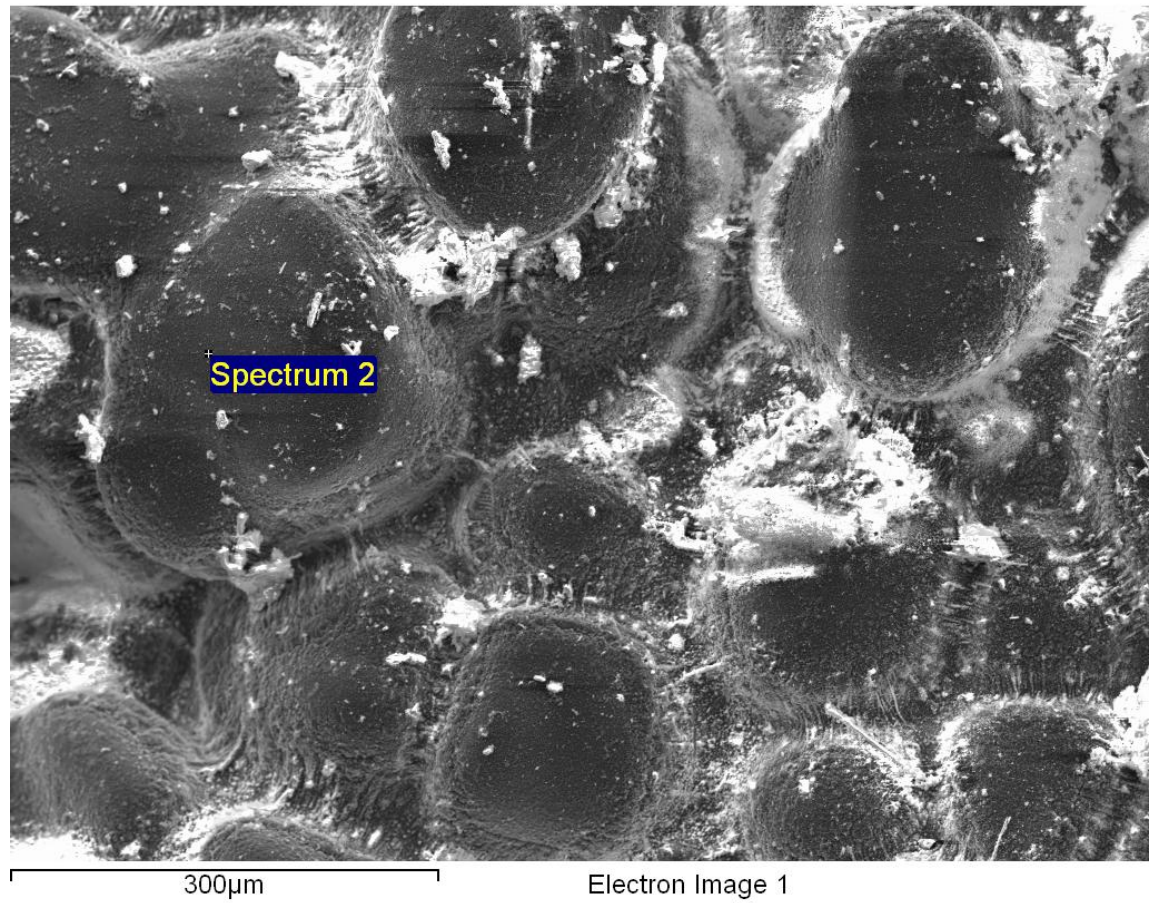

Figure 4.41 Sample #5. BSE image of 5083 alloy with oxidised interior following the bubble capture experiment with Ar + Cl. No gas detected using the Pore Gas Analyser. The interior is largely oxidised.

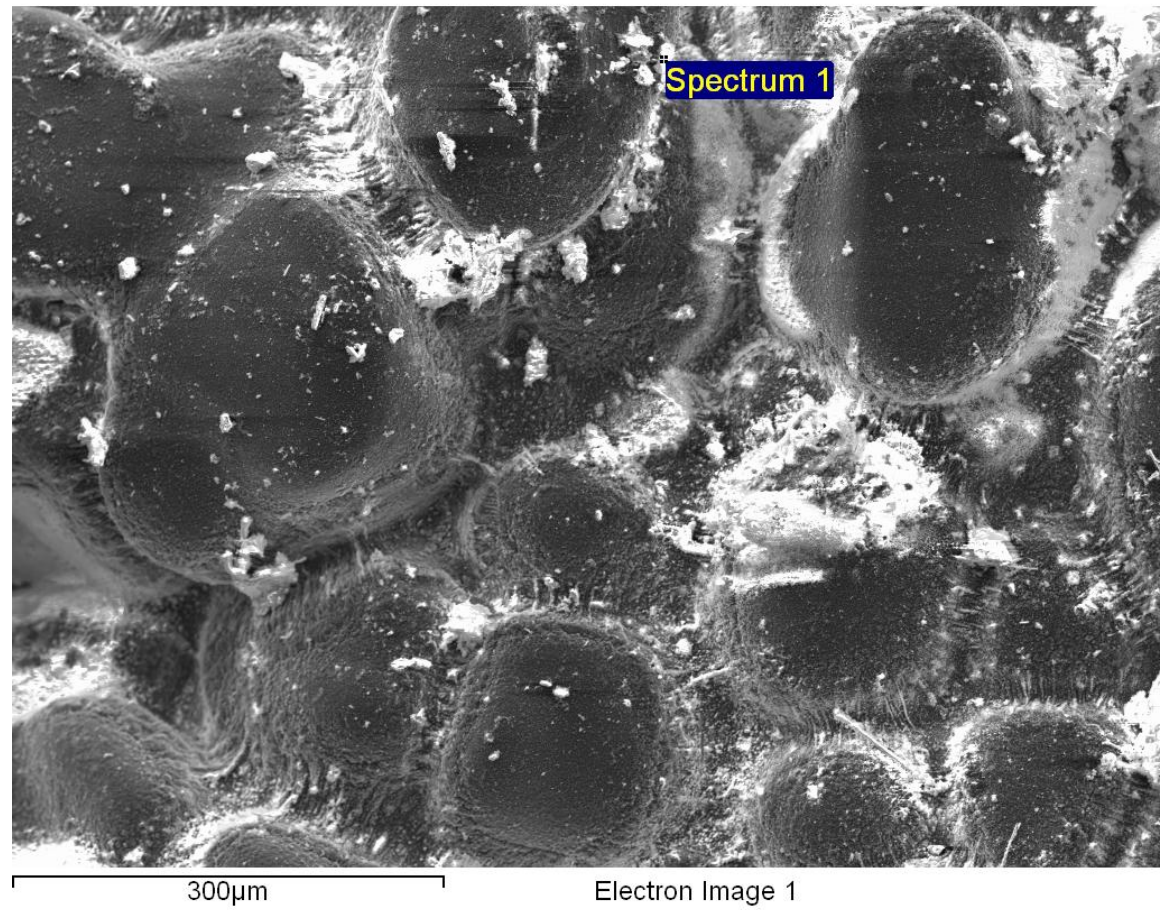

Figure 4.42 Sample #5. BSE image of 5083 alloy with oxidised interior following the bubble capture experiment with Ar + Cl. No gas detected using the Pore Gas Analyser. Oxidised particles trapped within the dendrites were found to contain traces of Ca, Na and Cl.

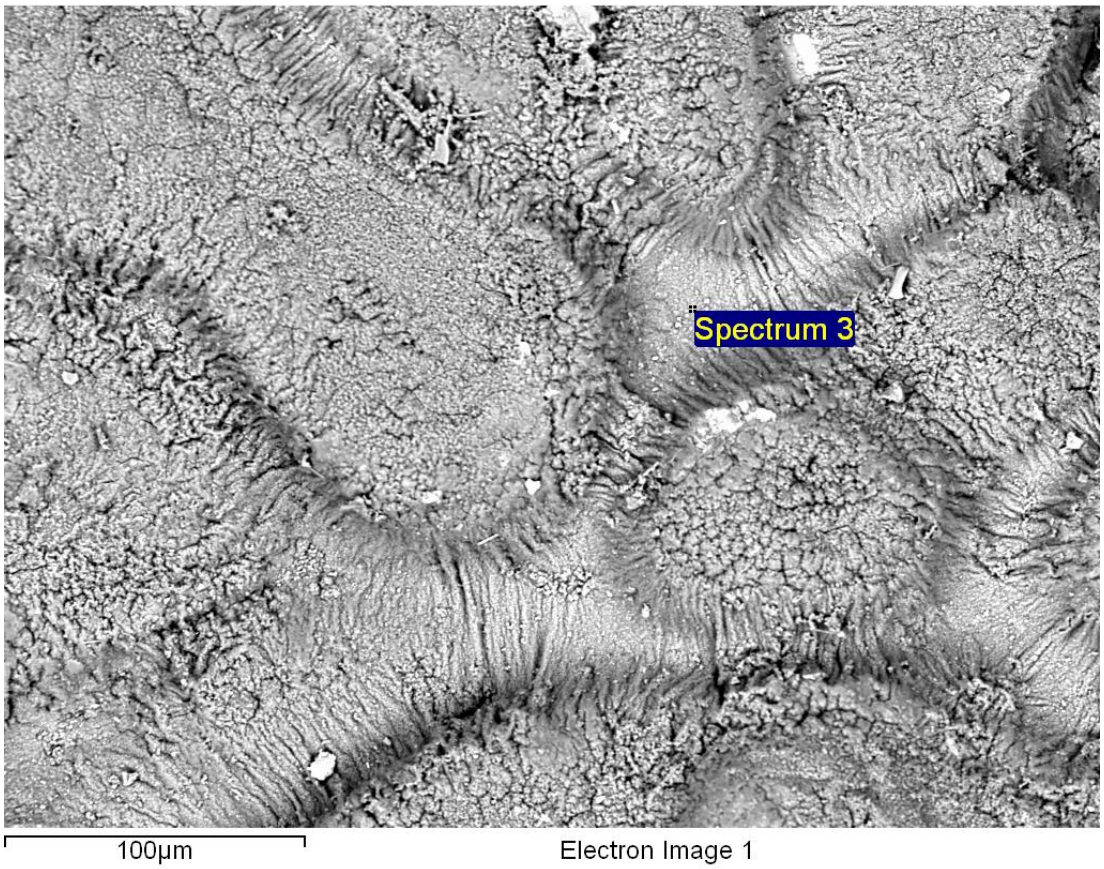

Figure 4.43 Sample #5. BSE image of 5083 alloy with oxidised interior following the bubble capture experiment with Ar + Cl. Only minute traces of Cl were found during the survey, along with Ca. No gas detected using the Pore Gas analyser.

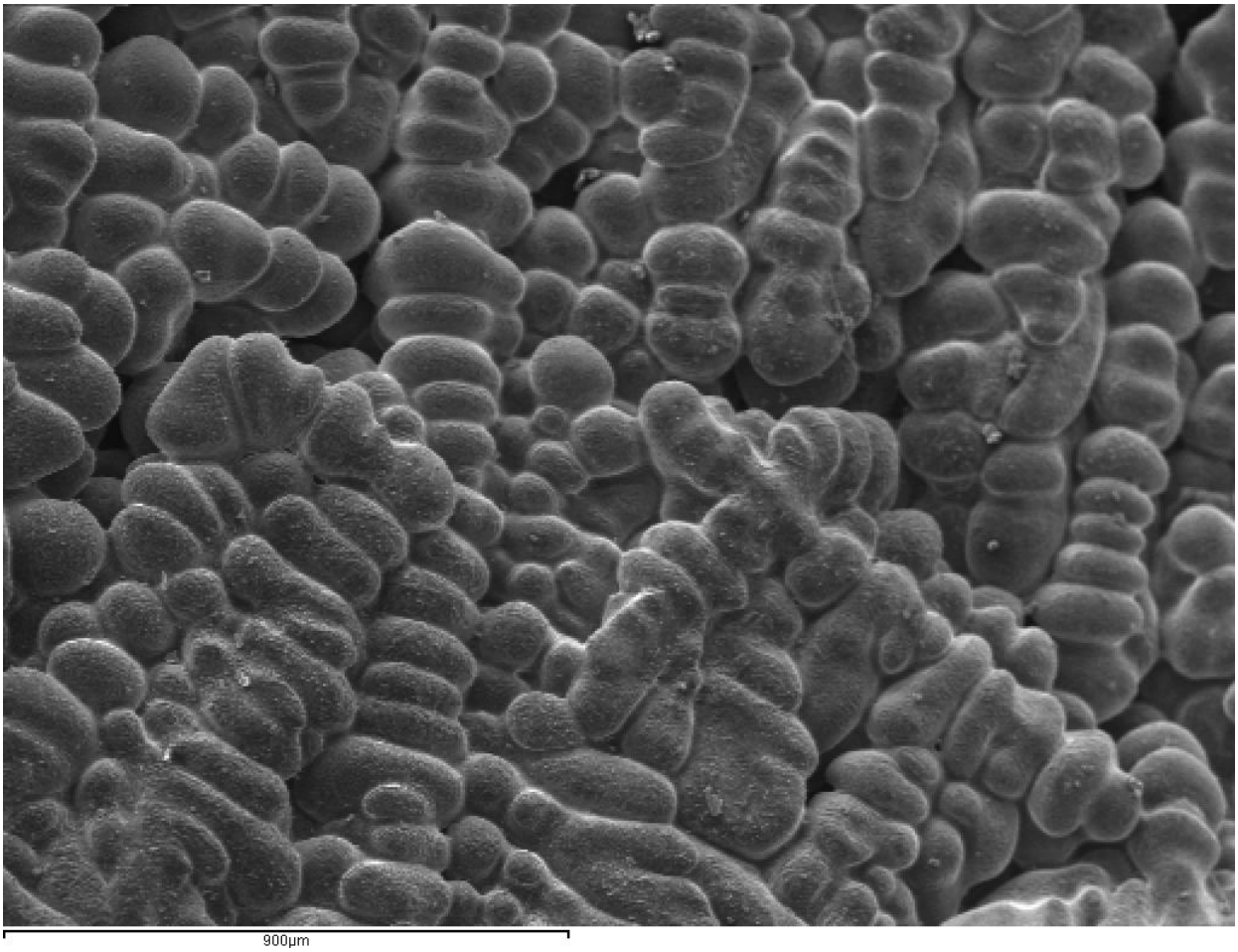

Figure 4.44 Sample #6. SE image of 7010 alloy with only minor oxidation of the interior created using Ar + Cl mixture. The dendritic structure is visible.

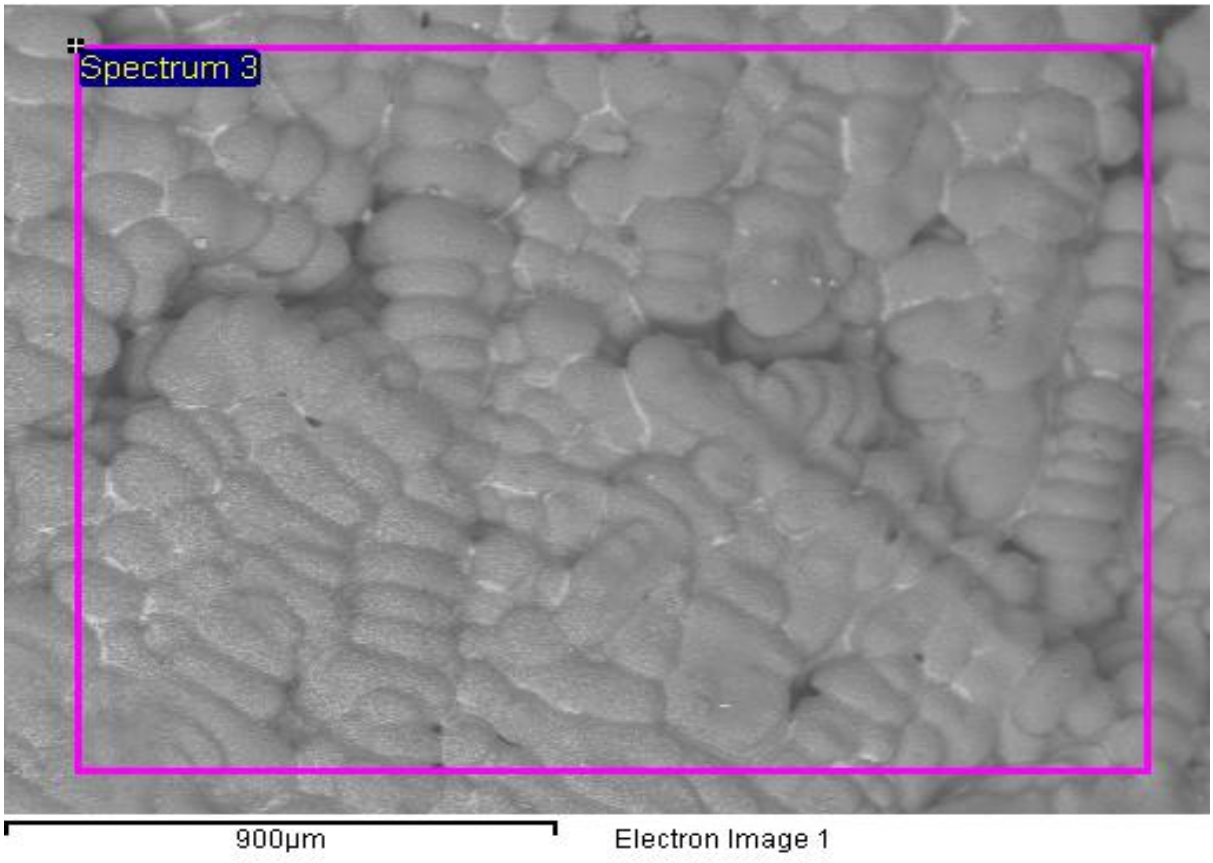

Figure 4.45 Sample #6. BSE image of 7010 alloy with only minor oxidation of the interior created using Ar + Cl mixture. Traces of Cl are identified, presumably coating the bubble as a thin layer of $MgCl_2$.

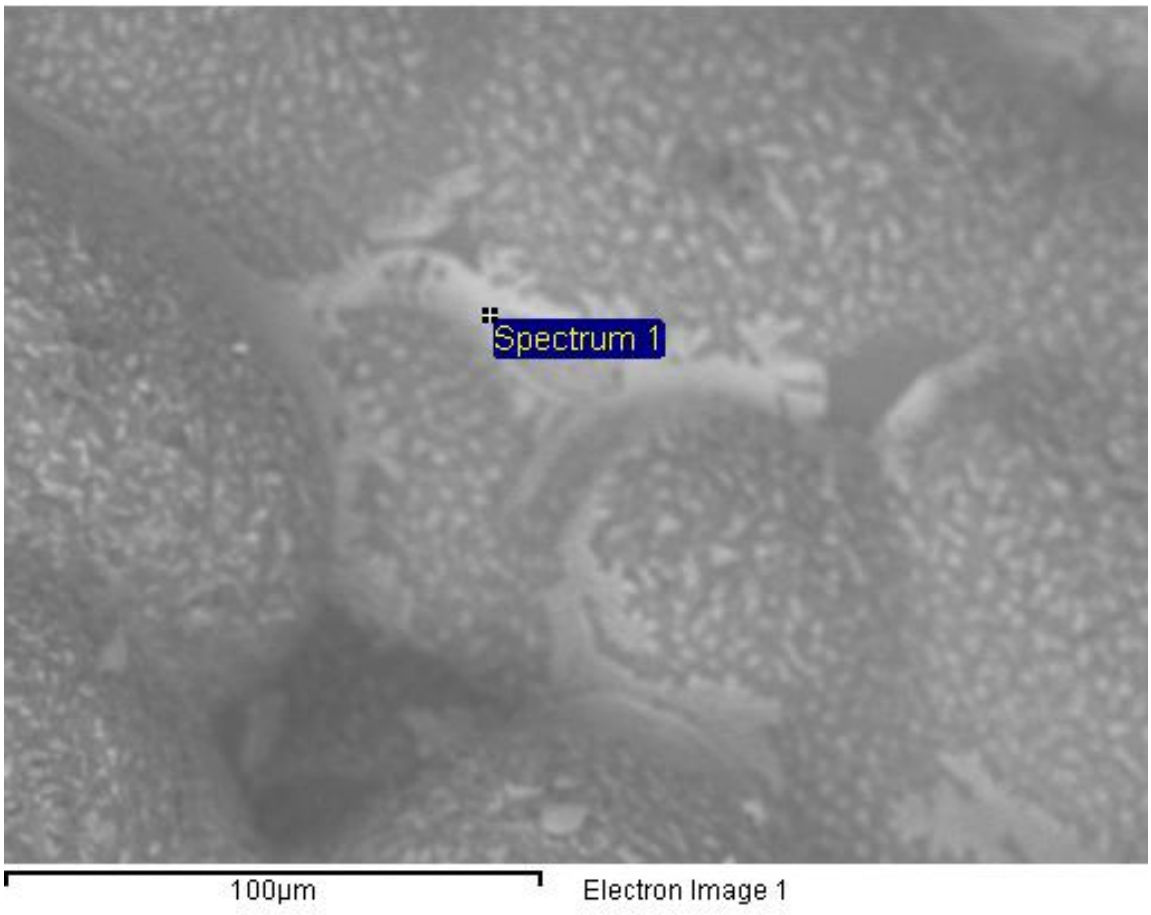

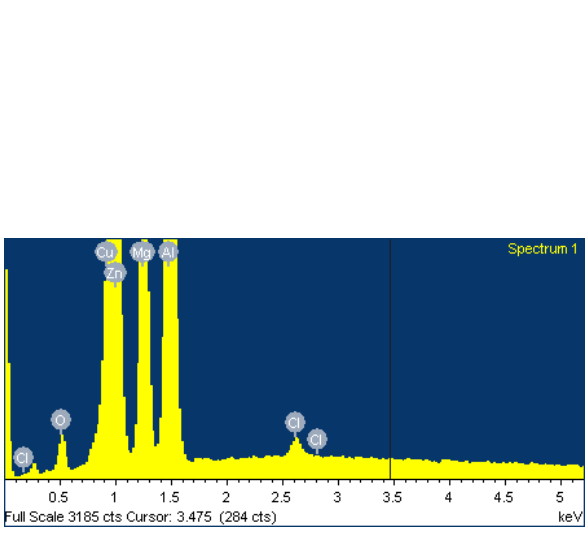

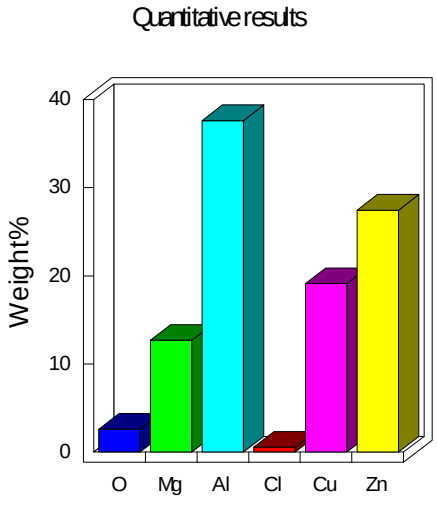

Figure 4.46 Sample #6. BSE image of 7010 alloy with only minor oxidation of the interior, created using Ar + Cl mixture. Traces of Cl are identified, presumably coating the bubble as a thin layer of $MgCl_2$. Chlorides are not found to be concentrated along with intermetallics.

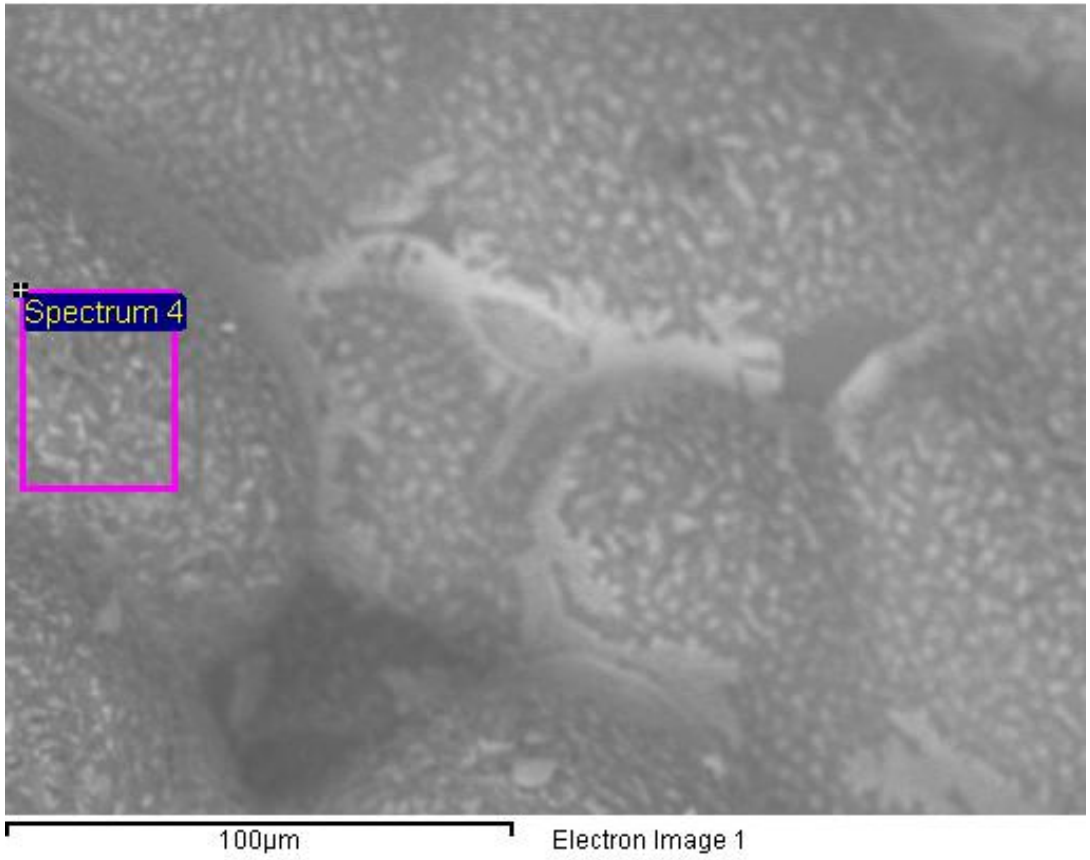

Figure 4.47 Sample #6. BSE image of 7010 alloy with only minor oxidation of the interior, created using Ar + Cl mixture. Traces of Cl are identified, presumably coating the bubble as a thin layer of $MgCl_2$. Chlorides are not found to be concentrated along with intermetallics.

There was a delay after puncturing the sample before pressure levels were observed to increase within the mass spectrometer detection system as the extracted gases take a few seconds to enter the spectrometer. The pressure of each gas detected was observed to increase quickly and peak at about 125 seconds ($1.6x10^{-6}$ Pa) in experiment #1 before slowly declining as these gases exited the mass spectrometer. The data obtained from the experiments, where samples contained gases (Pore Gas Analyser samples #1 and #3, and after applying the sensitivity factors discussed in section 3.3.1), are shown in Figures 4.48 and 4.49.

The sample from experiment #1 contained mostly H (82%) and N_2 (14%). Trace levels of water vapour were detected (4%), but no traces of Ar or O_2 were detected during the analysis.

The sample from experiment #3 also contained primarily H_2 (80%) and N_2 (12%). Amounts of water vapour and Ar were also found within this sample; 3% and 5% respectively, and no O_2 was deteced. Lower gas pressures were observed in the second sample and the gas collection time was shorter, because the bubble contained less gas.

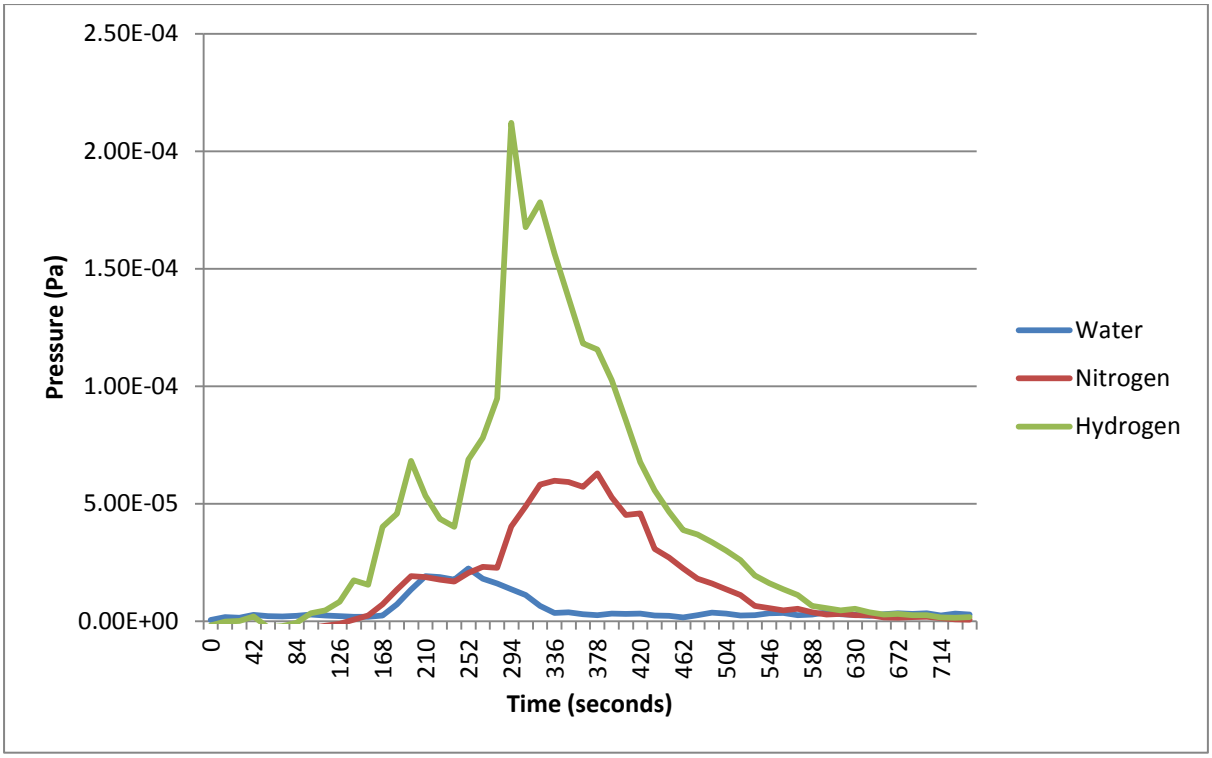

Figure 4.48 2L99 sample #1: Gases observed in the analyser once the sample had been punctured.

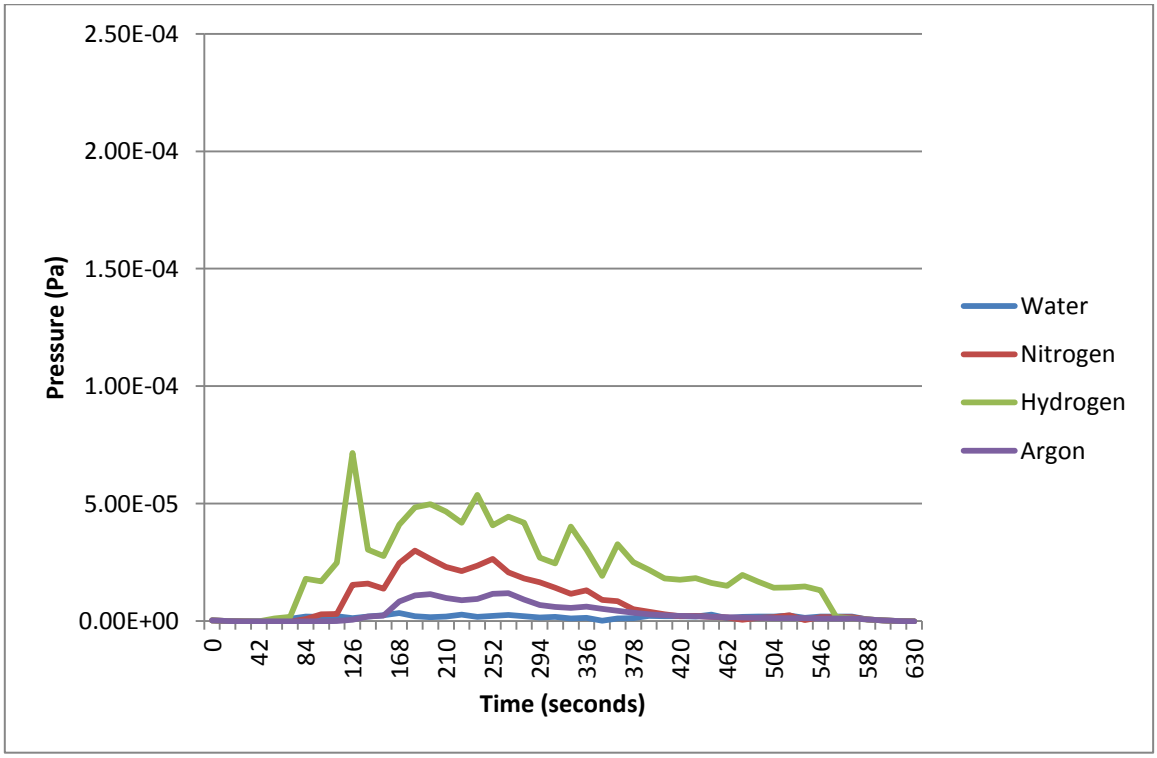

Figure 4.49 2L99 sample #3: Gases observed in the analyser once the sample had been punctured.

4.4: Hydrogen removal from 7xxx aluminium alloys using a SNIF reactor with and without chlorine gas additions.

The effects of Cl on the degassing of 7xxx Al alloys was investigated using a statistical approach. In total 169 individual readings were taken during this survey. 82 readings were from casts with Cl (half of which were pre-degasser and half were post-degasser), and 87 readings were from casts without Cl (half of which were pre-degasser and half were post-degasser). As discussed in section 3.3.1, two readings (one pre and one post) were used to generate a single efficiency value.

All of the efficiency values that were obtained are presented together in a frequency table and chart in Figure 4.50, and they are compared using a standard distribution plot in Figure 4.51. Beneath this graph the mean, standard deviation and t-test results are presented to determine the significant differences between the two data sets. The degassing efficiency values for each individual alloy, with and without Cl additions are then presented in the same fashion. In casts made with Cl additions the Cl addition rate was 1.5% in rotor 1 and 0.8% in rotor 2 as per the Table 3.2. The results for the 7010 alloy can be seen in Figures 4.52 and 4.53, the results for the 7050 alloy in Figures 4.54 and 4.55 and finally the 7075 alloy in Figures 4.56 and 4.57. These three alloys are 7xxx alloys with minor differences in the major alloying elements (Cu, Mg and Zn) and minor alloying elements (Zr, Cr, Fe, Si, Ti). The compositions of the alloys examined in this survey (minimum maximum and averages) are listed in Table 4.2, and this shows the differences between the three alloys investigated in this review.

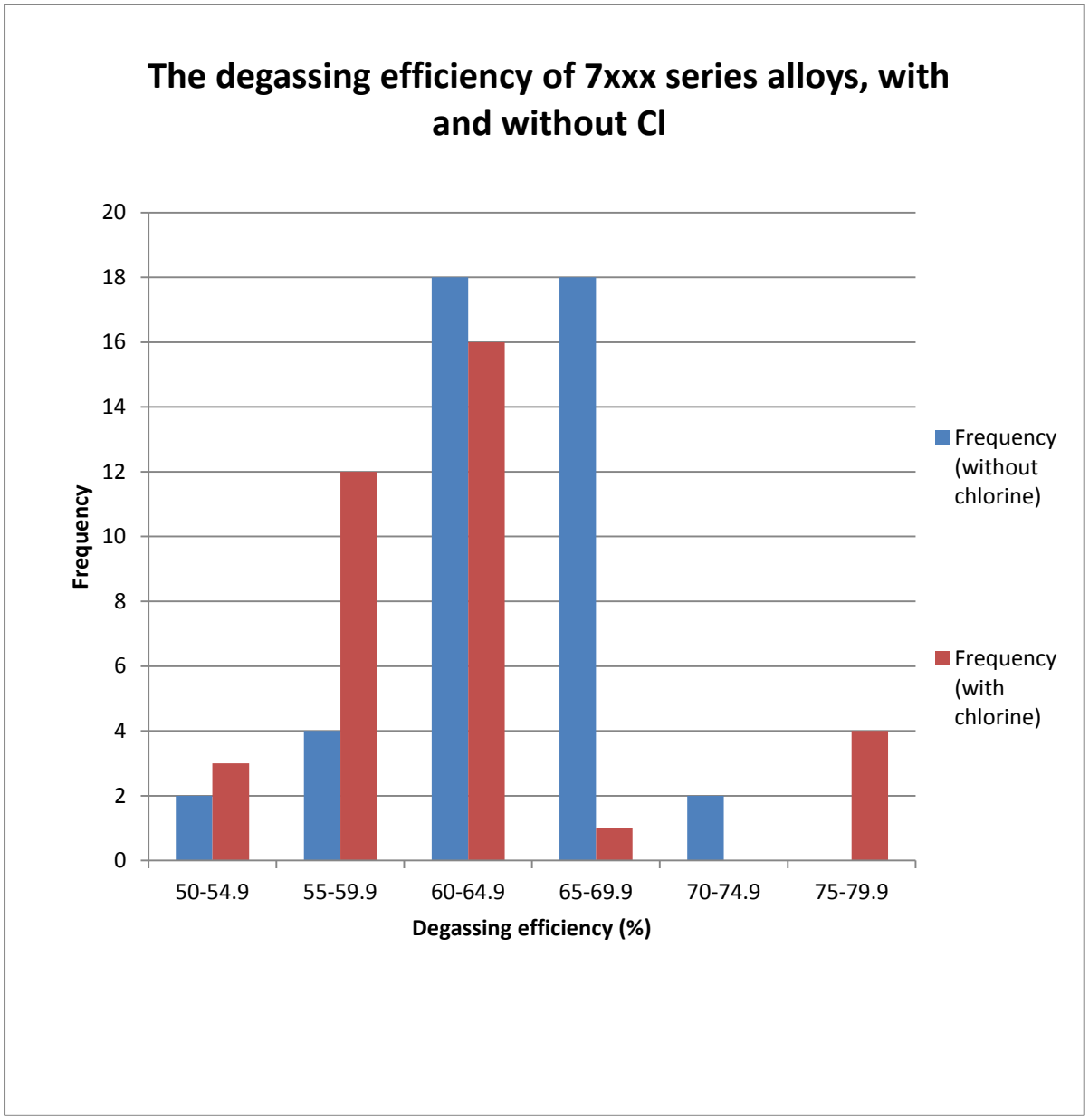

Efficiency range (%)	50-54.9	55-59.9	60-64.9	65-69.9	70-74.9	75-79.9
Frequency (without Cl)	2	4	18	18	2	0
Frequency (with Cl)	3	12	16	1	0	4

Figure 4.50 The measured degassing efficiencies of all three alloys, with and without Cl additions.

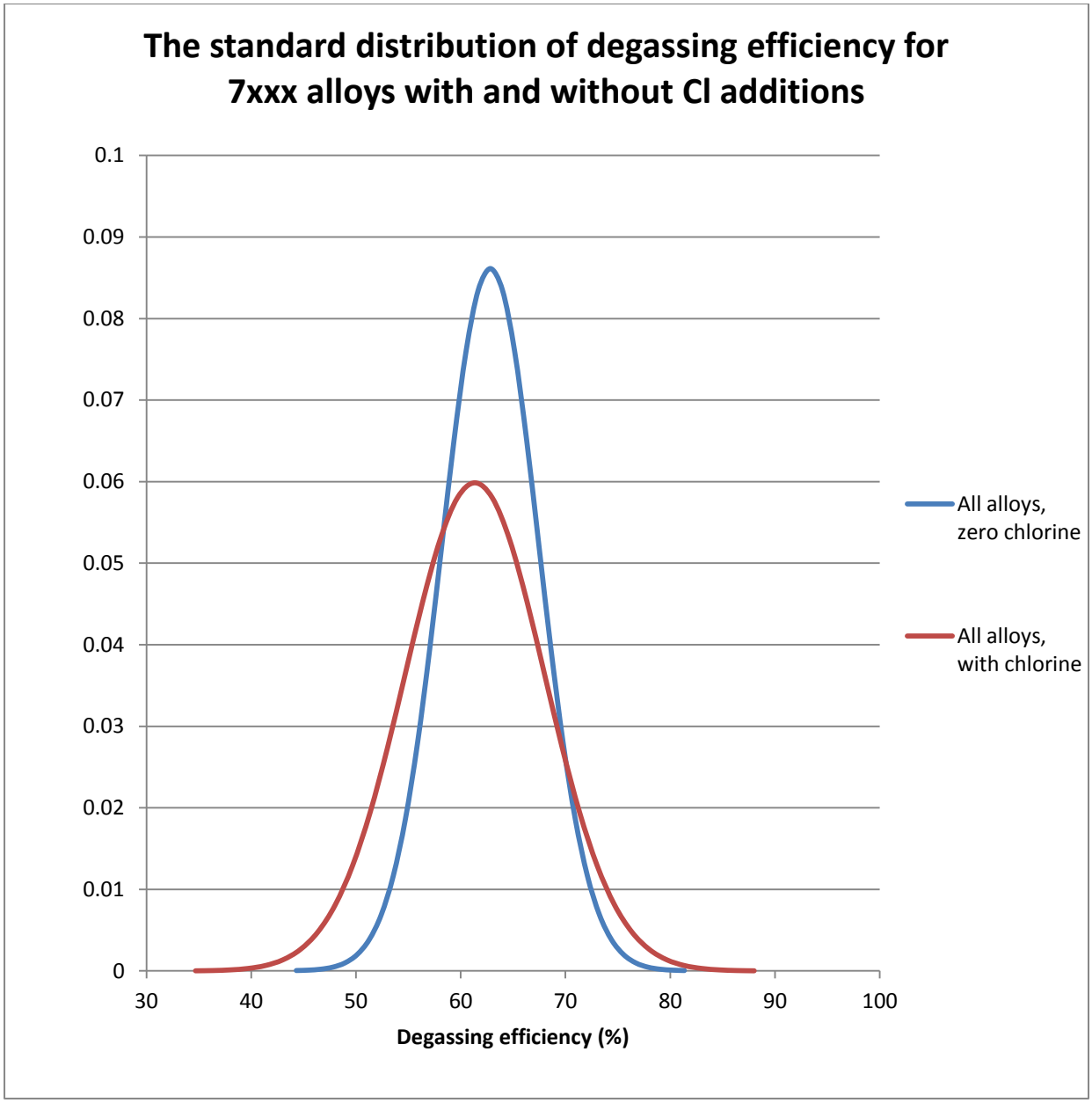

	Mean	Standard deviation	t-test (p)
No Cl	62.8	4.6	0.26
With Cl	61.3	6.7	

Figure 4.51 The standard distributions of the degassing efficiencies of all three alloys a) without and b) with Cl additions. The average (mean) and standard distribution for each data set are detailed, as is the t-test result that compares the two data sets.

The results from all measurements shown in Figures 4.50 and 4.51 suggest that there was no significant difference in degassing efficiency when 7xxx alloys are treated with either pure Ar, or an Ar + Cl gas mixture. This is demonstrated by the predominantly overlapping standard distribution curves in Figure 4.51, the very similar means (62.8 % without Cl and 61.3 % with Cl) and the t-test result of 0.26, which suggests there is only a 26% chance that there is a difference in efficiency when casts are degassed with the two different gas compositions.

The standard distribution curves shown in Figure 4.51 suggest a slight reduction in efficiency when using Cl additions as this curve is moved slightly to the left due to the difference in mean values, but that effect is very small within this overall data set. The average degassing result was only 1.5 % lower in those casts degassed with Cl additions. Those casts treated with the Ar + Cl gas mixture were slightly more variable, with an increased standard distribution (6.7 % compared to 4.6 %), and an increased range of results (28.7 % compared to 21.9 %).

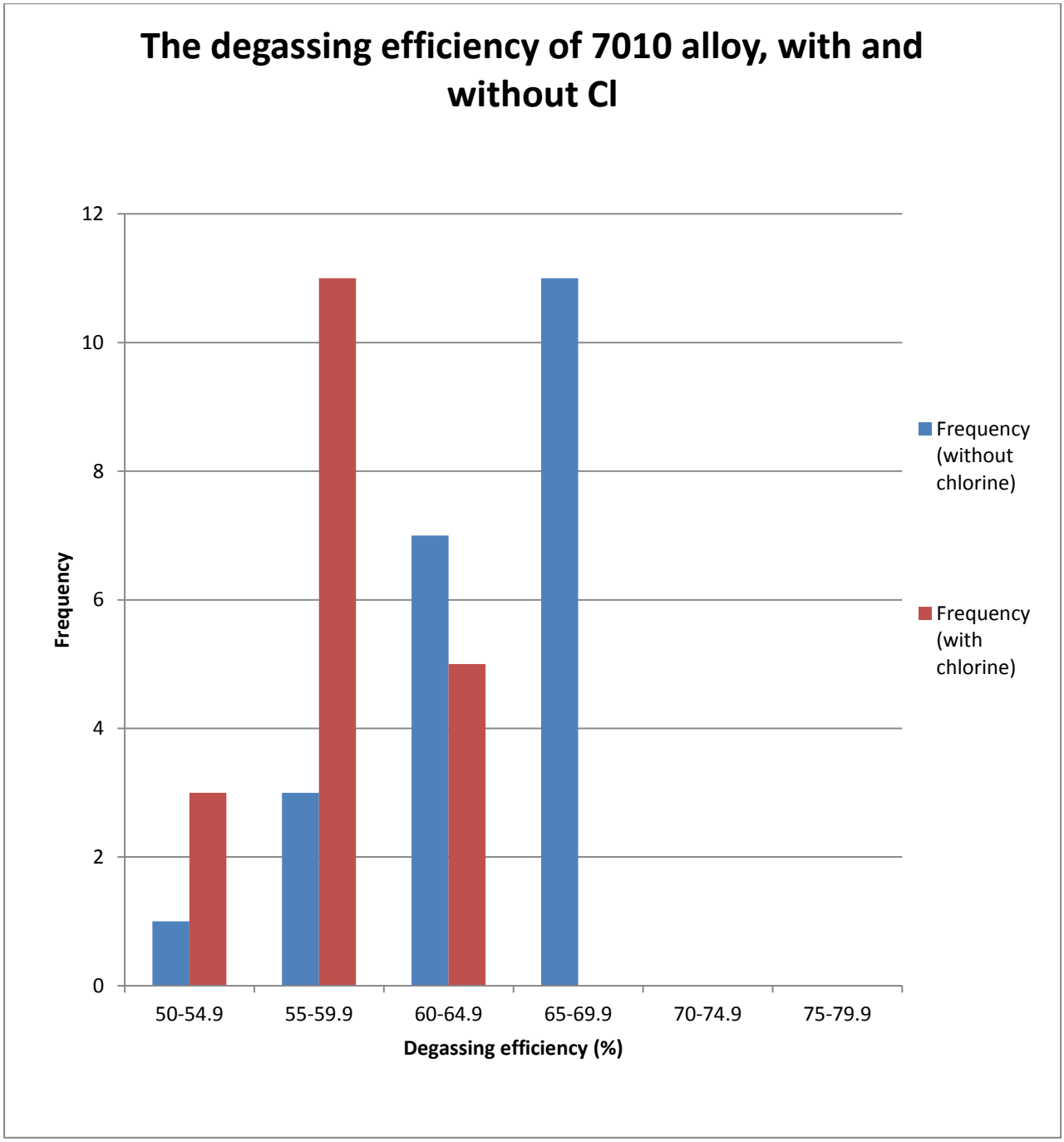

Efficiency range (%) 7010	50-54.9	55-59.9	60-64.9	65-69.9	70-74.9	75-79.9
Frequency (without Cl)	1	3	7	11	0	0
Frequency (with Cl)	3	11	5	0	0	0

Figure 4.52 The measured degassing efficiencies of the 7010 alloy, with and without Cl additions.

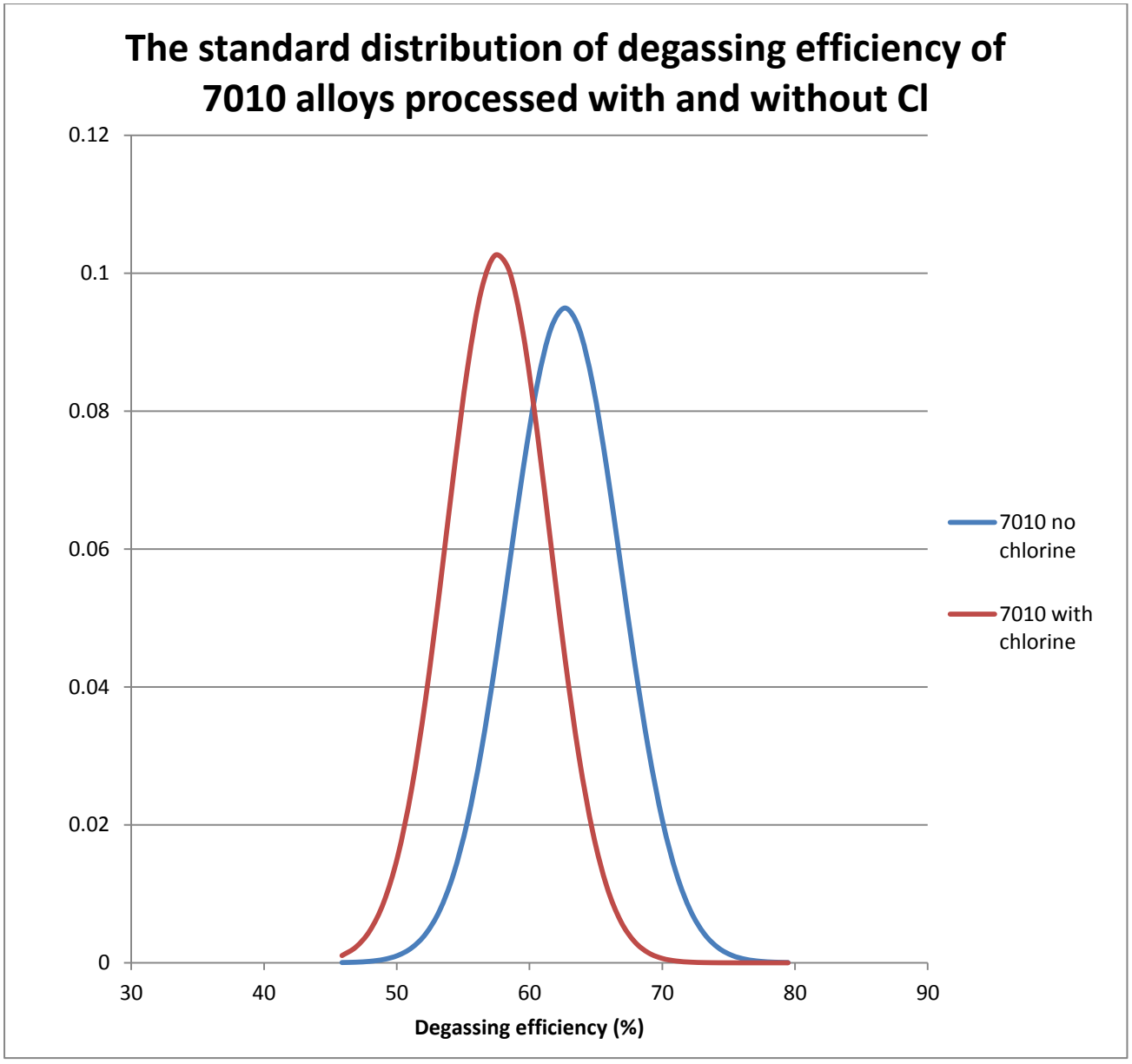

	Mean	Standard deviation	t-test (p)
No Cl	63	4.2	0.0003
With Cl	58	3.88	

Figure 4.53 The standard distributions of the degassing efficiencies of the 7010 alloy a) without and b) with Cl additions. The average (mean) and standard distribution for each data set are detailed, as is the t-test result that compares the two data sets.

When the data obtained from the 7010 alloy casts are interpreted alone, the results were observed to be quite different. The standard distribution curves in Figure 4.53 are clearly separate and demonstrate a reduction in degassing efficiency in 7010 alloy when using Cl additions. This was shown to be significant by the t-test, which produced a p value of 0.003, below the 0.05 confidence threshold, so in this instance we should reject the null hypothesis (that Cl has no effect on degassing efficiency) and conclude that Cl retards the degassing process.

The data was approximately the same in terms of standard deviation (4.2 and 3.88 %) and range of results (13.8 and 13.6 %) when comparing casts without Cl to casts with Cl additions respectively, but the mean degassing efficiency was reduced by 5 % when using an Ar + Cl mixture.

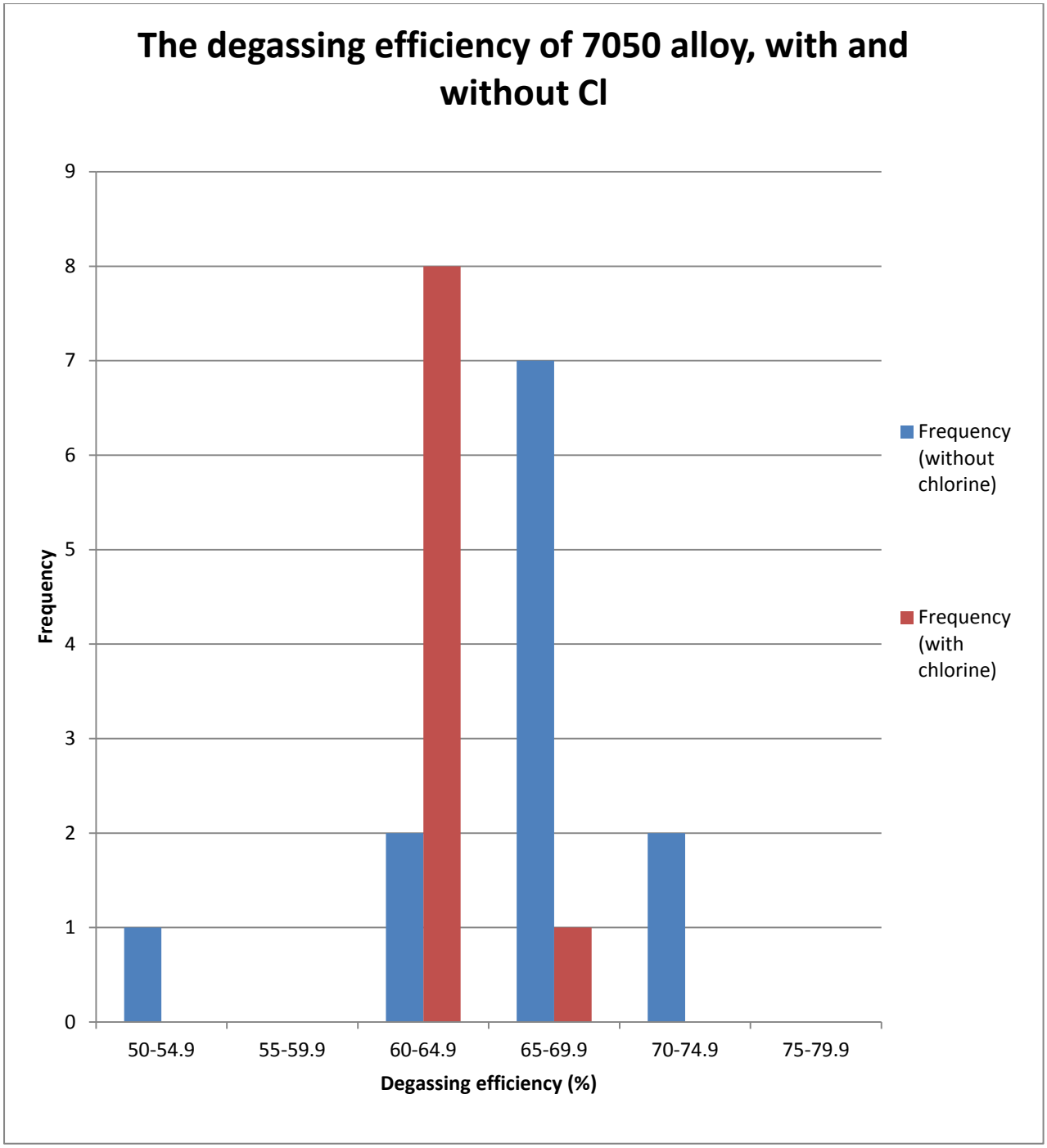

Efficiency range (%) 7050	50-54.9	55-59.9	60-64.9	65-69.9	70-74.9	75-79.9
Frequency (without Cl)	1	0	2	7	2	0
Frequency (with Cl)	0	0	8	1	0	0

Figure 4.54 The measured degassing efficiencies of the 7050 alloy, with and without Cl additions.

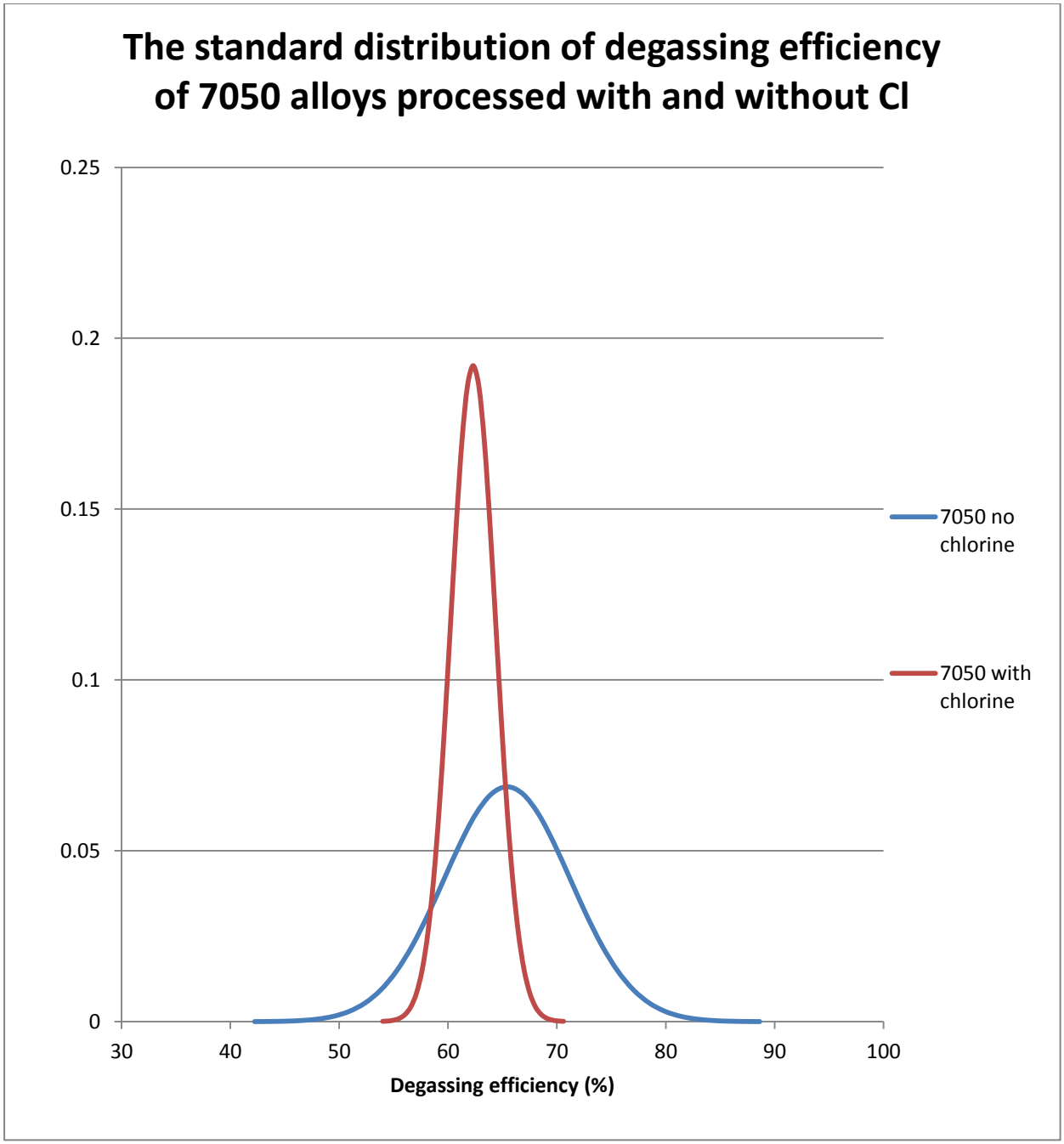

	Mean	Standard deviation	t-test (p)
No Cl	65	5.80	0.11
With Cl	62	2.08	

Figure 4.55 The standard distributions of the degassing efficiencies of the 7050 alloy a) without and b) with Cl additions. The average (mean) and standard distribution for each data set are detailed, as is the t-test result that compares the two data sets.

The results from the analysis of the 7050 alloy (Figures 4.54 and 4.55) shows that there was no statistically significant difference in degassing efficiency when using Ar or an Ar + Cl gas mixture. This is demonstrated by the t-test P value of 0.11.

The average degassing efficiency value for those casts with Cl additions was observed to decrease by 3% but the data was quite varied; with a standard deviation of 5.8 compared to 2.08 and a range of 21.7 % compared to 7.1 %. The deviation and range reduce the ability to accurately resolve a difference between the two data sets.

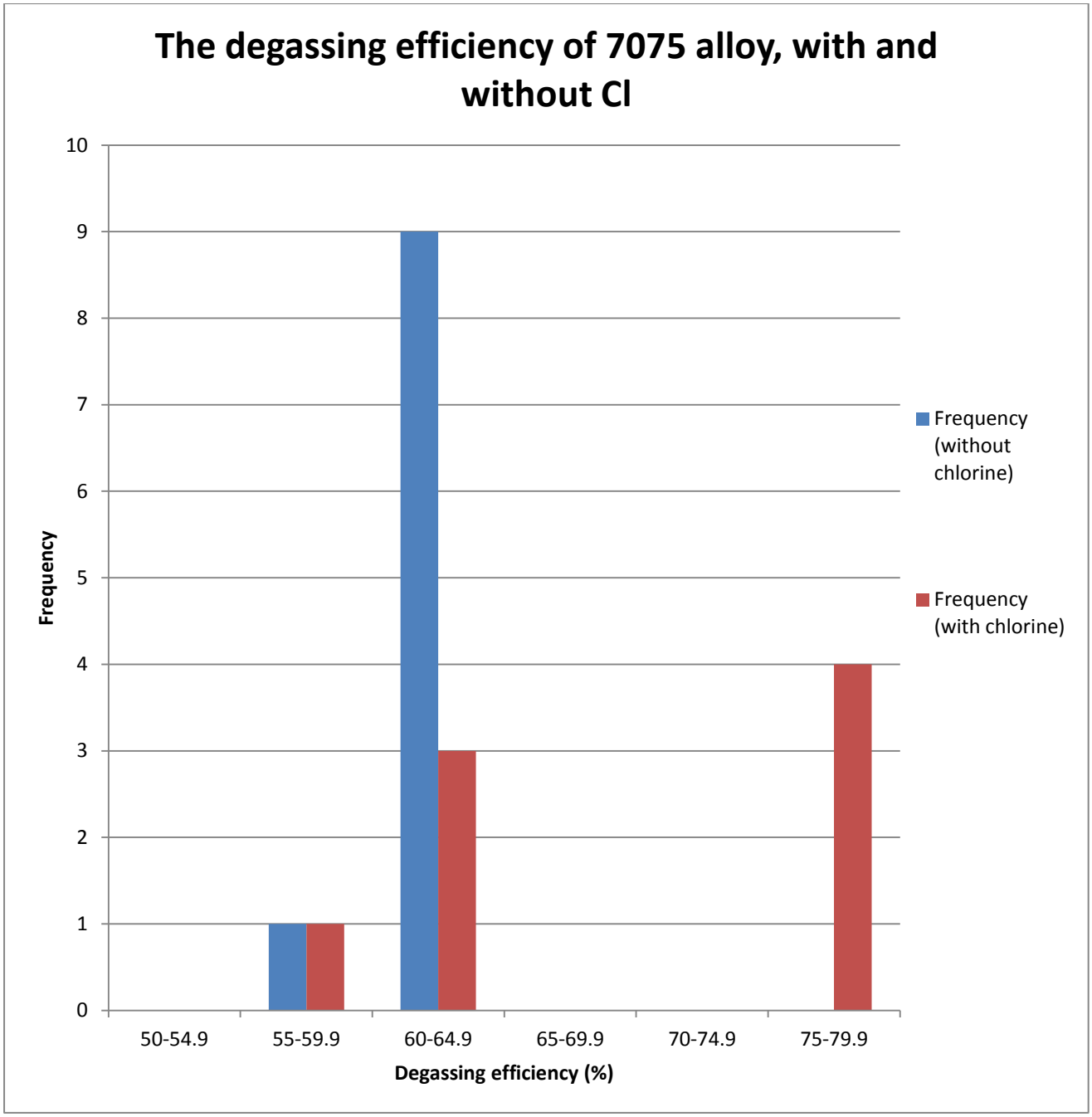

Efficiency range (%) 7075	50-54.9	55-59.9	60-64.9	65-69.9	70-74.9	75-79.9
Frequency (without Cl)	0	1	9	0	0	0
Frequency (with Cl)	0	1	3	0	0	4

Figure 4.56 The measured degassing efficiencies of the 7075 alloy, with and without Cl additions.

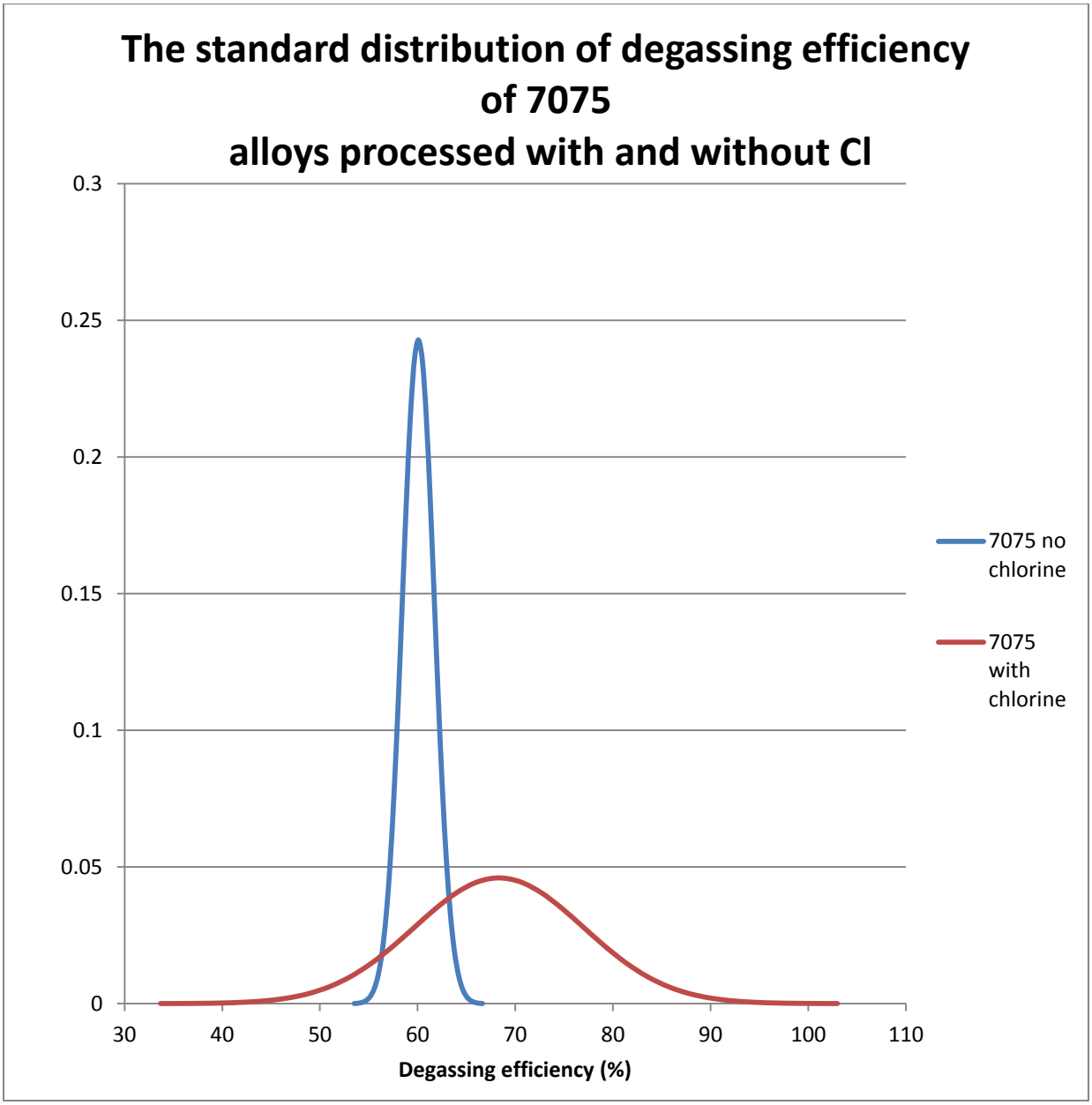

	Mean	Standard deviation	t-test (p)
No Cl	60	1.64	0.02
With Cl	68	8.66	

Figure 4.57 The standard distributions of the degassing efficiencies of the 7075 alloy a) without and b) with Cl additions. The average (mean) and standard distribution for each data set are detailed, as is the t-test result that compares the two data sets.

The results from the 7075 alloy series, in contrast to those from the 7010 and 7050 alloys, showed an increase in degassing efficiency when an Ar + Cl mixture was compared to Ar alone. This was demonstrated to be statistically significant by the t-test result of 0.02, lower than the 0.05 confidence level. Therefore in this instance we reject the null hypothesis as Cl appears to increase the degassing efficiency of this alloy. See Figures 4.56 and 4.57.

The average degassing efficiency was observed to be increased by 8% when Cl is present. The standard deviation, (8.66 compared to 1.64), and range of data (20 .2 % compared to 6.6 %), for those casts with Cl were far more varied and had a greater range than those without Cl.

4.4.1: Alloy compositions:

The 7010 alloy was observed to be affected by the addition of Cl; the average degassing value was reduced by 5% when an Ar + Cl mixture was used. The 7010 alloy was observed to possess an average composition between that of the 7050 and 7075 alloys when considering the three major alloying elements Mg, Cu and Zn, see Table 4.2. Theoretically Cl could react to form chlorides with any of these elements, but from this simple comparison it seems unlikely that interactions between the Cl and these three major alloying elements had an influence on degassing performance in this alloy.

The 7010 and 7050 alloys were observed to contain significantly more Zn than the 7075 alloy (6.26 and 6.48 vs. 5.8 wt% Zn respectively), more Zr than the 7075 alloy (0.11 and 0.11 vs 0.02 wt% Zr respectively) and less Cr (0.01 and 0.00 vs 0.20 wt% Cr respectively).

The Ti content was not observed to vary significantly between the three alloys. The Fe and Si contents were quite varied as the 7050 alloy had a very low Fe and Si content but this does not appear to fit any trend.

	7010			**7075**			**7050**		
	Min	*Mean*	*Max*	*Min*	*Mean*	*Max*	*Min*	*Mean*	*Max*
Cu	1.69	1.78	1.80	1.61	1.63	1.66	2.02	2.06	2.11
Fe	0.104	0.130	0.137	0.137	0.150	0.160	0.039	0.040	0.049
Mg	2.30	2.34	2.37	2.46	2.51	2.56	1.82	1.90	1.98
Si	0.040	0.050	0.056	0.061	0.070	0.072	0.023	0.020	0.027
Zn	6.15	6.26	6.36	5.72	5.80	5.89	6.46	6.48	6.52
Ti	0.034	0.04	0.039	0.036	0.040	0.041	0.022	0.020	0.027
Cr	0.007	0.010	0.011	0.194	0.200	0.206	0.001	0.000	0.006
Zr	0.104	0.110	0.112	0.017	0.020	0.022	0.108	0.110	0.113

Table 4.2 The minimum, average (mean) and maximum compositions for the three alloys used in the SNIF ALSCAN survey.

In summary, the 7010 and 7075 alloys appeared to interact with Cl, reducing the efficiency in 7010 alloy and increasing the efficiency in 7075 alloy. There was no obvious effect of Cl on the degassing efficiency of the 7050 alloy. When the three alloy series are brought together to represent the general 7xxx alloys there is no apparent effect of small amounts of Cl (1.5 and 0.8% Cl in Ar) on the degassing efficiency.

4.5 The degassing efficiency of aluminium alloys, achieved with and without chlorine and measured using ALSPEK H.

In this section small Al melts were degassed using a static lance and the progressive reduction in H was recorded using the ALSPEK H. In each experiment the time was measured as the melt H content fell by 0.01 ml/100g over the range 0.35 – 0.15 ml/100g.

An example of a degassing curve (experiment #1) where pure Al in the temperature range of 730 – 750^{o}C was degassed using Ar is shown in Figure 4.58. The H content of this melt was observed in each experiment to be reduced quickly at first, and then more slowly as the degassing procedure continued and the H content of the melt decreased. A reduction in H removal rate occurred for two reasons 1) H was being absorbed from the environment at a faster rate, slowing the overall progress of the degassing procedure, 2) as the amount of H within the melt decreases, so does the difference in H content between the melt and the bubble(s) as there is less of a diffusion gradient between bubble and melt so the rate at which H enters the bubble decreases.

The results of the degassing experiments are tabulated in Table 4.3. The results are presented linearly (in the order they were performed) and separated into three groups by alloy type; pure Al, 5083 alloy and 7010 alloy. The temperature range during degassing, the gas composition used and the total time taken to degas the melt from 0.35 to 0.15 ml/100g are listed for each experiment. As batches of experiments (e.g. all of the experiments using pure Al) were done on a single day the relative humidity for that day (RH%) was also recorded, determined using the average local met-office published figures. The times at which the alloy was changed or metal of the same type was replaced, (to prevent chlorides in the melt interfering with further experiments of the same alloy type) are noted, as are

probe changes, and used to separate out each batch of experiments. No probe failures occurred during the analyses but probes were noted to have failed after being removed from the melt, left over night and re-inserted into the melt, most likely due to thermal shock.

No results for low temperature range pure Al degassing are given because the lower temperature range (680 – 695^{o}C) temperature was close to the solidification temperature of the pure Al, approximately 660^{o}C.

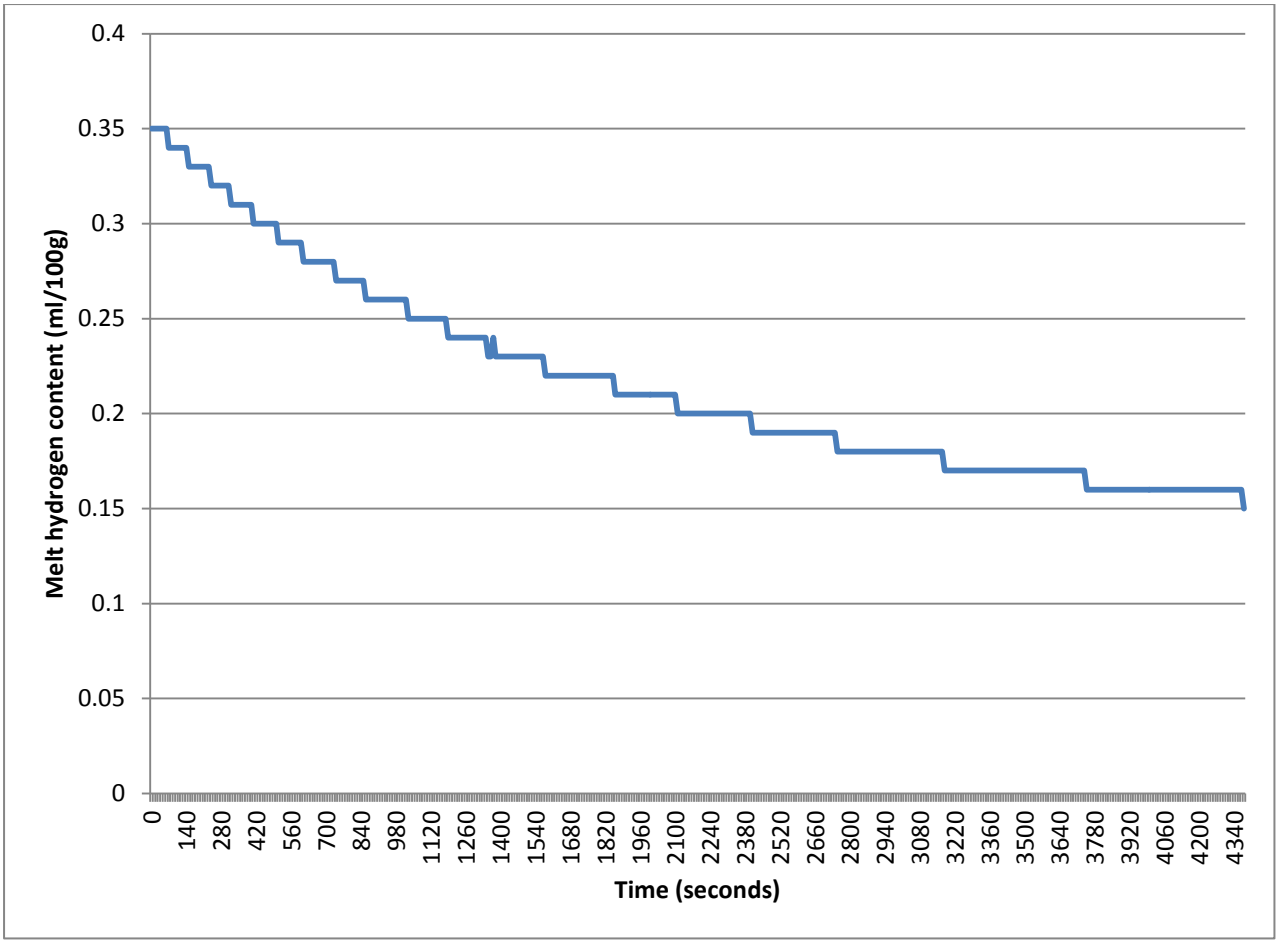

Figure 4.58 The degassing curve of pure Al using a static lance (experiment one) measured using ALSPEK H.

Experiment reference number	Alloy	Temperature range	Gas composition	Relative humidity (RH%)	Time to degas the melt (minutes)	Mean degassing time (minutes)
#1	Pure Al	730 - 750^{o}C	Ar	79	73	
#2	Pure Al	730 - 750^{o}C	Ar	79	60	66.5
#3	Pure Al	730 - 750^{o}C	Ar + Cl	79	71.5	71.5
*Pure Al – 5083 alloy change						
#4	5083	730 - 750^{o}C	Ar	89	49	
#5	5083	730 - 750^{o}C	Ar	89	33	41
#6	5083	730 - 750^{o}C	Ar + Cl	89	45	
#7	5083	730 - 750^{o}C	Ar + Cl	89	35	40
*Fresh 5083 alloy melt prepared and probe changed.						
#8	5083	680 - 695^{o}C	Ar	74	46	46
#9	5083	680 - 695^{o}C	Ar + Cl	74	40	40
* 5083 – 7010 alloy change						
#10	7010	730 - 750^{o}C	Ar	76	36	
#11	7010	730 - 750^{o}C	Ar	76	33.5	34.75
#12	7010	730 - 750^{o}C	Ar + Cl	80	56.5	
#13	7010	730 - 750^{o}C	Ar + Cl	80	50	

#14	7010	730 - 750°C	Ar + Cl	80	48	51.5
*Fresh melt prepared and probe changed.						
#15	7010	680 - 695°C	Ar	68	42	38.5
#16	7010	680 - 695°C	Ar	68	35	
#17	7010	680 - 695°C	Ar+ Cl	68	60	55.5
#18	7010	680 - 695°C	Ar+ Cl	68	51	

Table 4.3 The experimental results of the ALSPEK H experiments.

4.5.1: Comparison of pure aluminium, 5083 alloy and 7010 alloy

The pure Al melt was shown to take a relatively long time to degas when compared to the 5083 and 7010 alloys. The mean time taken to degas the pure Al using Ar was 66 minutes compared to 41 and 35 minutes for the 5083 alloy and the 7010 alloy using Ar, respectively. The variation in degassing time between 5083 and 7010 alloy degassed with Ar in the 730 - 750°C range, was 6 minutes (an overall variation of approximately 15%). The variation is likely due to the differences in relative humidity (RH%) at the time of these experiments. The RH% was higher in the 5083 alloy compared to the 7010 alloy (89% RH and 76% RH respectively) which is likely to of led to the increased rate of H absorption into the 5083 alloy, slightly decreasing the overall rate of H removal.

Pure aluminium, 730 - 750°C temperature range, Ar / Ar + Cl comparison

When the pure Al was degassed using Ar and Ar + Cl there was very little difference in degassing efficiency. When degassed using Ar only, the melt H content decreased from 0.35

– 0.15 ml/100g in 73 and 60 minutes (experiments #1 and #2). When the pure Al was degassed using the Ar + Cl mixture the degassing time was 71.5 minutes (experiment #3). By comparing experiment #1 and #3 directly there was only a 90 second difference in degassing time and this suggests that the reaction between molten Al and Cl gas during the degassing process (to form aluminium chloride, $AlCl_3$) had no apparent influence on the removal rate of H.

5083 alloy, 730 - 750°C temperature range, Ar / Ar + Cl comparison

The average time to degas the 5083 alloy in the 730 – 750°C range using Ar was 41 minutes and when using Ar + Cl was 40 minutes. At this temperature any $MgCl_2$ (which is proposed in the literature to affect the degassing efficiency of aluminium alloys, see section 2.5.7) formed should be a liquid and this should (theoretically) effect degassing rate, but there was no apparent variation in degassing efficiency detected during these measurements.

5083 alloy, 680 - 695°C temperature range, Ar / Ar + Cl comparison

There appeared to be very little difference between the data obtained when the 5083 was processed at using the two different temperature ranges, 680 - 695°C compared to 730 - 750°C.

7010 alloy, 730 - 750°C temperature range, Ar / Ar + Cl comparison

The degassing rate of the 7010 alloy was observed to be affected by the addition of Cl. The average degassing rate for the Ar experiments was 34.75 minutes, compared to 51.5 minutes for the Ar + Cl mixture, a variation of 32.5%.

7010 alloy, 680 - 695°C temperature range, Ar / A r+ Cl comparison

The Cl additions were observed to have an increased influence on the degassing rate of the 7010 alloy in the lower (680 - 695°C) temperature range. The experiments that degassed the melt using Ar only achieved degassing on average in 38.5 minutes compared to the Ar + Cl mixture which took on average 55.5 minutes, an increase of 30%.

In both temperature ranges the 7010 alloy was observed to have been affected significantly by the presence of Cl, with degassing rates being reduced significantly when using Cl additions.

4.6 Degassing of aluminium and analysis of hydrogen absorption using LECO.

In this section the LECO H determination device is evaluated as a degassing tool and to add confidence that the device is capable of accurately assess the H content of Al samples.

The two 5083 alloy samples that were degassed ten times using the LECO and left in laboratory air conditions were re-analysed ten weeks later and both had picked up H by reaction with water vapour in the air, as shown in Figure 4.59. This presumably occurred because the 5083 alloy contains a relatively high Mg content (4.5 wt.%) and was therefore covered with a Mg oxide layer. Mg oxide is porous and not protective and allows further reaction between the metal and the environment. The two samples were shown to have picked up almost as much H as the initial reading, suggesting that this was the limit to which the alloy could absorb H. This limit is probably dictated by a combination of lattice defects and internal pore structures, the combined volume of which would provide a maximum H content for each sample.

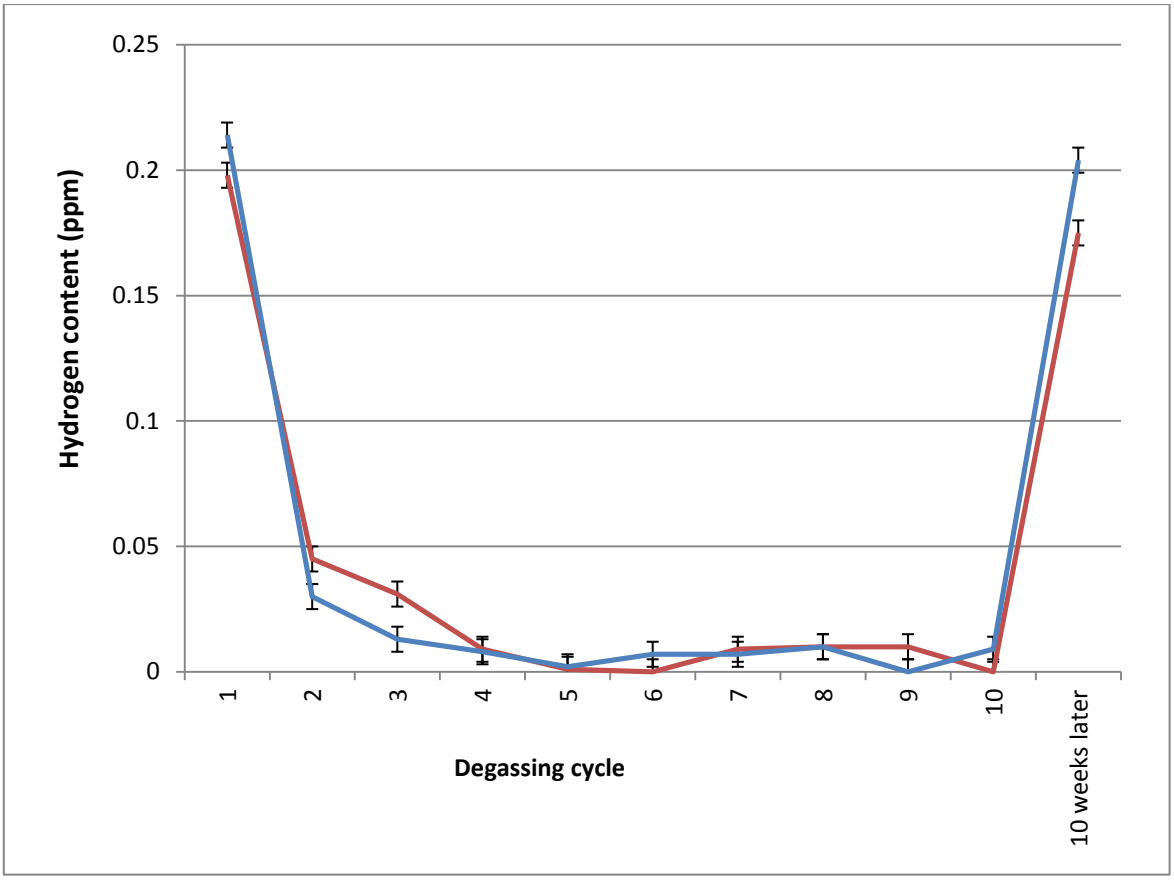

Figure 4.59 Two 5083 alloy LECO samples that were degassed 10 times and then left in a laboratory environment for 10 weeks absorbed H from water vapour in the air.

Analysis cycle number	Sample 1 (ppm)	Sample 2 (ppm)
1	0.198	0.214
2	0.045	0.03
3	0.031	0.013
4	0.009	0.008
5	0.001	0.002
6	0	0.007
7	0.009	0.007
8	0.01	0.01
9	0.01	0
10	0	0.009
10 weeks later	0.175	0.204

Table 4.3 The degassing of two 5083 pin samples using the LECO. The samples are analysed 10 times and then subsequently tested ten weeks later. Both samples were observed to of re-absorbed H.

The results for the other 5083 alloy samples that were degassed using the LECO (degassed 3 times) and analysed over a number of days or weeks before being re-analysed are shown in Figure 4.60. The average degassed value shows the mean value of H that remained in the samples after they were degassed using the LECO. One sample was then analysed every 24 hours to measure the H absorption. The rate of absorption was shown to occur rapidly over the first 24 hours (1 day), and then absorption proceeds relatively slowly over the following 7 days (48 hours = 2 days 72 hours = 3 days, 96 hours = 4 days and 168 hours = 7 days). The

first sample, (left for 24 hours before being analysed), was observed to have absorbed 0.09 ppm of H. After four days had past the average H content was still only 0.09 ppm. It was only after 336 hours (14 days) that the H content was observed to increase markedly, from an average of 0.085 to 0.125 ppm.

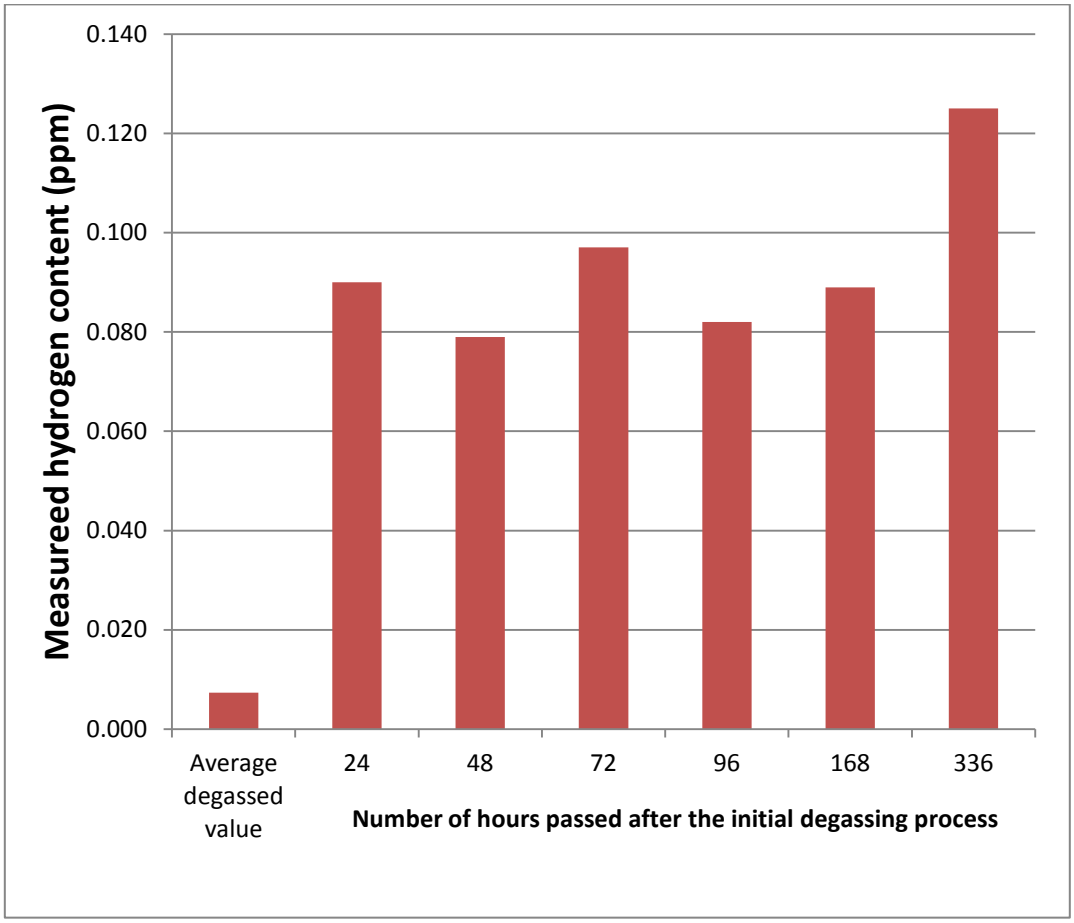

Figure 4.60 The absorption of H into 5083 alloy pin samples over time.

The results for the 5083 samples degassed and placed in different environments were analysed and the results are shown in Figure 4.61. Each sample was processed in the LECO three times, (referred to as degassing cycles #1, #2 and #3 in Figure 4.61), and a decrease in H content was observed after each cycle. The fourth column shows the amount of H extracted from a fourth analysis cycle, which was performed after the sample had rested in

an environment for four days. The sample submerged in water and the sample in laboratory air absorbed 0.164 and 0.145 ppm of H respectively. In both cases moisture was readily available for reaction with the alloy and provided a source of H for the metal to absorb. The sample that was placed in a sealed container, (i.e. having limited water vapour), was observed to have absorbed only 0.024 ppm of H after four days. The limited amount of water vapour in the container minimised the amount of H and led to less absorption. The sample submerged in acetone also absorbed very little H, only 0.038 ppm, so apparently there was very little reaction between the hydrocarbon and the Al surface. Clearly the practice of washing samples in acetone to remove grease has no significant effect on the measured H content.

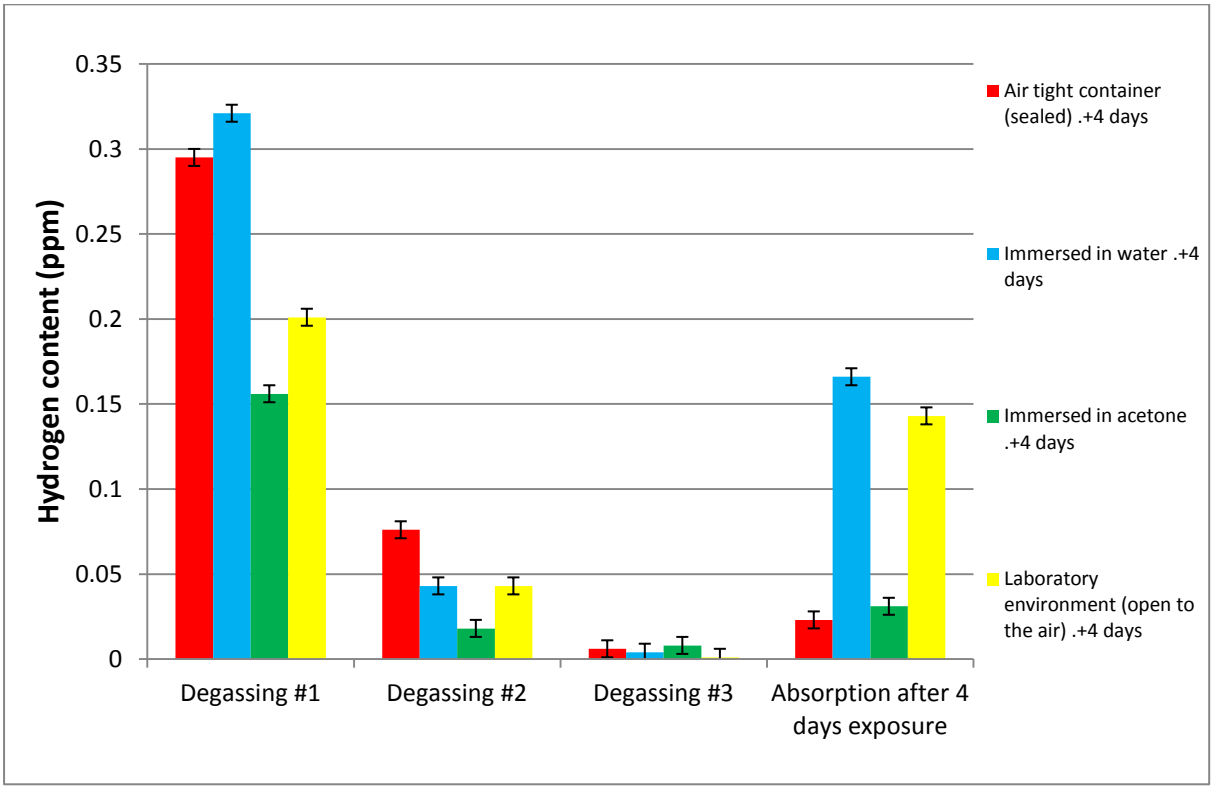

Figure 4.61 The absorption of H into 5083 pin samples that were first degassed three times and then exposed to four different environments for four days.

4.7 Modification of LECO sample surface using air and nitrogen gas

In this section Al samples degassed using the LECO were exposed to either air or N_2 gas, heated to 700^{o}C and held at temperature for 15 minutes. As the samples melted the freshly exposed Al reacted with the O_2 or N_2. Samples were then exposed to H for one hour. The samples were then cooled and immediately transported to the LECO, (transported in sealed glass jars), and the absorption of H was measured. The purpose was to simulate the H absorption into double oxide film defects as they are expected to react with the surrounding melt.

The LECO samples that were heated in the furnace experiments were confirmed to have melted during the procedure, (the samples were observed to have elongated and partially flattened when compared to unprocessed samples). The pure Al 2L99 alloy and 5083 alloy specimens that were heated in air remained predominantly silvery / grey in appearance but the pure Al and 2L99 samples that were heated in a N_2 atmosphere were observed to have become blackened at the surface, shown in Figure 4.62.

Figure 4.62 Pure Al samples heated in a N_2 atmosphere.

4.7.1 Sample H absorption after exposure to pure hydrogen gas, measured using LECO.

Table 4.6.2 shows the atmosphere in which each sample was heated, the degassing results, (each sample was degassed three times), and those values combined to give a total absorption of H. The results were also averaged for comparison, which is also shown in Figure 4.63. The results for the pure Al samples that were heated in air and N_2 were compared against each other using a t-test in order to observe any differences between the two data sets, and these results are given in Table 4.5.

Alloy / Heating atmosphere	LECO #1 (H, ppm)	LECO #2 (H, ppm)	LECO #3 (H, ppm)	Total H extracted (ppm)	Average (mean, H ppm)
Pure Al /Air	0.035	0.005	0.006	0.046	0.041
Pure Al /Air	0.023	0.003	0.002	0.028	
Pure Al /Air	0.03	0.004	0.001	0.035	
Pure Al /Air	0.045	0.005	0.004	0.054	
Pure Al / N_2	0.043	0.01	0.007	0.06	0.081
Pure Al / N_2	0.064	0.012	0.006	0.082	
Pure Al / N_2	0.068	0.01	0.002	0.08	
Pure Al / N_2	0.085	0.014	0.003	0.102	
2L99 / Air	0.024	0.015	0.003	0.042	0.045
2L99 / Air	0.034	0.013	0.001	0.048	
2L99 / N_2	0.022	0.019	0.006	0.047	0.056
2L99 / N_2	0.043	0.02	0.002	0.065	
5083 / Air	0.235	0.067	0.004	0.306	0.279
5083 / Air	0.206	0.039	0.006	0.251	

Table 4.4 The H content of pure Al, 2L99 alloy and 5083 alloy LECO samples heated in air and N_2 atmospheres.

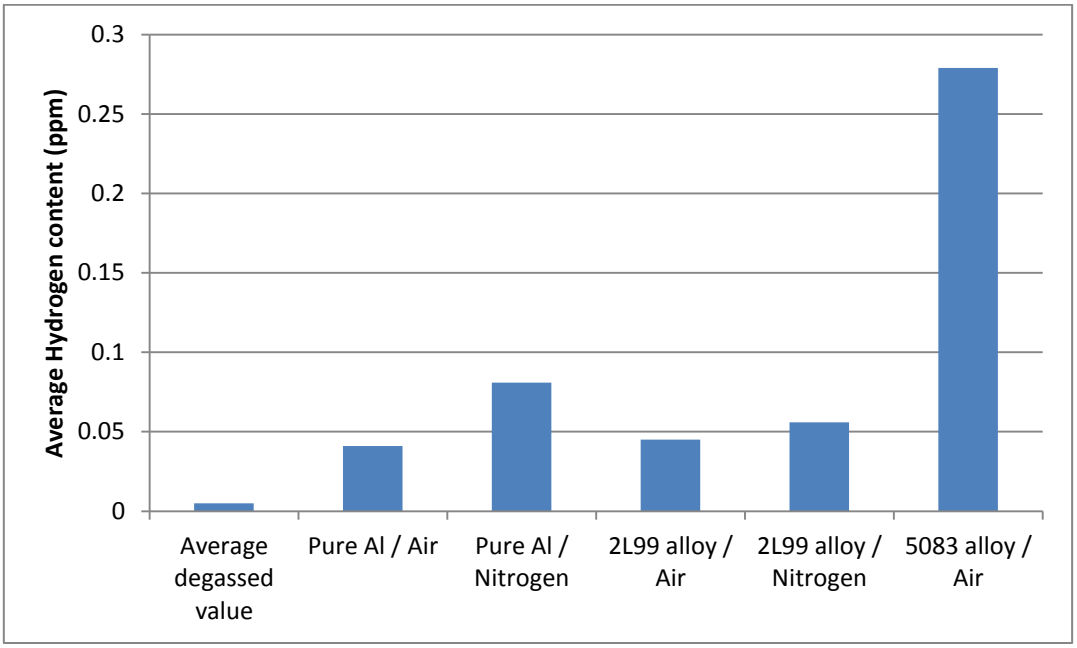

Figure 4.63 The average H content measured using the LECO. The average degassed value is 0.002 ppm H.

Samples absorbed H in the range of 0.028 – 0.307 ppm, demonstrating that H was able to pass into the samples either by diffusing through or circumventing the surface film(s), that is the MgO, Al_2O_3, spinel and AlN layers to be found on the sample surface, at least to some extent.

The 5083 alloy samples heated in air absorbed, on average, 0.279 ppm of H. This occurred presumably because Mg oxide had formed on the surface and was not protective, allowing H to be absorbed. The H absorption into the pure Al samples that were heated in N_2 appears to be greater compared to those that were heated under air, although both sets had absorbed relatively small amounts compared to the 5083 alloy samples. The mean H content of pure Al samples heated in air was 0.041 ppm compared to those heated in N_2, which was 0.081 ppm. The 2L99 samples heated in both air and N_2 were found to be similar, 0.045 and 0.056 ppm respectively. These values are also relatively low when compared to the 5083 alloy samples.

Comparing the measured H absorption of the pure Al samples heated in air and N_2 using a t-test showed that the pure Al samples heated under N_2 absorbed significantly more H (on average 0.081 ppm vs 0.041 ppm) than those that were heated in air, (shown in Table 4.6). The t-test result value was 0.009, so in this instance we reject the null hypothesis and conclude that samples heated in N_2 absorb more H than those heated in air. The 2L99 samples that were heated in air absorbed an average of 0.045 ppm H and those heated in N_2 absorbed an average of 0.056 ppm H. When compared using a t-test these values were not found to be significantly different ($p = 0.42$), so there was no apparent increase in H absorption when these samples were heated under N_2, (shown in Table 4.7).

Pure Al / Air	Pure Al / N_2
0.046	0.06
0.028	0.082
0.035	0.08
0.054	0.102
t-test (p)	0.009

Table 4.5 The total H extracted from pure Al samples heated in air and N_2. The t-test result comparing these two sets is found below.

2L99 alloy / Air	2L99 alloy / N_2
0.042	0.047
0.048	0.065
t-test (p)	0.42

Table 4.6 The total H extracted from 2L99 alloy samples heated in air and N_2.

4.7.3 SEM investigation of the surface of specimens

The Mg oxidised at the surface of the 5083 samples forming MgO, which cracked as it formed (the Pilling-Bedworth ratio of MgO is 0.73, see section 2.2.3). A value less than 1 indicates that the oxide cracks and as the oxide was cracked, when the sample was exposed to H there were few barriers to prevent H from being absorbed into the samples.

The surface of the pure Al specimens before heating was shown to have almost no surface oxidation. This indicated that the Al_2O_3 on the surface was so thin that the interaction volume, the penetration depth of the electron beam was not sensitive enough to evaluate

the oxide film entirely. The machined surface of an Al specimen is shown in Figures 4.64 – 4.66.

When the pure Al samples were heated in air the oxide film was found to have grown, having grown by reaction with the O_2 in the air when the Al was molten. The Al_2O_3 film was found to be covered with cracks, also covered with Al_2O_3, as shown in Figures 4.66 – 4.68. Figure 4.69 shows presumably a large crack that was covered with Al_2O_3. The oxide grew when the crack formed in the original Al_2O_3 layer during heating.

No evidence of AlN formation was found during the examination. The original aluminium oxide film present on the surface of the commercial purity Al is continuous (PBR = 1.12) but would have cracked during heating, due to thermal expansion, as the surface area of the cylinder increased by approximately 20% from room temperature to 700^{o}C. As the oxide film cracked the Al beneath was exposed to the air. Instantaneous oxidation of the Al occurred and this effectively healed the cracks as soon as they formed. When they were exposed to H, the gas diffused through the oxide film and into the sample.

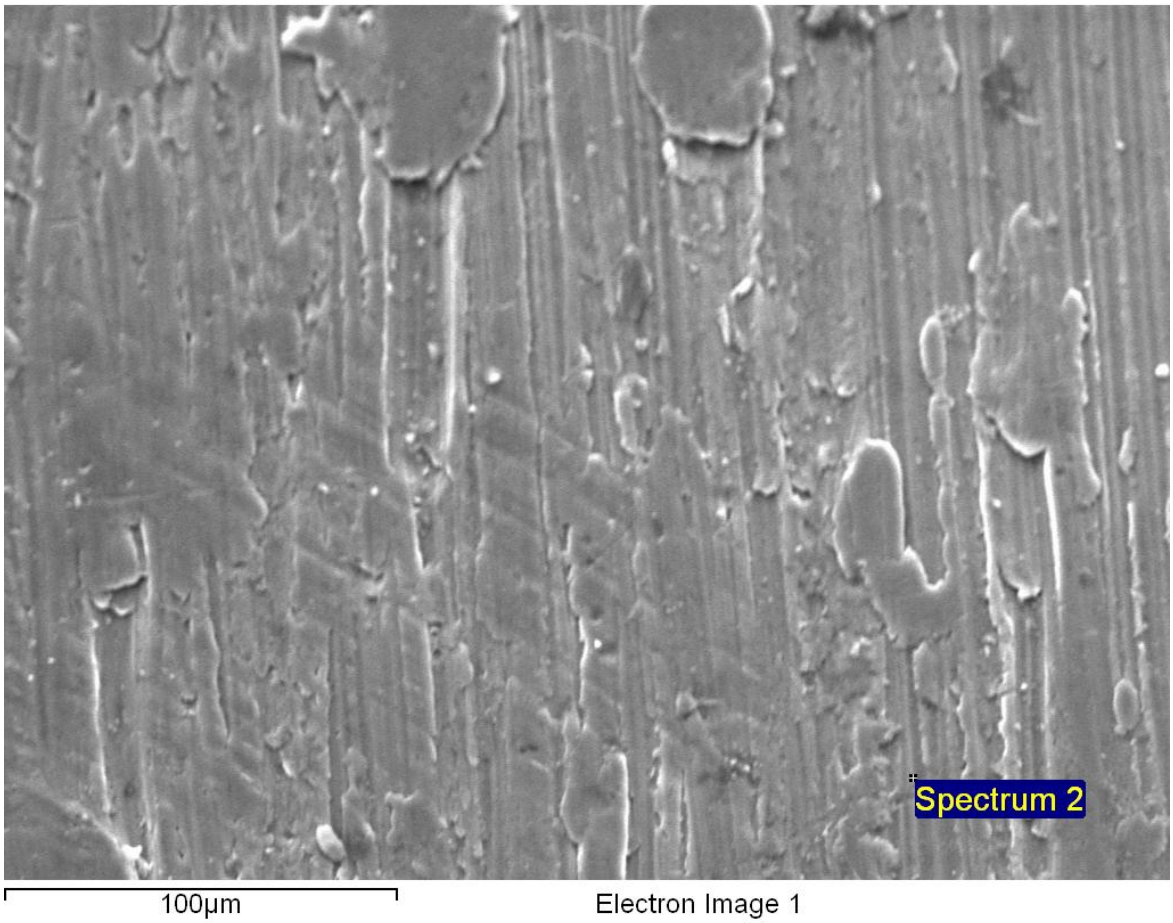

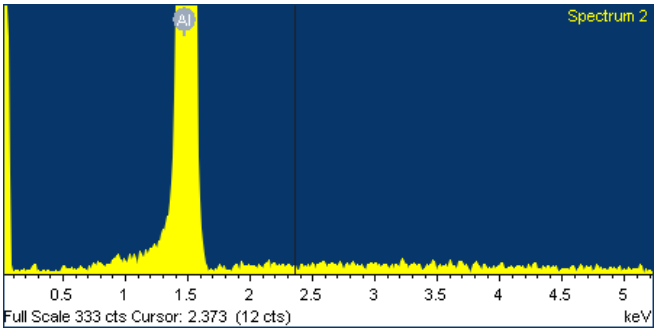

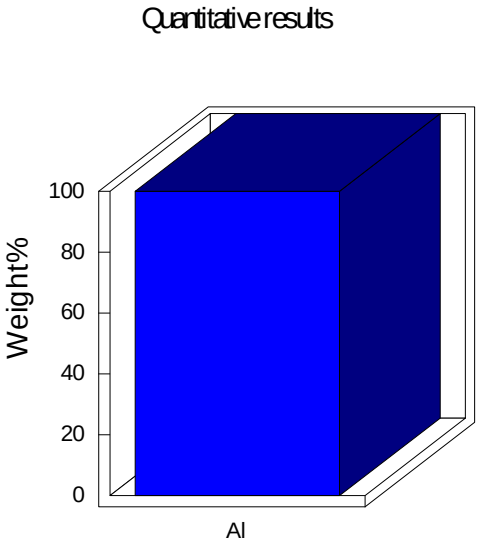

Figure 4.64 SE image of the machined surface of the pure Al samples. No significant traces of oxygen are found.

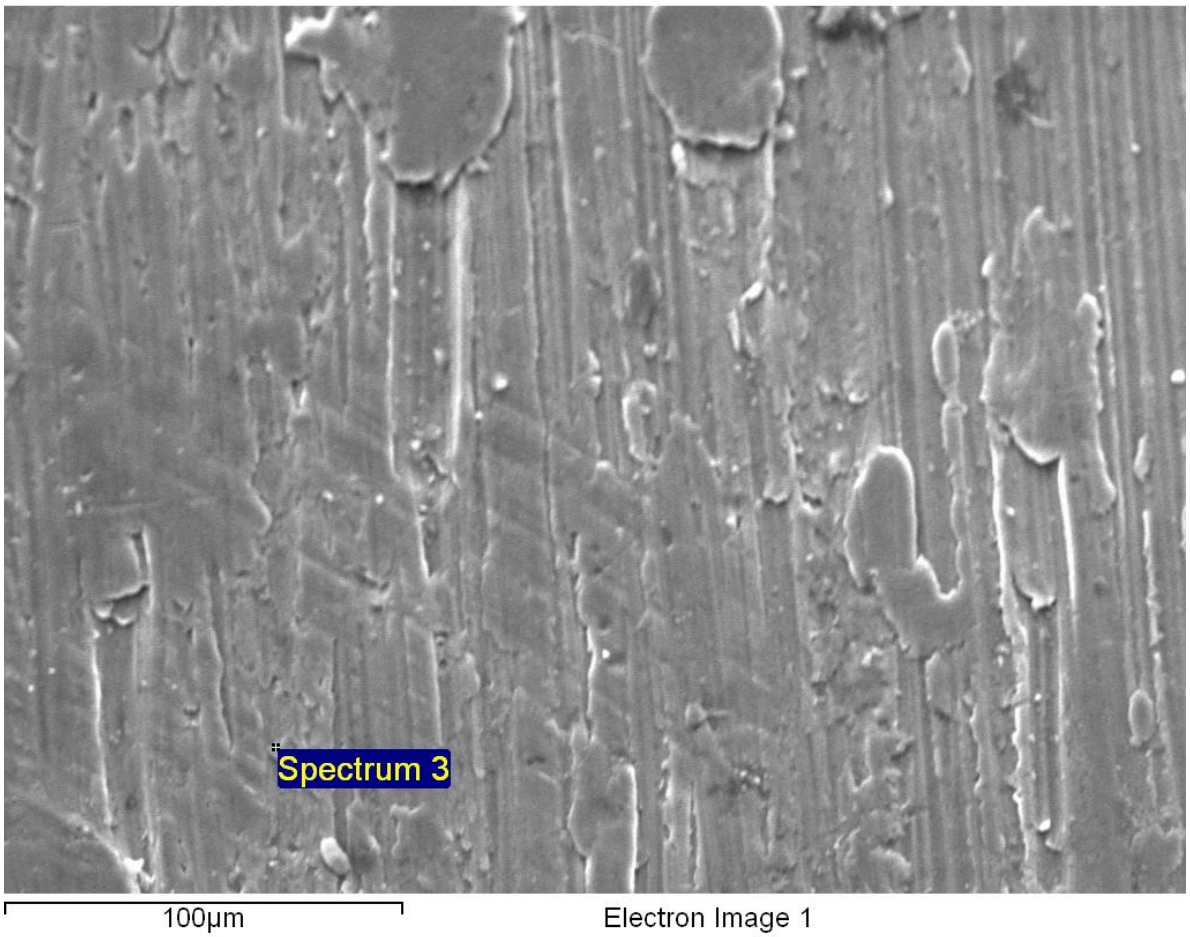

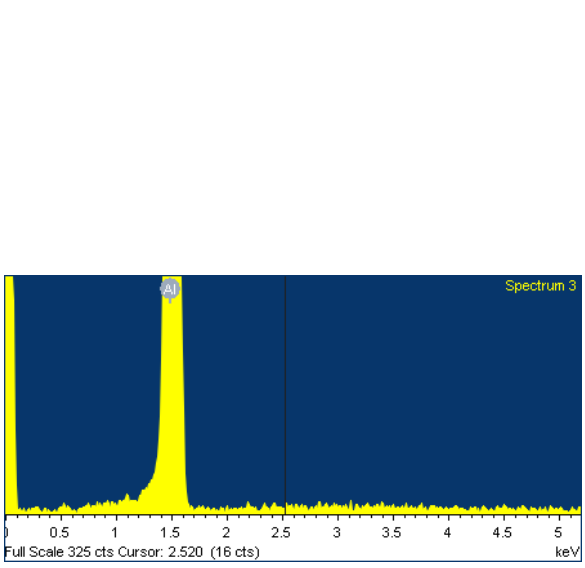

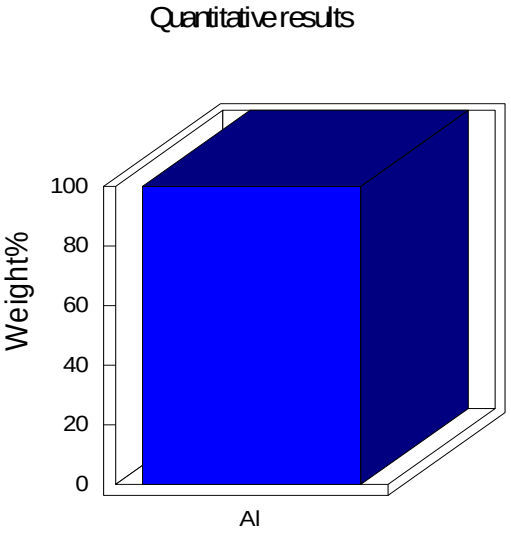

Figure 4.65 SE image of the machined surface of the pure Al samples. No significant traces of oxygen are found.

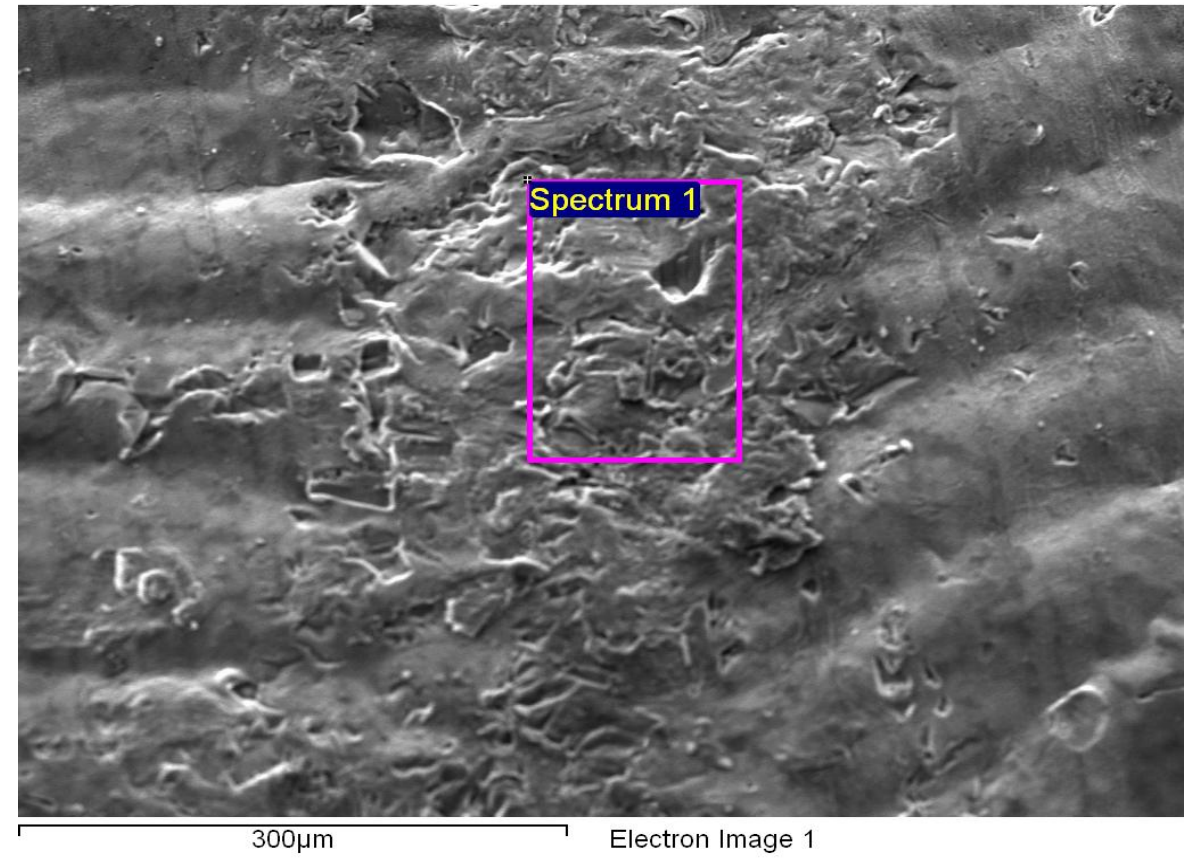

Figure 4.66 SE image of the surface of the pure Al sample heated in air. Surface defects are found to be slightly oxidised.

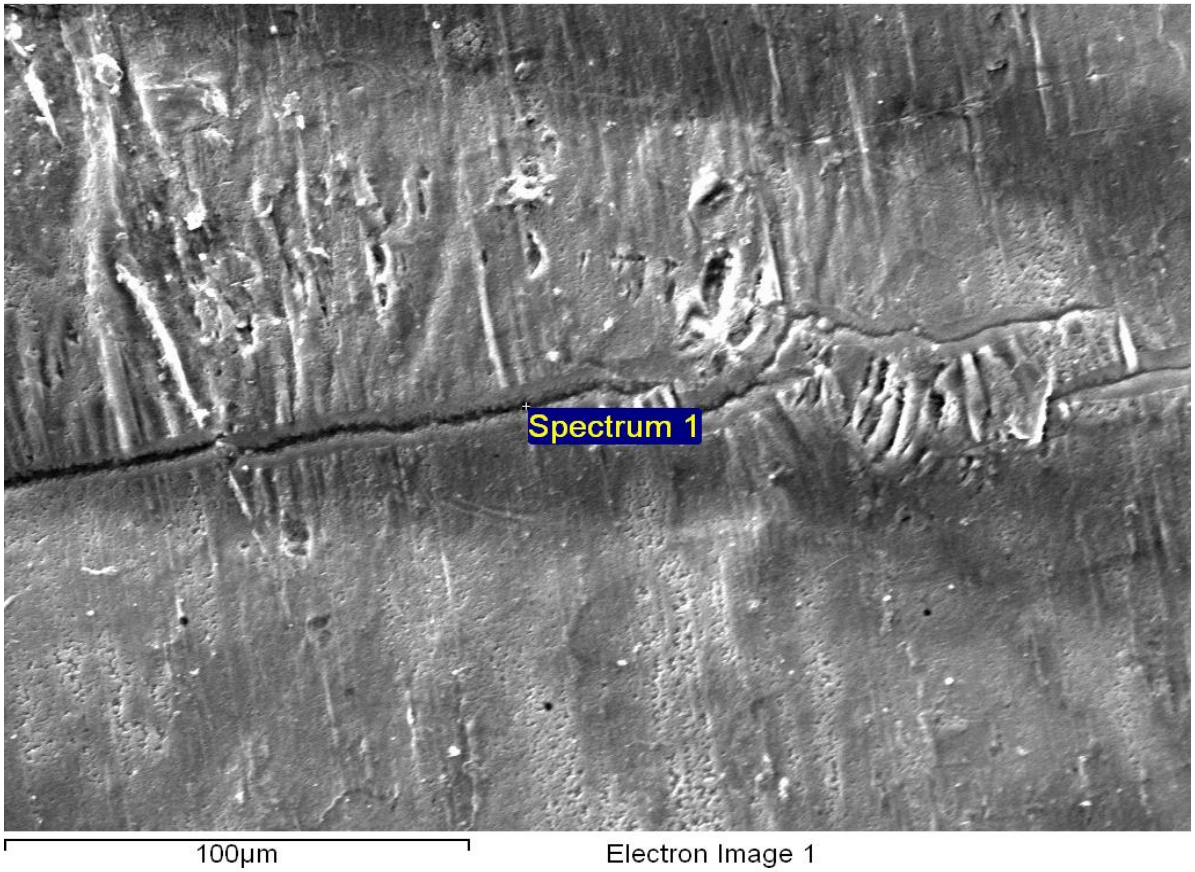

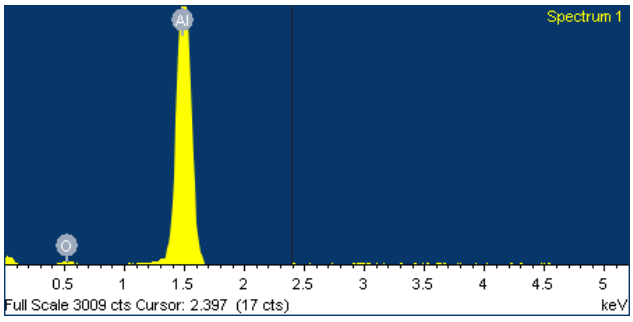

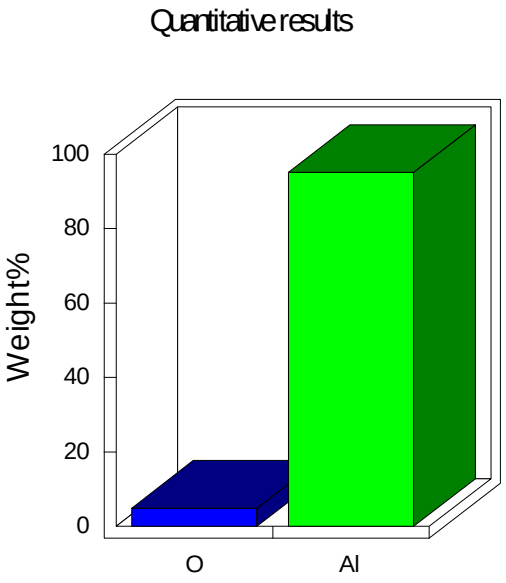

Figure 4.67 SE image of the surface of the pure Al sample heated in air. Small cracks in the oxide film are found to be covered with Al_2O_3.

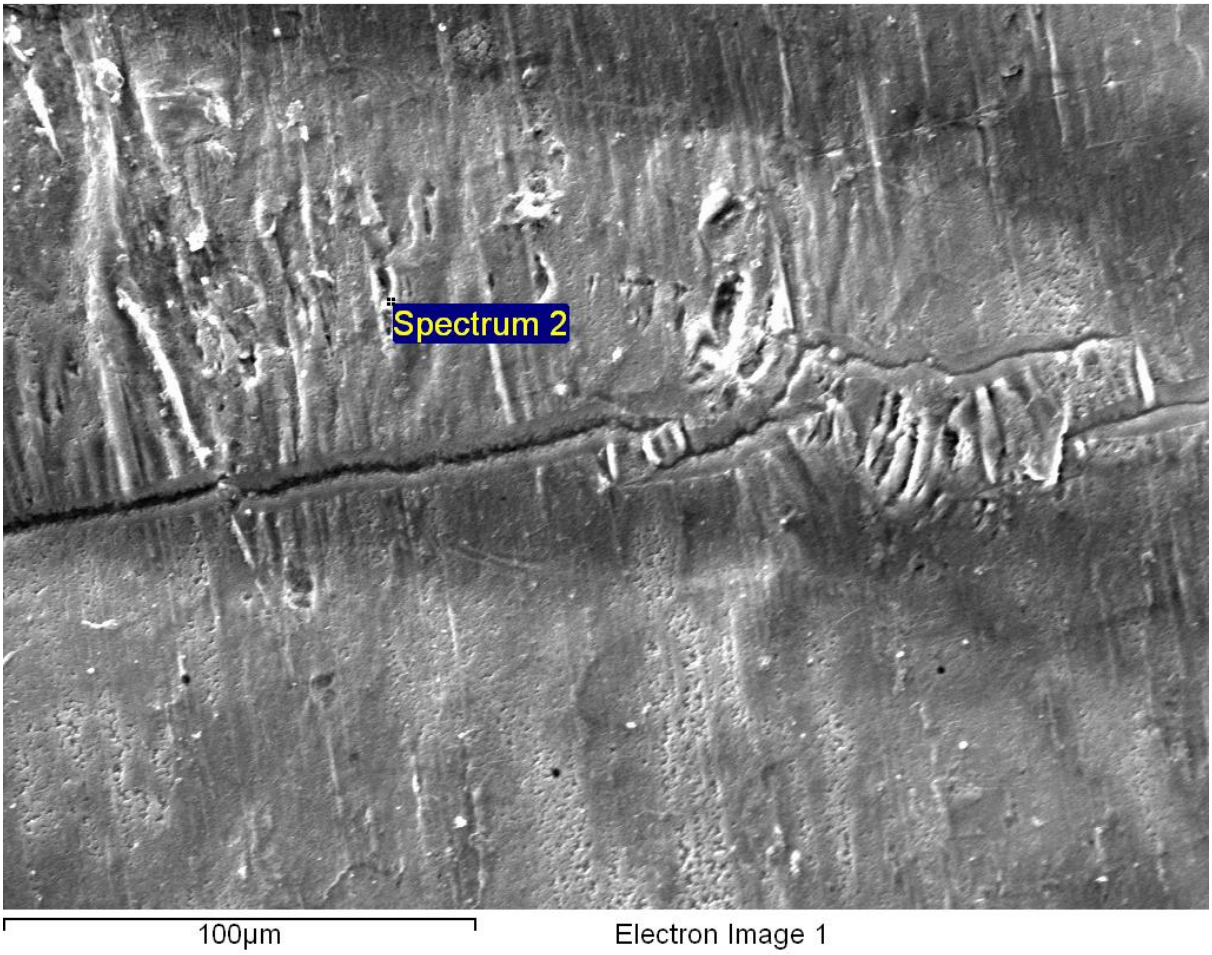

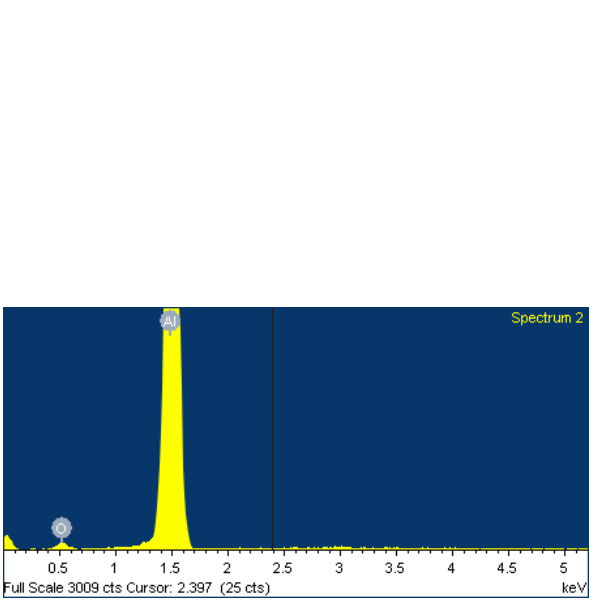

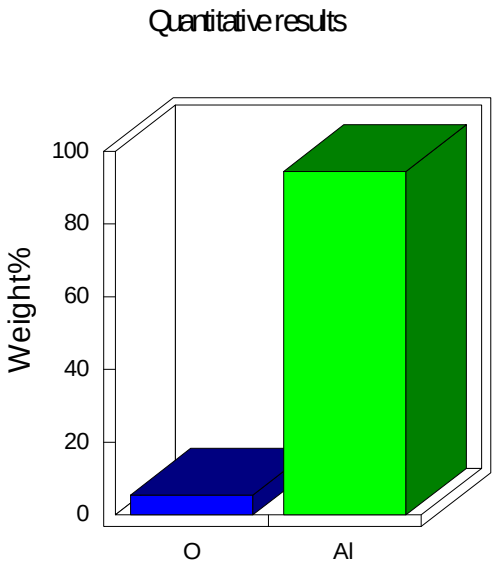

Figure 4.68 SE image of the surface of the pure Al sample heated in air. Small cracks in the oxide film are found to be covered with Al_2O_3, as is the surrounding area.

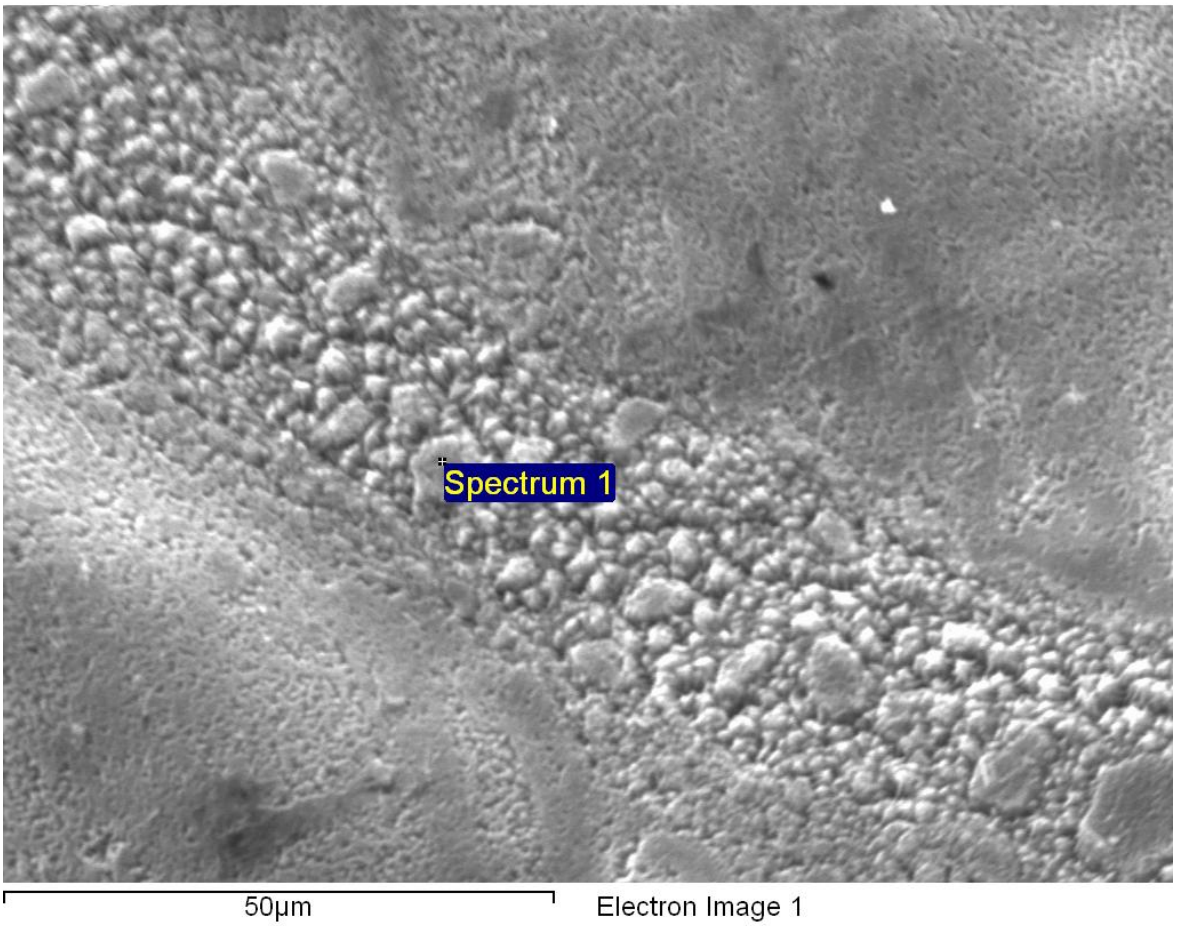

Figure 4.69 SE image of the surface of the pure Al sample heated in air. Larger cracks in the original oxide film are found to be covered with small 'islands' or nodules of Al_2O_3.

The surface of the commercial purity samples heated in N_2 was also found to contain large and fine cracks in the original oxide film, and these cracks varied in size and length just like those in the samples heated in air. Examples of the larger cracks in the oxide film are shown in Figures 4.70 and 4.71.

These cracks were found to be covered with AlN. Evidently when the commercial purity Al samples were heated in N_2, cracks in the oxide film formed and the Al reacted with the N_2 gas to form AlN. An overview of the typical compositions of the cracks and of the area surrounding them is shown in Figures 4.72 – 4.73. The composition of the oxide and nitride change across the five different areas are described below:

a) Spectrum 1 (Figure 4.72) shows the original Al_2O_3 layer, with a very thin layer of nitride formed on, in or around it.
b) Spectrum 2 (Figure 4.72) shows a large crack (approximately 10 µm width), is observed to be covered with a film composed of a mixture of both Al_2O_3 and AlN in roughly equal quantities. These large cracks were distributed across the entire surface of the specimen
c) Spectrum 3 (Figure 4.72) shows a fine crack in the Al_2O_3 film (approximately 5 µm width). The AlN appears to be found in its highest concentration along this type of crack when considering the quantitative weight % analysis of spot 3 in Figure 4.74.
d) Spectrum 4 (Figure 4.73) shows a mixed Al_2O_3 and AlN layer similar to that found in spectra 1.
e) Spectrum 5 (Figure 4.73) shows the typical composition of the bulk of the sample surface. The surface was found to be largely composed of Al_2O_3, although small traces of AlN were found, suggesting that the nitrides were not only forming within

the cracks and the immediate area surrounding them, but were in fact forming across the entire surface of the specimens. The area surrounding the cracks (as shown in spectra 1 and 4 in Figures 4.72 and 4.73 respectively) was found to be composed primarily of Al_2O_3, however evidence of AlN formation was also found, suggesting discrete AlN crystals had formed within the Al_2O_3 layer, as shown in Figures 4.75 - 4.78. These small, discrete AlN crystals presumably formed when very small cracks or pin holes opened up in the oxide film during heating, creating small localised cracks. Although the bulk of the nitrides were concentrated along the large cracks in the Al_2O_3 film, nitrides were actually dispersed all over the specimen surface in the form of these smaller pin holes. On the larger cracks, nitrides appeared to have nucleated from the edge of the crack in the Al_2O_3 layer, and grown inward across the surface, shown in Figures 4.74 and 4.79.

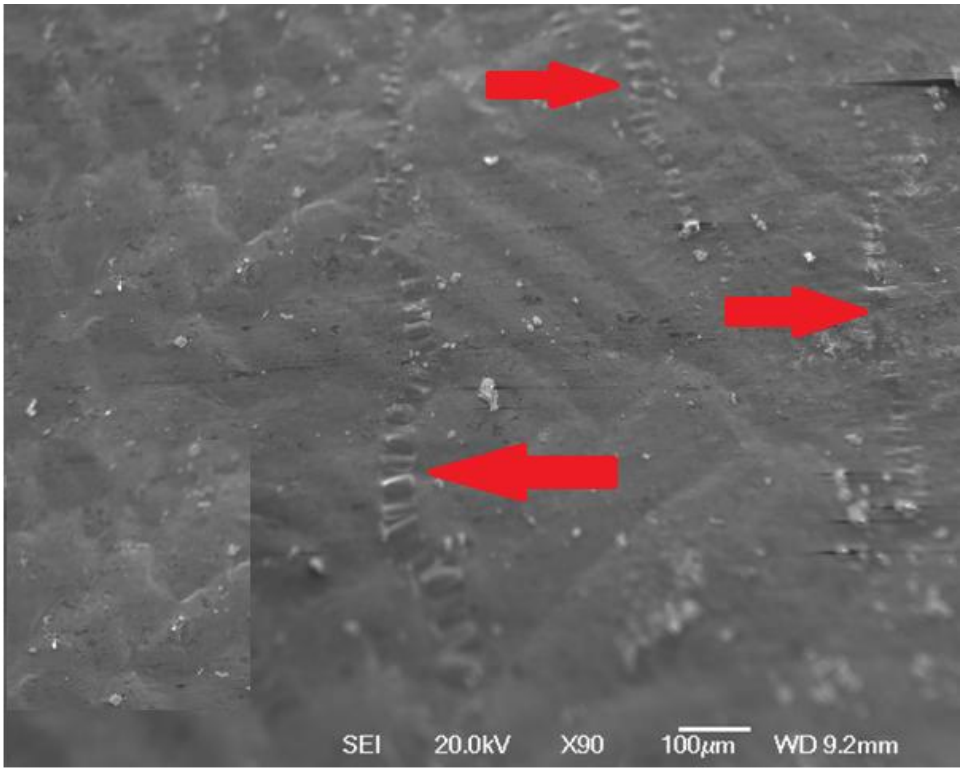

Figure 4.70 SE image of the pure Al sample heated in N_2. Cracks that were observed in the original Al_2O_3 film are highlighted by arrows.

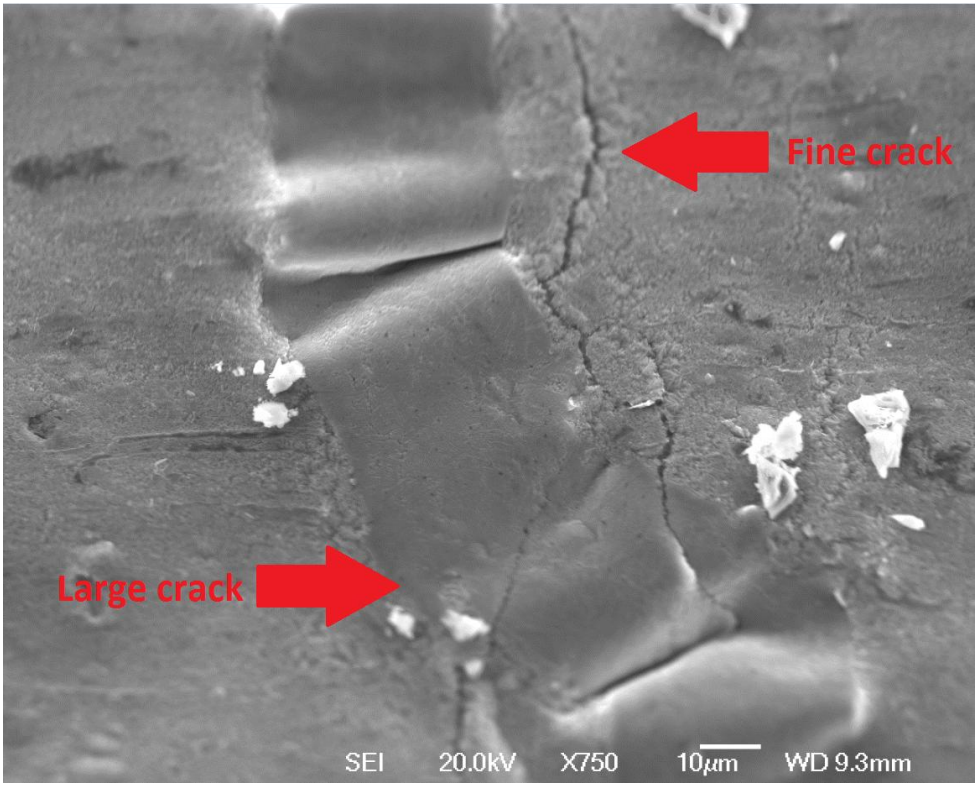

Figure 4.71 SE image of the pure Al sample heated in N_2. Large and small cracks were observed at the sample surface.

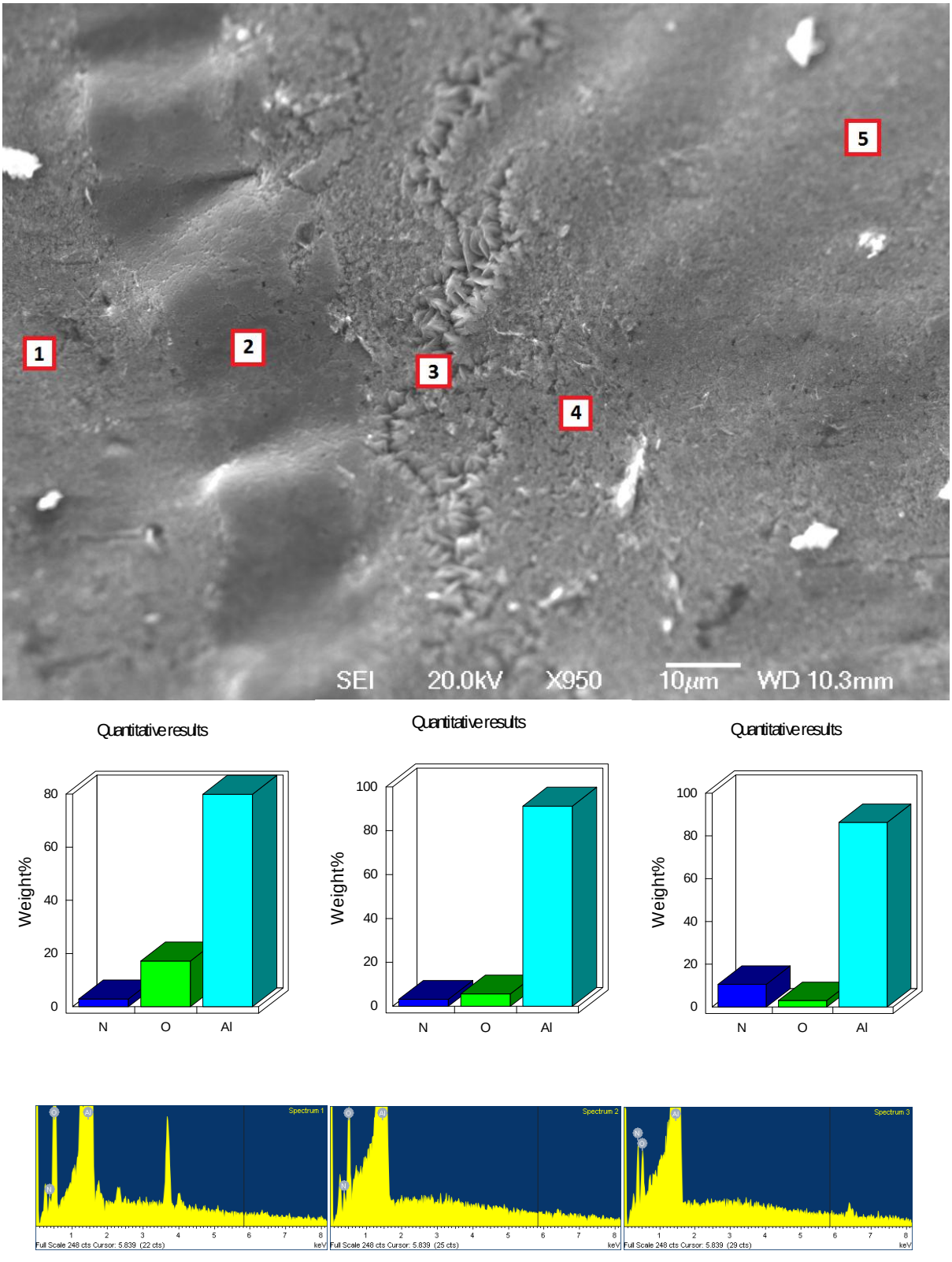

Figure 4.72 SE image of the pure Al sample heated in N_2. The composition of spectrum scans 1, 2 and 3. Nitrides are found concentrated on cracks in the Al_2O_3 film.

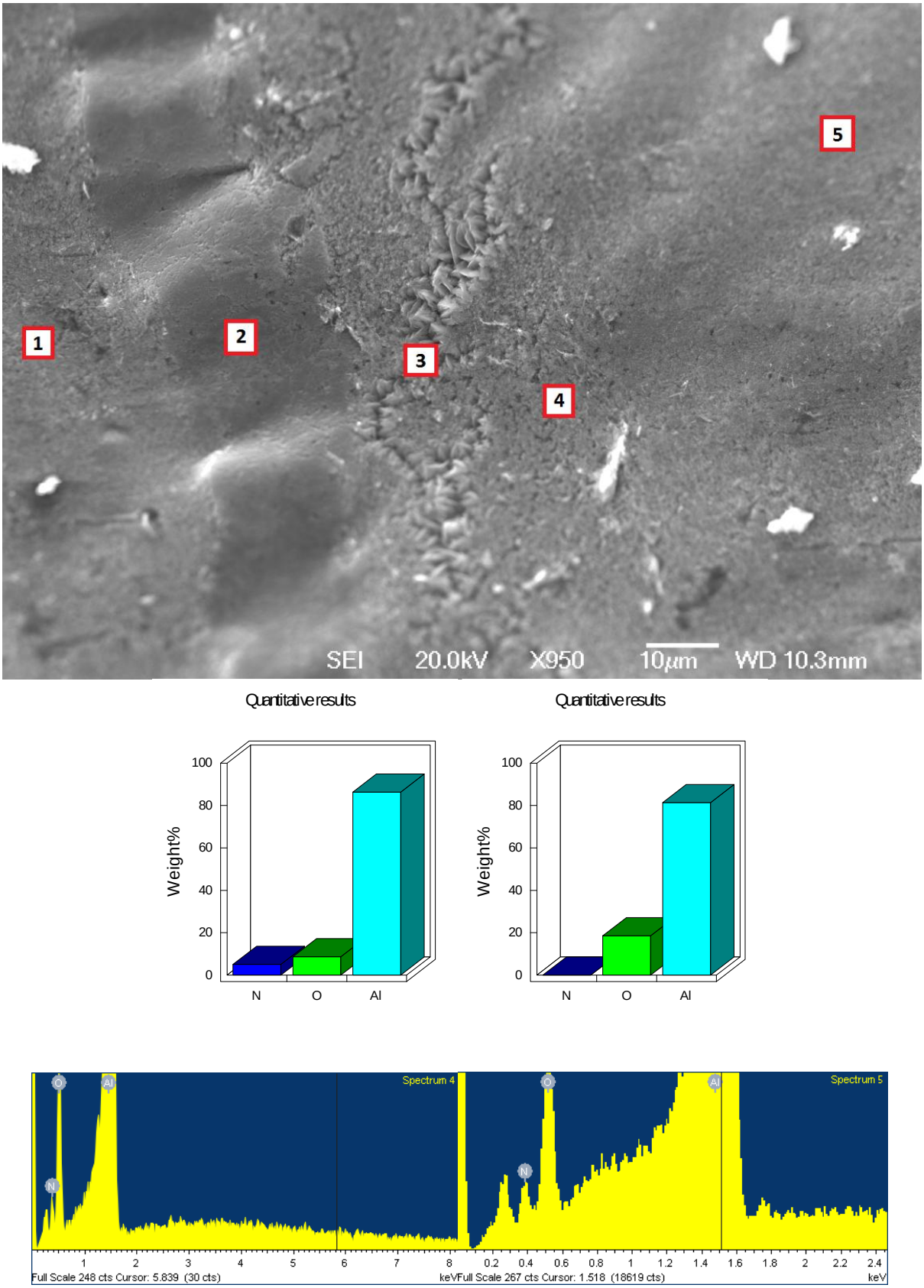

Figure 4.73 SE image of the pure Al sample heated in N_2. The composition of spectrum scans 4 and 5. Nitrides are found concentrated on cracks in the Al_2O_3 film, AlN was also found across the surrounding area.

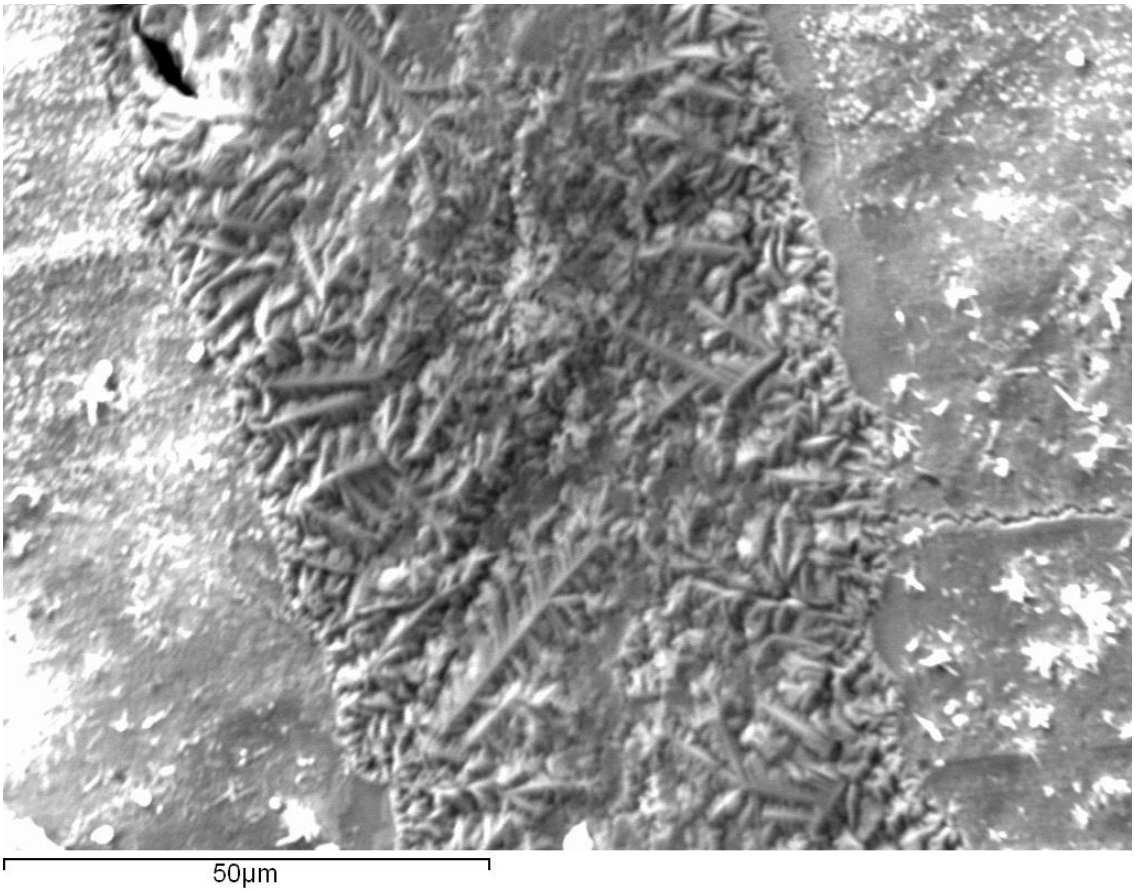

Figure 4.74 SE image of the pure Al sample heated in N_2. Nucleation of AlN crystals appears to have occurred at the edges of a crack that has formed in the original Al_2O_3 film.

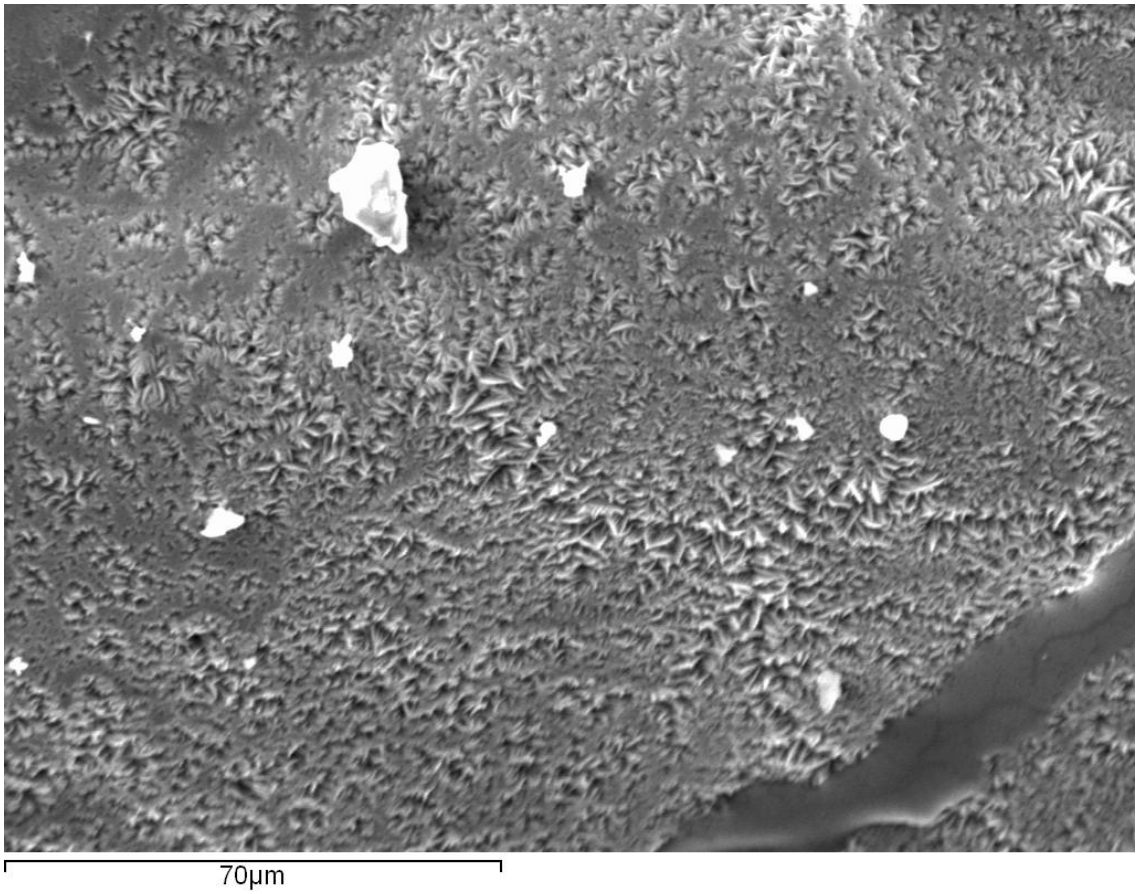

Figure 4.75 SE image of the pure Al sample heated in N_2. An overview of an area surrounding a crack in the original Al_2O_3 film. In this region extensive growth of AlN crystals has occurred within the Al_2O_3.

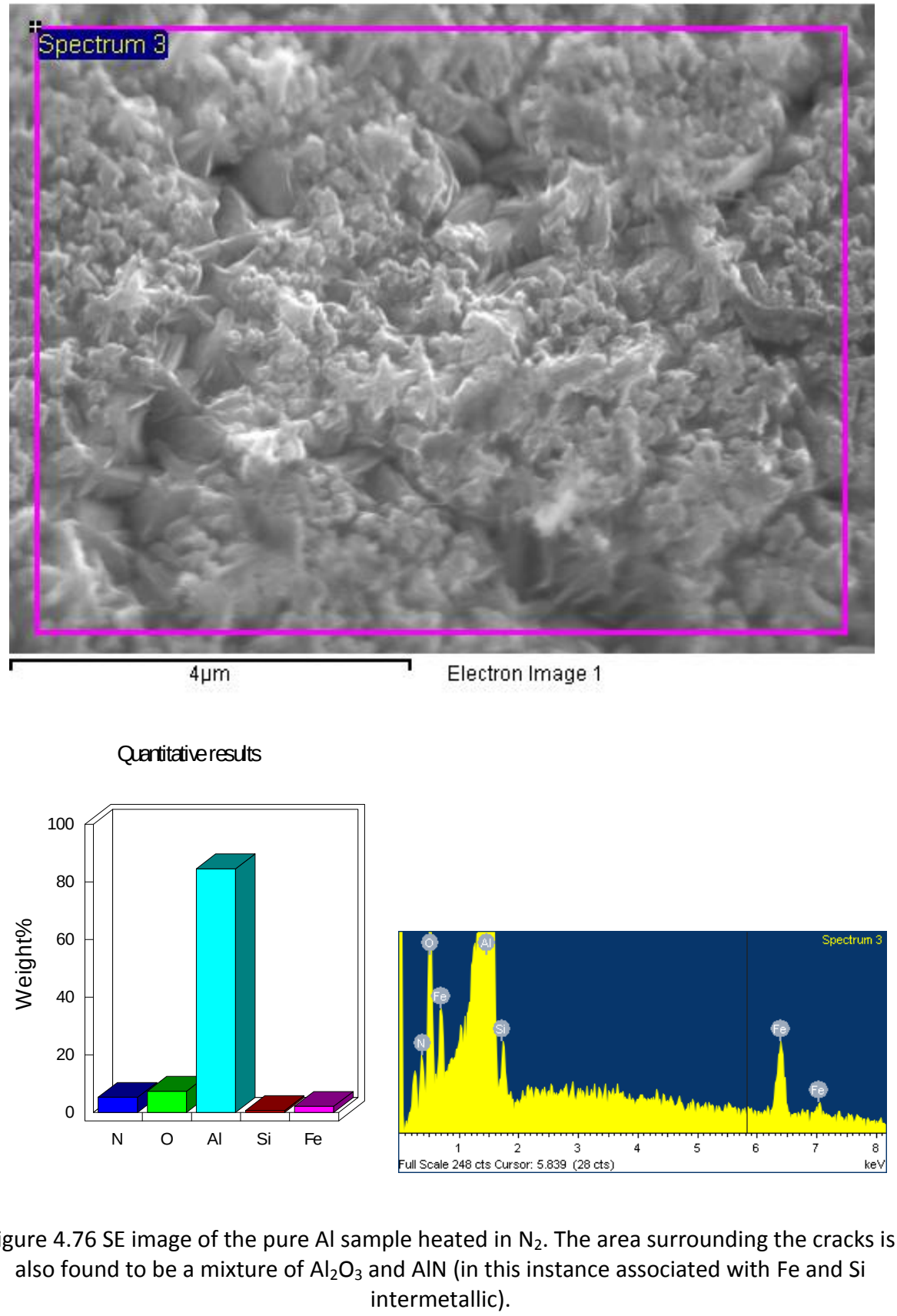

Figure 4.76 SE image of the pure Al sample heated in N_2. The area surrounding the cracks is also found to be a mixture of Al_2O_3 and AlN (in this instance associated with Fe and Si intermetallic).

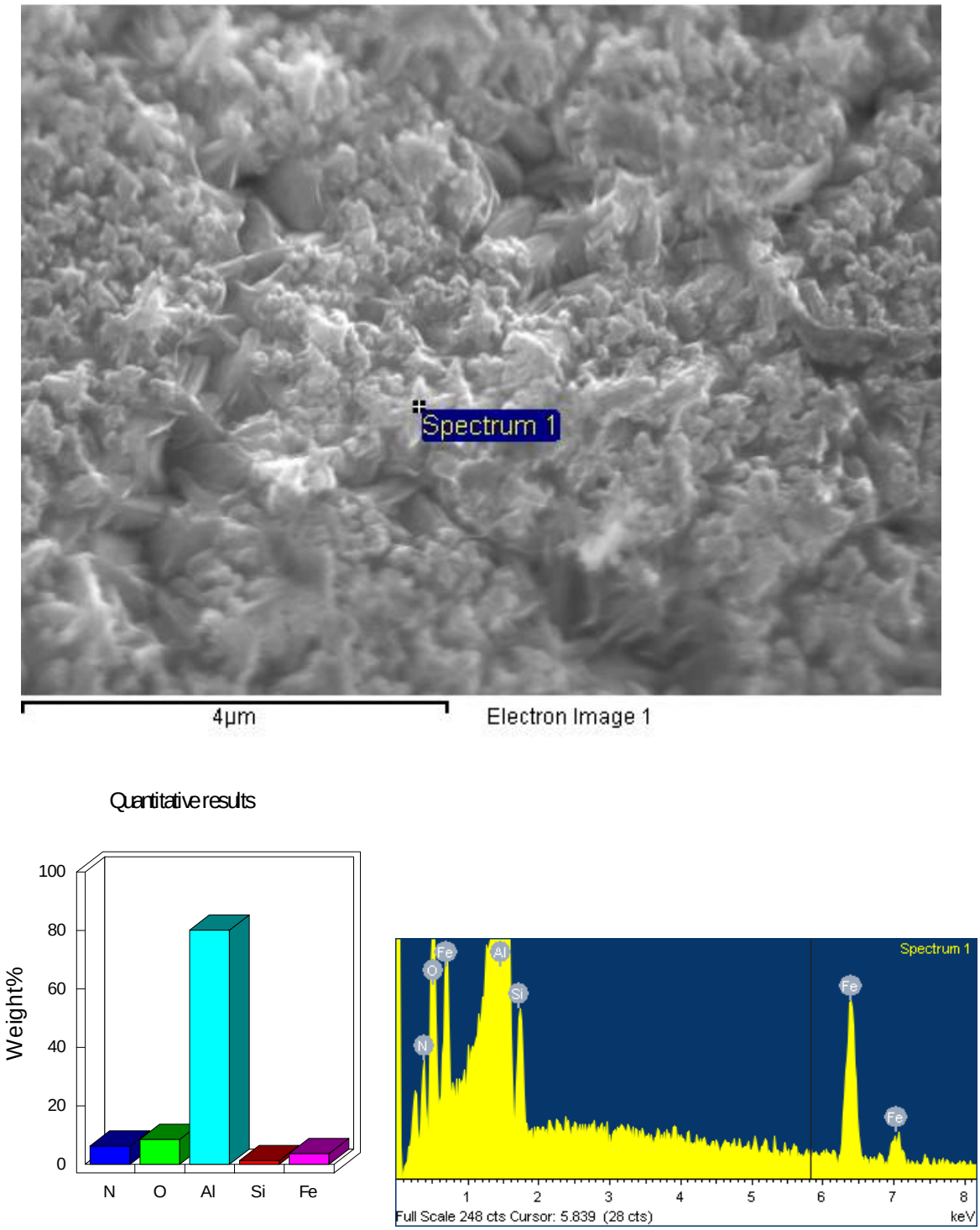

Figure 4.77 SE image of the pure Al sample heated in N_2. The area surrounding the cracks is also found to be a mixture of Al_2O_3 and AlN.

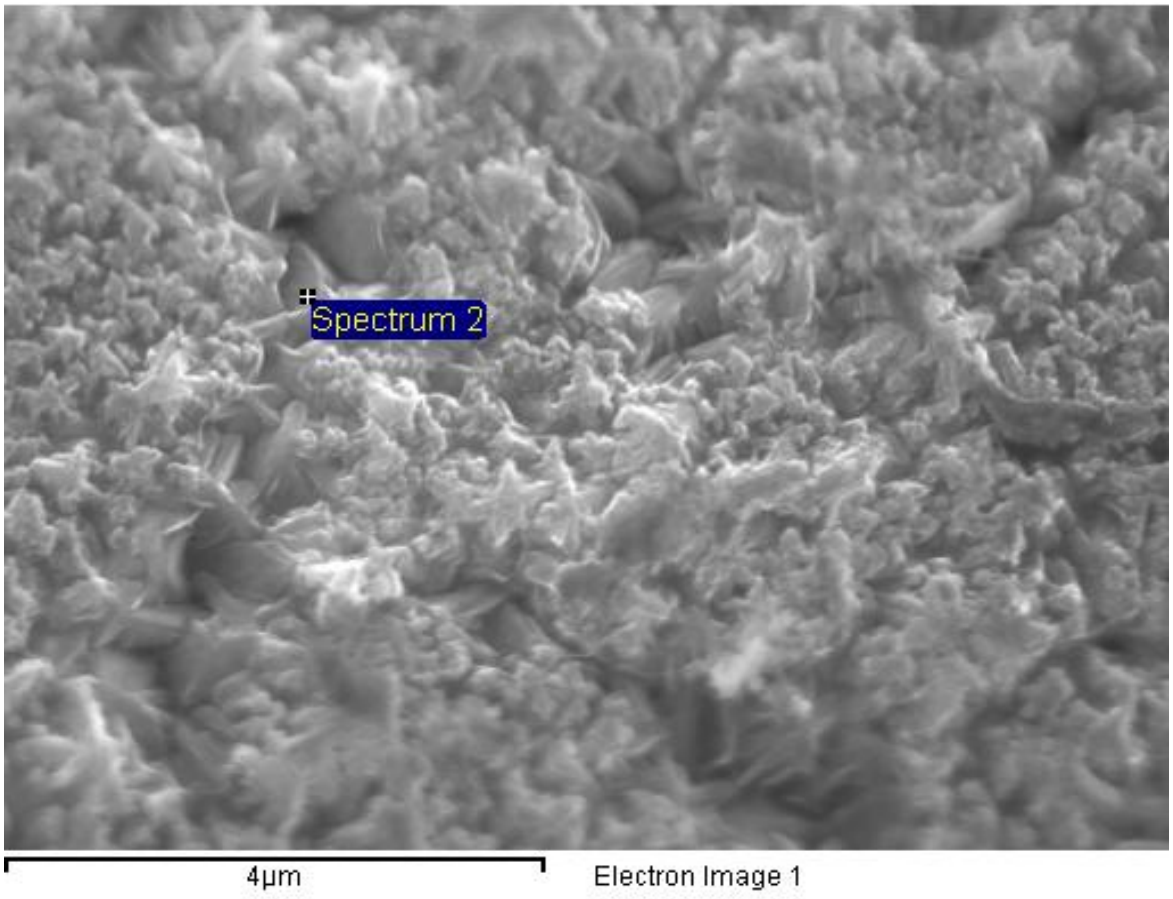

Figure 4.78 SE image of the pure Al sample heated in N_2. The area surrounding the cracks is also found to be a mixture of Al_2O_3 and AlN. The oxide rich area is broken up by the presence of small AlN crystals.

The large cracks (as shown in spectra 2, Figures 4.72 and 4.73) were found to be covered with a fine feather-like dispersion of crystals, as shown in Figures 4.74 and 4.79. The surrounding area was also found to be a mixture of Al_2O_3 and AlN. A seam was visible along the centre of the nitride crystals, shown in Figure 4.79 where the AlN crystals have impinged on one another. Evidently, AlN crystals nucleated and grew from both edges of the original Al_2O_3 film, until they met, impinged, and completely covered the crack.

The fine cracks (as shown in spectra 3, Figures 4.72 and 4.73) were covered with coarser, claw-like AlN crystals, as shown in Figure 4.80. These crystals interlocked in a zip-like fashion and were also surrounded by a mixture of Al_2O_3 and AlN.

The permeability of H into the pure Al samples heated in N_2 was greater compared to the pure Al samples heated in air (0.081 vs. 0.041 ppm H respectively) presumably because the diffusion of H through the nitride crystals was greater (compared to the oxide) and thus these samples absorbed significantly more H. The claw-like coarse AlN crystals shown in Figure 4.80 are interlocked in a zip-like fashion, and it is proposed that the crystal structure has greater permeability of H because of this zip-like morphology. In the mechanism proposed by Nyahumwa et al.[8], once the melt has reacted with the O_2 and the N_2 within the bifilm there remains a small reservoir of Ar into which H can diffuse. The experiments here demonstrate that H can diffuse through both Al_2O_3 and AlN layers, and that the thickness, structure and perfection of these films likely influence the rate at which H can diffuse into the envelope over time.

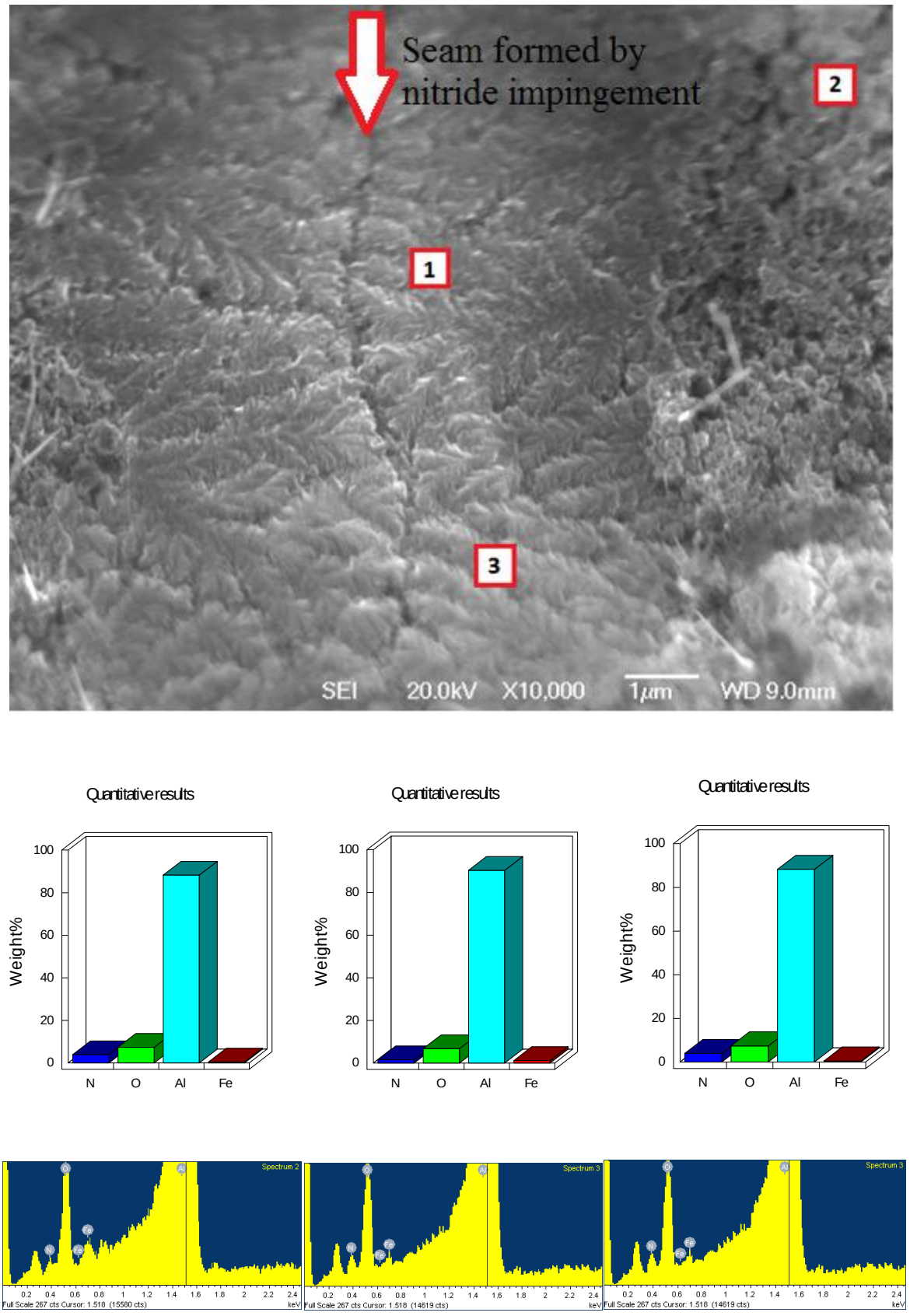

Figure 4.79 SE image of the pure Al sample heated in N_2. The larger cracks in the original Al_2O_3 were covered with a fine dispersion of feather-like AlN crystals, nucleated from the oxide at the edges of the crack.

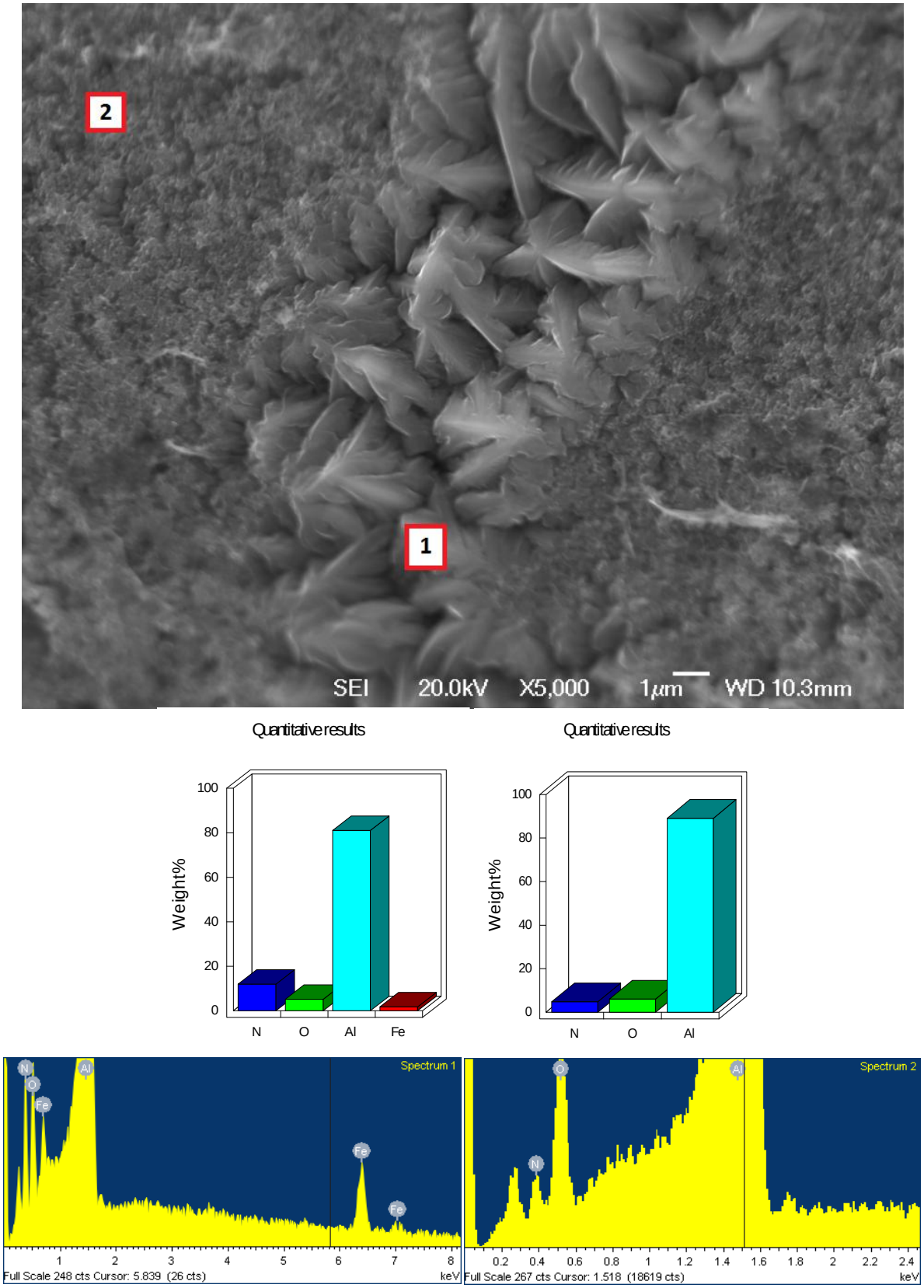

Figure 4.80 SE image of the pure Al sample heated in N_2. The fine cracks in the original Al_2O_3 were covered with coarse, claw-like AlN crystals that were interlocked in a zip-like fashion.

The surface of the 2L99 alloy samples heated in air were observed to be covered with a dispersion of spherical nodular protrusions. EDX analysis showed that some of these nodules appeared to be Si rich, (as shown in Figure 4.81), and others appeared to be low in Si (as shown in Figure 4.82). These protrusions are thought to be spinel and are shown Figure 4.83.

The surface of the 2L99 alloy samples heated in N_2 were also found to be covered with nodular protrusions, but instead of appearing spherical they were more crystalline, being roughly rectangular in shape but with rounded edges, as shown in Figure 4.84. These structures also varied in Si composition, but once again no evidence of nitride formation was found during the examination of the surface. The absence of nitrides seems to suggest that the surface Al_2O_3 layer that was formed was protective in both air and N_2 conditioned samples, and this is likely why not much additional H or nitrogen was absorbed into the 2L99 sample heated under N_2 atmosphere, compared to those heated in air.

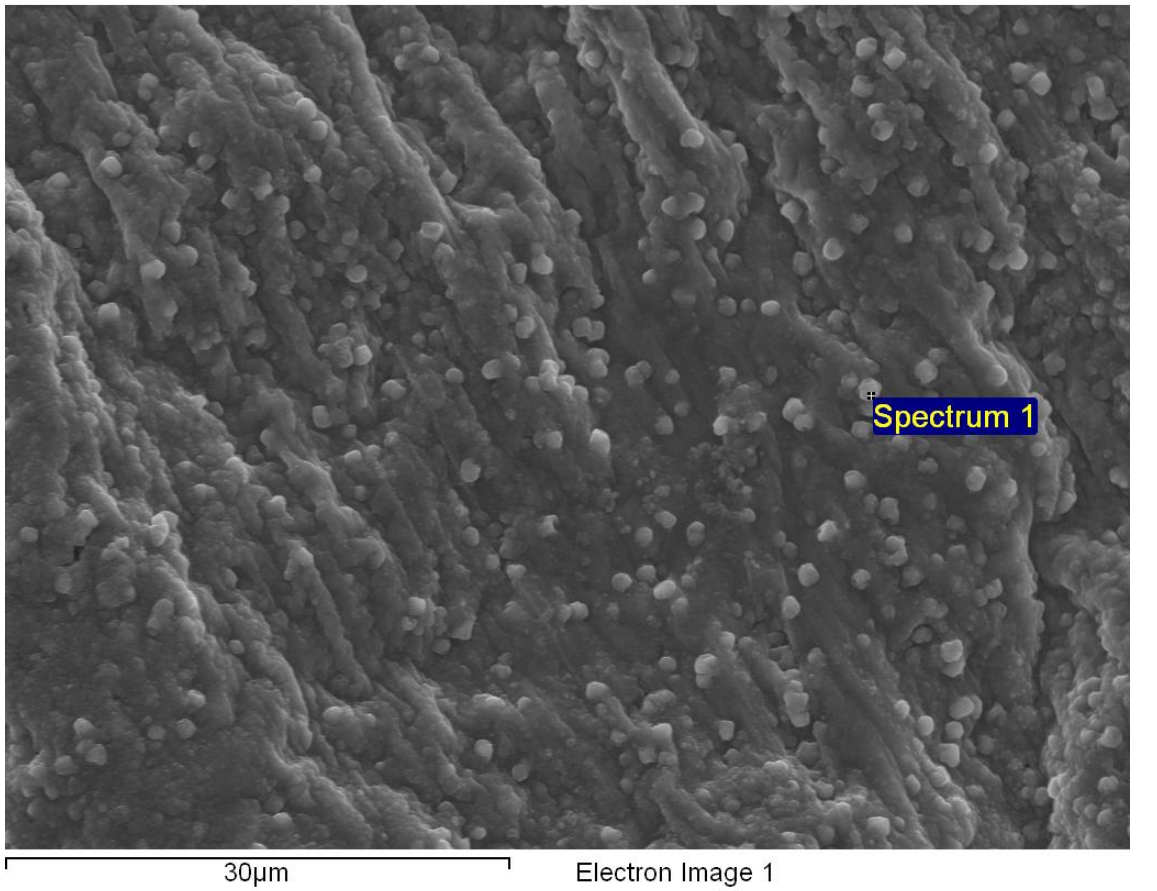

Figure 4.81 Nodular protrusions found on the surface of the 2L99 sample heated in air (SE image). These protrusions are thought to be a mixture Al_2O_3 and MgO.

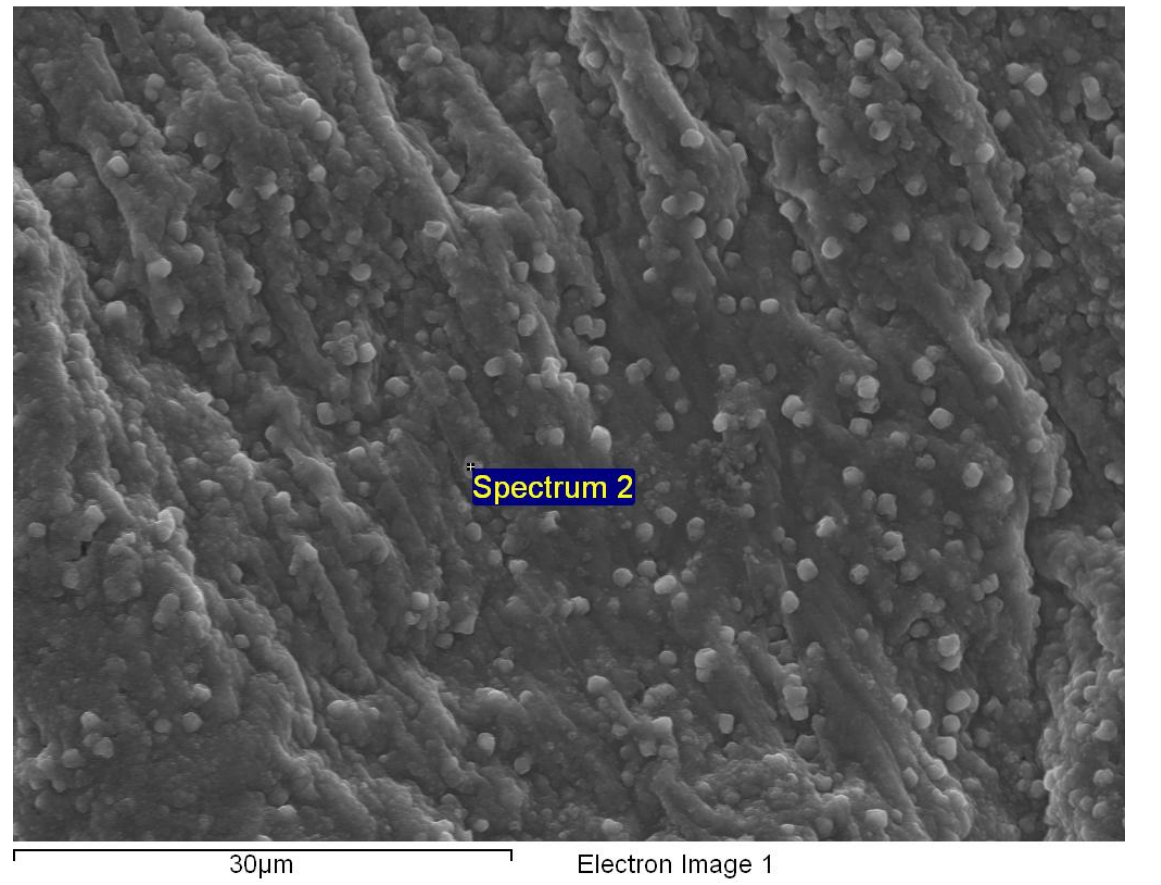

Figure 4.82 Nodular protrusions found on the surface of the 2L99 sample heated in air (SE image). These protrusions are thought to be a mixture of Al_2O_3 and MgO.

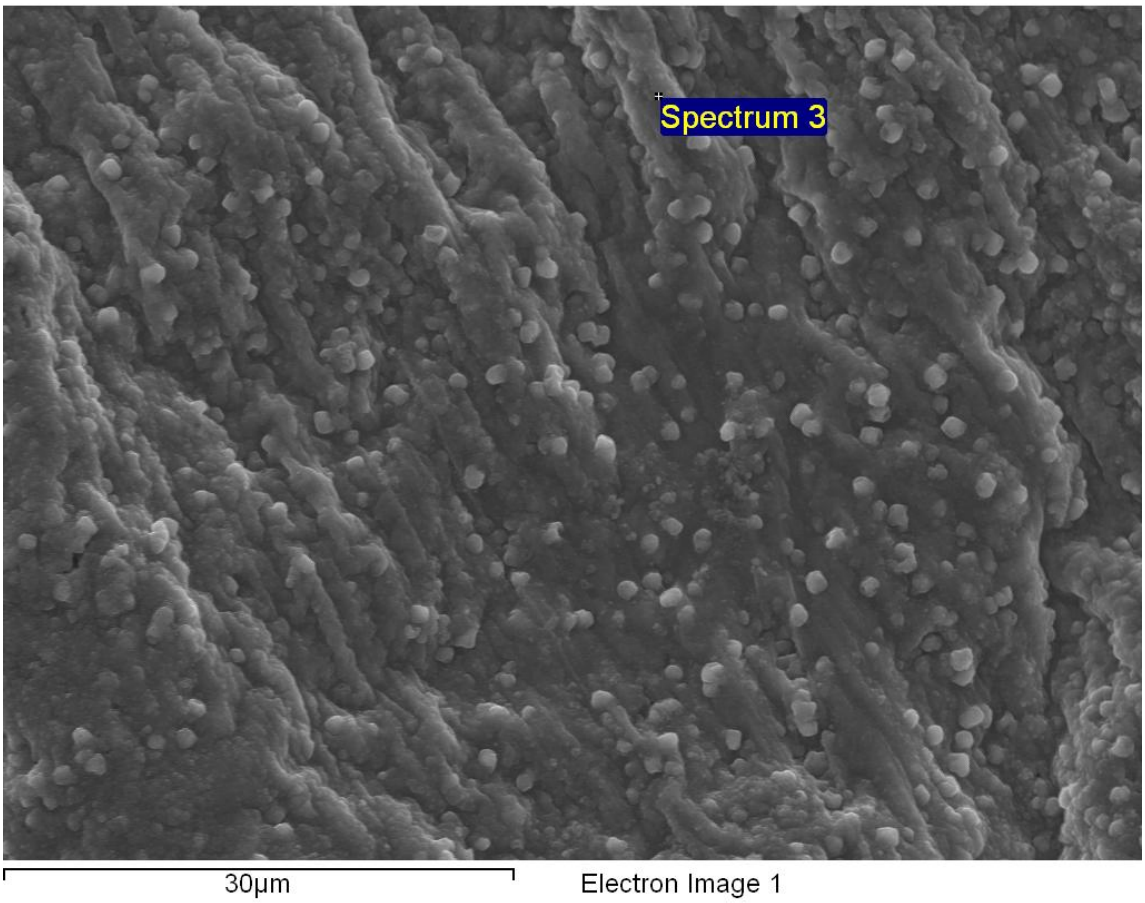

Figure 4.83 Nodular protrusions found on the surface of the 2L99 sample heated in air (SE image). These protrusions are thought to be a mixture of Al_2O_3 and MgO.

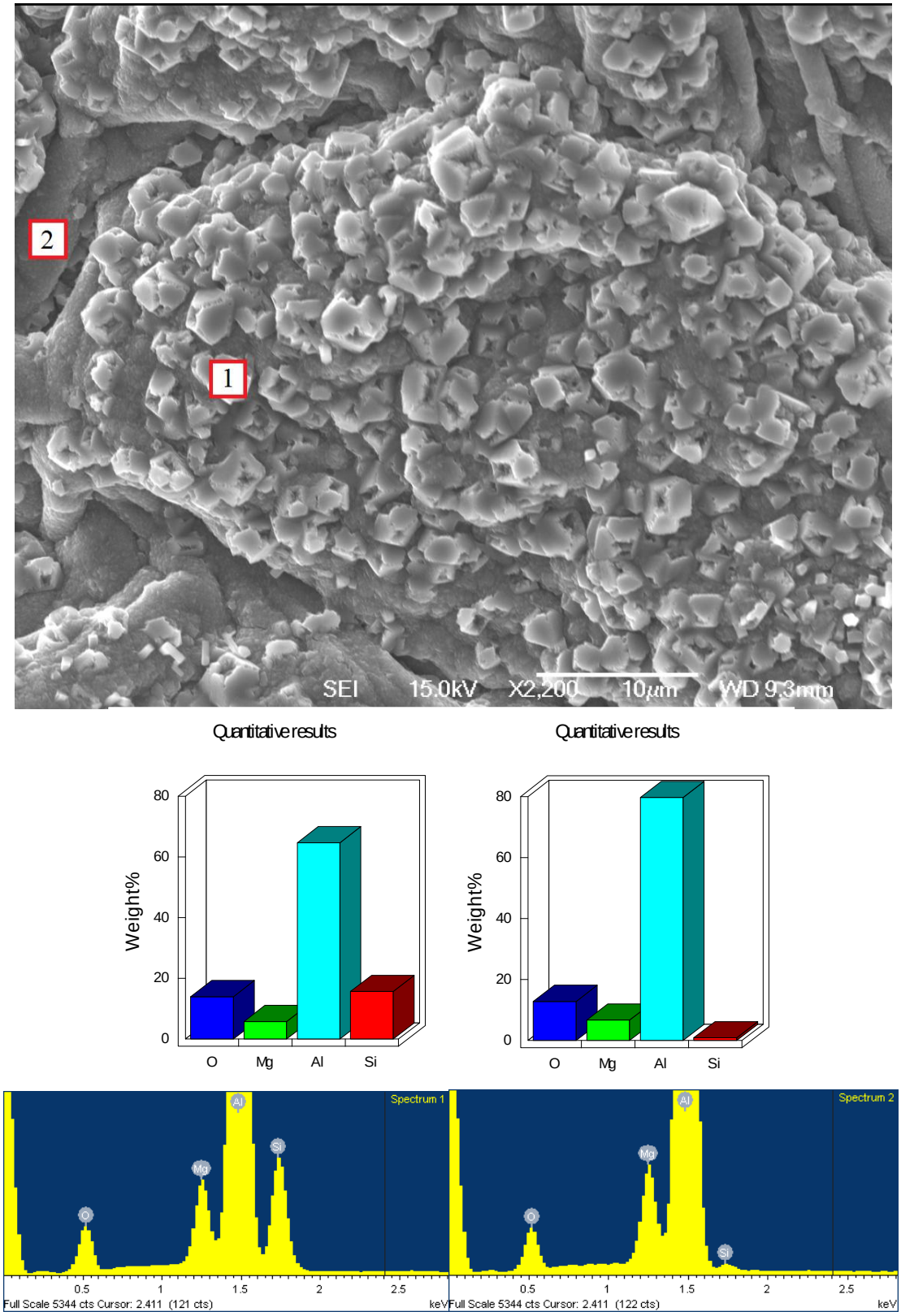

Figure 4.84 Crystalline protrusions were found on the surface of the 2L99 sample heated in N_2 (SE image). These protrusions also varied in Si content, likely due to eutectic beneath the surface, but are thought to be a mixture of Al_2O_3 and MgO.

Chapter 5 Discussion

5.1: Point defect indications in 7050 alloy plate

The point defects identified in 7050 'AE' alloy plate were found to be composed of two phases, as shown in Figures 4.3 – 4.13. One was a mixture of Al, Mg and Ca oxides, combined with $MgCl_2$ and $CaCl_2$. The second phase was a mixture of Zr aluminide and Ti aluminide Intermetallics, $Zr(Ti)Al_3$.

The oxides of Al, Mg and Ca may enter the melt at any point while the metal is molten and exposed to air or water vapour. Oxides can easily up build on furnace walls, and can form a significant part of the dross layer in the degassing unit [162] through submergence of alloying additions, surface metal turbulence, or in any situation where the melt surface is disturbed. There are so many potential sources of oxides that it was impossible to isolate the exact point of origin. Salts, however, are likely formed within the holding furnace or degassing unit as these are the locations where Cl is deliberately added into the melt to remove alkaline metals such as Li, K, Na and Ca, and the salts found in these inclusions are most likely the by-products of such reactions.

It was difficult to establish the exact composition of the salt part of the inclusion as all of the metallic elements will react with Cl to form salts (and the interaction volume of the SEM beam penetrated into the sample, and probably interacted with the alloy as well as the inclusion). All of the SEM images included in this section were made using beam energies of 20 keV and using the equation from Potts the interaction volume was calculated to be 2.1 –

3.4 μm, given that the densities for Al_2O_3, $ZrAl_3$ and $TiAl_3$ are 3.95, 3.4 and 4.1 g/cm3 respectively [163] [164].

$$x\ (\mu m) = \frac{0.1.E_o^{1.5}}{\rho} \qquad \text{Eq.18}$$

where E_o = accelerating voltage (keV) and ρ = density (g/cm^3).

The average Ca content of the 7050 alloy after treatment in the holding furnace and degassing unit (during Q4 2008 and Q1 2009) was found to be just 1 ppm in both AE and AT alloys. Interestingly the three AE casts 8V051, 8T944 and 8V220, (from which the plates were produced, shown in Figures 4.1 – 4.3), contained higher than average Ca after the degassing unit, with an average Ca of 3 ppm. Cast 8V051 had the highest Ca content, (post-SNIF), of all casts during this period, containing 6 ppm Ca. These casts also had higher than average incoming Ca contents, (i.e. pre-SNIF), with an average of 9 ppm Ca compared to an average of just 5 ppm in the other AE and AT alloys cast during this period.

The removal of Ca occurs by reactions with Cl or other reactive products (e.g. $AlCl_3$, $MgCl_2$, as described in section 2.5) and if there is more Ca coming into the SNIF then there will be more $CaCl_2$ present within the degassing unit and this salt could then form part of the inclusions found in this work. There is also the additional consequence that any $MgCl_2$ formed within the melt that would normally be free to react with inclusions is in competition with Ca. Presumably $CaCl_2$ forms preferentially so there would be a reduced amount of $MgCl_2$ available to react with and remove inclusions.

Zr and Ti are minor alloying additions to the 7050 alloy, added in relatively small amounts (typically <0.15 wt.% Zr and <0.04 wt.% Ti) and because Zr and Ti were found to be concentrated within the inclusions their presence prompted further investigation.

Ti is added into the melt in quantities of <0.030 wt.% in the melting furnace, and in even smaller quantities (approximately 100 and 20 ppm respectively of Ti and B, added as a grain refiner (in master alloy form to increase the speed of dissolution into the melt). If there was an issue with the grain refiner, (for instance poorly dispersed, dissolved or agglomerated grain refiner particles), one would expect both Ti and boron to be present within the inclusions. Boron would not be detected by EDX so it was not possible to establish if this was the case.

Zr is added into the melting furnace in either pure form, (as a powder compact), or as a 6 wt.% Zr-Al master alloy depending on the desired charge composition and melting practices, (pure metal compacts would not be added to the holding furnace due to the lower temperatures and thus poor dissolution rate). Zr is added to control recrystallisation in the plate product [153], and is known to precipitate from the melt if metal temperatures fall below a critical temperature during liquid metal processing [165]. The Al - Zr - Ti phase diagram was not considered to be useful when studying the light phase of the inclusions as the 7050 alloy contains Cu, Zn and Mg which would influence the solubility of these phases, [166] and lead to false conclusions.

The lattice parameter of $ZrAl_3$ and $TiAl_3$ intermetallic mixtures have been measured to be almost equal to that of pure Al. The lattice parameter of $Al_3(Ti_{0.6}Zr_{0.4})$ has been shown to be approximately 0.4008 nm [167] and pure Al is 0.405 nm [168], a difference of about 1%, which leads to the conclusion that these particular intermetallics may be nucleated on α-Al.

Chu [169] [166] noted that Zr and Ti were precipitating out of solution in 7050 and 7055 Al alloys below a critical temperature that depended on the Zr, Ti, Zn, Mg and Cu contents of the alloy, (these exact details were not made available in the document). He found that when the combined Zr + Ti content of the melt exceeded a critical level (at a fixed temperature and known Zn, Mg, Cu composition) both $ZrAl_3$ and $TiAl_3$ were precipitated from the melt simultaneously [166].

Chu developed an alloy 'protection' calculator based on the 7050 alloy composition using Thermocalc® software.. With a fixed Zr content, the effects of decreasing temperature or increasing Ti content of the alloy were shown to increase the likelihood of precipitation of the $Zr(Ti)Al_3$ phase.

The two 7050 alloy variants AE and AT have identical casting parameters (target casting temperature, water flow rates, etc.) and the SNIF temperature for both alloys was 690 - 700^{o}C. The Ti contents were identical (the specification for both alloys was <0.04 wt% Ti) but they were noted to have different Zr specifications. The more "problematic" alloy , AE, (in that there were significantly more ultrasonic defects noted in this alloy), had a Zr range of 0.11 – 0.15 wt% Zr, which was higher than the 'AT' variant that had a range of only 0.11 - 0.14 wt% Zr. The typical chemistry of the AE alloy cast during Q1 2009 was established to be 0.036 wt.% Ti and 0.119 wt.% Zr, compared to 0.035 wt.% Ti and 0.110 wt% Zr in the AT alloy, so on average the AE alloy Zr content was approximately 0.01 wt.% higher during this period.

3.9% of AE alloy plate produced during 2008 went on to fail ultrasonic evaluation at the tanks, (specifically ultrasonic inclusions/defects). The chemistry of those plates combined with the chemistry of the three plates that failed in Q1 2009 (shown in Table 5.1) was

compared to the rest of the 'good' AE casts. The results are compared using standard distribution curves in Figure 5.1.

The combined Zr + Ti content of normal plates ranged from 0.147 – 0.164%, with a mean of 0.156%. In contrast combined Zr + Ti content of the defective plate ranged from 0.154 – 0.166% with a mean of 0.160% showing that the defective material was higher in Zr + Ti content by about 0.04 wt.%. The t-test result comparing this data was calculated to be (P) = 0.001, so there was strong statistical evidence that higher combined Zr + Ti content correlated with the presence of inclusions.

Cast number / alloy	Combined Zr + Ti content
8T944 (AE)	0.159
8V051 (AE)	0.161
8V220 (AE)	0.166

Year	Average Zr + Ti content (AE alloy)	Max Zr + Ti content (AE alloy)
2008	0.156	0.166
Q2 – Q4 2009	0.148	0.165
2010 - 2014	0.142	0.159

Table 5.1 A summary of the Zr + Ti contents of the three plates examined in this study and the average and maximum combined Zr + Ti contents of 2008, 2009 and 2010 - 2014.

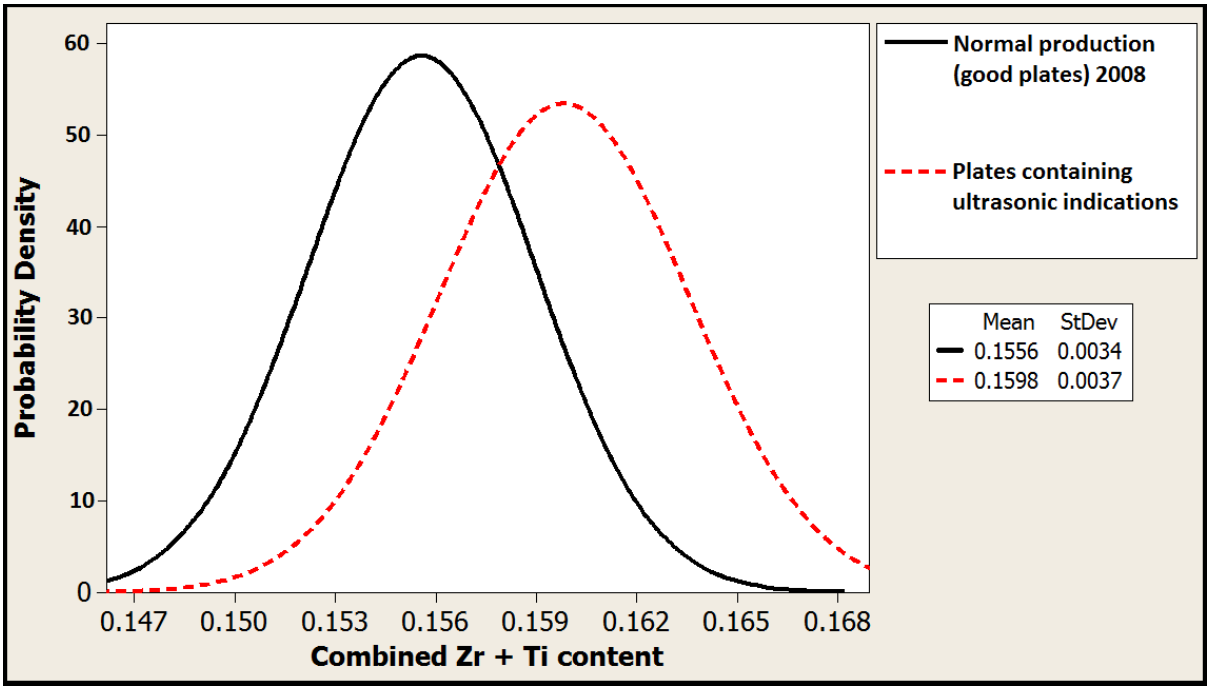

Figure 5.1 A comparison of combined Zr + Ti content cast chemistry data (normal production - casts without defects Vs. plates containing ultrasonic indications).

5.1.1 Modification of the alloy chemistry and processing:

Using the calculator [166], the precipitation temperature for these Intermetallics with a fixed Zr content of 0.11 wt.% Zr and 0.035 wt% Ti was calculated to be 687^{o}C.

The maximum Zr content of both AE and AT alloys was therefore reduced to a tighter range of 0.11 - 0.13 wt.% Zr, to control the upper Zr limit in an effort to reduce any peaks in the Zr content that could occur in future production. Lowering the specification for either Zr + Ti could lead to issues with grain morphology in the plate product. To combat the precipitation problem the SNIF temperature, originally set to a control limit of 690 – 700^{o}C, was increased to 705 - 715^{o}C in order to increase the solubility of the Zr and Ti and thus reduce the likelihood of precipitation of these inclusions within the degassing unit.

5.1.2 Effects of chemistry and process modifications:

The increase in minimum SNIF temperature made an immediate and positive effect, reducing the occurrence of these inclusions and the scrap rates for both of the 7050 alloys, particularly AE. The combined Zr + Ti content was managed so that the overall combined value was reduced over time, through the period 2010 – 2014.

In Q2 2009 only 0.18% of the AE alloy plate produced was scrapped for ultrasonic indications, (compared to 3.6% in Q1 2009), and there was zero AT alloy plate scrapped during this period (compared to 0.7% in Q1 2009) [2]. The scrap generated (for this type of "point defect" ultrasonic indication) during Q2 2009 is shown, (by contributing alloy), in Figure 5.2. The contributions of the AE and AT 7050 alloys to the total are noted to have decreased significantly, contributing just 6% (AE) and 0% (AT) compared to 45% (AE) and 19% (AT) during Q1 2009 (see Figure 1.4).

Evidently there were casts where the combined Zr and Ti content was sufficiently high and the metal temperature of the AE alloy was sufficiently low that precipitation of $ZrAl_3$ and $TiAl_3$ intermetallics occurred, and were a major contributor to the development and formation of these particular point defect ultrasonic indications. Based on the tonnage scrapped in 2008 and the apparent improvements in rejections this aspect of the project is estimated to have saved £50,000 per annum.

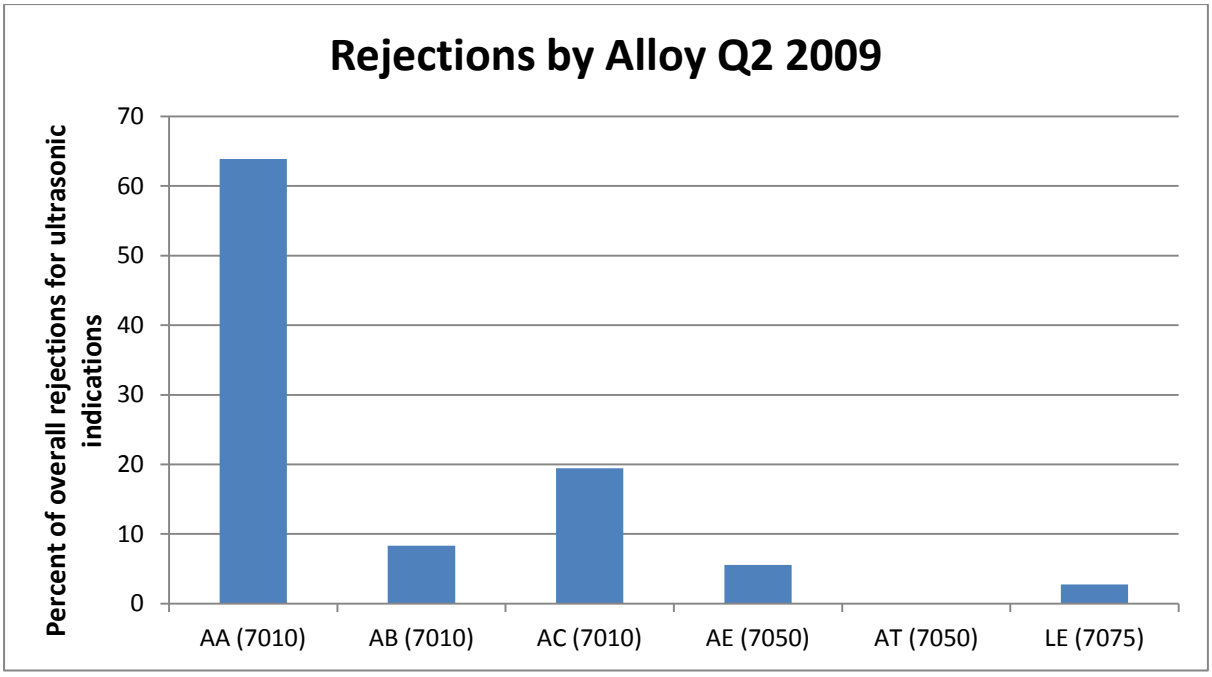

Figure 5.2 Rejection rates for common alloys produced at Alcoa during 2009 [1].

5.1.3: Bubbles and precipitation of $Zr(Ti)Al_3$ within a degassing unit.

Gas bubbles are deliberately introduced into the molten metal within rotary degassing units in order to remove inclusions and H. The literature reviewed in section 2.5 shows that for both inclusion and H removal we should use the smallest bubble size possible, as this increases the surface area of the bubble for reactions to take place, and reduces the buoyancy of the bubble, prolonging the residence time within the melt [25].

Micro-bubbles of 10-30 µm diameter [170] are known to interfere with the operation of the LiMCA inclusion monitoring device if it is placed after a degassing unit [171], reducing the accuracy of LiMCA readings, or even making analysis impossible [172]. This suggests that bubbles do not float immediately out of the melt, but survive within the metal stream for a considerable distance after the degassing unit. Sigworth [25] noted that bubbles were

observed to break the surface of the melt after 10 m of travel in the launder after an A622 degassing unit. The launder exiting the SNIF unit from DC units 1, 2 and 3 are each less than 3 meters in length, so it is theoretically possible, if not extremely likely, that some bubbles survive into the ingot head. These could be incorporated into the casting or trapped by the distribution bag and allowed to agglomerate before release into the casting. Due to the dispersion of the inclusions on the C-scan pictures, (see Figures 4.1 – 4.3), being similar in shape to the ingot sump, the likelihood is that that these inclusions build up in number within the distribution bag, (the location of which is shown in Figure 2.1), and are released in a flush when disturbed during casting.

These bubbles could interact with other features within the melt, such as suspended oxide films or precipitated intermetallics. If a chlorinated bubble was trapped underneath an oxide film that was floating or circulating within the degassing unit, then salts could form or be deposited on the surface of the film by interaction of Cl with metallic elements within the melt, such as Mg and Ca. These salts would then be deposited and retained on the surface of the oxide. Precipitated intermetallics, (such as $Zr(Ti)Al_3$), floating within the melt could also collide and stick to the bubble by metal turbulence, agglomerating and increasing the size of the inclusion [173].

The densities of both $TiAl_3$ and $ZrAl_3$ are 3.4 and 4.1 g/cm^3 respectively [164], which are both high compared to that of the liquid Al (approximately 2.345 g/cm^3) [5]. Once these intermetallics begin to deposit on the surface of the inclusion it becomes more and more likely that the inclusion will remain suspended or sink down into the metal, either within the launder or a degassing unit (this speculation was also made by Campbell [174]).

One of the flaws of this discussion is that the typical size of these inclusions entering the ingot head is not known, because the ultrasonic tanks at Alcoa are not suitable for examining ingots. During hot rolling the inclusions are flattened and elongated to a degree dependant on the characteristics of the inclusion and the surrounding matrix [91] and the rolling profile employed e.g. the temperature, force applied and number of passes during the rolling process [69]. Assessment of the defect in the liquid metal might establish the exact aetiology of these defects and lead to effective countermeasures (such as filtration systems, improved SNIF design and better cleaning procedures) all to eliminate these inclusions from the melt. Alcoa does not utilise ceramic foam filters (CFF) as a standard metal cleanliness tool and theoretically these could be quite effective at removing precipitates and solid salts from the liquid metal.

5.2 Near surface indications at the edges of thin gauge (<45mm) 7475 alloy plate.

The ultrasonic indications at the edges of 7475 alloy thin gauge plate were found to be caused by a coarse grain structure and not porosity, which was originally suggested by the operators of the ultrasonic equipment. Previous Alcoa studies that suggested rolled porosity to be a cause of ultrasonic edge defects in rolled plate [69] [68] were therefore not relevant. The coarse grain structure caused attenuation of the ultrasound and gave a response similar to that of porosity, but it was not until the defect was evaluated during this project that the exact cause became known.

Porosity is known to reduce the mechanical properties of cast products [175]. The mechanical properties of rolled plates would be expected to be reduced in the coarse grain regions due to the relationship between grain size and strength. A decreasing grain size increases strength because the grain boundary area increases and grain boundaries are regions of disorder that act as pinning points, impeding the movement of dislocations from one grain to another.

5.4% of the total plates produced during 2008 contained this type of defect. Those plates were shown, (by statistical analysis of plant data), to have originated primarily from the larger ingots that Alcoa produced; those with 440 and 525 mm cross sections.

48% of all the plates were produced from 325 mm ingots, but none of the defective plates came from this ingot size. 27% of the total production originated from 440 mm cross-section ingots, and 4.8% of those contained this particular defect (1.3% of the total), and finally 25% of the total production originated from 525 mm cross-section ingots and 16% of these

contained this type of defect (4.4% of the total). Clearly there was a correlation between increasing starting ingot size and the occurrence of this particular defect.

Plates are first cross-rolled in order to obtain the desired plate width. This is done before the plate is rolled to length, because cross rolling long plates is not possible on the mill (a sketch is shown in Figure 5.3).

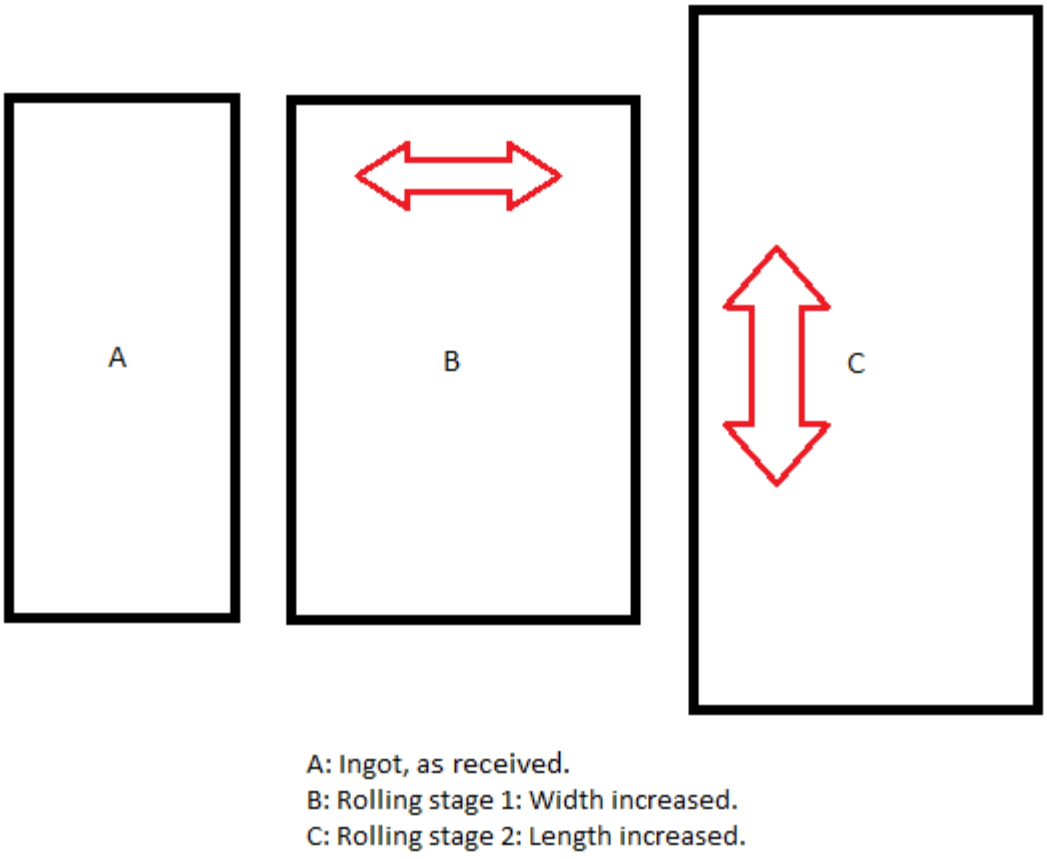

Figure 5.3: A sketch of the rolling process. Ingots are widened and then elongated due to limitations on the rolling mill.

The amount of widening depends on both customer specifications and the desired number of smaller plates, (referred to as malts), that are to be cut from a large plate. It became

apparent that when ingots were widened above a certain level the coarse grain defects at the edges were statistically significantly more likely to occur, as shown in Figure 4.27.

A management review of this data led to the production of thin gauge 7475 alloy plates from the larger cross section ingots (525, 440 mm) being discontinued, so that only the 325 mm ingots were used to produce thin gauge plate for this alloy. This effectively eliminated this defect from production, but also prevented defective material becoming available for further study. Elimination of this defect from the thin gauge 7475 plate is estimated to have saved the company between £17,000 - 25,000 per annum.

5.2.1 Potential cause of the coarse grain defect

The grain size in DC casting is controlled by additions of grain refining inoculants (TiBAl), and by rapidly solidifying the ingot (achieved by direct water impingement on the solidifying ingot) which further reduces the overall grain size.

A part or total failure of the grain refiner supply to the ingot during casting would have affected the entire width of the ingot, with coarse grain appearing at the point where there was insufficient grain refiner in the melt. This problem would have presented itself as a band across the full width of the ingot, (as shown in Figure 2.61). The cooling of DC cast ingot occurs at the surface of the cast ingot; first as the liquid metal makes contact with water chilled mould, and then water jets. The point of heat extraction, (the external ingot surface area), should have the most rapid solidification rate and thus have a finer grain size when compared to the centre of a large ingot, the opposite of what was observed in this defect.

A thermo-mechanical process that might have been responsible for grain growth and recrystallisation was identified as a potential cause of the change in grain size and

morphology in 7xxx Al alloys during rolling (as discussed in section 2.7). Zr and Cr are added to 7xxx wrought alloys to control the grain structure, (although only Cr is added in the 7475 alloy) and these elements form small coherent precipitates that restrict grain growth by Zener-pinning [176]. In contrast Fe and Si are present in the alloy as impurities and give rise to constituent particles which are detrimental to most of the mechanical properties of the alloy and are known to lower the temperature for nucleation of recrystallisation to occur. Fe containing intermetallics were identified in the coarse grain region, as shown in Figure 4.23, and these particles were in the region of about 2 - 50 µm, larger than those found in 7075 alloy by Atkinson et al. [177], who found particles of 1 - 30 µm. Although not proven, theoretically these intermetallics could have promoted recrystallisation.

This theory is supported by the statistical analysis of the chemical elements in the defective plates, as it shows that they contained, on average, higher levels of Fe and Si, (although these were not statistically significant), and lower Cr contents, (found to be statistically significant) when compared to defect free castings, (see Figures 4.24 and 4.25). A combination of high Fe and Si and low Cr levels combined with excessive widening (increased strain) could have increased the likelihood of this type of defect occurring. This theory is undermined, however, by the fact that the images obtained during the grain size examination, (Figure 4.22), do not appear to show evidence of recrystallisation nuclei at the grain boundaries. The grains were deformed in the rolling direction of the plate, and are not equiaxed, as would be expected after recrystallisation process has occurred.

It is possible that during the rolling process recrystallisation occurred near the surface, causing localised grain growth until the plate microstructure was entirely recrystallised (O-temper, see Figure 2.59). If there was a delay in the rolling procedure the plate would have

been left at temperature for a period of time, (allowing recrystallisation to take place), and at some later time the final rolling stages took place and the coarse grain material was rolled, creating coarse but elongated grain structures at the surface of the plate.

5.3: Bubble trapping in liquid aluminium alloys

The interactions between Cl and the melt were investigated by trapping gaseous bubbles within molten metal. The change in gas composition was evaluated using the Pore Gas Analyser and the metal – gas interface was examined using SEM and EDX. This was done in an in an effort to increase the understanding of the effects of Cl on degassing of Al alloys.

While bubbles were successfully caught in the solidifying metal, only two extracted specimens contained gas. The X-ray images showed that combined gas – shrinkage porosity (as described by Anson [178]) around the bubble was extensive, and probably connected to the bubble. The porosity found within the metal that surrounded the bubble is thought to have provided a series of leak paths through which the gas escaped, especially during the machining and evacuation process in the Pore Gas Analyser.

However the composition of the gases in the bubbles containing gas, established using the Pore Gas Analyser was not as expected. Ar was used to create the bubbles in both experiments yet there was very little Ar retained within either of the samples, in fact only one bubble contained any Ar at all, and it made up only a small fraction (5%, see sample #1 in Figure 4.49) of the gas volume. The largest fraction of gas in both bubbles was H, contributing 82 and 80% respectively, which diffused into the bubble during solidification. The second most common gas found was N_2 which could only have come from air. The presence of N_2 within the bubble was not expected, and indicated that there was a leak of air into the samples at some point while the metal was still molten, although no O_2 was detected. It seems unlikely that air would leak into the gas lines as these were under a positive pressure and Ar would have leaked out of the pipe system instead. If air was

somehow able to get into the gas supply one would have expected a minor contamination of N_2 and O_2 into the Ar, and not dilution or complete displacement of the Ar.

The Ar gas used in the experiment was 99.998% Ar, expected to contain 2 ppm O_2 as an impurity and / or moisture [179]. The surface area of a 10 mm diameter bubble is 314 mm^2 and at 2 ppm an oxide with negligible thickness (less than one molecule thick) would have been expected to form across the metal – gas interface. The Ar and Cl mixture was also composed of Pureshield Ar (99.998% Ar) and 0.8 % Cl (99.5% Cl). The maximum total impurities from the Cl would therefore be no more than 0.5% of 8000 ppm Cl, or 40 ppm. If we assume that this was all O_2, then the total maximum O_2 content of the gas would be 42 ppm, max. At 42 ppm an oxide formed on the bubble surface was calculated to be 0.4 µm thick, again negligible, (the interaction volume of the SEM beam is calculated to be 2.3 µm at 20keV [163]). It is therefore impossible that all the O_2 contamination came directly from the Ar or Cl gases that were used in these experiments.

The gas within the bubble must have been encapsulated and / or trapped in some way or it would have been removed from the sample during processing in the Pore Gas Analyser, (by the application of the vacuum). A possible explanation for the presence of N_2 is that gas was able to diffuse from the surface into the bubble interior through bubble trails that were formed by the trace O_2 and moisture contents of the gases, as described by Campbell [174], shown in Figure 5.4. The Ar therefore leaked out of the sample and was gradually replaced with air. When the atmospheric O_2 and water vapour entered the bubble interior they reacted with the surrounding Al, coating the interior of the bubble with an Al_2O_3 film, and sealing the interior so that gas could not escape. When the liquid metal contracted during solidification the bubble trail would have ruptured, preventing the bubble from being

subsequently evacuated, and the gas would have been contained in the bubble by the oxide film that then coated the bubble interior.

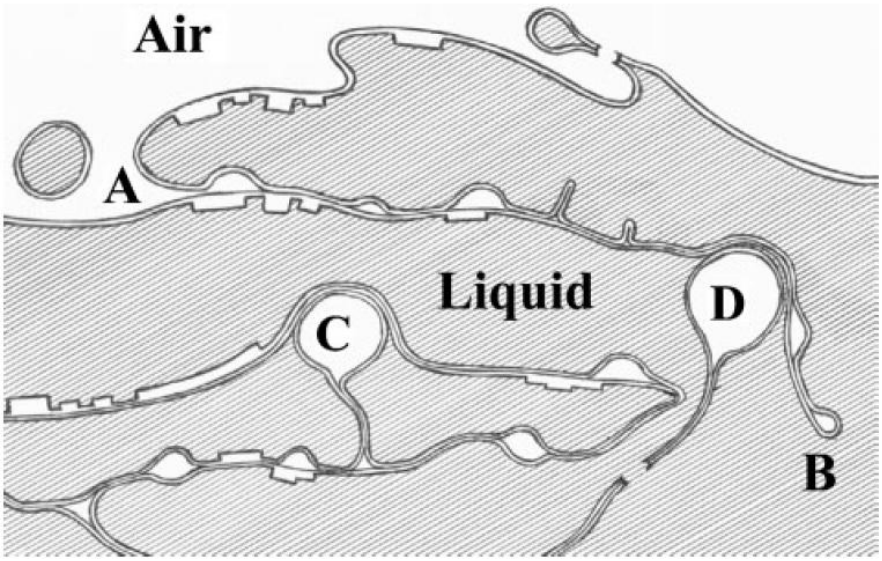

Figure 5.4 Small entrained bubbles could form gas porosities (A, B) while buoyant O_2 containing bubbles (C, D) moving through the liquid metal would react with the surrounding melt and surrounded themselves with a bifilm. In this manner they would also leave oxidised trails behind them in the melt [174].

One weakness to this theory is that, if air was able to enter into the bubble then there is an absence of O_2 within the bubble that must be explained. Air contains 19% O_2 so it is proposed that any O_2 or water vapour that did not react with the Al melt, later reacted with the H_2 that diffused into the interior of the bubble and the reaction of the H with O_2 produced water vapour. Water vapour was found in both gas containing samples in roughly the 4:1 ratio of N_2 to O_2 found in air; sample #1 contained 14% N_2 and 4% H_2O (78% N_2, 22% H_2O) and sample #3 contained 12% N_2 and 3% H_2O (80% N_2, 20% H_2O).

The fractured oxides found in samples #1 and #3 during SEM analysis, (see s 4.32 – 4.37), suggests that air entered into the bubble while the alloy was still molten. The Si-rich eutectic

was observed to have penetrated through the oxide layer. This suggests that the oxide film had already formed and sealed the interior of the bubble before the metal was completely solidified. The presence of an oxide film might also explain why some samples contained gas and others did not. If air entered a bubble then an oxide film would have formed across the interior of the bubble and could potentially have sealed the bubble away from the surrounding interdendritic porosity, therefore when the samples were cut the contents of the bubbles did not leak away through the porosity network during examination in the Pore Gas Analyser.

Very little $MgCl_2$ was found during the experiments with 5083 alloy and the Ar + Cl mixture. There was no Cl evident on the dendrites by EDX (see 4.41) but salts were found to have formed, present as small clusters between the dendrites (see Figures 4.42 and 4.43). Ca, Na and Mg were found during the analysis and, due to their Free Energy of Formation (see section 2.5) it is most likely that these were $CaCl_2$ or NaCl. The results are not conclusive however as the amount of Al_2O_3 and MgO found during SEM analysis (see 4.43) suggests that this sample had also been exposed to air while molten. As the reactions of Ca, Mg and Na with O_2 are more favourable than the reaction to form $MgCl_2$, the O_2 would have reacted with these elements first and limited the amount of $MgCl_2$ that formed, (but not eliminating it). In comparison the 7010 alloy that was processed with Ar + Cl appeared to contain very little oxygen and the dendrites were observed to be coated with a chloride, presumably as $MgCl_2$, (see Figures 4.45 - 4.47) because this was the most reactive element detected. The presence of Cl appeared to be quite uniform, with ~1wt.% Cl observed across the specimen surface. This means that the Cl was not concentrated on either the matrix or the intermetallic-rich regions. No evidence of Na, Ca, Zr or Ti was found during the survey.

5.4 Hydrogen removal from 7xxx aluminium alloys using a SNIF reactor with and without chlorine gas additions, measured using ALSCAN.

The effects of Cl on the degassing efficiency of Al alloys was found to be conflicting in the literature (see section 2.5). The degassing performance of 7xxx Al alloys was investigated using the ALSCAN and a statistical approach. Cl is also added to the Ar gas in order to float inclusions out of molten Al and if Cl was detrimental to the degassing process, better degassing efficiencies might be obtained by separating the degassing and inclusion removal processes. If Cl was removed entirely there would be advantages in regards to environmental, health and safety aspects (EHS) and cost savings, but the major disadvantage would be that there would potentially be an increase in inclusion related issues within the castings and plate products. Considering that the work here suggests variations of only 3 - 5% in H removal, there is no attractive benefit in removing the Cl, as there may only be a minor increase in H removal, at the expense of a detrimental increase in the number of inclusions in the plate product.

It is worth nothing at this point that if these experiments were repeated on other alloys, (for instance, those with a higher Mg content, such as 5083 alloy), the influence of Cl might be found to be more substantial.

When all of the data from the three alloys was collected and presented together there was no apparent effect of Cl addition (1.3 % Cl in rotor one and 0.8 % Cl in rotor two, balance Ar) on the degassing of 7xxx Al alloys processed using a SNIF unit. The standard distribution curves were almost identical (see 4.51), and with a t-test p-value of 0.26 there was no statistical evidence to suggest that Cl enhanced or reduced the degassing rate. The casts processed with Ar + Cl were observed to be more variable than those with Ar alone, having a

greater range and standard distribution, but the difference between the two means was less than 1% (62.8% no Cl and 61.3% with Cl) and the t-test showed that that the two data sets were not significantly different. Statistically speaking, as more samples are drawn from a population then the more accurate the results. Based on that theory this is potentially the most useful data set simply because it contains the greatest number of data, with 80 individual degassing results.

As this data consolidates information from three different alloys, this may draw data from three separate populations and that blending them together is not possible. From one perspective these alloys can be grouped together as the major alloying elements (Cu, Mg and Zn) of the 7xxx series are all found in similar quantities, (each is less than 1 wt.% different from the other), but significant variations in degassing efficiencies were observed within these individual data sets that require explanation.

The 7010 series was the largest individual alloy data set that was obtained, (containing 40 individual degassing results), and showed a clear reduction in degassing efficiency when Cl was present in the Ar. The mean degassing efficiency was reduced by 5% when using Cl additions (63% no Cl, and 58% with Cl), as shown in Figure 4.53. There were no out-lying results and the data had similar ranges and relatively small standard distributions. The p-value was calculated to be 0.0003; strong statistical evidence that there is a detrimental effect on degassing efficiency when using Cl additions to degas 7010 alloy, agreeing with the research by Stevens [143] who proposed that $MgCl_2$ increased the interfacial resistance at the bubble boundary layer, and retarded H diffusion into the gas bubbles.

There was no apparent effect of Cl on the degassing efficiency of the 7050 alloy. The mean degassing efficiency values differed by 3%, (65% no Cl and 62% with Cl), but the t-test p

value was 0.11 (i.e. not statistically significantly different) probably because the standard deviation of the "no-Cl" data was quite large, being 5.8 compared to just 2.08 in the "with-Cl" data. This made it difficult to draw any conclusions.

In contrast to the 7010 alloy, however, there was an 8% mean improvement in degassing efficiency when the 7075 alloy was processed with Cl additions (60% "no-Cl" and 68% "with-Cl"), see Figure 4.57. In the data obtained during the 7075 alloy analysis, four readings were found within the 75 – 79.9% degassing range, (the highest division), and these readings came from one individual cast. The presence of these four outlying readings is concerning as they are far removed from the bulk of the data, which was typically in the 55 – 64.9% degassing efficiency range, as shown in Figure 4.56. If these four values were removed then there would be no statistically significant effect of Cl on degassing in 7075 alloy and the overall conclusions would change. The analysis of the three alloys previously discussed would shift, (those results are shown in Figure 5.5), so that the overall effects of Cl on the 7xxx alloys would become slightly negative. The mean degassing efficiency would be 3% lower in Ar + Cl mixtures compared to Ar only, and with a t-test p value of 0.0009 there would be strong statistical evidence that Cl slightly reduces degassing efficiency. It is therefore tempting to remove these four readings although they are within the expected degassing ranges observed by other authors [25] [128] [180]. When these values are retained, the effects of Cl on the degassing of 7075 alloy appear to be slightly positive, contrasting that of the 7010 alloy.

After reviewing the combined data for the three 7xxx alloys, (the 7010, 7050 and 7075, see Figures 4.50 and 4.51), the results obtained tend to agree with researchers Sigworth [110] and Engh [24], in that Cl has no significant effects on the diffusion of H into inert gas bubbles

during degassing, at least when Cl is added in relatively small quantities (1.3% and 0.8% Cl) in 7xxx alloys. There are significant variations between different alloy groups however, that should be investigated further.

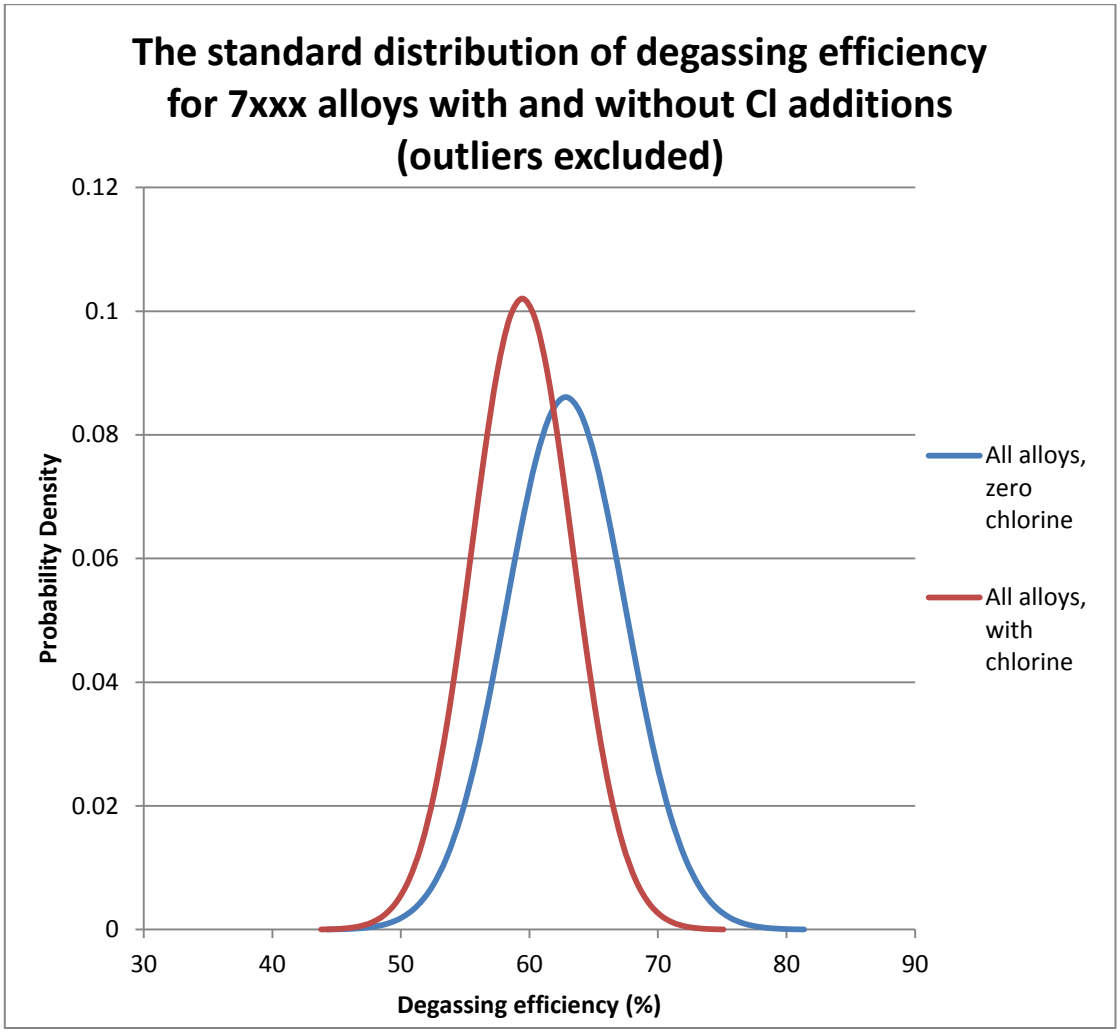

	Mean	Standard deviation	t-test (p)
No Cl	62.8	4.6	0.0009
With Cl	59.4	3.9	

Figure 5.5 The standard distributions of the degassing efficiencies of all three alloys a) without and b) with Cl additions. The average (mean) and standard distribution for each data set are detailed, as is the t-test result that compares the two data sets.

5.4.1: Alloy chemistry and variations in degassing efficiency:

The purpose of this study was to consider the effects of Mg and Cl, (and $MgCl_2$), on degassing efficiencies. When the three Mg contents are compared with the degassing results they do not support the conclusion that Mg interacts with Cl to affect degassing efficiency.

The mean Mg contents of the alloys were ranked: 7075 (2.51% Mg) > 7010 (2.34% Mg) > 7050 (1.90% Mg). However the degassing efficiencies were ranked 7075 > 7050 > 7010 when considering degassing rates with Cl additions. The variations observed therefore do not appear to be influenced by variations in Mg content. This is not entirely unexpected as the $MgCl_2$ would not be molten, as the processing temperature for all alloys was below 714^{o}C, the melting point of $MgCl_2$. Any $MgCl_2$ formed would be expected to be a solid and therefore not expected to coat the bubble surface completely, affecting H transfer across the bubble – melt interface.

Interestingly, the combined Zr and Ti contents of these alloys do rank with the degassing performance. For instance the degassing of the 7075 alloy appears to have been positively influenced by Cl additions, containing the lowest amounts of these elements (0.04 wt.% Ti 0.02 wt.% Zr). The 7050 alloy contained the second highest levels of Zr + Ti (0.02 wt.% Ti and 0.10 wt.% Zr) and the degassing of this alloy appeared to be negatively influenced by Cl additions, although not significantly. The 7010 alloy had the highest combined value of Ti + Zr (0.03 wt.% Ti and 0.11wt.% Zr) and the negative impact of Cl additions was most apparent in this alloy.

In sections 4.1.1 and 5.1.1 the presence of Zr and Ti and Cl have been identified in inclusions in 7050 alloy plates. Perhaps the Zr and Ti are influencing the degassing process in 7xxx alloys more so than $MgCl_2$, especially at these lower (<714^{o}C) temperature conditions.

If the Zr (and / or Ti) react with Cl to form salts, these liquid chlorides could also influence the degassing rate by retarding the diffusion of H into bubbles during degassing.

5.5 The degassing efficiency of aluminium alloys, achieved with and without chlorine and measured using ALSPEK H.

The degassing rates for pure Al, 5083 alloy and 7010 alloy were monitored using the ALSPEK H H determination device in real time, over the range of dissolved H of 0.35 – 0.15 ml/100g.

The degassing time required for repeated experiments decreased consistently. The initial measurement was always higher than a following repeat measurement. For example, experiment #2 was a repeat of experiment #1. Experiment #1 took 73 minutes for the melt to be degassed from 0.35 to 0.15 ml/100g, while experiment #2 took only 60 minutes (13 minutes less) to achieve the same amount of degassing. This applied to all of the repeated experimental results, as follows:

1) #1 > #2,

2) #4 > #5,

3) #6 > #7

4) #10 > #11,

5) #12 > #13 > #14,

6) #15 > #16,

7) #17 > #18.

The variations between the first and second (repeated) experiments are shown in Table 5.5.1. The value obtained from a repeat experiment was on average 18% lower than the

initial measurement and the variation was demonstrated to be statistically different using a paired t-test, producing a p-value of 0.0015.

Initial experiment and repeat experiment	Initial value (time, minutes)	Repeat experiment value (time, minutes)	% difference
#1 and #2	73	60	18
#4 and #5	49	33	33
#6 and #7	45	35	23
#10 and #11	36	33.5	7
#12 and #13	56.5	50	11.5
#15 and #16	42	35	17
#17 and #18	73	60	18
Average	53.5	43.79	18
t-test	0.0015		

Table 5.2 The time required to degas repeated experiments are compared using a t-test. The initial and secondary degassing processes are found to be significantly different, indicating that the second degassing run proceeds faster than the initial.

The reduction in required degassing time and apparent increase in degassing efficiency for sequential experiments suggests that, even though H was added back into the melt by addition of the organic matter, H did not fully equilibrate, (to the starting level of 0.35 ml/100g), within the melt before the next experiment began. This suggests that error in the results has been generated because the exact same amount of H was not present within the

melt in each experiment. The average difference in degassing for the same experiments (repeats, e.g. experiments #1 and #2) was 18%, with a minimum of 7% and maximum of 33% observed. This suggests that separate experiments and melts using different alloy types cannot be compared to each other because the melt H content was not consistent at the start of the experiment.

The diffusion of H in the melt is described by Eq.23 [52] and Eq.24.

$$d = (Dt)^2 \qquad \text{...Eq.19}$$

$$t = \frac{x^2}{2D} \qquad \text{...Eq.20}$$

Where t is time in seconds, x is the diffusion distance in m, and D is the diffusion coefficient for H in Al, in m^2s^{-1}. The ALSPEK H probe was inserted to a constant depth of 150 mm within a melt, 340 mm deep. The organic matter added to generate H was added at the surface, so H incorporated at the surface would have diffused from the surface towards the probe position and then into the liquid metal at the bottom of the crucible, over twice the distance. When the H content of the metal surrounding the probe had reached 0.35 – 0.45 ml/100g the H content of the melt closer to the source would have been higher, and at the bottom of the crucible it would have been lower.

The reported diffusivity of H in liquid Al is $3.5x10^{-7}m^2.s^{-1}$ [58], so the H would be expected to diffuse from the source to the probe tip in about 9 hours, but would need approximately 21 hours to reach the bottom of the crucible.

This calculation excludes the obviously significant influences of convection that would have enhanced the rate of flux of H within the melt, but this cannot be calculated. Due to convection the flux of H over this distance would have been increased significantly. It is

proposed that the distance was great enough for a measureable difference in H content and this led to variation between experiments.

The consequence is that, after the initial degassing cycle the melt H content was reduced to 0.15 ml/100g. When a new H source was added at the surface, the H content around the probe was raised to the range of 0.35 – 0.45 ml/100g, but the H content at the bottom of the crucible would have been lower compared to the previous experiment(s), thus the degassing process appeared to take less time. The repeated experiments, (when they were performed directly after one another) cannot be used as the true H content at the beginning of the second degassing process was not accurately known. It also brings the results of the initial experiments into question, as these could also have had varying starting H contents.

Each experiment was setup in the same manner. The alloy was melted in an induction furnace and transferred into the wire resistance furnace and left for over an hour within the crucible and during this time both the temperature and melt H content would have come to equilibrium with the environment. As the same amount of organic matter was added each time, the initial H content for each initial experiment would likely have been the same.

5.5.1 Degassing rates; pure aluminium, 5083 alloy and 7010 alloy.

As the pure Al melt contained primarily Al atoms (and approximately 0.1 wt.% Fe and 0.1 wt.% Si) the mean-inter atomic spacing will be constant. During degassing H protons will diffuse through the interstitial spaces between the Al atoms, and towards the Ar gas bubbles, due to a diffusion gradient. The 5083 and 7010 alloys contain a variety of alloying additions (Mg, Zn, Cu, etc.) thus the mean atom size and the mean interstitial spaces between atoms would be increased. As Mg increases the solubility of H in the melt (see section 2.2.1) it suggests

that the interstitial spaces for H to reside in are larger, accommodating more protons, also suggesting that H diffusion can occur more quickly. The consequence is that pure Al takes significantly longer to degas compared to the 5083 and 7010 alloys as the latter have higher Mg contents and higher H contents. Surface tension is not thought to have played a role in increasing or decreasing the H diffusion rate as the work by Anson et al. [181] showed that the surface tension of A356 alloy did not change appreciably with increasing Mg content, although his experiments were undertaken in the range of 0 – 0.8 wt.% Mg, whereas the Mg content is greater in the 7010 and 5083 alloys.

5083 alloy measurements.

According to Stevens [143], above 714^{o}C the formation of $MgCl_2$ at the bubble – metal interface should dramatically reduce the rate of H removal. In these experiments no significant variation in degassing efficiency was observed when the 5083 alloy was in the 730 – 750^{o}C range. The bubbles were delivered into the melt using a lance, which is a relatively poor method for obtaining smaller gas bubbles. As the surface area of the bubbles would have been quite large and the Cl content of the gas was small, 0.8% wt.% Cl, it is possible that liquid $MgCl_2$ formed on the bubble surface only has an appreciable effect on the removal of H when the gas bubbles are below a certain size, or if the Cl content of the gas mixture is relatively high. There appeared to be very little difference between the data obtained when the 5083 alloy was processed at different temperatures of 680 - 695 and 730 – 750^{o}C.

7010 alloy measurements

A surprising trend identified within the data was that the degassing rate of the 7010 alloy was negatively influenced (680 – 695 and 730 – 750^{o}C) by the presence of Cl. In the higher temperature range the degassing rate was decreased by 32.5% and in the lower range the rate was decreased by 42% when the Ar + Cl gas mixture was used.

Due to the variation in degassing rates it is difficult to build up reliable statistical data from these results. Repeating the experiment with a smaller crucible would reduce the amount of metal and thus decrease the distance over which H would have to diffuse. This would eliminate the error identified in the repeat experiments. The method could also be improved by application of a small rotary degassing unit to decrease the bubble size, increase melt turbulence and better disperse the bubbles within the crucible. Increasing the Cl gas levels would also be desirable, but presents a significant safety risk.

As the 5083 alloy contained 4.5 wt.% Mg and the 7010 alloy contained only 2.1 wt.% Mg there was no obvious relationship between Mg content and degassing efficiency (with or without Cl).

Discounting Mg, (for a comparison against the 5083 alloy), the 7010 alloy contains Cu and Zn as the major alloying elements and Zr as a minor alloying addition, (0.10 - 0.16 wt.% Zr, 5.7 – 6.7 wt.% Zn and 1.5 – 2.0 wt.% Cu). The Ellingham diagram suggests that zirconium chloride, $ZrCl_4$, is the most stable compound (ΔG^o -368 kJMol^{-1}) followed by $AlCl_3$ (ΔG^o -354.5 kJMol^{-1}) $ZnCl_2$ (ΔG^o -285 kJMol^{-1}) and finally CuCl (ΔG^o -184 kJMol^{-1}).

Since the Zr content of the alloy was low (0.11 - 0.15 wt.%) and there was no apparent influence of $AlCl_3$ on the degassing rate, (demonstrated by comparing experiment #1, pure

Al, Ar only, degassed in 73 minutes and experiment #3, pure Al, Ar + Cl degassed in 71.5 minutes), the next significant chloride expected to form at the metal – gas interface would be $ZnCl_2$. The 7010 alloy contains up to 6.7% Zn, (about three times as much Mg), and $ZnCl_2$ is molten above 206^{o}C, and therefore could affect the diffusion of H into the gas bubble in a similar way to $MgCl_2$. Perhaps the formation of $ZnCl_2$ is responsible for the general reduction in degassing efficiency of 7xxx alloys.

<u>The effects of salts on degassing:</u>

It is interesting to speculate on the effects of salts on H diffusion. Cl is electronegative and reactive, and after an electron has transferred from the metal to the Cl atom during reduction / oxidation reaction, the metal and Cl ions will be held together by attractive ionic bonds. The negatively charged Cl and positively charged metal ions would bond together and create a complex network of polarised links where electron density would be higher. The anions and cations would be held at a distance that is balanced by the attractive and repulsive forces of neighbouring ions, potentially leaving a channel of roughly neutral charge in the centre of the lattice structure through which H protons could diffuse to reach the bubble. The diffusion of H is known to be low in alumina, and this would suggest that other ionically bonded structures such as salts might also present barriers to H diffusion. It seems likely that the dense electron field between the metal and Cl atoms might initially attract the positively charged proton, but in order to pass between the atoms and through to the gaseous Ar bubble the protons would need to pass by the positively charged metal ions, perhaps making transfer through the salt layer more difficult. Assuming that the density of the salt increases during melting, there should be greater inter-atomic distance between atoms, and perhaps this increases the rate of H flux through the salt.

5.6 Hydrogen absorption measured using the LECO

The LECO has been demonstrated to be an effective and reliable way to extract H from small Al samples. Two 5083 samples degassed 10 times showed a progressive reduction in H content, but which after three repeated analyses was below the limit of detection. After the first analysis, approximately 85% of H was removed from each sample, and after three analyses nearly 100% of the H was removed. Subsequent analyses were on average 0.005 ppm, which is the reported accuracy of the device in high accuracy mode [182].

Two 5083 samples were found to have absorbed a large amount of H after being left to stand in laboratory conditions for 10 weeks. During this time atmospheric water vapour was able to react with the Mg at the sample surface and H entered the metal. The literature supports this explanation as Mg oxide is a discontinuous film that is not protective and allows reactions to continue (see section 2.2.3). Interestingly, after ten weeks the absorbed H levels were lower than, but close to, the original degassed value (analysis 1). This indicates that trap sites such as lattice defects, grain boundaries and internal pores provided a limit to which H could be absorbed. It is unlikely that pores would collapse during the measurements as the sample does not melt. The voids were presumably evacuated during the degassing process and filled again when H re-entered the sample from the atmosphere.

The rate of H absorption into the 5083 alloy samples was initially rapid and significant quantities of H (~0.1 ppm) were measured after only 24 hours post degassing. The absorption rate appeared to slow down over time and the H content became significantly higher weeks after the initial degassing procedure. The various samples used in this

experiment appeared to absorb H at slightly different rates, and this is probably because each individual sample has varying amounts of internal trap sites for H to reside.

The 5083 alloy sample submerged in water and the sample left in laboratory air for four days absorbed 0.164 and 0.145 ppm of H respectively. In both cases moisture was readily available for reaction with the Al surface. The sample that was placed in a sealed container (i.e, limited water vapour available for reaction), was observed to have absorbed only 0.024 ppm of H after four days. The sample submerged in acetone also absorbed very little H, only 0.038 ppm, so apparently there was very little reaction between the hydrocarbon and the Al surface. As a standard practise at Alcoa samples are washed in acetone before analysis to remove any soluble contaminants from the surface. Washing samples in acetone should have no significant effect on the H content, and there is no need to change this practise.

5.6.1: Absorption of hydrogen across aluminium oxide and nitride layers

The initial dimensions of the cylindrical Al LECO samples was 8 mm diameter and 50 mm length, giving an approximate volume of 2514 mm^3 and an approximate surface area of 1357 mm^2. Pure Al has a density of 2.7 g/cm^3 at room temperature and approximately 2.357 g/cm^3 when molten [149] so the volumes increase by 12% upon melting. As the volume of the sample increases so does the surface area and a volume increase of 12% would be accompanied by a surface area increase of 20%. As the sample expands during heating the pre-existing surface oxide layer would be placed under tension and cracks form within it, exposing fresh un-oxidised Al underneath.

In the experiments where specimens were heated in air, the exposed Al reacted with O_2, almost instantaneously sealing the cracks with a fresh layer of Al_2O_3. When the specimens

were subsequently exposed to H the gas would be obliged to diffuse through the oxide layer and / or structural defects in this film. Oxidation of the surface would also be expected to cause additional thickening of the original Al_2O_3 film [183].

In experiments where specimens were heated in N_2, when the oxide layer cracked, the freshly exposed Al would react first with any residual O_2, and then with N_2, (because the reaction with O_2 is more favourable at 1000 K). This preferential reaction of O_2 was found to be deleterious to commercial AlN production by Zheng and Reddy [184] [185] who attempted to produce AlN by bubbling commercial purity N_2 through liquid Al. The Gibb's Free Energy of formation of Al_2O_3 and AlN are -908 $kJmol^{-1}$ and -423 $kJmol^{-1}$ respectively [186], [187]. In these experiments the N_2 reacted with the Al between cracks in the oxide film. This is concluded because traces of oxygen were detected in the EDX analysis of the AlN crystals that covered cracks in the pre-existing oxide film, as shown in Figures 4.72 - 4.78. Due to the presence of oxygen in the analysis it is not clear if the crystal structures that formed in the cracks were composed exclusively of AlN, that had nucleated and grown on top of a thin Al_2O_3 film, or if they were an aluminium oxy-nitride spinel with the formula $(AlN)_x{\cdot}(Al_2O_3)_{1-x}$ [188].

AlN crystals and Al_2O_3.AlN mixtures were found across the surface of the specimens. Nitride crystals were observed to have grown within the Al_2O_3 (see Figures 4.75 - 4.78). These discrete crystals presumably formed on smaller cracks and defects in the Al_2O_3 layer which were opened during the heating and melting, and expansion and failure, of the original oxide film.

The crystals that formed in the cracks had a featherlike morphology (see Figure 4.79). A seam was observed to run down the centre of the feather like crystals, suggesting that they

nucleated from the sides of the cracks in the original Al_2O_3 film, and grew in towards the centre of the crack and eventually impinged on one another. Smaller cracks in the oxide film, (as shown in Figure 4.80), were covered with crystals with a more claw-like morphology, (these crystals appeared to be thicker than those in Figure 4.79). It is proposed that the coarser, claw-like crystal structure has greater permeability for H (compared to alumina) because of this morphology. The experiments here demonstrate that H can diffuse through both Al_2O_3 and AlN layers, but that the thickness and structure of the films likely influences the rate at which H can diffuse into the envelope over time and that AlN offers less of a barrier to the passage of H than does alumina.

The implications of this are that, as double oxide film defects are initially expected to be contained within an alumina layer, as cracks appear in the film the O_2 content will be depleted and eventually the N_2 will react with the melt to form AlN. As this process occurs the transport of H into the interior of the bifilm would be expected to increase, as H diffusion is greater over AlN.

When these samples were exposed to H, more H was absorbed by the specimens heated in N_2, most likely because these feather-like and claw-like crystals were porous, possibly due to their shape, compared to the fully dense alumina film. The results demonstrated that H can diffuse through both Al_2O_3 and AlN layers, but that the thickness and structure of the films likely influences the rate at which H can diffuse into the envelope of a double oxide film over time, and that AlN offers less of a barrier to the passage of H than does alumina. The amount of AlN that forms on the surface likely increases the amount of H absorbed for this reason.

The 5083 LECO samples that were heated and melted under an air atmosphere were shown to have absorbed H after subsequently being exposed to H_2. This occurred as a MgO oxide layer should form at the surface, that was not protective, cracking extensively, and did not present a barrier to H diffusion. In an Al 4.5 wt% Mg the oxide formed at the surface should be entirely MgO and this is discontinuous (the Pilling-Bedworth ratio for MgO is <1, see section 2.2.3).

Raizideh and Griffiths [100] showed that, in air bubbles trapped in liquid Al, O_2 reacted first and then N_2 began to react, once nearly all the O_2 was consumed. In low O_2 conditions (such as a mid-life bifilm, where there is little or no O_2 remaining - as represented in these experiments), cracks in the oxide layer would form and allow N_2 to react to form nitride crystals by reaction with the melt. This mechanism would repeat until all the available N_2 was consumed and only the residual un-reacted gases remained, (theoretically H_2 and Ar).

Interestingly the formation of AlN upon cracks was often associated with the presence of Fe and Si, (presumably as an intermetallic in the area beneath the oxide film, as shown in Figures 4.76 - 4.80). Fe-rich phases have been suggested to nucleate on oxide film defects within the melt during solidification and are responsible for a loss in mechanical properties [30], [189]. The presence of Fe and Si below the surface suggests that the cracks that formed in the Al_2O_3 lay above Fe rich intermetallics and thus the oxide film nucleated and grew on top of them. If Fe and Si intermetallics were near the surface of Al then the Al_2O_3 film might be discontinuous. Perhaps cracks open up in the alumina films more readily in these regions, due to Fe-Al-Si intermetallics substituting for Al atoms close to the surface.

The Gibbs Free Energy of Formation for Mg_3N_2 is -257.14 $kJMol^{-1}$ [108], less than that of AlN, indicating that AlN was the more favourable nitride to form. There was no evidence of

nitride formation on the surface of the 2L99 alloy (that contained 0.2 – 0.45 wt.% Mg), however. There appears to be difficulty forming nitrides in low Mg containing alloys, perhaps because in small amounts Mg inhibits the nucleation of both AlN and Mg_3N_2, an effect that was also experienced by El-Sayed [157]. The spinel surface layer is apparently effective at preventing H diffusion, comparable to an Al_2O_3 film.

5.7 The influence of alloying elements on the degassing of 7xxx aluminium alloys

Three independent studies (see sections 5.1, 5.4, 5.5) have suggested that Zr and Ti might react with Cl in a manner that is detrimental to the quality of Al alloys. Zr and Ti intermetallics have been found mixed with Ca and Cl salts as inclusions in rolled Al plate. In section 4.3 there was an apparent reduction in degassing efficiency when 7050 and 7010 alloys were degassed using an Ar and Cl gas mixture. These alloys contained significant quantities of Zr, (0.11 wt% Zr), when compared to the 7075 alloy, (0.02 wt% Zr), which saw no such reduction in degassing efficiency. In section 4.4 the time required to degas 7010 alloy with an Ar and Cl gas mixture was greater than with both pure Al and 5083 alloy, in both of the temperature ranges investigated (680 - 695^{o}C and 730-750^{o}C) and the degassing rate of the 7010 alloy processed with Ar and Cl was lower, compared to the rate for Ar alone.

A possible mechanism of inclusion formation was discussed earlier that involved the interaction of chlorinated bubbles with oxides, and the precipitation of Zr and Ti compounds from the melt. The precipitation of these intermetallics on the surface of bubbles (perhaps on salts or oxides) within the reactor could be responsible for a decrease in degassing performance.

Unfortunately, there is no evidence that Zr or Ti had reacted significantly with Cl when Cl containing gas bubbles were caught in a 7010 alloy melt (as described in section 4.2). If Zr was present on the interior of these bubbles it was not detected during the SEM/EDX analysis, suggesting that there was no agglomeration or adherence of $ZrTiAl_3$ particulates to the gas bubble in this particular experiment, or if there was the equipment was not sensitive enough to detect it. The presence of $MgCl_2$, $ZnCl_2$ or any other chloride was difficult to establish using the SEM images in section 4.2, as Mg and Zn make up substantial portions of

the alloy composition and Cl is present in such small quantities (< 1 wt.%), and any chloride is expected to form a fine coating. For example there was no clear difference in Cl concentration in matrix or eutectic phase / intermetallics (see EDX analysis in Figures 4.46 and 4.47). It is therefore impossible to differentiate between the type of salts that might be formed.

5.8: The internal atmosphere of a double oxide film defect

The results presented in sections 4.6, 4.7 (and 5.6) show that H can pass through alumina and nitride films and successfully pass through the surface of Al alloy, and it also shows that H can be extracted back out of the samples once these various films are formed on the surface of the samples. This suggests that H can diffuse into double oxide defects through these layers.

The consequences of H recombining inside a double oxide film defect have not been considered. The reaction of protons to form a diatomic molecule is a highly exothermic process (see section 2.4.1), giving off -436 kJ mol H_2. If we assume that protons enter the oxide film defect towards the end of solidification, (this is logical as the partitioning of H from solution into the liquid ahead of the solidification process is expected to concentrate H), the protons would enter into the envelope, recombine and release energy in the form of heat, which would cause expansion of the gas and an overall expansion of the bifilm. This would occur not only because H recombines to form a gas phase, but because the gas is heated due to the energy of the reaction (although heat would also be conducted away from the bifilm and into the Al melt).

Assuming that a single bifilm is a simple cylinder and has dimensions of 2 mm and a radius of 0.5 mm, it will occupy a volume of 1.57 mm^3 and contain $1.57x10^{-6}$ Kg of air. This bifilm will act as a reservoir for protons during and at the end of solidification.

The atomic mass of Al is 26.98, therefore 100 g of molten Al contains 3.71 mol Al ($2.23x10^{24}$ Al atoms). If 100 g Al contains between 0.1 - 0.4 ppm of protons then the internal proton content of 100 g Al would range from $2.19x10^{-7}$ to $1.33x10^{-6}$ mol H.

Protons will partition during solidification, some will be trapped in solid solution, others in trap sites, (primarily grain boundaries) and remainder will be forced into a bifilm. Talbot [18] reported that the solubility of H at the point of solidification was 0.041 ppm in pure Al (see Figure 2.4), so a portion of the protons would not reach the bifilm.

If the protons were to enter and react within the bifilm then they would release energy and increase the temperature of the air within the bifilm. The temperature increase caused by the reaction of these protons is calculated using Eq.25, and the results summarised in Table 5.3. The temperature increase of the gas inside a single bifilm was calculated to be only 30 – 180 K.

$$\Delta T = Q/m.Cp \quad \ldots Eq.25$$

where T is the temperature in Kelvin, Q is heat energy in Joules, m is the mass of air in kilograms and Cp is the specific heat capacity of air, which is taken to be 1 kJ/kg.

ppm H in liquid Al	0.1	0.2	0.3	0.4
ppm H not retained in solid solution	0.059	0.159	0.259	0.359
Moles of H (not in solid solution)	2.19×10^{-7}	5.89×10^{-7}	9.60×10^{-7}	1.33×10^{-6}
Heat evolved in Joules	0.10	0.26	0.42	0.58
Temperature increase (K)	30	80	130	180

Table 5.3 The temperature increase of the air within a double oxide film defect by reaction of protons to form diatomic H.

There would be numerous bifilms per 100 g of metal so the heating effect would also be reduced for each bifilm. The DPI inspection reviewed in section 4.1.4 suggests that typically 0 - 20 pores per $inch^2$ (25.4 mm^2) Al might occur. If this is extrapolated to consider how many

pores might be present in 100 g of Al, it suggests that the temperature increase within each pore, (assuming they are all bifilms), is significantly smaller and thus insignificant.

There would be scope for H to react with any residual O_2 within a bifilm to form water vapour, and for the vapour to react with the surrounding melt to form Al, increasing the local temperature further. One would also have to consider the pressure of the gas within the bifilm and the effect of the gas expansion on the surrounding area, the solidification conditions, (primarily solidification rate, as this would have an effect on the rate and degree of segregation of H and formation of porosity) [66], the protons retained in trap sites and the solubility of H at grain boundaries and the ability of H to diffuse or “short circuit” along grain boundaries and through grains towards pores [190] [191]. One would also have to consider the conduction of heat away from the oxide film into the surrounding alloy and the influence of latent heat released during solidification of the surrounding alloy.

Chapter 6 Conclusions

1. Inclusions in 7050 plate were composed of Zr Ti aluminide intermetallics, oxides of Ca, Mg and Al, and $CaCl_2$ and $MgCl_2$.
2. The prevalence of these inclusions in 7xxx alloy plate, (such as 7050 alloy), can be decreased by decreasing the amounts of Zr and Ti in the alloy, or increasing the melt temperature during degassing. This occurs because the solubility of Zr and Ti in the alloy decreases with temperature and subsequently Zr and Ti precipitates come out of solution.
3. An unknown phenomenon causes agglomeration of the intermetallics, oxides and salts, but these three components develop into inclusions in the final plate product that are detectable as they are hot rolled, becoming flattened and elongated.
4. A coarse grain structure was found to be the cause of near-surface ultrasonic defects in the edges of thin gauge 7475 alloy plate, not near surface porosity as initially proposed.
5. There was strong statistical evidence that the coarse grain structure was more common in plates that were produced from ingots with greater cross sectional areas (440, 525 mm) that were widened over 130%. Restricting thin gauge plate to 325 mm cross section ingots eliminated these defects.
6. Small amounts of Cl added into Ar gas in a SNIF unit (1.5% Cl rotor one, 0.8% Cl rotor two) did not significantly influence the degassing of 7xxx wrought alloys.
7. Degassed 5083 alloy specimens absorbed H by reaction with atmospheric water vapour, as did specimens that were immersed in water. Specimens that were

degassed and sealed in an air-tight container absorbed very little H over a period of four days, measured using the LECO.

8. 5083 alloy specimens that were degassed using the LECO, melted in air and exposed to H_2 readily absorbed H as the porous Mg oxide surface film did not impede the diffusion of H.
9. In a low O_2 atmosphere, (such as might exist in a double oxide film defect), N_2 will react with Al to form AlN at cracks or tears in oxide film.
10. Commercial purity Al specimens that were heated in air or N_2 (forming Al_2O_3 or AlN on the surface, respectively) were both observed to absorb H. Absorption into samples that were heated in N_2 was significantly greater, (0.081 vs. 0.041 ppm), and this was probably due to the formation of porous AlN crystals that grew within cracks in the original Al_2O_3 film.
11. The reaction of protons within a double oxide film defect has been calculated to be insignificant, increasing the temperature of the air within a bifilm by only 30 – 180 K when the H content ranged 0.1 – 0.4 ppm.

Chapter 7 Future work

1. To evaluate the effects of Ca and Cl concentration on the formation of inclusions in Zr and Ti containing alloys (such as 7010 and 7050).
2. Repeat the experiments using the ALSPEK H device, using a smaller crucible, or reducing the amount of metal. If this work was to be repeated, the results might be more easily clarified by monitoring the degassing rates of custom alloys such as Al-5wt.% Zn, Al-5wt.%Mg, Al-5wt% Zr etc. to isolate the influences of each specific alloying addition on the degassing efficiency.
3. To take and compare pre-SNIF and post-SNIF H contents (using ALSCAN) on high Mg containing alloys such as 5083 (4.5 wt.% Mg), to gauge the influence of $MgCl_2$ on degassing efficiency.
4. To further investigate the interactions of O_2 and H within bifilms, to calculate or model the distribution of H during solidification (into solid solution, grain boundaries, lattice defects etc.), to calculate the expansion of the gas phase by diffusion of H into the bifilm and the energy released and conducted away into the surrounding alloy during this process. These calculations could also be used to evaluate the effects in Mg and Mg alloys where the H content would be greater.
5. Modifications to the pore gas analyser could be used to incorporate a drill and larger sample holder into the system to make it more suitable for extracting gases from castings.
6. An experiment to test the H diffusivity through liquid and solid salts (such as $MgCl_2$) could be designed. Perhaps linking a H source to one end of a glass u-tube,

(containing the salt) and a thermal conductivity cell to the other end. This experiment could be used to measure the permeation of H through the salt over a period of time.

Chapter 8 References

1. *Alcoa Internal Rejections Database.* **Ellis, T.** 2013.

2. *Kitts Green Process Management V5 Document.* **Morris, A J. Merill, N.** October 2009.

3. *Aluminium Handbook Volume 1: Fundamentals and Materials.* **Kammer, C.** Aluminium-Verlag, 1999. Page 150. ISBN 3870172614.

4. *Aluminium and Aluminium Alloys: ASM Speciality Handbook.* **Davis, J.** The Materials Information Society, 1993. Page 3. ISBN 0-87170-496-X.

5. *Aluminium Alloys. Their Physical and Mechanical Properties. Volume 2.* **Hirsch, J. Skrotzki, B. Gottste, G.** Wiley-VCH. Pages 16 - 36. ISBN 978-3-527-32367-8.

6. *Aluminium: Technology, Applications and Environment.* **Altonpohl, D G.** TMS-AIME, 1998. Pages 72 - 89. ISBN-10: 0873394062.

7. Verfahren zum Gießen von Metallblöcken mit Ausnahme solcher aus Leichtmetallen, **Roth, W.** Patent 974203, filed 1936.

8. Method for Rapidly Casting Aluminium Alloys. **Ennor, W T.** US Patent 2301027, filed 1938.

9. *Macrosegregation in Direct Chill Casting of Aluminium Alloys.* **Nadella, R. Eskin, D G. Du, Q.** Netherlands Institute for Metals Research, Progress in Materials Science, 2008, Vol. 53, Issue 3. Pages 421 - 480.

10. *Mechanisms of Formation of Hydrogen Porosity in 7x50 and 2x24 Aluminium Alloys. Effects on Mechanical Behavior.* **Marquis, F D S.** Gas Interactions in Non-Ferrous Metals Processing. The Minerals, Metals & Materials Society, 1996. Pages 44 - 63.

11. *Physical Metallurgy of Direct Chill Casting of Aluminium Alloys.* **Eskin, D G.** CRC press, 2008. Pages 16 - 18, 24, 108. ISBN 13:978-1-4200-6281-6.

12. *Grain Refining of Aluminium and its Alloys using Innoculants.* **McCartney, D G.** International Materials Reviews, 1989, Vol. 34, Issue 5. Pages 247 - 260.

13. *Grain Refinement of Aluminium and its Alloys by Heterogeneous Nucleation and Alloying.* **Murty, B S. Kori, S A. Chakraborty, M.** International Materials Reviews, 2002, Vol. 47, Issue 1. Pages 3 - 29.

14. *Aluminium Alloys, Products, Processes and Applications*. **Rouns, T N.** Alcoa Technical Centre, Metal Treatment and Ingot Casting, 2008. Pages 11 - 13.

15. *The Energy Required to Produce Materials: Constraints on Energy-Intensity Improvements, Parameters of Demand.* **Gutowski, T.** Philosophical Transactions - Royal Society. Mathematical, Physical and Engineering Sciences, 2013, Vol. 371. Pages 1364 - 1503.

16. *The Complete Castings Handbook.* **Campbell, J.** Butterworth-Heinemann, 2011. Pages 5 - 16, 31, 36, 67 - 72, 78. ISBN-13: 978-1-85617-809-9.

17. *Gases in light metals.* **Sokol'skaya, L I.** Protheroe, London, Pergamon press, 1961. Pages 102 - 111.

18. *The Effect of Hydrogen in Aluminium and its Alloys.* **Talbot, D J.** Maney Publishings. The Institute of Materials, Minerals and Mining, 2004. Pages 5 - 8, 31, 46, 71, 77, 81 - 83, 95, 131 - 133, 147, 154 - 156, 164, 175 - 176, 236, 244 - 246. ISBN 1-902653-73-4.

19. *Modeling the Hydrogen Solubility in Liquid Aluminum Alloys.* **Harvey, J P. Chartrand, P.** Metallurgical and Materials Transactions B, 2010, Vol. 41B. Pages 908 - 924.

20. *Hydrogen Bubbles in Metals.* **Condon, J B. Schober, T.** Journal of Nuclear Materials, 1993, Vol. 207. Pages 1 - 24.

21. *The Solubility of Hydrogen in Liquid Binary Al-Li alloys.* **Granger, D A. Talbot, D E J. Anyalebechi, P N.** Metallurgical Transactions B, 1988, Vol. 19B. Pages 227 - 232.

22. *Diffusion in Liquid Aluminium.* **Ransley, C E. Talbot, D E J.** Z. Metallkunde, 1955, Vol. 46. Page 328.

23. *Alkali Removal and Reduced Chlorine use During Furnace Fluxing.* **Williams, E M.** Light Metals (TMS), 2000. Pages 1053 - 1059.

24. *Removal of Hydrogen from Molten Aluminium by Gas Purging.* **Engh, T A. Pedersen, T.** Journal of Metals, 1983, Vol. 35, Issue 12. Pages 1329 - 1345.

25. *Gas Fluxing of Molten Aluminum: An Overview.* **Sigworth, G K. Williams, E M. Chesonis, C D.** Light Metals (TMS), 2008. Pages 581 - 586.

26. *Analysis of the Effects of Alloying Elements on Hydrogen Solubility in Liquid Aluminium Alloys.* **Anyalebechi, P N.** Scripta Metallurgica Et Materialia, 1995, Vol. 33, Issue 8. Pages 1209-1216.

27. *Attempt to Predict Hydrogen Solubility Limits in Liquid Multicomponent Aluminium Alloys.* **Anyalebechi, P N.** Scripta Materialia, 1995, Vol. 34. Pages 513 - 517.

28. *Effects of Hydrogen in Aluminium, Magnesium, Copper, and their Alloys.* **Talbot, D E J.** International Materials Reviews, International Metallurgical Reviews, 1975, Vol. 20, Issue 1. Pages 166 - 184.

29. *Mechanism of Nucleation and Growth of Hydrogen Porosity in Solidfying A356 Aluminium Alloy: An Analytical Solution.* **Li, K. Chang, E.** Acta Materialia, 2004, Vol. 52. Pages 219 - 231.

30. *Castings, Second edition.* **Campbell, J.** Butterworth-Heinemann, 2003. Pages 1 - 4, 17 - 69, 275 - 279. ISBN 0080488447.

31. *The Diffusion and Trapping of Hydrogen in High Purity Aluminium.* **Young, G A, Scully, J R.** Acta Metallurgica, 1998, Vol. 46, Issue 18. Pages 6337 - 6349.

32. *Soublity of Hydrogen in Aluminium.* **Sieverts, A.** Z. Metall. 1929. Page 112.

33. *The Oxidation of Liquid Aluminium.* **Dholiwar, R.** PhD thesis, Brunel University, 1983. Pages 256 - 289.

34. *Oxide Films on Aluminium.* **Dignam, M J.** Journal of the Electrochemical Society, 1962, Vol. 109, Issue 3. Pages 184 - 191.

35. *Natural and Thermally Formed Oxide Films on Aluminum.* **Fowle, M S. Hunter, P.** Journal of the Electrochemical Society and Alcoa Research Laboratories, 1956, Vol. 103, Issue 9. Pages 482 - 485.

36. *The Kinetics of the Oxidation of Al in Oxygen at High Temperature.* **Beck, A F.** Corrosion science, 1967, Vol. 7, Issue 1. Pages 1 - 22.

37. *Oxidation of Molten High Purity Aluminium in Dry Oxygen.* **Sleppy, W C.** Journal of the Electrochemical Society and Alcoa Research Laboratories, 1961, Vol. 108, Issue 12. Pages 1097 - 1102.

38. *Basic Processes of Surface Preparation and Bond Formation of Adhesively Joined Aluminium.* **Olefjord, L. Kozma, I.** Materials Science and Technology, October 1987, Vol. 3. Pages 860 - 874.

39. *Oxidation of Molten High Purity Aluminium in Dry Oxygen.* **Sleppy, W C.** Journal of the Electrochemical Society and Alcoa Research Laboratories, 1961, Vol. 108, Issue 12. Pages 1097 - 1102.

40. *The Influence of Surface Preparation and Pretreatments on the Oxidation of Liquid Aluminium and Aluminium - Magnesium Alloys.* **Impey, S.** Microscopy of Oxidation 2, 1993. Pages 323 - 336.

41. *Preliminary Investigations on the Deformation Behaviour of an Oxide Scale on Molten Aluminium.* **Fray, K S. Agema, D J.** Cambridge: Department of Materials Science and Metallurgy, University of Cambridge, 1989. Pages 324 - 326.

42. *Mechanism of Scale Growth on Liquid Aluminium.* **Impey, S A. Stephenson, D J. Nicholls, J R.** Materials Science and Technology, 1988, Vol. 4. Pages 1126 - 1132.

43. *The Nucleation Sites of Gamma Alumina Crystals in Thermal Oxide Films on Aluminium.* **Shimizu, K.** Microscopy of Oxidation. Department of Chemistry, Keio University and University of Manchester Institute of Science and Technology, 1991. Pages 144 - 148.

44. *A Study of the Effect of Magnesium Additions on the Oxide Growth Morphologies on Liquid Aluminium Alloys.* **Impey, S.** Microscopy of Oxidation, 1989. Pages 238 - 244.

45. T*he Oxidation of Liquid Aluminium.* **Dholiwar, R.** PhD Thesis, Brunel University, Department of Metallurgy, 1985. Pages 24 - 106.

46. *The Absorption of Hydrogen from Humid Atmospheres by Molten Aluminium and an Aluminium Magnesium Alloy.* **Stephenson, D J.** PhD thesis, Brunel University, Department of Metallurgy 1978. Pages 12 - 98.

47. *The Oxidation of Metals at High Temperatures.* **Pilling, N B. Bedworth, R E.** Institute of Metals, 1923, Vol. 29. Pages 529 - 591.

48. *Oxide Bifilms in Aluminium Alloy Castings - A Review.* **Gopalan, R. Prabhu, N K.** Materials Science and Technology, 2011, Vol. 27, Issue 12. Pages 1757 - 1769.

49. *High Temperature Oxidation of an Al-0.5wt% Magnesium Alloy.* **Shimizu, K.** Microscopy of Oxidation, 1996, Vol 3. Pages 396 - 405.

50. *Oxidation of Aluminium Magnesium Melts in Air, Oxygen, Flue Gas and Carbon Dioxide.* **Cochran, C N. Belitskus, D L. Kinosz, D L.** Metallurgical and Materials Transactions B, 1977, Vol. 8B. Pages 323 - 332.

51. *Light Alloys, 3rd edition.* **Polmear, I J.** London : Arnold, 1995.Pages 5 - 256. ISBN 9780340491751

52. *Complete Castings Handbook.* **Campbell, J.** Butterworth-Heinemann, Elsevier, 2011. Pages 8 - 12. ISBN-13: 978-1-85617-809-9.

53. *Effect of Oxide Flms, Inclusions and Fe on Reproducibility of Tensile Properties in Cast Al–Si–Mg Alloys: Statistical and Image Analysis.* **Eisaabadi, G.** Materials Science & Engineering A, 2012, Vol. 558. Pages 134 - 143.

54. *Effects of Oxides on Tensile Properties of Al-Si-Mg Cast Alloys.* **Eisaabadi, G, et al.** Materials Science and Engineering A, 2012, Vol. 552. Pages 36 – 47.

55. *Curvature of Micropores in Al-Cu Alloys: An X-ray Tomography Study.* **Felberbaum, M. Rappaz, M.** Acta Materialia, 2011, Vol. 59, Issue 18. Pages 6849 - 6860.

56. *Fatigue Crack Growth in Al-Cu Alloy A206 with Different Levels of Porosity.* **Rading, G O. Li, J. Berry, J T.** AFS Transactions, 1994, Vol 102. Pages 57 - 61.

57. *The Solubility of Hydrogen in Liquid and Solid Aluminium.* **Ransley, C E. Neufeld, H.** Journal of the Institute of Metals, 1948, Vol.74, Issue 12. Pages 599 - 620.

58. *Castings, Second edition.* **Campbell, J.** Butterworth-Heinemann, 2003. Pages 1 - 4, 17 - 69, 275 - 279. ISBN 0080488447.

59. *Degassing of Aluminum Alloys during Re-Melting.* **Zhao, L.** Materials Letters, 2012, Vol. 66, Pages 328 – 331.

60. *TALAT - Training in Aluminium Application Technologies.* **Campbell, J and Harding, R.** European Aluminium Association, 1999.

61. *Grain Refinement of Aluminum Casting Alloys.* **Sigworth, G K. Kuhn, T A.** International Journal of Metalcasting, 2007, Vol. 1, Issue 1. Pages 31 - 40.

62. *Porosity Formation in Modified and Unmodified A356 Alloy Castings.* **Granger, D A. Fang Q T.** AFS Transactions, 1989, Vol. 97. Pages 989 - 1000.

63. *Simulations of Hydrogen Diffusion at Grain Boundaries in Aluminum.* **Pedersen, A. Jonsson H.** Acta Materialia, 2009, Vol. 57. Pages 4036 – 4045.

64. *Diffusion Controlled Growth of Hydrogen Pores in Aluminium-Silicon Castings: In Situ Oberveration and Modelling.* **Atwood, R C, et al.** Acta materialia, 2000, Vol. 48. Pages 405 - 417.

65. *Hydrogen-Induced Gas Porosity Formation in Al–4.5 wt% Cu–1.4 wt% Mg alloy.* **Anyalebechi, P N.** Journal of materials science, 2013, Vol 48, Issue 15. Pages 5342 - 5353.

66. *Effects of Solidification Conditions on Hydrogen Porosity in Aluminum Alloy Castings.* **Granger, D A. Fang, Q T. Anyalebechi, P N.** AFS Transactions. 1989.

67. *Simulation of Hot Rolling Process to Eliminate Davenport 7085 Thick Plate Edge Porosity.* **Ulysse, P. Li, M. Venema, G B.** Physical Metallurgy Division of Alcoa Research Laboratories, 2006.

68. *The Effects of Hot Rolling Reduction on the Ultrasonic Response and the Formation and Growth of Edge Band Porosity in 7079-F thick plate.* **Rudolph, F F.** Physical Metallurgy Division of Alcoa Research Laboratories. 1971. Report number 13-71-DU267.

69. *The Effect of Additional Hot Rolling on The Ultrasonic Response, Metallographic Structure and Short Transverse Mechanical Properties of 4-3/4", 7079-T651 Plate Containing Edge Band Porosity.* **Rudolph, F F.** Physical Metallurgy Division of Alcoa Research Laboratories. 1968. Report no. 13-68-DU-267.

70. *Interpretation of Vacuum Gas Test Results for Aluminium Alloys.* **Brondyke, K J. Hess, P D.** Transactions of the Metalurgical Society of AIME, 1964, Vol. 230. Pages 1542 - 1546.

71. *Influence of Melt Cleanliness on Pore Formation in Aluminium-Silicon Alloys.* **Chen, X G. Gruzleski, J E.** Journal of Cast Metals Research, 1996, Vol. 9. Pages 17 - 26.

72. *Origin of Gas Bubbles in Aluminum.* **Tiwari, S N. Beech, J.** Metal Science, 1978, Vol. 12, Issue 8. Pages 356 - 362.

73. *Gas Porosity and Metal Cleanliness in Aluminium Castings Alloys.* **Laslaz, G. Laty, P.** AFS Transactions, 1991, Vol. 40. Pages 83 - 90.

74. *Origin of Gas Bubbles in Aluminum.* **Tiwari, S N. Beech, J.** Metal Science, 1978, Vol. 12, Issue 8. Pages 356 - 362.

75. *Experimental Study on Pore Nucleation by Inclusions in Aluminum Castings.* **Mohanty, P S. Samuel, F H. Gruzleski, J E.** AFS Transactions, 1995, Vol. 103. Pages 555 - 564.

76. *The Concept of the Fatigue Potential of Cast Alloys.* **Nyahumwa C. Green, N R. Campbell J.** Journal of Mechanical Behaviour of Metals, 1998, Vol. 9, Issue 2. Pages 227 - 235.

77. *Strength and Fracture of Aluminium Alloys.* **Kobayashi, T.** Materials Science and Engineering A, 2000, Vol. 280, Issue 1. Pages 8 - 16.

78. *Fatigue Behavior Of A356 Aluminum Cast Alloys. Part I Effects Of Casting Defects.* **Wang, Q C. Apelian, D. Lados, D.A.** Journal of Light Metals, 2001, Vol. 1. Pages 73 - 84.

79. *Fatigue behavior of A356 Aluminum Cast Alloys. Part II: Effect Of Microstructural Constituents.* **Wang, Q C. Apelian, D. Lados, D.A.** Journal of Light Metals, 2001. Vol. 1. Pages 85 - 97.

80. *Fatigue Behaviour of Hot Worked Cast Aluminium Alloys with Different Si Contents.* **Kobayashi, M et al.** International Journal of Cast Metals Research, 2012, Vol. 25, Issue 1. Pages 31 - 37.

81. *Inclusion Transport Phenomena in Casting Furnaces.* **Instone, S. Buchholz, A. Gruen, G U.** Light Metals (TMS), 2008. Pages 811 - 816.

82. *Non-metallic inclusions in the secondary Aluminium Industry for the Production of Aerospace Alloys.* **Prillhofer, B.** Light Metals (TMS). 2008. Pages 603 - 608.

83. *Effect of Iron-Containing Intermetallic Particles on the Corrosion Behaviour of Aluminium.* **Ambat, R. Davenport, A J. Scamans, G M.** Corrosion Science, 2006, Vol. 48, Issue 11. Pages 3455 - 3471.

84. *Mechanical Analysis of Toughness Degradation due to Prematrure Fracture of Coarse Inclusions in Wrought Aluminium Alloys.* **Toda, H. Kobayashi, H. Takahashi, A.** Materials Science and Engineering A, 2000, Vol. 280. Pages 69 - 75.

85. *Application of Digital Image Processing for Automatic Detection and Characterization of Cracked Constituent Particles/Inclusions in Wrought Aluminum Alloys.* **Lee, S G.** Materials Characterization, 2009, Vol. 60. Pages 964 – 970.

86. *Aluminum Foil: Its Typical Quality Problems and Their Causes.* **Keles, O. Dundar, M.** Journal of Materials Processing Technology, 2007, Vol. 186. Pages 125 - 137.

87. *Investigation of the Clustering Behaviour of Titanium Diboride Particles in Aluminium.* **Watson, I G, et al.** Composites A: Applied Science and Manufacturing, 2005, Vol. 36. Pages 1177 - 1187.

88. *A Summary of Four Years of Electron Microprobe Experience in Analyzing Inclusions and Other Unwanted Particles, Comprising 147 Jobs on Plant Material.* **Gray, G D. Frickle, W G.** Alcoa Technical Library, 1970.

89. *Constituent Particle Break-Up During Hot Rolling of AA 5182.* **Moulin, N.** Advanced Engineering Materials, 2010, Vol. 12. Pages 20 - 29.

90. *Void Initiation Close to a Macro-Inclusion During Single Pass Reductions in the Hot Rolling of Steel Slabs: A Numerical Study.* **Ervasti, E and Stahlberg, U.** Journal of Materials Processing Technology, 2005, Vol. 170, Issues 1–2. Pages 142 – 150.

91. *Deformation of Inclusions During Hot Rolling of Steels.* **Luo, C. Stahlberg, U.** Journal of Materials Processing Technology, 2001, Vol. 14, Issue 1. Pages 87 – 97.

92. *The Properties and Uses of Fluxes in Molten Aluminium Processing.* **Utigard, T A, et al.** Journal of Materials, 1998. Pages 38 - 43.

93. *The Science and Technology of Molten Metal And Direct Chill (DC) Casting.* **Evans, P.** Aluminium Federation, Technology Strategy Consultants (TSC), 2009.

94. *Oxide Bifilms in Aluminium Alloy Castings - A Review.* **Gopalan, R. Prabhu, N K.** Materials Science and Technology, 2011, Vol. 27, Issue 12. Pages 1757 - 1769.

95. *An Overview of the Effects of Bifilms on the Structure and Properties of Cast Alloys.* **Campbell, J.** Metallurgical and Materials Transactions B, 2006, Vol. 37A. Pages 857 - 863.

96. *Effect of Mold-Filling Turbulence on Fatigue Properties of Cast Aluminium Alloys.* **Nyahumwa, C. Green, N R. Campbell, J.** AFS Transactions, 1998, Vol. 58. Pages 215 - 223.

97. *A Semi-Empirical Mathematical Model to Estimate the Duration of the Atmosphere within a Double Oxide Film Defect in Pure Aluminium Alloy.* **Raiszadeh, R. Griffiths, W D.** Metallurgical and Materials Transactions B, 2008, Vol. 39, Issue 2. Pages 298 - 303.

98. *A Method To Study The History Of A Double Oxide Film Defect In Liquid Aluminium Alloys***. Raiszadeh, R. Griffiths, W D.** Metallurgical and Materials Transactions B, Vol. 37, Issue 6. Pages 865 - 871.

99. Possibility of the Elimination of Double Oxide Film Defects from Aluminium by Keeping it in the Holding Furnace. **Raeiszadeh, R.** *PhD Thesis.* The Univerity of Birmingham, 2006.

100. *A Method To Study The History Of A Double Oxide Film Defect In Liquid Aluminium Alloys***. Raiszadeh, R. Griffiths, W D.** Metallurgical and Materials Transactions B, Vol. 37, Issue 6. Pages 865 - 871.

101. *Porosity, Hydrogen and Bifilm Content in Al Alloy Castings.* **Dispinar, D. Campbell, J.** Structural Materials Porperties Microstructure and Processing, 2011, Materials Science and Engineering A, Vol. 528. Pages 3860 - 3865.

102. *Entrainment Defects.* **Campbell, J.** 2006, Materials Science and Technology, Vol. 22. Pages 127 - 145.

103. *Permeability of Aluminium to Hydrogen.* **Cochrane, C N.** Journal of the Electrochemical Society, 1961, Vol 108. Page 317.

104. *Hydrogen permeation barrier – Recognition of Defective Barrier Film from Transient Permeation Rate.* **Zajec, B.** International Journal of Hydrogen Energy, 2011, Vol. 36, Issue 12. Pages 7353 – 7361.

105. *Hydrogen Permeation Barrier Performance Characterization of Vapor Deposited Amorphous Aluminum Oxide Films Using Coloration of Tungsten Oxide.* **Yamada-Takamura, H, et al.** Surface and Coatings Technology, 2002, Vol. 153. Pages 114 - 118.

106. *Use of Amorphous Aluminum Oxide on a Capacitor Sidewall for use as a Hydrogen Barrier.* **Aggarwal, S.** *US Patent No. 6876021 B2, filed* 2005.

107. *Determination of the Diffusion Coefficient of Proton in CVD Gamma Aluminum Oxide Thin Films.* **Yu, G T. Yen, S K.** Surface & Coatings Technology, 2003, Vol. 166. Pages 195 - 200.

108. *The Strengths of Chemical Bonds 2nd edition.* **Cottrell, T L.** *Butterworth, London, 1958. Darwent, National.*

109. *Physicochemical Mechanism for the Continuous Reaction of Gamma Alumina Modified Aluminium Power With Water.* **Deng, Z Y. Ferreira, J M F.** Journal of the American Ceramic Society, 2007, Vol. 90, Issue 5. Pages 1521 - 1526.

110. *Chemical and Kinetic Factors Related To Hydrogen Removal From Aluminium.* **Sigworth, G K. Engh, T A.** 1982, Metallurgical Transactions B, Vol. 13B. Pages 447 - 460.

111. *Theoretical and Experimental Iinvestigation of Furnace Chlorine Fluxing.* **Celik, C. Doutre, D.** Light Metals (TMS), 1989. Pages 792 - 800.

112. *The Effect of Microhydrodynamics on Bubble–Particle Collision Interaction.* **Firouzi, M. Nguyen, A V.Hashemabadi, S H.** Minerals Engineering, 2011, Vol. 24. Pages 973 - 986.

113. *Prediction of the Optimum Bubble Size for Inclusion Removal from Molten Steel by Floatation.* **Wang, L. Lee, H G. Hayes, P.** International Department of Mining and Metallurgical Engineering. The University of Queensland, 1996, Vol. 36. Pages 7 - 16.

114. *Removal of Inclusions from Molten Aluminium by Flotation in a Stirred Reactor: A Mathematical Model and a Computer Simulation.* **Mirgaux, O, et al.** International Journal of Chemical Reactor Engineering, 2008, Vol. 6. Article A52.

115. *Alumininium Floatation in Stirred Reactor: A Mathematical Model and a Computer Simulation Coupling CFD and Population Balance.* **Mirgaux, O, et al.** Light Metals (TMS), 2009. Pages 743 - 748.

116. *The Removal of Solid Particles from Molten Aluminium in the Spinning Nozzle Inert Floatation Process.* **Szekely, A G.** Metallurgical Transactions B, 1976, Vol. 7B. Pages 259 - 270.

117. *Inclusion Removal by Bubble Flotation in Continuous Casting Mold.* **Zhang, L. Aoki, J. Thomas, B G.** MST Conference Proceedings, 2004. Pages 161 - 177.

118. *Removal of Suspensions of Fine Particles from Water by Colloidal Gas Aphrons (CGAs).* **Mansur, E. Wang, Y. Dai, Y.** Separation and Purification Technology, 2006, Vol. 48. Pages 71 - 77.

119. *Mathematical Modeling of Flows in Molten Aluminium Holding Furnaces and a New and Simple Probe for In-Line Analysis of Hydrogen in Aluminium Alloys.* **Frayce, D, et al.** Journal of Metals, 1989, Vol 81. Pages 76 - 102.

120. *Removal of Inclusions From Aluminium Through Filtration.* **Damoah, L N. Zhang, L.** Light Metals (TMS). Metallurgical and Materials Transactions B, 2010, Vol. 41, Issue 4. Pages 886 - 907.

121. *Deep Filtration of Molten Aluminum using Ceramic Foam Filters and Ceramic Particles with Active Coatings.* **Zhou, M.** Metallurgical and Materials Transactions A, 2003, Vol. 34A. Pages 1183 - 1191.

122. *Online Metal Cleanliness Determination in Molten Aluminium Alloys Using the LiMCA-II Analyser.* **Martin, M. Hachey, P. Painchaud, S.** Light Metals (TMS), 1994. Pages 915 - 920.

123. *Improving fluxing of Aluminium Alloys.* **Beland, G. Dupuis, C. Martin, J P.** Light Metals (TMS), 1995. Pages 1189 - 1195.

124. *In-line Salt Fluxing Process: The Solution to Chlorine Gas Utilization In Casthouses.* **Leboeuf, S, et al.** Light Metals (TMS), 2007. Pages 623 - 628.

125. *Inclusion Removal and Detection in Molten Aluminum: Mechanical, Electromagnetic, and Acoustic Techniques.* **Makarov, S. Apelian, D. Ludwig, R.** AFS Transactions, 1999. Pages 727 - 742.

126. *Mathematical Modeling and Computer Simulation of Molten Aluminum Cleansing by the Rotating Impeller Degasser Part II. Removal of Hydrogen Gas and Solid Particles.* **Warke, V S. Shankar, S. Makhlouf, M M.** Journal of Materials Processing Technology, 2005, Vol. 168. Pages 119 – 126.

127. *Chloride Salt Injection to Replace Chlorine in the Alcoa A622 Degassing Process.* **Chesonis, C D. DeYoung, D H.** Light Metals (TMS), 2008. Pages 569 - 574.

128. *An Evaluation of a SNIF unit as an Inclusion Removal and Degassing Device.* **Eister, W C. Krumme, W R.** Light Metals (TMS), 1991, Pages 1171 - 1177.

129. **Bell, S, et al.** *Final Report on Refining Technologies of Aluminum.* Enhanced Recycling, Action Plan on Climate Change, Minerals and Metals Program. The Government of Canada Action Plan, 2000. Report No. 2003-21(CF).

130. *Gas Fluxing of Aluminium: Comparison of Computational Fluid Dynamics Models and Experiments.* **Fjeld, A. Evans, J. Chesonis, C D.** Light Metals (TMS), 2006, Vol. 4. Pages 771 - 776.

131. *Inclusion Removal Kinetics During Chlorine Fluxing Of Molten Aluminium.* Light Metals (TMS), 2001, **Roy, R R. Utigard, T A. Dupuis, C.** Pages 991 - 998.

132. *Mechanisms of Sodium, Calcium and Hydrogen Removal From an Aluminioum Melt in a Stirred Tank Reactor - The Alcoa A622 process.* **Stevens, J G. Yu, Ho.** Molten Metal Processing Division, Alcoa Laboratories, Alcoa Technical Centre. Pages. 437 - 443.

133. *Thermodynamic condiserations of Aluminium Refining and Fluxes.* **Utigard, T.** Extraction, Refining and Fabrication of Light Metals, 1991, Vol. 24. Pages 353 - 365.

134. *Improved Molten Metal Quality at the Outlet of the Furnace Through IRMA Treatment.* **Brun, P L. Mathis, A.** Light Metals (TMS), 2004. Pages 789 - 792.

135. *Improved Understanding of the Melting Behaviour of Fused Magnesium Chloride- Potassium Chloride Based Refining Fluxes.* **Courtenay, J H.** Light Metals (TMS), 2008. Pages 637 - 642.

136. *Chloride Salt Injection to Replace Chlorine in the Alcoa A622 Degassing Process.* **Corleen, C D. DeYoung, D H.** Light Metals (TMS), 2008. Pages 569 - 574.

137. *Chlorine Fluxing for Removal of Magnesium from Molten Aluminum: Part I. Laboratory-Scale Measurements of Reaction Rates and Bubble Behavior.* **Qian, F. Dong, X. Evans, J W.** Metallurgical and Materials Transactions B, 1998, Vol. 29B. Pages 971 - 978.

138. *Kinetics of Hydrogen Degassing of Molten Aluminium by Purge Gases.* **Botor, J.** Aluminium; Institute Of Non-Ferrous Metals, 1980, Vol. 56, Issue 8. Pages 519 - 522.

139. *On the Kinetics of Removal of Sodium from Aluminium and Aluminium - Magnesium Alloys.* **Kulunk, B. Guthrie, R.** Light Metals (TMS), 1992. Pages 963 - 975.

140. *Ellingham Diagrams. Standard Gibb's Energies of Formation for Chlorides, Nitrides, Oxides And Other Compounds.* Free Energies of Formation of Binary Compounds. **Howard, S M.** MIT Press, 2006.

141. *The Roles of Molten Salts in the Treatment of Aluminium.* **Utigard, T A. Roy, R R. Friesen, K.** Canadian Metallurgical Quarterly, 2001, Vol. 40, Issue 3. Pages 327 - 334.

142. *Chlorine Fluxing for Removal of Magnesium from Molten Aluminum: Part I. Laboratory-Scale Measurements of Reaction Rates and Bubble Behavior.* **Fu, Q. Dong, X. Evans, J W.** Metallurgical and Materials Transactions B, 1998, Vol. 29B. Pages 972 - 978.

143. *A Computer Model Investigation Of The Effects Of Operation Parameters On The Hydrogen Reemoval Rate In The Alcoa 622 Process.* **Stevens, J G. Yu, H.** 1992, Light Metals (TMS). Pages 1023 - 1029.

144. *The Detection of Hydrogen in Molten Aluminium.* **Lapham, D P, et al.** 8th EuroConference on Ionics, 2002. Pages 391 - 401.

145. *AlSCAN Manual Analyzer for Hydrogen In Liquid Aluminum.* ABB BOMEM, 2007. IMZ9165 Revision 1-4. Page 1.13.

146. *RH-402 Hydrogen Analyser Manual.* LECO Corporation. Pages 1 - 16.

147. *AlSCAN Manual Analyzer for Hydrogen In Liquid Aluminum.* ABB BOMEM, 2007. IMZ9165 Revision 1-4. Pages 3.21 - 3.25, 4.52, A.119 - A.202.

148. *Technical Report: Simultaneous Oxygen, Nitrogen and Hydrogen Determination of Metals.* **Lawrenz, D. Hawkins, J.** LECO Corporation, St Joseph, Michigan, USA. 209-141-004 4/03.

149. *Aluminium: Properties and Physical Metallurgy.* **Hatch, J E.** American Society for Metals, 1984. Pages 3 - 5, 117 - 120. ISBN 0871701766.

150. *Materials Science and Engineering: An introduction. 7th Edition.* **Callister, W D.** 2001. Pages 194 - 198. ISBN-10: 0006970117.

151. *Review of Fatigue and Fracture Research on High Strength Aluminium Alloys.* **Sanders, T H. Staley, J T.** Alcoa Metallurgical Sourcebook, 1978.

152. *Recrystallisation Resistance of Al Alloy 7150.* **Ranganathan, K. Sanders, T H.** Proceedings of the Third International Conference on Aluminium Alloys: Their Physical and Mechanical Properties, 1992, Vol. 2. Pages 355 - 360.

153. *The Effect of Zirconium Additions on the Recrystallization Behavior of hot Rolled and Solution Heat Treated AA 6013.* **Thanaboonsombut, B. Sanders, T H. Lapasset, G.** Metallurgical and Materials Transactions A, 2004.

154. *Non Destructive Testing Handbook, Volume 7. Ultrasonic testing. 3rd edition.* **Wrorkman, G L, Kishoni, D. Omoore, P.** American Society for Non-Destructive Testing. Pages 38 - 39, 407 - 409 ISBN 978-1-57117-105-4.

155. *International Alloy Designations and Chemical Composition Limits for Wrought Aluminum and Wrought Aluminum Alloys.* Registration Record Series Teal Sheets. The Aluminum Association, 2009.

156. *Metals handbook. 9th Edition, Metallography and Microstructures.* **Dieter, G E.** American Society for Metals, 1985. Pages 354 - 355. ISBN 0-87170-015-8.

157. *Double Oxide Film Defects and Mechanical Properties in Aluminium Alloys.* **El-Sayed, M A.** PhD thesis. College of Engineering and Physical Sciences of the University of Birmingham, 2012.

158. *Gas Fluxing Of Molten Aluminium, Part 1, Hydrogen Removal.* **Sigworth, G K.** Light Metals (TMS), 1999. Page 641.

159. *Critical Review of Reported Values of Hydrogen Diffusion in Solid and Liquid Aluminum and its Alloys.* **Anyalebechi, P N.** Light Metals (TMS), 2003. Page 857 - 872.

160. *The Production of AlN-rich Matrix Composites by the Reactrive Infiltration of Al Alloys in Nitrogen.* **Swaminathan, S. Srinivasa, R B. Jayaram, V.** Acta Materialia, 2002, Vol. 50. Pages 3095 - 3106.

161. *The Influence of Oxygen Impurities on the Formation of AlN-Al Composites by Infiltration of Molten Al-Mg.* **Swaminathan, S. Srinivasa, R B. Jayaram, V.** Materials Science and Engineering A, 2002, Vol. 337. Pages 134 - 139.

162. *Maximising the Quality of DC Cast Aluminium Billet.* **Fielding, R A.** Light Metals (TMS), 2006. Pages 897 - 906.

163. *Electron Probe Microanalysis.* **Potts, P J.** A Handbook of Silicate Rock Analysis, Chapter 10, 1987. Pages 326 - 382. ISBN 978-0-216-93209-8.

164. *Particle distribution and Orientation in Al-Al3Zr and Al-Al3Ti FGMs Produced by the Centrifugal Method.* **Sequeira, P D. Watanabe, Y. Rocha, L A.** Materials Science Forum, Functionally Graded Materials 8, 2005, Vols. 492 - 493. Pages 609 - 614.

165. *Solubility Limits of Zr in 7055 Alloy.* **Chu, M G.** Alcoa Metallurgical Sourcebook, 1997. Report number 01F011B.

166. *The Effect of Ti content on the Formation of Primary Al3(Zr,Ti) Intermetallic in 7050 and 7055.* **Chu, M G.** Alcoa Metallurgical Sourcebook, 1998. Report number 01F011F.

167. *Structural Peculiarities of Al-Ti-Zr Modifying Ligatures.* **Pastukhov, E A. Popova, E A. Kotenkov, P V.** Institute of Metallurgy, Urals Branch of RAS, 2012. Pages 149 - 155.

168. Aluminium Alloys, Structures and Properties. **Witt, W.** Z. Naturforsch A, 1967, Vol. 22A. Pages 92 - 95.

169. *Maximizing Dispersoid Content : Solubility Limits of Zr in 7050 Alloy to Avoid Coarse Intermetallic in Ingot.* **Chu, M G.** Memorandum, 1997, Vol. Alcoa Metallurgical Sourcebook. Report number 01F011G.

170. *Effect of Pressure Cycle and Extension Probe on LiMCA Measurement of Inclusions.* **Cooksey, M. Ware, T. Couper, M J.** Light Metals (TMS), 2001. Pages 965 - 971.

171. *Measurement of the Performance of In-Line Processes Using LiMCA.* **Ware, T N. Cooksey, M. Couper, M J.** Aluminium Cast House Technology (TMS), 2001. Pages 45 - 54.

172. *Measurement of Non-Metallic Inclusions in the Size Range of 10-20 Microns by LiMCA.* **Badowski, M. Instone, S.** Light Metals (TMS), 2012. Pages 1077 - 1084.

173. *A Contribution To Inclusion Measurement After In-line Degassers With PoDFA and LiMCA.* **Krug, H P. Schneider, W.** Light Metals (TMS), 1998. Pages 863 - 870.

174. *Materials Perspective: Entrainment Defects.* **Campbell, J.** Materials Science and Technology, 2006, Vol. 22. Pages 127 - 145.

175. *Aluminium Alloy Castings.* **Kaufman, J G. Rooy, E L.** AFS, 2005. ISBN 0-87170-803-5.

176. *Current Issues in Recrystallization.* **Doherty, R D. Hughes, D A. Humphreys, F J.** Materials Science and Engineering A, 1997, Vol. 238. Pages 219 - 274.

177. *Recrystallisation in the Semi-Solid State in 7075 Aluminium Alloy.* **Atkinson, H V. Burke, K. Vaneetveld, G.** Materials Science and Engineeing A, 2008. Pages 266 - 276.

178. *The Nucleation and Growth of Microporosity in Aluminum - 7GA. Silicon Foundry Alloy.* **Anson, J P.** PhD thesis. Department of Minging and Metallurgical Engineering, McGill University, 2000. Document number: 0-612-69848-3.

179. *Pureshield Argon Safety data sheet / MSDS.* British Oxygen Corporation (BOC), 17/08/06. NR: 300-00-0001.

180. *Technical Report: Startup and Evaluation of the First SNIF SHEER™ System at Kaiser Aluminum, Trentwood Works.* **Buehler, J E. Frank, A R.** Light Metals (TMS), 1993. Pages 126 - 132.

181. *The Surface Tension of Molten Aluminum and Al-Si-Mg Alloy under Vacuum and Hydrogen Atmospheres.* **Anson, J P. Drew, R A. Gruzleski, J E.** Metalluirgical and Materials Transactions B, 1999, Vol. 30B. Pages 1027 - 1032.

182. *RH-402 Hydrogen Analyser Manual.* LECO Corporation. Pages 1 - 16.

183. *Oxidation of Aluminum in the Temperature Range 400–600°C.* **Smeltzer, W W.** Journal of the Electrochemical Society, 1956, Vol. 103. Pages 209 - 214.

184. *Mechanism of In-Situ Formation of AlN in Al melt using Nitrogen gas.* **Zheng, Q. Reddy, R G.** Journal of Materials Science, 2004, Vol. 39. Pages 141 - 149.

185. *In-Situ Porcessing of Al Alloy Composites.* **Zheng, Q. Wu, B. Reddy, R.** Advanced Engineering Materials, 2003, Vol. 5. Pages 167 - 172.

186. *Feasibility of Aluminium Nitride Formation in Aluminum Alloys.* **Hou, Q. Mutharasan, R. Koczak, M.** Materials Science and Engineering, 1995, Vol. A195. Pages 121 - 129.

187. *JANAF Thermochemical Tables.* **Chase, M W.** Michigan: American Chemical Society / American Institute of Physics for the National Bureau of Standards: Journal of Physical and Chemical Reference Data, 1985, Vol. 14.

188. *Phase Relations and Reaction Sintering of Transparent Cubic Aluminum Oxynitride Spinel (ALON).* **McCauley, J W . Corbin, N D.** Journal of the American Ceramic Society, 1979, Vol. 62. Pages 476 - 479.

189. *The Nucleation of Fe-rich Phases on Oxide Films in Al-11.5Si-0.4Mg Cast Alloys.* **Campbell, J. Cao, X.** Metallurgical and Materials Transactions A, Physical Metallurgy and Materials Science, 2003, Vol. 34A. Pages 1409 - 1420.

190. *Grain-Boundary Effect on Diffusion of Hydrogen in Pure Aluminium.* **Ichimura, M. Sasajima, Y. Imabayashi, M.** Materials Transactions (JIM), 1991, Vol. 32. Pages 1109 - 1114.

191. *Diffusion of Hydrogen in Pure Large Grain Aluminium.* **Outlaw, R A. Peterson, D T. Schmidt, F A.** Scripta Metallurgica, 1982, Vol. 16. Pages 287 - 292.

192. *An Experimental Study of Hydrogen Solubility in Liquid Aluminium.* **Liu, H. Bouchard, M. Zhang, L.** Journal of Materials Science, 1995, Vol. 30. Pages 4309 - 4315.

Appendix I:

Ellingham diagram, formation of chlorides.

Appendix II:

Published work

A.J. Gerrard and W.D. Griffiths. *The Formation of H Related Porosity by Double Oxide Film Defects in Al Alloys.* 5th Shape Casting Symposium. TMS Annual Meeting & Exhibition, Feb 16 – 20th, 2014. San Diego, California (conference paper).

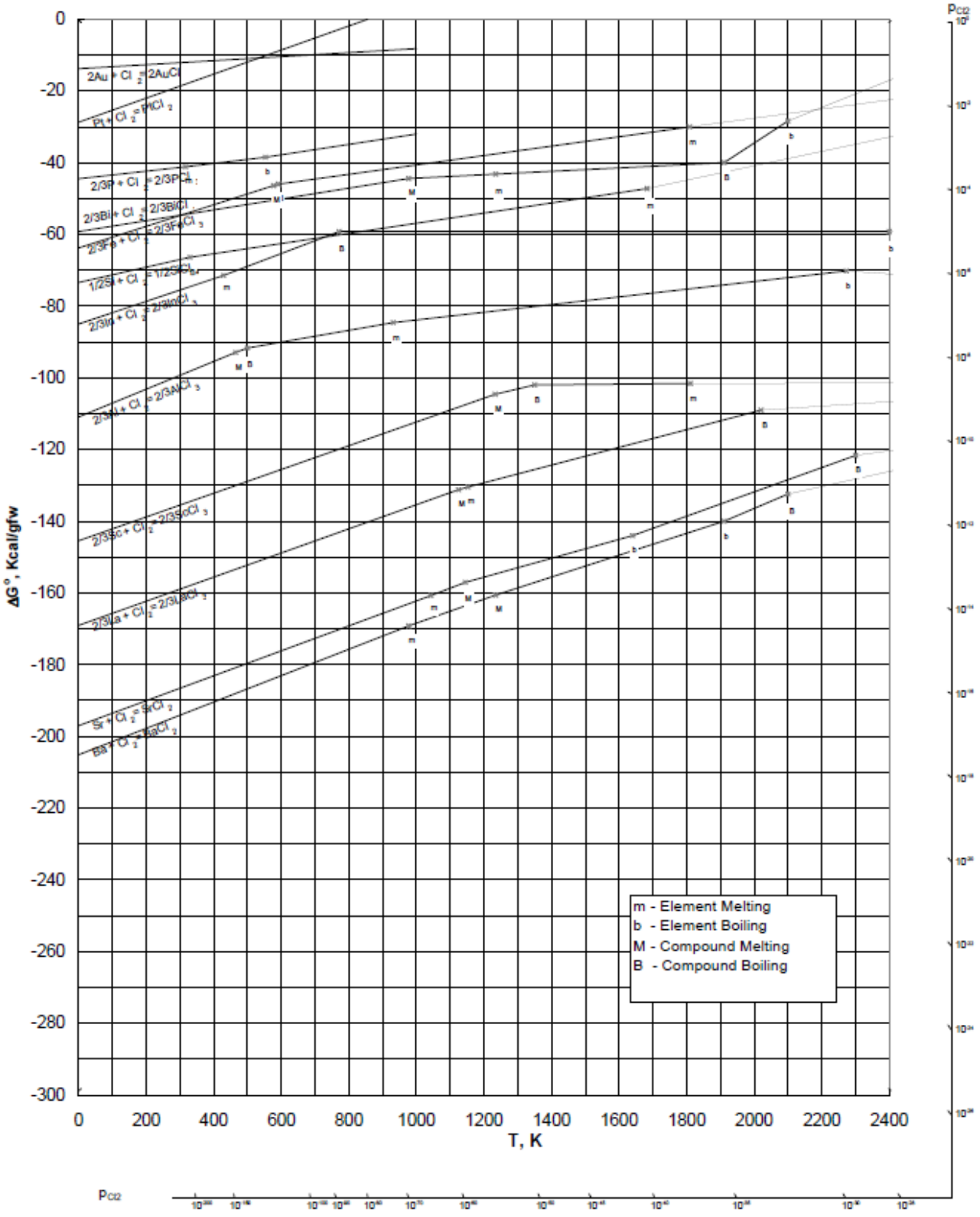
ΔG°, Kcal/gfw
T, K
P_{Cl2}
2Au + Cl 2 = 2AuCl
Pt + Cl 2 = PtCl 2
2/3P + Cl 2 = 2/3PCl 3
2/3Bi + Cl 2 = 2/3BiCl 3
2/3Fe + Cl 2 = 2/3FeCl 3
1/2Si + Cl 2 = 1/2SiCl 4
2/3W + Cl 2 = 2/3WCl 6
2/3Al + Cl 2 = 2/3AlCl 3
2/3Sc + Cl 2 = 2/3ScCl 3
2/3La + Cl 2 = 2/3LaCl 3
Sr + Cl 2 = SrCl 2
Ba + Cl 2 = BaCl 2
m - Element Melting
b - Element Boiling
M - Compound Melting
B - Compound Boiling

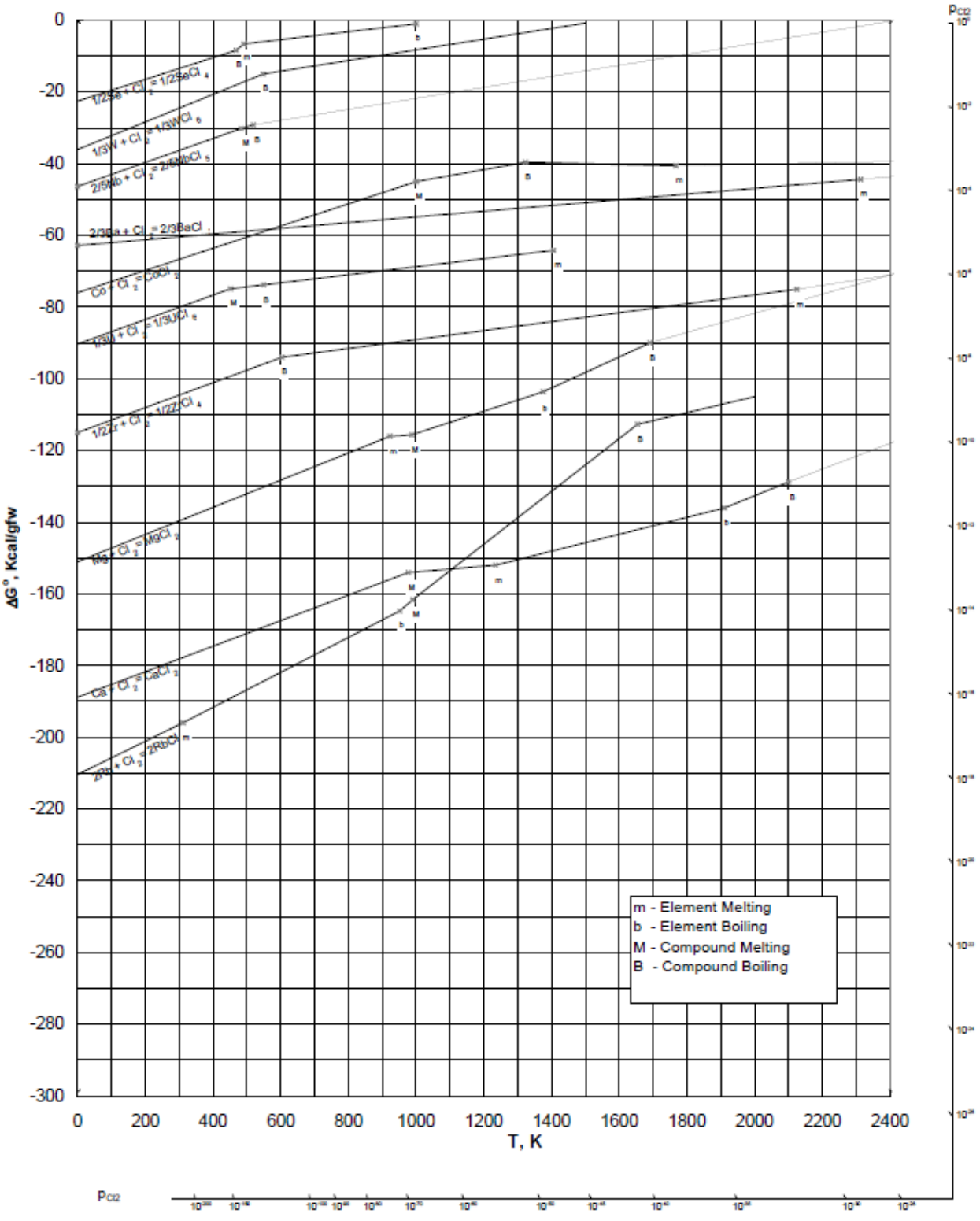
ΔG°, Kcal/gfw
T, K
m - Element Melting
b - Element Boiling
M - Compound Melting
B - Compound Boiling
1/2Se + Cl2 = 1/2SeCl4
1/3W + Cl2 = 1/3WCl6
2/5Nb + Cl2 = 2/5NbCl5
2/3Ba + Cl2 = 2/3BaCl2
Co + Cl2 = CoCl2
1/3U + Cl2 = 1/3UCl4
1/2Zr + Cl2 = 1/2ZrCl4
Mg + Cl2 = MgCl2
Ca + Cl2 = CaCl2
Rb + Cl2 = 2RbCl
PCl2

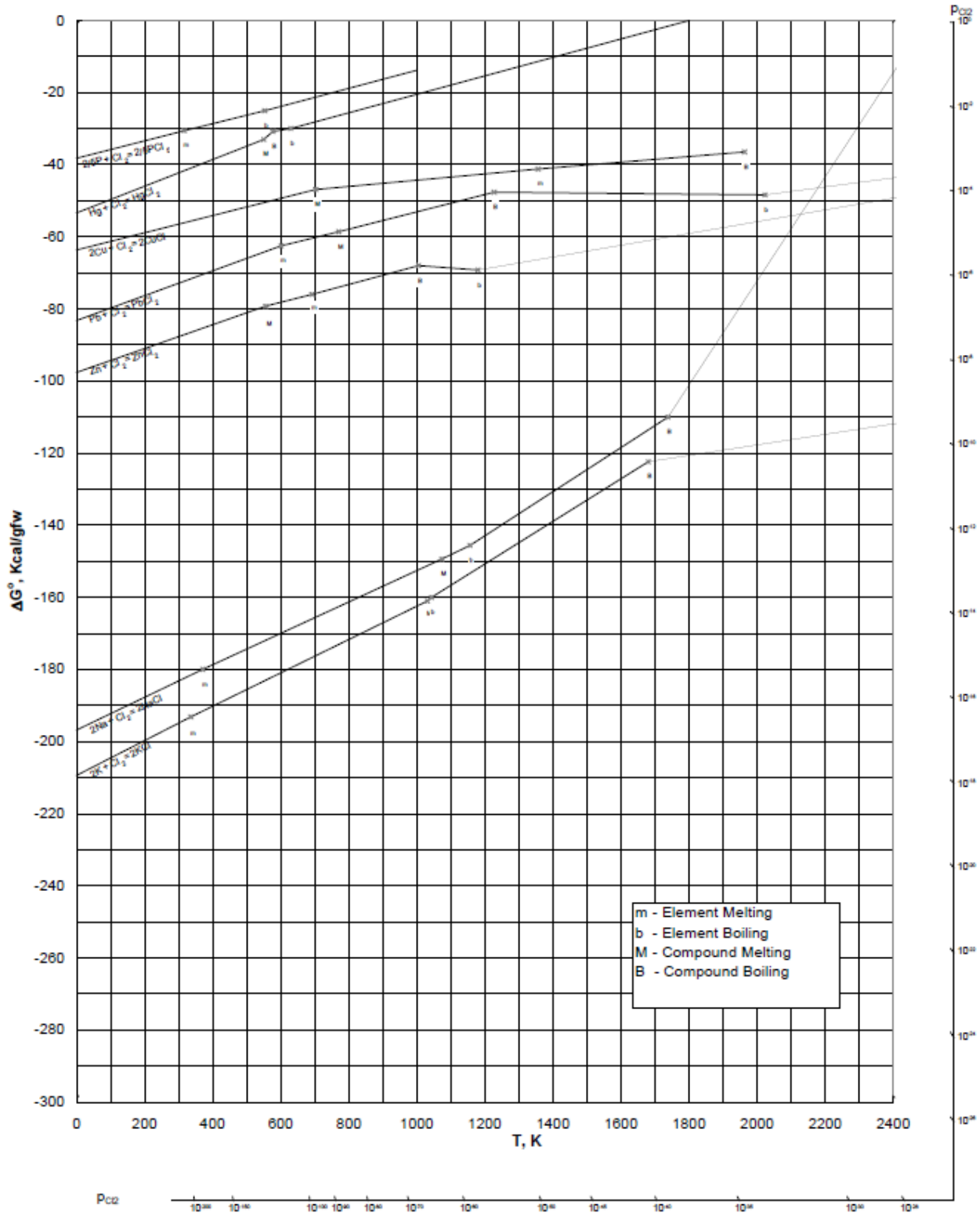
ΔG°, Kcal/gfw
T, K
m - Element Melting
b - Element Boiling
M - Compound Melting
B - Compound Boiling
PCl2

The Formation of H Related Porosity by Double Oxide Film Defects in Al Alloys

A.J. Gerrard[1] and W.D. Griffiths[2]

[1]Alcoa Europe, Kitts Green, Birmingham, UK, B33 9QR.
[2]School of Metallurgy and Materials, College of Engineering and Physical Sciences, University of Birmingham, Edgbaston, Birmingham, UK, B15 2TT.

Keywords: Oxide Films, Aluminium Alloys, Aluminium Oxide, AlN, H Porosity.

Abstract

Liquid aluminium readily forms a surface oxide film, and during melting, casting and metal transfer operations double oxide film defects may be readily entrained into the liquid metal. Dissolved H is thought to diffuse into these defects and re-combine to form diatomic H_2 molecules, leading to the formation of H porosity in the solid casting. However the diffusion of H into double oxide film defects may be considered unlikely as even thin Al oxide films have been reported to be effective barriers to the diffusion of H. In the experiments reported here, solid samples of commercial purity Al alloy were degassed by repeated use of a LECO H measurement device, then melted and exposed to an atmosphere of either oxygen or nitrogen. This created a surface containing Al_2O_3, or Al_2O_3 and AlN, respectively. When exposed to a H_2 gas atmosphere, the absorption of H was found to be greater in specimens containing AlN on the surface. The results suggest that AlN can form in cracks in an existing oxide layer and allowed greater diffusion of H when compared to samples with only alumina on their surface.

Introduction

An oxide film rapidly forms on the surface of molten aluminium and aluminium alloys due to their high chemical affinity for oxygen. These surface oxide films can fold over due to surface turbulence of the melt, such as that generated by a poor running system, resulting in the formation of double oxide film defects, (also referred to as bifilms), in a process initially proposed by Campbell [1]. Campbell also suggested that H dissolved in the melt, (which originates from the reaction between molten aluminium and water vapour), could diffuse into bifilms and inflate them, leading to the development of H gas porosity. This occurs because bifilms will encapsulate and entrap atmospheric gases during their entrainment (probably consisting principally of air) [2], and provide a pre-existing gas phase into which H can diffuse [3]. Diffusion of H into this gaseous envelope could cause expansion of the defect into spherical bubbles with dimensions far greater than the original bifilm [4]. Bifilms present a convenient solution to the problem of nucleation of H_2 gas porosity during solidification, as both homogeneous and heterogeneous nucleation have been suggested to be unlikely to occur due to the high internal gas pressures required [1,5,6,7]. A pre-existing gas phase eliminates the requirement for nucleation of a gas pore.

Following entrainment and formation of a bifilm the gases within have been suggested to be consumed by reaction with the melt. Nyahumwa *et al.*[8] suggested that the continuous amorphous alumina formed on the surface of the melt is entrained, and then transforms to γ-Al_2O_3 and then to α-Al_2O_3, resulting in a 24% reduction in oxide volume. This transformation leads to rupture of the oxide film, allowing the gases within the bifilm to react with the surrounding melt. Raiszadeh and Griffiths [9] trapped an air bubble in an inert ceramic tube held in an Al melt, and observed a reaction between aluminium and oxygen, forming aluminium oxide, followed by a quicker consumption of gases after

about 5 hours, perhaps attributable to break away oxidation and failure of the oxide film as described by Sleppy [10]. Once all the available oxygen was consumed the nitrogen contained within the bubble started to react with the melt (through the cracks in the oxide film) to form AlN.

For a bifilm to be a precursor to gas porosity, H must first be able to enter the bifilm envelope. H in solution exists in the form of protons, diffusing interstitially throughout the liquid metal [7,11]. Protons would be expected to diffuse through or circumvent the ceramic bifilm and to recombine in the bifilm interior to form diatomic H_2 molecules, which is an exothermic process [12]. H might also react with O to form H_2O. Aluminium oxide however, has been shown to be an effective barrier to the diffusion of H [13]. The diffusion coefficient of protons through alumina has been measured to be as little as $6.5x10^{-18}$ cm^2s^{-1} at 25^{o}C [14]. Films of aluminium oxide as little as 20 nm thick are used as surface deposition barrier coatings in chemical and electrical engineering applications to control the diffusion of H. Relating this to double oxide film defects, aluminium oxide films that crack or tear should be quickly sealed by formation of aluminium oxide, which means that the theory that bifilms are a precursor to hydrogen porosity is undermined by the apparent inability of protons to diffuse into the defect through the oxide walls.

However, once all or most of the oxygen in the interior atmosphere has been consumed in this way, AlN should then form. It is unclear if H can diffuse through AlN structures, and this work is aimed at determining if H can diffuse into the bifilm defect interior atmosphere more readily through AlN than through alumina.

Experimental Procedure

Accurately assessing the H content of solid aluminium alloys is challenging because there are no standards to which measurements can be compared. The LECO H determination device heats solid specimens and extracts the H contained within into a nitrogen carrier gas. The H content is established by assessing the thermal conductivity of the resulting N_2 and H_2 gas mixture, however the extraction proces is not repeatable.

Commercially pure Al (>99.7% Al) and 5083 wrought alloy were used in these experiments. The composition of the alloy influences the oxide that forms on the sample surface; pure aluminium forms aluminium oxide (Al_2O_3) and 5083 (containing 4.0-4.9 wt.% Mg) forms MgO oxide (MgO), respectively [1]. Several specimens were machined from each alloy of 8 mm OD and 50 mm length, for determination of H content using a LECO. In each instance the LECO was first prepared by heating it five times using a high temperature outgassing procedure (>700^{o}C) that drives moisture from the furnace and the graphite crucible used in the measurement. The machine was then calibrated by dosing the thermal conductivity cell with pure H gas (>99.9995% H). Low oxygen nitrogen (>99.998% N) was used as a carrier gas to extract H from the samples.

In the first experiment the degassing potential of the LECO was evaluated by repeatedly analysing two 5083 alloy samples 10 times. After 10 analyses the two samples were left to stand exposed to air in the laboratory for 10 weeks, before being re-measured by the LECO, in order to determine the H absorption over this period.

In the second experiment analysed/degassed samples were placed in different environments to observe their influence on the absorption of H. Four 5083 alloy samples were analysed/degassed using the LECO (three times), and then placed in different atmospheric conditions for four days before their H absorption was determined using the LECO. A single sample was placed in each of the following environments; (1) submerged in a glass container filled with water, (2) placed in a glass jar open to the atmosphere, (3) sealed in a glass container (limiting the available water vapour), and (4) submerged in a glass container filled with acetone.

In a third experiment the composition of the surface film was modified by melting the alloy samples in different atmospheres. Pure aluminium and 5083 alloy samples were degassed using the LECO (three times), then placed in a furnace with a controlled atmosphere, with different experiments conducted as detailed in the following:

Experiment 3(a):
Two commercial purity aluminium samples were degassed and then sealed into the furnace at room temperature in an atmosphere of air. The furnace was heated to 700^{o}C at a rate of 40 Kmin^{-1} and the samples first expanded, cracking any surface oxide film, and then melted. The surface of these samples would therefore be oxidised during heating and melting in the air, forming an Al_2O_3 surface oxide film over the entire surface of the samples. They were held at 700^{o}C for 15 minutes, after which the air was removed to a vacuum pressure of 1 Pa. The furnace was then filled with H_2 gas to a pressure of 150 kPa and held at this temperature and pressure for one hour. The furnace was then cooled at a rate of 20 Kmin^{-1} per minute to 50^{o}C before the H was removed and the samples taken out. The samples were placed in sealed glass jars and their H content measured in the LECO.

Experiment 3(b):
Two degassed commercial purity aluminium samples were inserted into the furnace along with a ceramic dish that contained approximately 50g of Hf turnings, (to act as an oxygen scavenger). The atmosphere was reduced to a pressure of 1 Pa of air, and then filled with Ar (99.999% purity) to a pressure of 100 kPa. The Ar was then removed by vacuum until a residual pressure of 1 Pa remained within the furnace. The system was pressurised with Ar and removed by vacuum five times to try to ensure that minimal atmospheric oxygen or water vapour remained within the furnace. The evacuated furnace was then filled with low oxygen nitrogen (>99.998% N) to a pressure of 150 kPa, before being heated to 700^{o}C and allowed to stand for 15 minutes in a nitrogen atmosphere. It was expected that these samples would form AlN (AlN) on any exposed Al surface occurring during heating or melting. The furnace was then evacuated, removing the nitrogen gas, and filled with H_2 gas to a pressure of 150 kPa and held at this temperature and pressure for one hour. The furnace was then cooled at a rate of 20 Kmin^{-1} per minute to 50^{o}C before the H was removed and the H content of the samples measured.

Experiment 3(c):
This was identical to the experiment described in 3(a) but used 5083 alloy samples instead of commercial purity aluminium.

Results

In experiment one, the repeated H measurements showed that about 85% of the initial H content was removed from each sample during the first analysis in the LECO. Nearly all of the H was removed from the sample after three analyses, after which an average of 0.005 ppm H remained, (see Figure 1), (the accuracy of the device is claimed to be ± 0.005 ppm). Ten weeks later, after resting uncovered in a laboratory environment, both samples had absorbed H. 5083 alloy would be expected to have a porous MgO oxide surface layer, which is not protective, and which would allow continued reaction between the surface and atmospheric water vapour. The two samples were shown to have picked up almost as much H as their initial content, suggesting that this was the limit to which the solid alloy could absorb H.

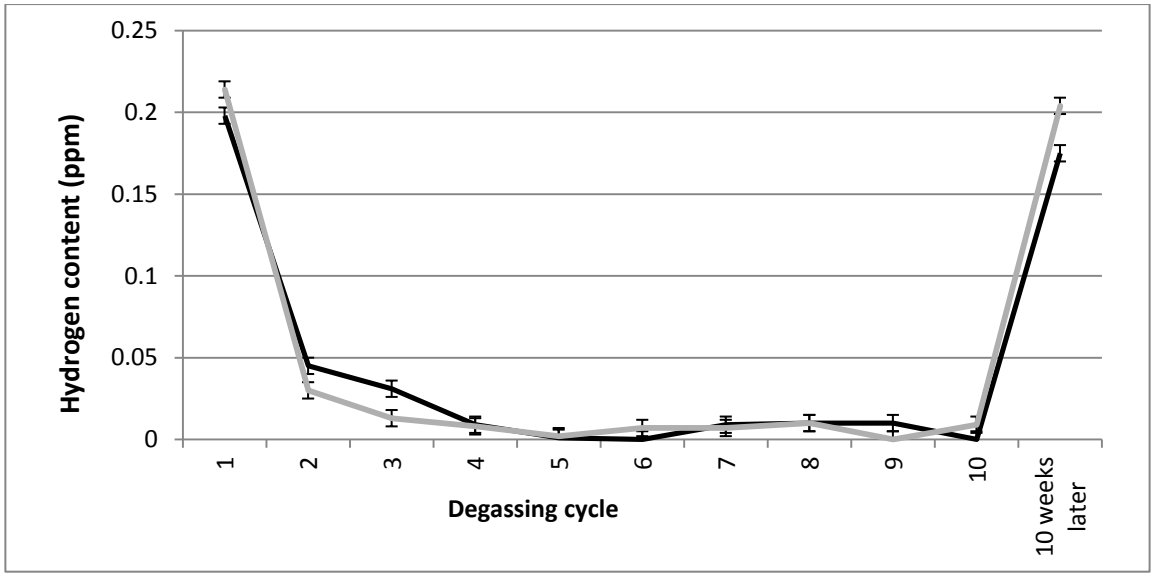

Figure 1: Two 5083 alloy samples measured using the LECO ten consecutive times. The absorption of H was evaluated ten weeks later.

Experiment two showed that the 5083 alloys placed in specific environments absorbed varying amounts of H. Figure 2 shows that the sample submerged in water and the sample in laboratory air absorbed 0.16 and 0.15 ppm of H respectively. In both cases moisture was readily available for reaction with the alloy. The sample that was placed in a sealed container (i.e. limited water vapour) was observed to have absorbed only 0.024 ppm of H after four days. The sample submerged in acetone also absorbed very little H, only 0.038 ppm.

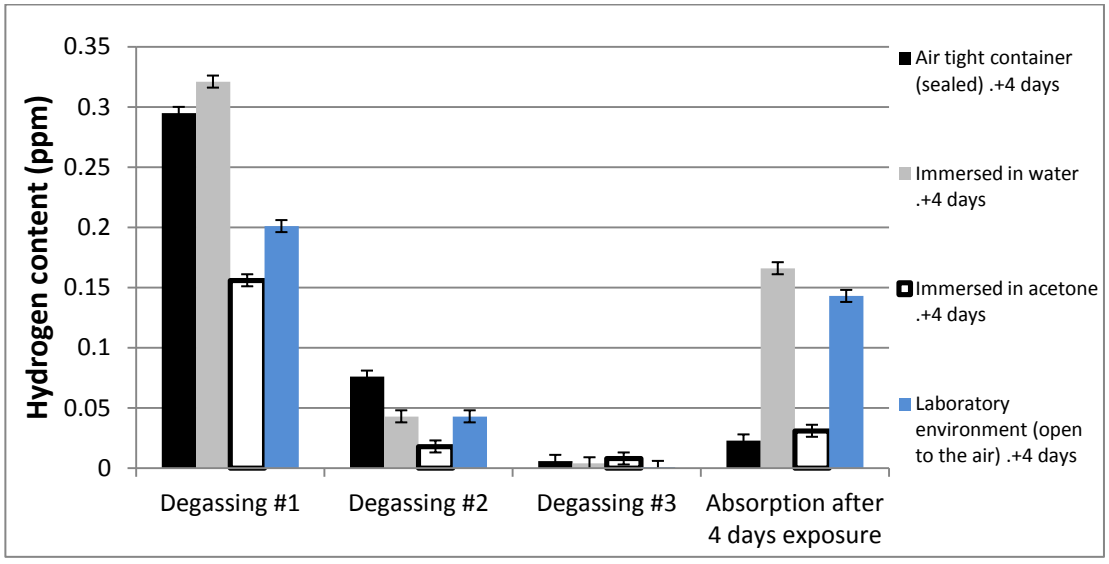

Figure 2: The degassing of 5083 alloy samples (three times) and the absorption of H into those samples after exposure to various environments.

In experiment 3, the H absorbed during each experiment, in air and in nitrogen, was determined by analysing each sample three times. The results are shown in Figure 3. The measured mean absorption

figures were, for Experiment 3(a) an increase of 0.04 ppm for the pure Al heated in air, for Experiment 3(b) an increase of 0.08 ppm for the pure Al heated in N_2 and, for Experiment 3(c) an increase of 0.279 ppm for the 5083 alloy heated in air.

SEM analysis of the commercial purity Al samples heated in nitrogen revealed that cracks that had developed in the original aluminium oxide film during expansion and melting were decorated with AlN crystals, (established by EDX). These crystals, shown in Figures 4(a) to 4(c), may have nucleated from the edges of the aluminium oxide layer and grown upon the aluminium exposed underneath,

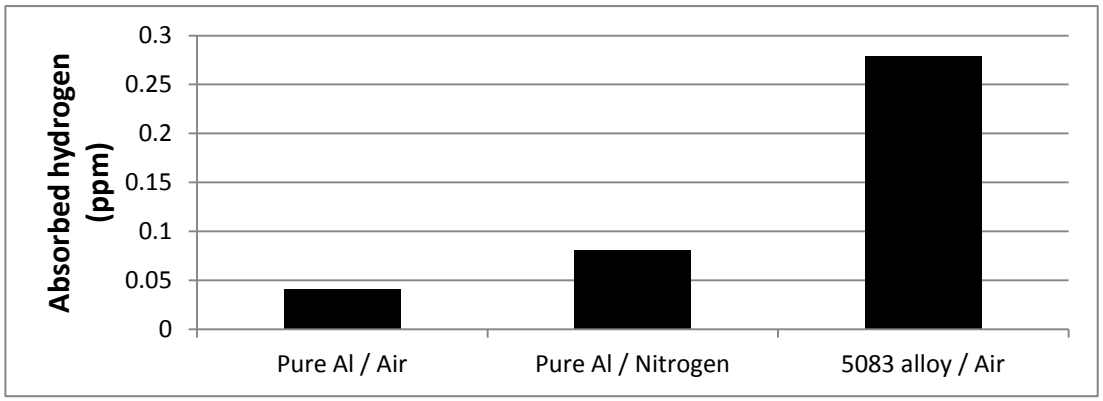

Figure 3: The absorption of H measured using the LECO.

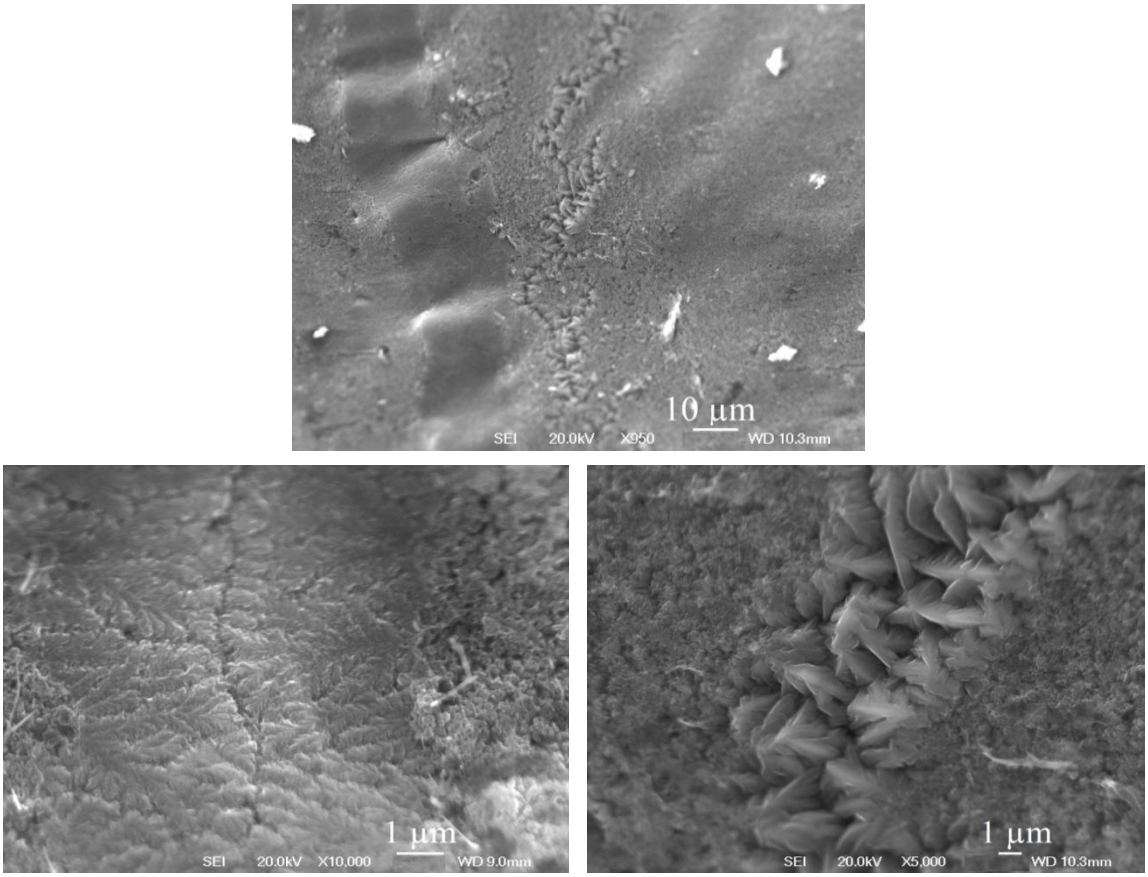

Figure 4: The surface of a commercial purity aluminium sample heated in nitrogen, showing cracks in the original oxide film (a). The cracks were observed to be covered with a mixture of (b) fine or (c) coarse AlN crystals.

Discussion

In experiment 3 the pure aluminium samples heated in both air and nitrogen absorbed measurable amounts of H. This demonstrated that H was able to diffuse through the aluminium oxide and nitride films on the surface of the specimens. But the H absorption of the pure aluminium samples heated in nitrogen was greater, by 0.04 ppm, or about double, a difference demonstrated to be statistically significant at the 95% level.

The original aluminium oxide film present on the surface of the commercial purity aluminium should have cracked during heating, due to thermal expansion. As the oxide film cracked the aluminium beneath was exposed to air, and instantaneous oxidation of the aluminium would occur, effectively healing the cracks as soon as they formed. When they were exposed to H, the gas must diffuse through the oxide film into the sample.

When the commercial purity aluminium samples were heated in nitrogen, however, the cracks in the oxide film that formed would allow the aluminium to react to form AlN, as shown in Figure 4. The AlN crystals may have nucleated and grew from both edges of the original aluminium oxide film, until they met and completely covered the cracks. The permeability of H through the nitride crystals was evidently greater (compared to the oxide) and these samples absorbed significantly more H. The

coarse AlN crystals shown in figure 4(c) appear interlocked, and it is proposed that the crystal structure has greater permeability for H because of this morphology. The experiments here demonstrate that H can diffuse through both aluminium oxide and AlN layers, but that the thickness and structure of the films likely influences the rate at which H can diffuse into the envelope over time, and that AlN offers less of a barrier to the passage of H than does alumina.

The 5083 alloy samples also readily absorbed H. This occurred because the MgO oxide that formed on the surface of the sample was permeable, allowing H to diffuse through the MgO. The internal atmosphere of a bifilm composed of MgO would be expected to react with the surrounding melt relatively quickly (compared to pure Al) because when the film cracks or tears, the oxygen contained within reacts with the melt to form a discontinuous oxide, which would easily tear again. Cracks that form in both MgO and any nitride that formed would also allow protons to diffuse into the internal atmosphere of the bifilm for continued reaction.

Conclusions

1. Repeated use of the LECO was used to degas aluminium samples to low H levels (<0.01 ppm).
2. Degassed 5083 alloy specimens absorbed H by reaction with atmospheric water vapour, as did specimens that were immersed in water. Specimens that were degassed and sealed in an air tight container absorbed very little H over a period of four days.
3. Degassed 5083 alloy specimens that were melted in air and exposed to H gas readily absorbed H as the porous MgO oxide surface film did not impede the diffusion of H.
4. In a low oxygen atmosphere, (such as might exist in a double oxide film defect), nitrogen will react with aluminium to form AlN at cracks or tears in oxide film.
5. Commercial purity aluminium specimens that were heated in air or nitrogen (forming Al_2O_3 or AlN on the surface, respectively) were both observed to absorb H. Absorption into samples that were heated in nitrogen was significantly greater, and about double, probably due to the formation of porous AlN crystals that grew within cracks in the original Al_2O_3 film.

Acknowledgements

The authors wish to thank EPSRC and Alcoa Europe for financial support.

References

[1] J. Campbell, Castings, 2nd Ed., Butterworth-Heinemann, Pp. 17-69, 2003.

[2] J. Campbell, "An Overview Of The Effects Of Bifilms On The Structure And Properties Of Cast Alloys," Metallurgical And Materials Transactions B, Vol. 37 A, Pp. 857-863, 2006.

[3] D. Dispinar And J. Campbell, “Porosity, H And Bifilm Content In Al Alloy Castings,” Materials Science And Engineering A, Vol. 528, Pp. 3860–3865, 2011.

[4] J. Campbell, “Entrainment Defects,” Materials Science And Technology, Vol. 22, Pp. 127-145, 2006.

[5] K. J. Brondyke And P. D. Hess, “Interpretation Of Vacuum Gas Test Results For Aluminium Alloys,” Transactions Of The Metallurgical Society Of Aime, Vol. 230, Pp. 1542 - 1546, 1964.

[6] X. G. Chen And J. E. Gruzleski, “Influence Of Melt Cleanliness On Pore Formation In Aluminium-Silicon Alloys,” International Journal Of Cast Metals Research, Vol. 9, Pp. 17-26, 1996.

[7] S. N. Tiwari And J. Beech, “Origin Of Gas Bubbles In Aluminium,” Metal Science, Vol. 12, No 8, Pp. 356-362, 1978.

[8] C. Nyahumwa, N. R. Green And J. Campbell, "Effect Of Mould Filling On Fatigue Properties Of Cast Aluminium Alloys," AFS Transactions, Vol. 58, Pp. 215-223, 1998.

[9] R. Raiszadeh And W. D. Griffiths, “A Method To Study The History Of A Double Oxide Film Defect In Liquid Aluminium Alloys,” Shape Casting: The John Campbell Symposium, Tms (The Minerals, Metals & Materials Society), Pp. 865-871, 2005.

[10] W. C. Sleppy, “Oxidation Of Molten High Purity Aluminium In Dry Oxygen,” Journal Of The Electrochemical Society, Vol. 108, Pp. 1097-1102, 1961.

[11] D. J. Talbot, The Effect Of H In Aluminium And Its Alloys, Leeds: Maney, Pp. 8-64, 2004.

[12] T. L. Cottrell, The Strengths Of Chemical Bonds, 2d Edition., London: Butterworth, 1958.

[13] T. H. Yamada, “H Permeation Barrier Performance Characterization Of Vapor Deposited Amorphous Aluminum Oxide Films Using Coloration Of Tungsten Oxide,” Surface And Coatings Technology, Vols. 153(2-3), Pp. 114-118, 2002.

[14] S. Aggarwal, “Use Of Amorphous Aluminium Oxide On A Capacitor Sidewall For Use As A H Barrier,” Patent , No. Us6876021 B2, 2005.

[15] N. B. Pilling And R. E. Bedworth, “The Oxidation Of Metals At High Temperatures,” Journal Of The Institute Of Metals, Vol. 29, Pp. 529-582, 1923.